Flow Facility Design and Experimental Studies of Wall-Bounded Turbulent Shear-Flows

by

Björn Lindgren

December 2002 Technical Reports from Royal Institute of Technology Department of Mechanics SE-100 44 Stockholm, Sweden



Björn Lindgren 2002 Flow facility design and experimental studies of wall-bounded turbulent shear-flows

Department of Mechanics, Royal Institute of Technology SE-100 44 Stockholm, Sweden

Abstract

The present thesis spans a range of topics within the area of turbulent flows, ranging from design of flow facilities to evaluation of scaling laws and turbulence modeling aspects through use of experimental data. A new wind-tunnel has been designed, constructed and evaluated at the Dept. of Mechanics, KTH. Special attention was directed to the design of turning vanes that not only turn the flow but also allow for a large expansion without separation in the corners. The investigation of the flow quality confirmed that the concept of expanding corners is feasible and may be successfully incorporated into low turbulence wind-tunnels. The flow quality in the MTL wind-tunnel at the Dept. of Mechanics, KTH, was also investigated confirming that it still is very good. The results are in general comparable to those measured when the tunnel was new, with the exception of the temperature variation that has decreased by a factor of 4 due to an improved cooling system.

Experimental data from high Reynolds number zero pressure-gradient turbulent layers have been investigated. These studies have primarily focused on scaling laws with e.g. confirmation of an exponential velocity defect law in a region, about half the size of the boundary layer thickness, located outside the logarithmic overlap region. The streamwise velocity probability density functions in the overlap region was found to be self-similar when scaled with the local rms value. Flow structures in the near-wall and buffer regions were studied and e.g. the near-wall streak spacing was confirmed to be about 100 viscous length units although the relative influence of the near-wall streaks on the flow was found to decrease with increasing Reynolds number.

The separated flow in an asymmetric plane diffuser was determined using PIV and LDV. All three velocity components were measured in a plane along the centerline of the diffuser. Results for mean velocities, turbulence intensities and turbulence kinetic energy are presented, as well as for streamlines and backflow coefficient describing the separated region. Instantaneous velocity fields are also presented demonstrating the highly fluctuating flow. Results for the above mentioned velocity quantities, together with the production of turbulence kinetic energy and the second anisotropy invariant are also compared to data from simulations based on the $k-\omega$ formulation with an EARSM model. The simulation data were found to severely underestimate the size of the separation bubble.

Descriptors: Fluid mechanics, wind-tunnels, asymmetric diffuser, turbulent boundary layer, flow structures, PDFs, modeling, symmetry methods.

Preface

This thesis concerns design and calibration of flow facilities (with special attention to wind-tunnels) as well as experimental studies of wall-bounded turbulent shear-flows (zero pressure-gradient boundary layer and plane asymmetric diffuser). Modeling aspects are tested by use of the data from the diffuser experiment and new theoretical ideas emanating from Lie group symmetry methods are evaluated by use of zero pressure-gradient turbulent boundary layer data. It is based on the following papers.

- **Paper 1.** Lindgren, B., Österlund, J. M. & Johansson, A. V. 1998 Measurement and calibration of guide-vane performance in expanding bends for wind-tunnels. Published in *Exp. in Fluids*, 24, 1998
- **Paper 2.** Lindgren, B. & Johansson, A. V. 2002 Design and evaluation of a low-speed wind-tunnel with expanding corners. Published as a Technical Report, TRITA-MEK 2002:14
- **Paper 3.** Lindgren, B. & Johansson, A. V. 2002 Evaluation of the flow quality in the MTL wind-tunnel. Published as a Technical Report, TRITA-MEK 2002:13
- **Paper 4.** Österlund, J. M., Lindgren, B. & Johansson, A. V. 1999 Flow structures in zero pressure-gradient turbulent boundary layers at high Reynolds numbers. Submitted to *Eur. J. of Mech. B / Fluids*
- **Paper 5.** Lindgren, B., Österlund, J. M. & Johansson, A. V. 2002 Evaluation of scaling laws derived from Lie group symmetry methods in zero pressure-gradient turbulent boundary layers. Submitted to *J. Fluid Mech.*

- **Paper 6.** Lindgren, B., Johansson, A. V. & Tsuji Y. 2002 Universality of probability density distributions in the overlap region in high Reynolds number turbulent boundary layers. Submitted to *Phys. Fluids*
- **Paper 7.** Lindgren, B. Törnblom O. & Johansson, A. V. 2002 Measurements in a plane asymmetric diffuser with 8.5° opening angle. Part I: General flow characteristics. To be submitted.
- **Paper 8.** Törnblom O., Lindgren, B., Gullman-Strand, J. & Johansson, A. V. 2002 Measurements in a plane asymmetric diffuser with 8.5° opening angle. Part II: Comparison with model predictions for turbulence characteristics. To be submitted.

Division of work between paper authors

The papers included in this thesis have been written in collaboration with other researchers. Below follows a description of the contribution the respondent made to the different papers. Prof. Arne V. Johansson acted as supervisor and project leader in all investigations. The respondent made a major part of the writing of the papers, if not otherwise stated below.

- Paper 1. This work was made by the respondent with Dr. Jens M. Österlund acting as a second supervisor introducing the respondent into the field of experiments. The respondent presented this work at the conference Wind-tunnels and wind-tunnel test techniques, Cambridge, UK, 1997, and a written contribution was included in the conference proceedings.
- Paper 2. The work in this paper was performed by the respondent. The work consisted in design and construction of the wind-tunnel parts, project managing including purchases and contact with subcontractors as well as the measurements and analysis of the flow quality when the construction work was finished.
- **Paper 3.** Most of the measurements of the flow quality were performed by the respondent but some measurements (total pressure and temperature) were performed by Msc. Valeria Durañona. The respondent performed the analysis of the experimental data.
- Paper 4. This paper also appears in Dr. Jens M. Österlund's thesis under a somewhat different name and content. The paper has been extended and rewritten. The measurements were carried out by Dr. Jens M. Österlund. The analysis of the experimental data was equally shared between Dr. Jens M. Österlund and the respondent. The respondent performed the extended analysis contained in the revised version of the paper. The respondent presented this work at the 8th European Turbulence Conference, Barcelona, Spain, 2000, and a written contribution was included in the conference proceedings.

- Paper 5. The measurements were performed by Dr. Jens M. Österlund and the respondent performed the analysis of the experimental data. The theoretical analysis was performed together with Prof. Arne V. Johansson. The main part of this work was presented as an invited talk at the IUTAM Symposium on Reynolds number scaling in turbulent flow, Princeton, USA, 2002 by Prof. Arne V. Johansson.
- Paper 6. This work was a collaboration with Prof. Yoshiyuki Tsuji from Nagoya University, Japan who for this purpose visited KTH in July 2002. The original ideas came from Prof. Tsuji who together with the respondent analyzed the experimental data. The measurements were performed by Dr. Jens M. Österlund. The respondent presented this work at the IUTAM Symposium on Reynolds number scaling in turbulent flow, Princeton, USA, 2002.
- Paper 7. This work was made in collaboration on equal terms with Msc. Olle Törnblom. It was presented at the 9th European Turbulence Conference, Southampton, UK, 2002 by Msc. Olle Törnblom and at the 11th International symposium on application of laser techniques to fluid mechanics, Lisbon, Portugal, 2002 by the respondent, with written contributions to the conference proceedings.
- Paper 8. Same as for paper 7 with the exception that the major part of the writing was done by Msc. Olle Törnblom and the simulations were performed by Lic. Johan Gullman-Strand. Parts of the work was presented at the 9th European Turbulence Conference, Southampton, UK, 2002 by Msc. Olle Törnblom and at the 11th International symposium on application of laser techniques to fluid mechanics, Lisbon, Portugal, 2002 by the respondent, with written contributions to the conference proceedings.



Contents

Prefa	ce	V
Div	ision of work between paper authors	vi
Chap	ter 1. Introduction	1
Chap	ter 2. Basic concepts in wall-bounded shear-flows	10
2.1.	Navier-Stokes and Reynolds equations	10
2.2.	Turbulent boundary layer flow	11
2.3.	Closure problem in turbulence models	13
2.4.	Basics of Lie group symmetry methods	14
Chap	ter 3. Results	16
3.1.	Wind-tunnel design and calibration	16
3.2.	Evaluation of turbulent boundary layer data	20
3.3.	Plane asymmetric diffuser flow	27
Chap	ter 4. Concluding remark and outlook	30
Ackn	$\mathbf{owledgment}$	32
Biblio	ography	33
Paper	rs	
Meas	urement and calibration of guide-vane performance in	
	expanding bends for wind-tunnels	41
1.	Introduction	41
2.	Methods of calculating total pressure-loss coefficient and lift coefficient	42
3.	Experimental apparatus	46
4.	Measurements of the total pressure-loss coefficient	47

x CONTENTS

5.	Calculations of infinite cascade with experimental vane	
	and vane optimization	53
6. Discussion		
	cknowledgments	59
Re	eferences	59
Desig	gn and evaluation of a low-speed wind-tunnel with expanding	;
	corners	63
1.	Introduction	63
2.	The wind-tunnel design	66
3.	Experimental setup	84
4.	Results	88
5.	Concluding remarks	101
6.	Acknowledgment	103
$R\epsilon$	eferences	103
Evalı	uation of the flow quality in the MTL wind-tunnel	109
1.	Introduction	109
2.	Experimental setup	115
3.	Results	120
4.	Concluding remarks	137
5 .	Acknowledgment	138
$\mathbf{R}\epsilon$	eferences	138
Ap	ppendix	141
Flow	structures in zero pressure-gradient turbulent boundary	
	layers at high Reynolds numbers	147
1.	Introduction	147
2.	Experimental facility	150
3.	Experimental procedure	151
4.	Results	154
5.	Concluding remarks	163
6.	Acknowledgments	164
$R\epsilon$	eferences	164
Evalı	nation of scaling laws derived from Lie group symmetry	
	methods in zero pressure-gradient turbulent bounda	$\mathbf{r}\mathbf{y}$
	layers	169
1.	Introduction and theoretical considerations	169

	CONTENTS	xi
2.	Results	175
3.	Concluding remarks	192
4.	Acknowledgment	193
$\mathbf{R}\epsilon$	eferences	193
5 .	Appendix A: Lie group symmetry methods for differential	l
	equations	195
6.	Appendix B: Derivation of an expression for the Reynolds	8
	shear-stress in the wake region	199
Univ	versality of probability density distributions in the overlap	
	region in high Reynolds number turbulent boundary	
	layers	205
1.	Introduction	205
2.	The KTH data-base of zero pressure-gradient turbulent	200
9	boundary layer flow	206
3.	Results Concluding remarks	206
4.	Concluding remarks	213
5. D	f Acknowledgment eferences	215 215
Rθ	eierences	213
Meas	surements in a plane asymmetric diffuser with 8.5° opening	3
	Angle. Part I: General flow characteristics	219
1.	Introduction	219
2.	Experimental setup	222
3.	Results	229
4.	Concluding remarks	240
5 .	Acknowledgment	242
$R\epsilon$	eferences	242
Meas	surements in a plane asymmetric diffuser with 8.5° opening	5
	angle. Part II: Comparison with model predictions	
	for turbulence characteristics	247
1.	Introduction	247
2.	Turbulence models	250
3.	Results	253
4.	Concluding remarks	259
5.	Acknowledgement	261
$\mathbf{R}\epsilon$	eferences	261

CHAPTER 1

Introduction

The development of tools enabling measurements of aerodynamic forces, *i.e.* forces exerted on solid bodies by fluids, such as wind-tunnels, are closely related to the development of heavier than air flying objects, the so called aerodynes. Man has dreamed of flying for a very long time. Most of the early attempts made were based on observations of birds in flight and therefore involved flapping wings, the so called ornithopters. These early attempts were all failures, except perhaps for Daedalus and his son Icarus who managed to take off and escape from the prison tower. Sadly Icarus flew to close to the sun with for us known consequences. In the late 15th and early 16th century Leonardo da Vinci was involved in creating flying machines but all his attempts were based on ornithopters and they failed. However, he also made other studies of fluids in motion, *e.g.* of water flowing past bridge pillars in rivers. This illustrates that the first facility used for flow studies was the nature itself. The unpredictable behaviour of nature later lead to the need for more controlled environments where studies of fluid motion could be performed.

In the 18th century a deeper understanding of the subject of aerodynamics was still lacking, although many studies were made, including measurements of aerodynamic forces. During these early experiments it was found that the force exerted by a fluid on a solid body was a function of the relative speed between the fluid and the body. This understanding lead to the fundamental principle on which all flow devices are based, namely that one can either move the body through the air or keep the body still and move the air, of which the second option is used in wind-tunnels. The first, and simplest, attempts were to make use of the natural wind. It was though abandoned because of the unreliable behaviour of the wind source, with varying speed and direction. The next step was to use a whirling arm, with the model (solid body) mounted at the end of an arm driven by a falling weight, to produce the relative speed between the model and the fluid. Robins, one of the earliest experimentalists in this field found in the 18th century that the relationship between body shape, orientation and flow was much more complex than predicted by the theories previously used.

It was not until the early 19th century that systematic investigations of lift and drag of airfoils were made. Cayley used a whirling arm to perform 2

such studies and from the results he found he made a small unmanned glider that is believed to be the first successful heavier than air machine. He also concluded that the wings should be fixed, and not flapping, and that the thrust should be produced by some other auxiliary power source. This, however, did not mean the end of the ornithopters. Many efforts have since been made to achieve bird-like flight resulting in nothing but a few good laughs watching old newsreels. However, nowadays there are actually small and light unmanned flying ornithopters driven by rubber band motors.

In the late 19th century it became apparent that the whirling arm was not the optimum tool for aerodynamic studies. A major drawback beside the rotation effects is that the model keeps flying into its own wake. This is not good since the chaotic motion of the fluid (turbulence) in a wake negatively affects the behaviour of the model. Instead wind-tunnels were developed where the model is still and the airflow, usually produced by a fan, passes by the model. The Wright brothers were among the first to understand the usefulness of wind-tunnels in aerodynamic design. They started out by measuring the aerodynamic forces in natural wind using a balance to quantify the effect of camber on lift. They soon found this method inadequate and started doing experiments using a bicycle to achieve the relative difference in velocity between the model and the air. The data they collected encouraged them to continue but instead using a wind-tunnel. They started with a simple tunnel but soon build a more sophisticated one including screens and honeycomb for better flow quality in the test section where the measurements are made. However, they made one error locating the fan at the tunnel inlet which resulted in a swirling flow in the test section. With this tunnel they could finally solve the handling problems of their No. 3 glider in 1902 and the year after they added a 12 hp engine and two counter rotating propellers for their famous 1903 Wright flyer. Next year (2003) there will be many celebrations, conferences and meetings celebrating the 100th anniversary of this event.

The impact of the Wright brothers flying machine was big and an understanding of the importance of wind-tunnels on aircraft development was growing, especially in Europe where government-founded laboratories started building large wind-tunnel facilities till the beginning of world war I in 1914. It was during this era that the two major types of wind-tunnels were developed. The open circuit tunnel or Eiffel tunnel, named after the famous French engineer, and the closed return circuit tunnel or the Prandtl (Göttingen) tunnel, that is named after Prandtl and the German university where it was first built.

There are many ways to classify wind-tunnels. Here I will shortly recapitulate some of the most common ones.

Wind-tunnels may be categorized by the kind of fluid it operates with. As the name wind-tunnel indicates, one commonly uses air but there are also tunnels where water or oil are used. Besides air sometimes other gases are used

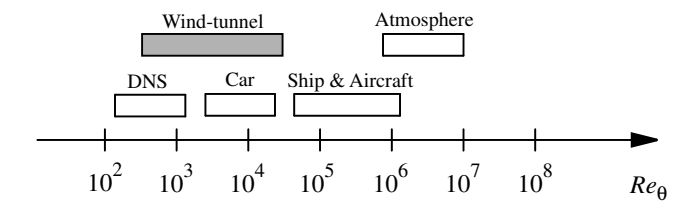


FIGURE 1.1. A sketch of the Reynolds number for different applications. (From Österlund (1999b) with permission.)

with the intended purpose of giving the tunnel more favorable properties. The reason for choosing a specific fluid may vary but one reason can be to maximize the Reynolds number. The Reynolds number, named after the famous British scientist who performed experiments on transition in a pipe using dye, (Reynolds (1883)), is a non-dimensional measure of the relative influence of inertial to viscous forces. The Reynolds number can be used as a scaling parameter. Equal Reynolds number in a model experiment and in reality means that the two cases are in some sense dynamically comparable. There are of course other factors that come into play as well but the Reynolds number is an important parameter. Depending on the choice of fluid, the speed of the fluid and the size of the model in the wind-tunnel different Reynolds numbers are achieved. Usually in real applications the Reynolds number is very large. Larger than what is achievable in most wind-tunnel tests, see figure 1.1. The most common choice of a fluid is air and the flow facilities described in this thesis all use air. For a given fluid, the Reynolds number may be increased by the use of larger models or faster test section speeds.

The speed of the air in the test section is common for classifying wind-tunnels. We have e.g. hypersonic, supersonic, transonic and subsonic wind-tunnels where the three first groups include wind-tunnels with very high speeds around or above the speed of sound where the compressibility of the air becomes important. The tunnels at the Department of Mechanics are nowadays all subsonic, i.e. with speeds well below the speed of sound. Subsonic tunnels may in turn be divided into high-speed and low-speed wind-tunnels and the tunnels referred to in this thesis are of the low-speed type that typically have maximum test section speeds below $100~\mathrm{m/s}.$

Another way to categorize wind-tunnels are by the intended purpose of use. There are e.g. smoke tunnels for flow visualization, automobile tunnels for testing cars, trucks etc, that often have moving floors to simulate the road. Remember that the car is still so the road has to move instead. There are meteorological-environmental tunnel to simulate earth boundary layers which are used to study flow around buildings etc. There are also low-turbulence

4 1. INTRODUCTION

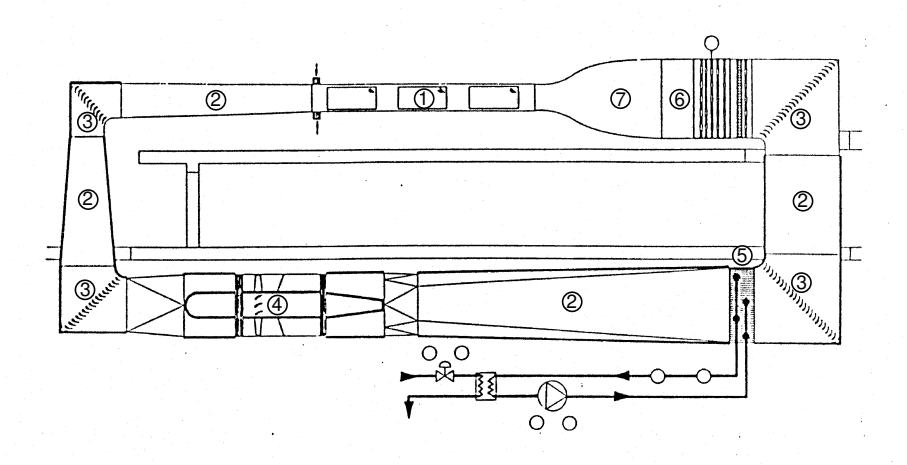


FIGURE 1.2. The MTL wind-tunnel at the Department of Mechanics, KTH.

tunnels that are used to study the fundamental physics of moving fluids. The tunnels treated in this thesis are of this last mentioned type.

The low-turbulence tunnels are characterized by, as indicated in the name, the low level of flow disturbances in the test section. This is achieved by the use of a high contraction ratio, screens and honeycombs which lower the turbulence level and mean flow variations. They are usually of closed circuit type with carefully designed guide-vanes in the corners turning the flow with minimum losses and flow disturbances. They have conservative design of diffusers etc to avoid boundary layer separation. They are also characterized by their relatively high ratio between test section length and cross section area which makes it possible to achieve high Reynolds numbers without high test section speeds. This is advantageous since the typical scales in the flow become larger and thereby easier to measure if the high Reynolds number is achieved by increasing size rather than speed. An example of a low turbulence wind-tunnel is the MTL wind-tunnel, shown in figure 1.2, which is the largest wind-tunnel at the Department of Mechanics, KTH. It has a 7 m long test section with a 1.2×0.8 m² cross section area. The main purpose of this wind-tunnel, and the other new wind-tunnel at the department, is to provide a good experimental environment where accurate measurements on transition and turbulence can be performed. Many successful experiments have been performed in the MTL tunnel since its inauguration in 1991. The MTL tunnel was later complemented by a new smaller wind-tunnel with similar characteristics (see figure 1.3) but with the special design feature of expanding corners.

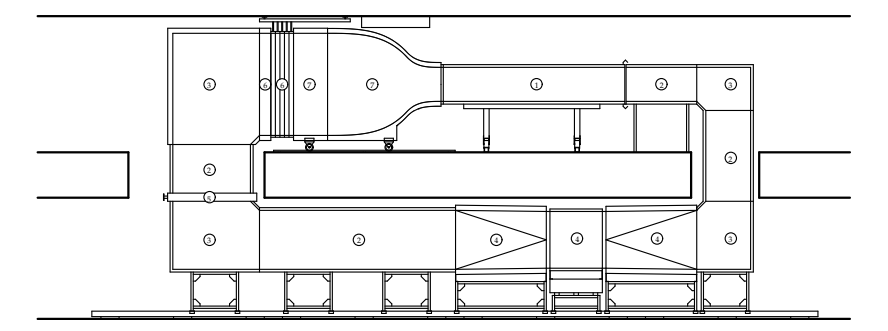


FIGURE 1.3. The new wind-tunnel at the Department of Mechanics, KTH.

One of the experiments performed in the MTL tunnel was that by Jens M. Osterlund (see Osterlund (1999b) from which mean flow data are available in a data-base at Osterlund (1999a)). The measurements were carried out in a turbulent boundary layer on a flat plate mounted in the MTL wind-tunnel. The experimental data collected have been used in this thesis in the three papers, Flow structures in zero pressure-gradient turbulent boundary layers at high Reynolds numbers, Universality of probability density distributions in the overlap region in high Reynolds number turbulent boundary layers and Evaluation of scaling laws derived from Lie group symmetry methods in zero pressure-gradient turbulent boundary layers. The flat plate boundary layer flow is a simple generic case which describes the flow close to body surfaces. Choosing a flat plate instead of a more complicated body simplifies the analysis and helps to interpret the physical phenomena in such flows. Boundary layer flows have been investigated for a long time and it was Prandtl who in 1904 (see Prandtl (1904)) invented the concept of boundary layers. He found that friction (viscosity) is important only in a layer very close to the body surface. If the Reynolds number is high enough the flow within this layer becomes chaotic or turbulent, i.e. a turbulent boundary layer. Most scaling laws derived for this kind of flow deals with infinite, or very high, Reynolds numbers which means that one of the main efforts is to achieve experimental results for as high Reynolds number as possible without compromising the measurement accuracy.

Among the early important work on turbulent boundary layer flow are those of Schultz-Grunow (1940), Ludwieg & Tillman (1950), Klebanoff (1955) and Smith & Walker (1959). There are also important review papers to mention, where a more thorough survey can be found like the classical paper by Coles (1962) and more recently by Fernholz & Finley (1996).

The Osterlund experiments were performed at fairly high Reynolds numbers, Re_{θ} , (based on momentum-loss thickness and free-stream velocity) up to about 30000. There are several other scientific groups currently performing

similar experiments on zero-pressure gradient turbulent boundary layers. For instance, the group of Hassan Nagib at IIT, Chicago, USA, have performed measurements of the streamwise mean velocity component on a flat plate at Reynolds numbers based on momentum-loss thickness up to approximately 70000 (see Hites (1997) and Nagib et al. (2002)). Experiments have also been performed in the commercial DNW tunnel in the Netherlands by Hans H. Fernholz's group from TU, Berlin, Germany. They have carried out measurements both directly on the wind-tunnel test section wall and on a separate boundary layer plate, and have achieved Reynolds numbers up to $Re_{\theta} = 115000$, (see Fernholz et al. (1995) and Knobloch & Fernholz (2002)). In Melbourne, Australia, measurements on a wind-tunnel floor were performed in an open tunnel with a 27 m long test section covering a Reynolds number range up to $Re_{\theta} = 60000$ (see Jones et al. (2002)). A problem with some of the measurements performed by the two latest groups is that the skin friction have not been measured independently. This somewhat limits the usefulness of the experimental data since an independent measurement of the skin friction is often fundamental in the validation of scaling laws. Experiments at extremely high Reynolds numbers ($\sim 10^6$) are currently under preparation by Alexander Smits et al. at Princeton University, Princeton, USA. They can achieve such Reynolds numbers by pressurizing the air and thereby increasing its density. The drawback of this method is that the turbulent scales become very small and difficult to resolve. There is also a prospect to build a very large wind-tunnel in Göteborg, Sweden, with very good flow quality and a 30 m long test section. This project goes under the name of the Nordic wind-tunnel and has an aim of enabling zero-pressure gradient turbulent boundary layer experiments at very high Reynolds numbers, (see Wosnik et al. (2002)).

The above mentioned measurements are all made with traditional techniques like hot-wire anemometry and Pitot tubes. In hot-wire anemometry a small wire with a diameter of 0.5-5 μ m and a length of about 1 mm depending on wire diameter is heated by an electrical current passing through the wire. The wire is then cooled by the passing air and by measuring the amount of power needed to keep the wire temperature constant or the wire temperature (resistance) for a given power input, the flow velocity and temperature can be measured. Pitot tubes measures the total pressure of the passing air and by relating this pressure to the static pressure the flow velocity can be measured.

Kähler et al. (2002) have made experiments at fairly high Reynolds numbers ($Re_{\theta} = 7800$) in a zero pressure-gradient turbulent boundary layer using Particle Image Velocimetry. The above mentioned techniques gives mean or time resolved velocity data but this technique enables instantaneous views of the flow field in a plane giving two or three velocity components. PIV is a fairly young measurement technique, invented in the 1980th and still under considerable improvement but it will become more widely used in boundary layer kind of flows in the future. It is especially useful when flow separation

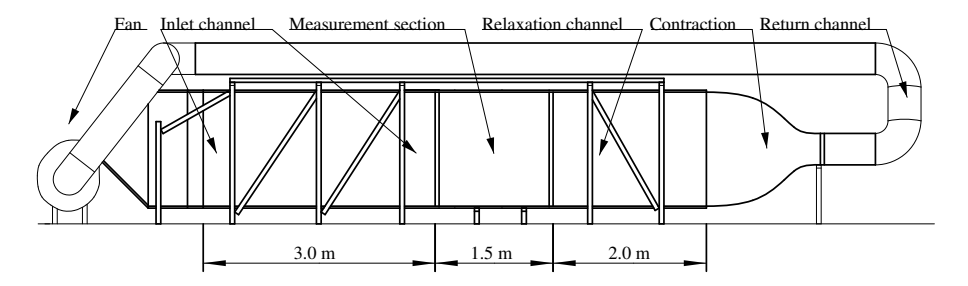


FIGURE 1.4. The flow facility used in the plane asymmetric diffuser measurements.

is present because it yields both direction and absolute value of the velocity. Separated turbulent boundary layer flow has been studied using PIV by e.g. Angele (2002).

During the last decade or so, also important numerical simulation work have been made on turbulent boundary layer flow. The first direct numerical simulation was performed by Spalart (1988), who achieved a Reynolds number of $Re_{\theta} = 1410$. More recently other contributions have been made including also simulations with adverse pressure gradients, see e.g. Spalart & Coleman (1997), Na & Moin (1998) and Skote et al. (1998). The fast advances made in computer processing speed decreases the gap in Reynolds number between direct numerical simulations and wind-tunnel experiments although at present date this gap is still rather large, see figure 1.1. Martin Skote (private communication) has calculated the time needed to perform a direct numerical simulation of a zero pressure-gradient boundary layer with $Re_{\theta} = 10000$ using all processors at the new Earth Simulator in Japan and found that it could be done in about six month. It would be very important if such a simulation could be performed, because the Reynolds number is high enough to significantly contribute in solving still open issues (e.g. the log-law vs. power-law behaviour of the streamwise mean velocity in the overlap region).

There are turbulent flows that are better studied in other measurement facilities than the all purpose wind-tunnel. It can be experiments where the pressure-drop will be so high that the fan, which is usually axial in a wind-tunnel, cannot deliver a high enough pressure increase for the experiments to be performed. In such cases a flow facility more suited for the particular experiment has to be built. In the early stages of a project involving flow measurements and control in a plane asymmetric diffuser, the intention was to perform the experiments in the newly built low-speed wind-tunnel, which is described in the paper Design and evaluation of a low-speed wind-tunnel with expanding corners, in this thesis. Due to some limitations of this all purpose wind-tunnel, like the pressure increase capacity of the fan and the limiting aspect ratio that could be achieved in the test section, the experiment

could not be successfully performed. Instead it was decided that a new flow facility (wind-tunnel), see figure 1.4, specifically designed for measurements in the plane asymmetric diffuser geometry, had to be built. This flow facility is driven by a centrifugal fan which delivers enough pressure for the experiments to be performed at the intended Reynolds number of 2000 based on the friction velocity and the inlet channel height.

Most measurements were performed using optical techniques like Particle Image Velocimetry and Laser Doppler Velocimetry which involves seeding particles, in this case from smoke. A return circuit was made to allow the smoke to be more evenly distributed in the test section and prevent the lab from being filled with smoke. The results from these measurements and comparisons with results obtained in simulations are presented in two papers in this thesis, Measurements in a plane asymmetric diffuser with 8.5° opening angle. Part I: General flow characteristics and Measurements in a plane asymmetric diffuser with 8.5° opening angle. Part II: Comparison with model predictions for turbulence characteristics. The plane asymmetric diffuser flow includes many interesting flow features, such as an adverse pressure gradient, flow separation, locally high values of turbulence intensity and anisotropy, and streamline curvature, which makes it a complex flow to study despite the simple geometry.

The measurements reported here are not the first in a plane asymmetric diffuser, Obi et~al.~(1993a), made measurements in the same kind of flow but with a larger opening angle. They also made some comparisons with $k-\varepsilon$ turbulence models. later they continued their efforts and studied the effect of blowing and suction in a spanwise slit on the inclined wall, (see Obi et~al.~(1993b)). In 1997 they made more control investigations and studied the process of momentum transfer in the diffuser (see Obi et~al.~(1997)). The two-dimensionality in their measurements was not quite satisfactory, which encouraged Buice & Eaton (2000) to perform new measurements in the same geometry. Those measurements were intended as reference data for a Large Eddy Simulation performed by Kaltenbach et~al.~(1999). To achieve better two-dimensionality of the mean flow they increased the aspect ratio of the plane asymmetric diffuser.

There has also been many efforts to test turbulence models in this demanding flow. Many of the features typical of this flow, as those mentioned above, are very difficult to predict in a simulation with turbulence models. This makes it a useful test case for turbulence model testing and development. Some examples of work in this field are Hellsten & Rautaheimo (1999), Apsley & Leschziner (1999), Gullman-Strand et al. (2002) and Kaltenbach et al. (1999). The models tested range from simple $k - \varepsilon$ models to LES, most with moderate success. To be able to learn more about what makes all these models fail in predicting some of the flow features it is important to have a complete set of experimental data for comparisons. However, in all the experiments mentioned above only the velocity components in the streamwise and wall-normal directions were measured. In the separated flow region close to the inclined

wall of the diffuser the amount of experimental data available is also limited. Therefore it was decided to perform new measurements using optical measurement techniques which are very suitable for measurements in separated flows. The opening angle was also changed to 8.5° from the previously used 10° to achieve a flow with a somewhat smaller separated region.

The purpose of these new measurements is to produce a complete data-base including experimental data for all three velocity components. This data-base will be made available for use by turbulence modelers and for comparisons with large eddy and direct numerical simulations. Finding methods of controlling the flow and eliminating the separation bubble is also included in the project. Limited control work have been done by applying a spanwise row of vortex generators which successfully eliminated the separation bubble. More advanced control methods will be tested in the future (see section 4)

The effort of understanding the flow phenomena in duct and diffuser flows and especially achieving efficient control of such flows in terms of eliminating separation and minimizing the pressure drop has increased recently. This kind of flow is very common in engineering and industrial application ranging from ventilation systems, through aircraft air intakes to hydro power plant draft tubes and many other cases. Optimizing these systems can lead to huge gains in energy saving and also improve the efficiency and prolong the expected lifetime of an apparatus by *e.g.* minimizing flow induced vibrations. Although much work has been done on internal flows there is still much more work to be done before a complete understanding of this flow is obtained.

CHAPTER 2

Basic concepts in wall-bounded shear-flows

2.1. Navier-Stokes and Reynolds equations

In the fluid flow cases treated in this thesis the flow is governed by the incompressible Navier-Stokes and continuity equations. Claude Louis Marie Henri Navier was born i Dijon, France in 1785 and died in Paris, France in 1836. Navier, once a student of Fourier, derived the Navier-Stokes equations for incompressible flow in 1821-1822 modifying the Euler equations. Without understanding the concept of shear-stress he instead took into account, what he considered as, forces between the molecules in the fluid. George Gabriel Stokes was born in Skeen, Ireland in 1819 and died in Cambridge, England in 1903. Stokes derived the Navier-Stokes equations in 1845 without knowing that these equations already were derived by Navier. Although he found out before publishing he decided that he had derived the equations in a sufficiently different manner compared to Navier and that his work was still worth publishing.

The incompressible Navier-Stokes equations and the continuity equation read

$$\frac{\mathrm{D}U_{i}}{\mathrm{D}t} = -\frac{1}{\rho} \frac{\partial P}{\partial x_{i}} + \nu \frac{\partial^{2} U_{i}}{\partial x_{i}^{2}} \tag{2.1}$$

$$\frac{\partial U_i}{\partial x_i} = 0 \tag{2.2}$$

where U_i is the velocity vector, P is the pressure, t is the time, x_i is the spatial vector, ρ is the density and ν is the kinematic viscosity of the fluid. The material time derivative can be written as

$$\frac{\mathrm{D}U_i}{\mathrm{D}t} = \frac{\partial U_i}{\partial t} + U_j \frac{\partial U_i}{\partial x_j} \tag{2.3}$$

For turbulent flows it is often useful to divide the velocity vector and pressure into a mean and a fluctuating part. This division is referred to as the Reynolds (1895) decomposition, after Osborne Reynolds (1842-1912), and for the velocity vector and the pressure it reads

$$U_i(x_i, t) = \overline{U}_i(x_i) + u_i(x_i, t), \tag{2.4}$$

$$P(x, y, z, t) = \overline{P}(x_i) + p(x_i, t), \qquad (2.5)$$

where the bar denotes averaged quantity and small letter denotes the fluctuating part. For the Reynolds decomposition to make sense the flow has to be steady, *i.e.*

$$\frac{\partial \overline{U}_i}{\partial t} = 0, \tag{2.6}$$

or varying on a time scale that is much larger than the time scales of the turbulence. Introducing this decomposition into the Navier-Stokes equations and averaging results in the Reynolds averaged equations which together with the continuity equation read

$$\overline{U}_{j}\frac{\partial \overline{U}_{i}}{\partial x_{j}} = -\frac{1}{\rho}\frac{\partial \overline{P}}{\partial x_{i}} + \nu \frac{\partial^{2} \overline{U}_{i}}{\partial x_{j}^{2}} - \frac{\partial \overline{u_{i}u_{j}}}{\partial x_{j}}, \qquad (2.7)$$

$$\frac{\partial \overline{U}_i}{\partial x_i} = 0 \tag{2.8}$$

where $-\rho \overline{u_i u_j}$ is the Reynolds stress tensor. This quantity dominates the momentum transfer in most parts of turbulent flows. It also introduces six more unknowns into the four equations represented by 2.7 and 2.8, and thereby the problem of closure that we also refer to as the turbulence modeling problem.

2.2. Turbulent boundary layer flow

One of the flows studied in this thesis is the incompressible turbulent zero pressure-gradient boundary layer flow. The governing equations for this flow can be obtained by introducing the boundary layer approximations, which are constant pressure in the wall-normal direction and zero streamwise diffusion, into the Reynolds averaged equations. If we introduce the mean and fluctuating velocities respectively as $U_i = (U(x,y,z),V(x,y,z),W(x,y,z))$ and $u_i = (u(x,y,z,t),v(x,y,z,t),w(x,y,z,t))$ into the Reynolds averaged equations we obtain

$$\overline{U}\frac{\partial \overline{U}}{\partial x} + \overline{V}\frac{\partial \overline{U}}{\partial y} = -\frac{\partial \overline{u}\overline{v}}{\partial y} + \nu \frac{\partial^2 \overline{U}}{\partial y^2}$$
 (2.9)

$$\frac{\partial \overline{U}}{\partial x} + \frac{\partial \overline{V}}{\partial y} = 0 \tag{2.10}$$

where the spanwise direction, z, is assumed to be homogeneous. The boundary conditions are

$$\overline{U}(x, y = 0) = 0, \tag{2.11}$$

$$\overline{V}(x, y = 0) = 0 \quad \text{and} \tag{2.12}$$

$$\overline{U}(x, y \to \infty) = U_{\infty}. \tag{2.13}$$

Unfortunately, it is not possible to solve this set of equations since there are more unknowns than equations. This is the closure problem and further information on the Reynolds shear-stress relating it to the mean flow is needed to solve (close) the problem.

The turbulent boundary layer may be said to be represented by two distinctly different governing length scales, representing characteristic scales for the boundary layer thickness itself and for a thin inner region where viscous stresses play an important role. Similarity solutions can be searched for in these inner and an outer layers (see Millikan (1938)). These solutions are then matched together in a region in between the two layers where both similarity solutions are valid. For the inner layer we have the governing length scale, $l_* = \nu/u_\tau$ where $u_\tau = \tau_w/\rho$ is the friction velocity formed using the wall shear-stress, τ_w , and the density, ρ . The non-dimensional wall-distance then reads $y^+ = y/l_*$. A generalized form for the mean velocity and Reynolds shear-stress in the inner layer can be written as

$$\frac{\overline{U}}{u_{\tau}} = f(y^+), \tag{2.14}$$

$$-\frac{\overline{u}\overline{v}}{u_{\tau}^2} = g(y^+). \tag{2.15}$$

For the outer layer the governing length scale is some measure of the boundary layer thickness, here called δ . This measure could be e.g. δ_{99} which is the wall-distance where the velocity has reached 99% of the free-stream velocity, the displacement thickness, δ_* , defined as

$$\delta_* = \int_0^\infty \left(1 - \frac{\overline{U}}{U_\infty} \right) \mathrm{d}y \tag{2.16}$$

(the distance which the streamlines are deflected due to the presence of a solid wall), the momentum-loss thickness, θ , defined as

$$\theta = \int_0^\infty \frac{\overline{U}}{U_\infty} \left(1 - \frac{\overline{U}}{U_\infty} \right) dy \tag{2.17}$$

(if multiplied by ρU_{∞}^2 equal to the loss of momentum in a boundary layer compared to potential flow), or the Clauser-Rotta length defined as $\Delta = \delta_* U_{\infty}/u_{\tau}$. The non-dimensional wall-distance in outer scaling reads $\eta = y/\delta$ and the generalized form for the mean velocity defect and Reynolds shear-stress respectively in the outer layer can be written

$$\frac{U_{\infty} - \overline{U}}{u_{\tau}} = F(\eta), \tag{2.18}$$

$$-\frac{\overline{uv}}{u_{\tau}^2} = G(\eta). \tag{2.19}$$

Alternatively, we may regard 2.18 as a first order approximation in an expansion of \overline{U}/U_{∞} in the small parameter $\gamma = u_{\tau}/U_{\infty}$ (i.e. $\overline{U}/U_{\infty} = 1 - \gamma F(\eta) + O(\gamma^2)$). The matching between the layers is achieved, assuming there is a large enough Reynolds number so that $l_* \ll y \ll \delta$, by letting $y^+ \to \infty$ and $\eta \to 0$ simultaneously.

The turbulent boundary layer problem has been investigated theoretically and experimentally since Prandtl (1904) defined the boundary layer. Especially the matching of the two layers has received much attention ever since. In recent years there have been a large debate on whether the classical theory is valid or not. Some of the early important work, in chronological order, are the work by von Kármán (1921, 1930), Prandtl (1927, 1932) and Millikan (1938). However this field of research have been active ever since and Rotta (1950, 1962), Coles (1956), Clauser (1956) and more recently e.g. Barenblatt (1993); Barenblatt & Prostokishin (1993), George & Castillo (1997), Zagarola et al. (1997), Österlund et al. (2000) and Perry et al. (2001) have all made important contributions.

2.3. Closure problem in turbulence models

In the field of numerical simulations the closure problem is usually dealt with assuming a simple relationship involving the concept of mixing length first introduced by Prandtl (1927). The mixing length in inner scaling is related to the Reynolds shear-stress and the mean flow gradient as

$$-\overline{u}\overline{v} = (l^+)^2 \left(\frac{\mathrm{d}\overline{U}^+}{\mathrm{d}y^+}\right)^2, \tag{2.20}$$

where $l^+ = \varkappa y^+$ is the mixing length. To account for the wall, a damping function can be applied see e.g. van Driest (1956). The Prandtl mixing length is based on the Boussinesq (1877) hypothesis which connects the Reynolds stress tensor, $-\overline{u_i u_j}$, through the anisotropy tensor, a_{ij} , to the mean rate of strain tensor, S_{ij} using the concept of turbulent viscosity, ν_T . This may be written as

$$a_{ij} = -2\frac{\nu_T}{K}S_{ij}, \text{ where}$$
 (2.21)

$$a_{ij} = \frac{\overline{u_i u_j}}{K} - \frac{2}{3} \delta_{ij}, \tag{2.22}$$

$$S_{ij} = \frac{1}{2} \left(\frac{\partial \overline{U}_i}{\partial x_j} + \frac{\partial \overline{U}_j}{\partial x_i} \right), \tag{2.23}$$

and where $K = \frac{1}{2}\overline{u_iu_i}$ is the turbulence kinetic energy and δ_{ij} the Kronecker delta. In the so called two equation models ν_T is commonly expressed as

$$\nu_T = C_\mu \frac{K^2}{\varepsilon} \tag{2.24}$$

where C_{μ} is a constant and ε the dissipation rate. Transport equations for the turbulence kinetic energy, K, and the dissipation rate, ε , are then solved (see e.g. Chou (1945)). Sometimes ε is replaced by the inverse time scale of large eddies, ω , (see e.g. Saffman & Wilcox (1974)), or the time scale of large eddies themselves, τ .

However, there are also other turbulence models not based on this simple relationship. The Explicit Algebraic Reynolds Stress Model, EARSM, where the advection and viscous diffusion terms in the transport equation for the anisotropy are neglected, is such a two-equation model with the Boussinesq hypothesis, replaced by a more generalized form of the anisotropy relation, see e.g. Gatski & Speziale (1993) and Wallin & Johansson (2000, 2002). The Wallin & Johansson (2000) version of the EARSM model is used in the paper Measurements in a plane asymmetric diffuser with 8.5° opening angle. Part II: Comparison with model predictions for turbulence characteristics for comparison with the experimental results in a flow with separation. The simulations were performed by Johan Gullman-Strand. There are also more accurate models like Differential Reynolds Stress Models, DRSM, without the above simplifications of the anisotropy transport equation. This level of modeling may be necessary to accurately capture the plane asymmetric diffuser flow, but it also requires a larger computational effort.

2.4. Basics of Lie group symmetry methods

Recently a new way of achieving scaling laws in turbulent shear-flows has been investigated by Oberlack (2001a). Exact solutions, or invariants, to differential equations are here obtained through a method based on Lie group algebra. Basic descriptions of symmetry methods for differential equations are given in e.g. Hydon (2000), Oberlack (2001a) and Oberlack (2001b). The basic idea of symmetry methods for differential equations is to construct methods of finding transformations of the (ordinary or partial) differential equation that do not change its functional form with the change of variables. That is

$$\mathbf{F}(\mathbf{x}, \mathbf{y}, \mathbf{y}_i) = 0 \Leftrightarrow \mathbf{F}(\mathbf{x}^*, \mathbf{y}^*, \mathbf{y}_i^*) = 0$$
(2.25)

where \mathbf{x} is the vector of independent variables, \mathbf{y} is the vector of dependent variables, index i denotes all derivatives of order i on \mathbf{y} and * denotes the transformed variables. Concentrating our efforts on Lie group symmetries we have analytic transformations that depend on a continuous parameter, ε (not to be confused with the dissipation rate also denoted by ε). We have

$$S_{\varepsilon} : \mathbf{x}^* = \phi(\mathbf{x}, \mathbf{y}; \varepsilon) \text{ and } \mathbf{y}^* = \psi(\mathbf{x}, \mathbf{y}; \varepsilon).$$
 (2.26)

Furthermore, an important property of the Lie groups is that all linear combinations of distinct symmetry groups, $S_{\varepsilon}^{(i)}$ also are symmetry groups.

Oberlack (2001a) discusses the symmetries of the Navier-Stokes and Euler equations, and analyzes further also the symmetries of the differential equation

(derived e.g. by Oberlack & Peters (1993)) for the two-point correlation tensor. The two-point correlation tensor is defined as,

$$R_{ij}\left(\mathbf{x},\mathbf{r};t\right) = \overline{u'_{i}\left(\mathbf{x};t\right)u'_{j}\left(\mathbf{x}+\mathbf{r};t\right)}$$
(2.27)

where \mathbf{r} is the separation vector. An important feature of analyzing the equation for the two-point correlation tensor, is that we can study essentially inviscid dynamics by restricting attention to separations that give length scales that are negligibly influenced by viscosity, and at the same time, restricting attention to positions in space where the influence of viscosity (e.g. through viscous stresses) is negligible. This means that all symmetries from the Euler equations carry over to this equation.

Furthermore, restricting ourselves to plane turbulent shear-flows with all mean quantities dependent only on the wall-normal coordinate, y, leaves us with four symmetries. These symmetries are the two scaling symmetries, \overline{X}_{s_1} and \overline{X}_{s_2} , here reduced due to the one-dimensional mean flow, $\overline{U} = \overline{U}(y)$, the traditional Galilean invariance in the streamwise direction, $\overline{X}_{\overline{U}}$, and the spatial translation symmetry $\overline{X}_{\overline{V}}$. Remembering the superposition property of Lie group algebra, we can combine the four symmetries into ,

$$\overline{X} = k_{s_1} \overline{X}_{s_1} + k_{s_2} \overline{X}_{s_2} + k_{\overline{U}} \overline{X}_{\overline{U}} + k_y \overline{X}_{\overline{V}}. \tag{2.28}$$

The four symmetries can then be expressed in a characteristic form (see e.g. Oberlack (2001a)) which reads

$$\frac{\mathrm{d}y}{k_{s_1}y + k_y} = \frac{\mathrm{d}r_{[k]}}{k_{s_1}r_{[k]}} = \frac{\mathrm{d}\overline{U}}{(k_{s_1} - k_{s_2})\overline{U} + k_{\overline{U}}} =
= \frac{\mathrm{d}R_{[ij]}}{2(k_{s_1} - k_{s_2})R_{[ij]}},$$
(2.29)

where [] means that there is no summation over the indices. By changing the values of the two scaling symmetry constants, k_{s_1} and k_{s_2} , the scaling laws for different shear-flow situations can be derived. Scaling laws derived from Lie group symmetries for the mean streamwise velocity and the two-point correlation function are tested against experimental data in the paper, Evaluation of scaling laws derived from Lie group symmetry methods in zero pressure-gradient turbulent boundary layers.

CHAPTER 3

Results

3.1. Wind-tunnel design and calibration

The demand for further experimental facilities at the Department of Mechanics, KTH, lead to the decision to design, construct and build a new low-speed closed return circuit wind-tunnel. There were mainly two factors that contributed to this demand. First, there had been an increase in the number of graduate students at the department requiring wind-tunnel time, and secondly a wish to allow undergraduate students to perform their laboratory exercises in a modern high quality flow facility.

Due to the limiting space available in the laboratory, drastic measures had to be taken to be able to fit a large enough test section for the new wind-tunnel to be interesting for research purposes. The solution was to include the use of expanding corners, which decreases the total wind-tunnel circuit length drastically for a given test section length, into the design of the wind-tunnel layout.

The idea of expanding corners, *i.e.* a corner with larger outflow than inflow cross-section area, is not new. Since the beginning of the wind-tunnel era this idea has been tested by numerous researchers *e.g.* Kröber (1932), Collar (1936), Friedman & Westphal (1952) and Wolf (1957). However, all these tests were considered failures, mainly due to the poor design of the turning or guidevanes and the vast amount of money spent in those days on these facilities which meant that wind-tunnel size was not a limiting factor. After studying these reports it was concluded that expanding corners could be a success if proper care was taken in the design of the guide-vanes.

The first experimental tests using a version of the guide-vane used in the MTL tunnel at KTH are reported in Lindgren et al. (1997). Various expansion ratios, i.e. the ratio between the outflow and the inflow areas, and vane spacings were tested. The results were very encouraging although the total pressure-loss of the corner increased significantly. This increase was thought to be caused by non-optimum shape of the guide-vanes used. Remember that the vane profile tested was highly optimized for a non-expanding corner configuration. The experiments were therefore complemented with calculations using a cascade code originally made for turbine applications. This code named MISES was

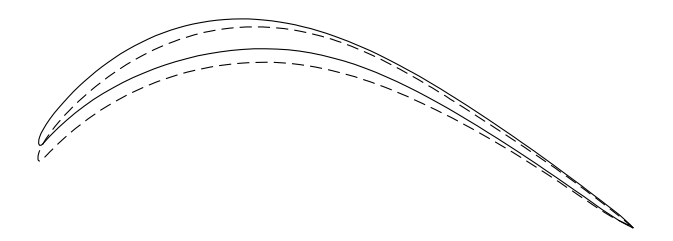


FIGURE 3.1. Solid line: 91L198 optimized for non-expanding corners, e=1 and $\epsilon=0.3$. Dashed line: L27132B the new vane optimized for expanding corners, $e=\frac{4}{3}$ and $\epsilon=0.27$.

developed by Youngren & Drela (1991) and is based on the Euler equations for the outer flow region (due to the compressibility effects encountered in turbines) coupled with boundary layer equations for the near-wall regions. One of the main advantages with this code is that there is an inverse optimization tool. Inverse optimization here means that the flow field around the guidevane profile is decided by the user, through the guide-vane surface pressure distribution, and the code then calculates a shape of the profile that provides a flow field that matches this distribution as close as possible. This has to be done in a step by step process since radical changes causes the code to explode. In this process the shape of the guide-vane slowly changes until the "optimum" pressure distribution giving low pressure-drop, and robustness towards flow angle variations have been achieved.

In figure 3.1 the guide-vane developed for an expansion ratio, e, of 4/3 and a separation between vanes, ϵ , of 0.27 chord lengths is presented (dashed curve) together with the original vane used in the MTL tunnel (solid curve). The total pressure-loss coefficient, defined as

$$\frac{\Delta H}{q_0} = \frac{p_{\text{t0}} - \overline{p_{\text{t1}}}}{\frac{1}{2}\rho U_0^2} \tag{3.30}$$

where p_{t0} is the total pressure at the corner inlet, $\overline{p_{t1}}$ is the mean total pressure at the corner outlet and U_0 is the mean velocity at the corner inlet, was found to be 0.041 for the new vane whereas the MTL tunnel vane has a total pressure-loss coefficient of 0.036. This slight increase in pressure-loss is somewhat compensated for by the reduced need for diffusers in the wind-tunnel circuit. The development of the new vane for expanding corners is reported in Lindgren et al. (1998)

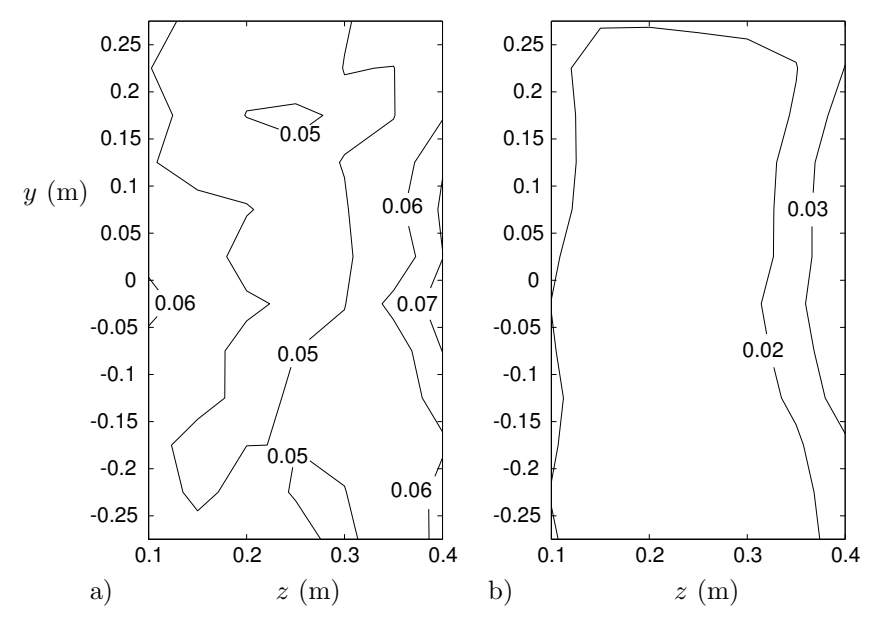


FIGURE 3.2. The streamwise turbulence intensity (in % of the streamwise mean velocity) in the new tunnel at a test section speed of 25 m/s. a) non-filtered data, b) high-pass filtered data with cut-off frequency 20 Hz.

The reason for choosing the rather large expansion ratio of 4/3 is that with a wind-tunnel contraction ratio, i.e. the ratio between the largest and smallest cross section areas in the tunnel circuit, of 9 and four corners accommodating all the expansion in one plane the expansion ratio needed in each corner is about 4/3. This means that the new wind-tunnel has two-dimensional diffusers that perform slightly worse than three-dimensional diffusers in terms of resistance to separation. A conservative design of the diffusers is therefore needed. The test section is 4 m long with a cross-section area of 0.5×0.75 m², and the contraction ratio is 9. A heat exchanger, a honeycomb and 5 screens enhance, together with the large contraction ratio, the flow quality in the test section. The maximum speed in the test section is approximately 45 m/s. The collected knowledge in wind-tunnel design from the construction of the MTL tunnel was used extensively in this project. For instance, the shape of the contraction is identical, the screen wire and mesh sizes are similar and the test section aspect ratio is identical etc. The purpose was not only to benefit from the earlier work but to facilitate relocation of scientific projects between the tunnels and create similar environmental conditions for the experiments.

The flow quality in the test section was extensively investigated and, as an example we may mention that the streamwise turbulence intensity component

 $(u_{\rm rms}/\overline{U})$ is less than 0.04% and the cross-flow intensity components are less than 0.06%. Furthermore, the total pressure variation $(\Delta \overline{P}(x,z)/(0.5\rho \overline{U}^2),$ where $\Delta \bar{P}(x,z)$ is the total pressure difference between a position in the test section and a reference in the stagnation chamber) was found to be less than $\pm 0.1\%$ and the temperature variation less than ± 0.07 °C. These values are slightly worse than for the MTL tunnel (see Lindgren & Johansson (2002b)), which is expected since the smaller test section cross section area makes the relative influence on the core flow region from the walls larger. In figure 3.2 the turbulence intensity in the streamwise direction is shown for a test section speed of 25 m/s. The figure to the left (a) is the raw data intensity without high-pass filtering of the velocity time signal and the figure to the right (b) is the filtered intensity. The filtering of the data is performed to remove low frequency disturbances not considered as turbulence. These are long wave oscillations stretching around the entire wind-tunnel circuit caused by pressure fluctuations over the axial fan. The design and flow quality measurements are reported in the technical report Lindgren & Johansson (2002a).

A similar investigation of the flow quality, as was performed in the new tunnel, was also performed in the MTL tunnel. Measurements of this kind were made when the MTL tunnel was new and are reported in Johansson (1992). However, it was felt that complementary measurements were needed and that they should be reported in an internal technical report, enabling future investigators measuring in the MTL tunnel to refer to this report regarding flow quality statements. The results obtained from the MTL flow quality measurements are reported in Lindgren & Johansson (2002b).

The flow quality in the test section of the MTL tunnel was found to essentially agree with the early investigation reported in Johansson (1992). The main difference is that the temperature variation over the test section cross section area was found to be less than $\pm 0.05^{\circ}$ C which is substantially lower than the early findings of $\pm 0.2^{\circ}$ C. This is explained by the improvements in the temperature control system that since have been implemented. The other main results are that the high-pass filtered streamwise turbulence intensity was found to be less than 0.025% and the cross-flow intensities less than 0.035% at a test section speed of 25 m/s. The total pressure variation was found to be less than $\pm 0.06\%$, which actually is slightly better than the result reported in Johansson (1992). This could perhaps be explained by different pressure transducers and truncation of the data in the two investigations.

In figure 3.3 the streamwise turbulence intensity is presented at a test section speed of 25 m/s. Note that if the corners of the measurement area are excluded in the high-pass filtered case (figure 3.3b) the streamwise turbulence intensity would drop below 0.015%. As shown by the difference in figures 3.3a and 3.3b these results are fairly sensitive to the choice of cut-off frequency.

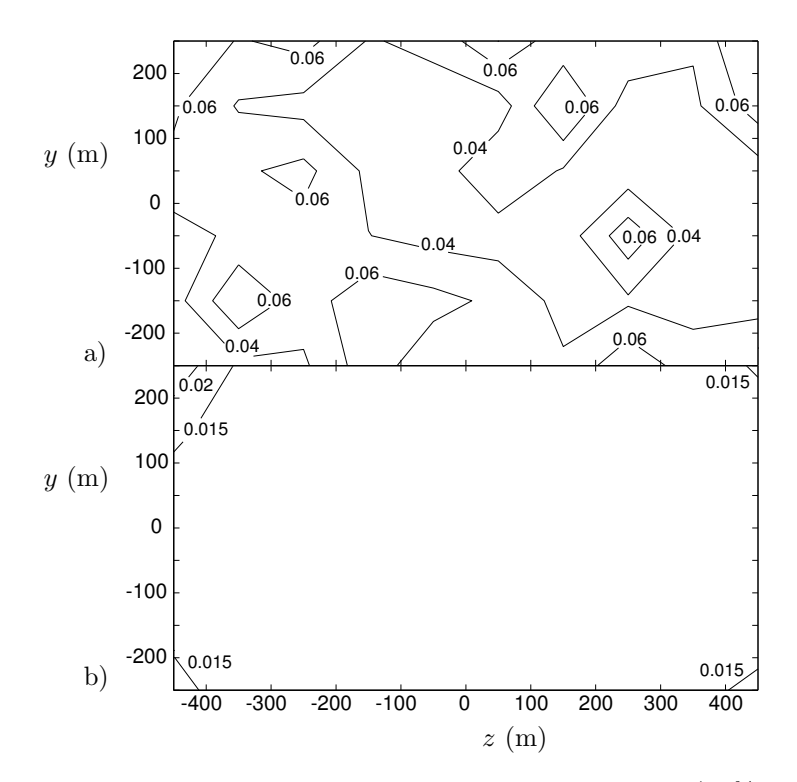


FIGURE 3.3. The streamwise turbulence intensity (in % of the streamwise mean velocity) in the MTL tunnel at a test section speed of 25 m/s. a) non-filtered data, b) high-pass filtered data with cut-off wave length of 2 m.

This choice is also rather subjective, therefore results both for filtered and non-filtered data are presented in the report.

3.2. Evaluation of turbulent boundary layer data

The zero pressure-gradient turbulent boundary layer flow have been studied in three papers in the thesis. They are Flow structures in zero pressure-gradient turbulent boundary layers at high Reynolds numbers, Evaluation of scaling laws derived from Lie group symmetry methods in zero pressure-gradient turbulent boundary layers and Universality of probability density distributions in the overlap region in high Reynolds number turbulent boundary layers. The experimental data used in these investigations are taken from the Österlund (1999b) data-base.

In the first of these papers flow structures in the near-wall and buffer regions are studied using a combination of a hot-film array MEMS sensor from

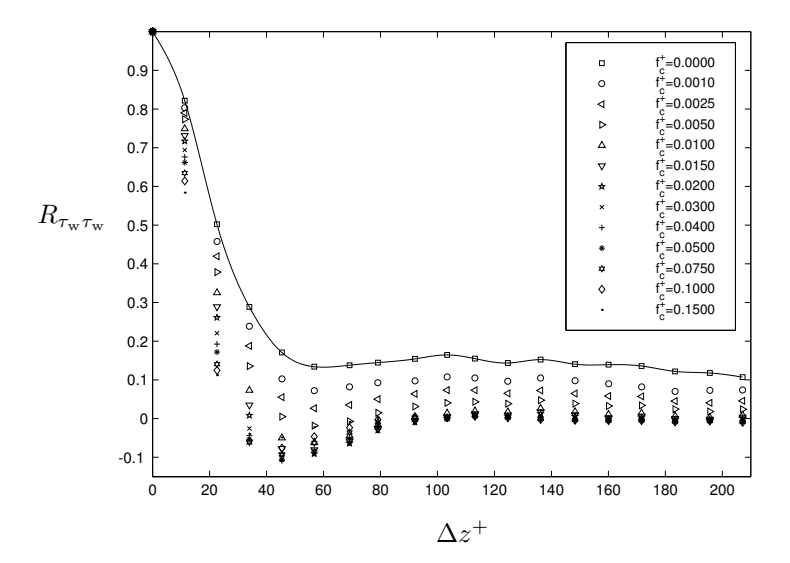


FIGURE 3.4. Determination of the optimum high-pass filter at $Re_{\theta} = 9500$. Two-point correlation function $R_{\tau_{\rm w}\tau_{\rm w}}(\Delta z^+)$ for various degrees of high-pass filtering, (cut-off frequencies given in diagram). The solid line is a spline fit to the unfiltered case.

UCLA/Caltech (see e.g. Jiang et al. (1996)) and single hot-wires traversed around and above the hot-film array. The hot-film sensor consists of 25 hotfilms flush mounted in a spanwise array on the boundary layer plate. The signals from these hot-films was used to calculate the spanwise spacing of nearwall streaks. It is calculated by identifying a local minimum of the correlation function, $R_{\tau_{\mathbf{w}}\tau_{\mathbf{w}}}(\Delta z^{+})$, where z^{+} is the spanwise coordinate normalized with inner variables. From the raw data, no clear minimum could be identified, see solid line in figure 3.4. The reason is that large scale energetic structures penetrate the near-wall region (so called sweeps) and the contribution to the correlation function from the near-wall streaks are drowned by these dominating large scale structures. This is a problem that increases with increasing Reynolds number since the scale separation then also increases. This kind of phenomenon have been observed both experimentally by Gupta et al. (1971) and Naguib & Wark (1992), and recently also in "high" Reynolds number $(Re_{\tau} = 640 \text{ based on half the channel height and the friction velocity})$ direct numerical simulations of channel flow by Kawamura et al. (private communication). The solution to extract the information from the near-wall streaks is to high-pass filter the wall-shear stress signals eliminating the contribution

from the largest scales. This has been done for many cut-off frequencies (see figure 3.4) and the "largest" minimum in the correlation function was found for a cut-off that corresponds to a typical length of a near-wall streak. The location of the minimum in the correlation function, i.e. half the streak spacing, is only slightly affected by the filtering process. With the "optimum" filtering the streak spacing was found to be approximately 96 inner length scales.

It is also worth mentioning that the frequency of occurrence of shear-layer events was found to scale best with a mixed scaling, i.e. $t_{\rm m} = \sqrt{t_{\rm i}t_{\rm o}}$ where $t_{\rm i}$ is the inner and $t_{\rm o}$ the outer time scale. This result agrees well with the findings for channel flow by Alfredsson & Johansson (1984). More recently Nagano & Houra (2002) investigated time scales in the buffer layer in turbulent boundary layer flow. They found that the Taylor time scale, i.e. $t_{\rm E} = \sqrt{2 \overline{u^2}/(\partial u/\partial t)^2}$, which is closely related to the mixed timescale, was best, also for adverse pressure-gradient flow.

Scaling laws derived from symmetry methods has recently attracted much attention. The idea is to find transformations of differential equations that leaves the functional form of the equations unchanged in the transformed variables. The advantage of these general methods is that the scaling laws derived are guaranteed to be admissible solutions to the original differential equation studied. From experience one may say that if a solution is admissible it is also likely to appear as a physical solution in nature.

A useful set of symmetries are the Lie group symmetries which are based on a continuous parameter. They are described in detail and applied to various flows by Oberlack *et al.* in *e.g.* Oberlack & Peters (1993); Oberlack (2001a). A nice property of the Lie Group symmetries is that any linear combination of the symmetries is also a symmetry.

By assuming parallel wall-bounded shear-flow and essentially inviscid flow dynamics, the four symmetry groups from the evolution equation of the two-point correlation can be written on the characteristic form of equation 2.29 where the ks are scalars to be determined. It is essentially the boundary conditions that impose restrictions on these symmetries but also other factors like viscosity reduce the number of symmetries allowed.

For a zero pressure-gradient boundary layer, we have an overlap region, which is essentially described by inviscid dynamics, and a restriction on free scaling of velocity since u_{τ} is the governing velocity there. Therefore, the parameters k_{s_1} and k_y in equation 2.29 have to be equal. Integrating the equation then gives the classical log-law but with an extra, higher order, correction term, A^+ .

$$\overline{U} = \frac{k_{\overline{U}}}{k_{s_1}} \ln \left(y + \frac{k_y}{k_{s_1}} \right) + B \quad \text{or in inner scaling}$$
 (3.31)

$$\overline{U}^{+} = \frac{1}{\varkappa} \ln (y^{+} + A^{+}) + B.$$
 (3.32)

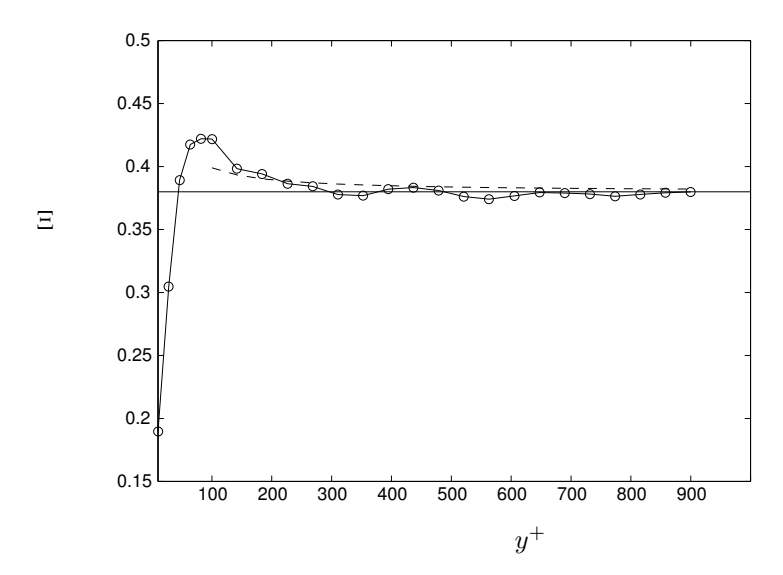


FIGURE 3.5. The diagnostic function Ξ . Solid straight line for classical log-law with $\varkappa=0.38$ (see Österlund *et al.* (2000)). Dashed curve for modified log-law with $A^+=5$.

As shown in figure 3.5, where the diagnostic function

$$\Xi = \left(y^{+} \frac{\mathrm{d}\overline{U}}{\mathrm{d}y^{+}}\right)^{-1} \tag{3.33}$$

should be constant for the classical log-law to be valid, the addition of the $A^+ \approx 5$ constant can be seen as a parameter which extends the logarithmic region towards the wall. However this constant is very small compared to y^+ in the actual overlap region and should primarily be seen as a higher order correction term not affecting the universality and Reynolds number independence of the log-law.

As an interesting note it may be worth mentioning that in the region of strong viscous influence $k_{s_2} = 2k_{s_1}$ (and $k_y = k_{\overline{U}} = 0$ near a boundary) and we simply retrieve the linear profile near the wall.

For the outer, wake, region the governing length scale is given by the boundary layer thickness, δ , which means that the scaling symmetry parameter k_{s_1} must be zero in this region. Integrating the equation yields an exponential

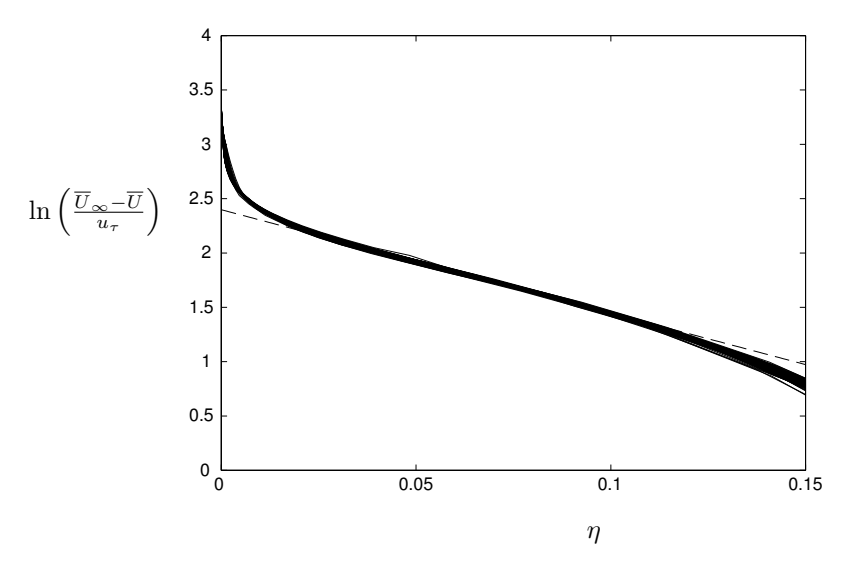


FIGURE 3.6. 70 experimental velocity deficit profiles in outer scaling (2500 $< Re_{\theta} < 27000$). Dashed line: exponential velocity deficit law with $C_1 = 11$ and $C_2 = 9.5$.

behaviour of the velocity defect.

$$\overline{U} = C_{exp} \exp\left(-\frac{k_{s_2}}{k_y}y\right) + \frac{k_{\overline{U}}}{k_{s_2}} \quad \text{or in outer scaling}$$
 (3.34)

$$\frac{\overline{U}_{\infty} - \overline{U}}{u_{\tau}} = C_1 \exp\left(-C_2 \eta\right). \tag{3.35}$$

In figure 3.6 the exponential velocity defect law, with $C_1 = 11$ and $C_2 = 9.5$, is plotted as a dashed straight line. It fits well to the 70 experimental velocity profiles in a region extending between $0.03 < \eta < 0.12$ corresponding to about half the boundary layer thickness. In the outermost part of the boundary layer there is a deviation of the experimental data away from the exponential velocity defect law. This can in part be explained by the high degree of intermittency encountered here but foremost by the non-parallel flow effects that are found to be important in this region and that are not accounted for in the derivation of the exponential velocity law.

The shape of the probability density distributions (functions), PDFs, in the overlap region was investigated with the purpose of testing if there is a selfsimilar behaviour in this region. Requiring self-similar PDFs is a very severe restriction since it implies that all higher moments are constant. Looking at the third and fourth moments (skewness and flatness) we see that they are fairly constant in a region larger than the overlap region as defined by Österlund et al. (2000). A similar investigation was performed by Tsuji & Nakamura (1999) for low Reynolds number turbulent boundary layer data ($Re_{\theta} < 5000$) and they concluded that a larger Reynolds number is needed to find an extended region of self-similar PDFs but that there was still some indications that such a region should exist. This is reasonable since Österlund et al. (2000) claims that a Reynolds number larger than $Re_{\theta} \approx 5000$ is necessary for a universal overlap region to be present.

A sensitive scalar measure of the variation in PDF shapes is the Kullback-Leibler divergence, KLD, (see Kullback (1959)). It is defined as

$$D(P||Q) \equiv \sum_{\{s\}} P(s_i) \ln(P(s_i)/Q(s_i)), \tag{3.36}$$

where P and Q are discrete probability density distributions. Here chosen as the experimental data distributions and the Gaussian distribution respectively, (see also Tsuji & Nakamura (1999)). The KLD measure is more sensitive to variations if the two distributions are similar. The choice of the Gaussian distribution as reference distribution is here natural since the experimental distributions are very close to Gaussian in the overlap region. A constant value of the KLD measure means self-similar PDFs.

In figure 3.7 the velocity profile in inner scaling and the KLD measure are shown for a Reynolds number based on momentum-loss thickness of 9700 (top two figures). As we can see the region of constant KLD measure (marked by black squares) is larger than the logarithmic overlap region (marked by black circles) extending further out towards the wake region. In the bottom figure data from all measurements in the Österlund data-base with hot-wire lengths less than 15 viscous length units are plotted together. As seen the collapse is rather remarkable and strongly suggests that the PDFs are indeed self-similar in the overlap region.

As mentioned above the constant KLD region (180 $< y^+$ and $y/\delta_{95} > 0.3$) is somewhat larger than the classical overlap region (200 $< y^+$ and $y/\delta_{95} > 0.15$). Some attempts have been made to establish a new outer limit for the overlap region using the self-similarity of the PDFs but so far no completely satisfying method have been found.

Since the PDFs in the overlap region are very close to Gaussian a truncated Gram-Charlier series expansion is a suitable tool in comparing the different experimental probability density distributions with each other. It is defined as

$$p(\zeta) = c_0 + \phi(\zeta) + \frac{c_1}{1}\phi'(\zeta) + \dots + \frac{c_n}{n!}\phi^{(n)}(\zeta)$$
 (3.37)

$$\phi^{(n)}(\zeta) = (-1)^n H_n(\zeta)\phi(\zeta) \tag{3.38}$$

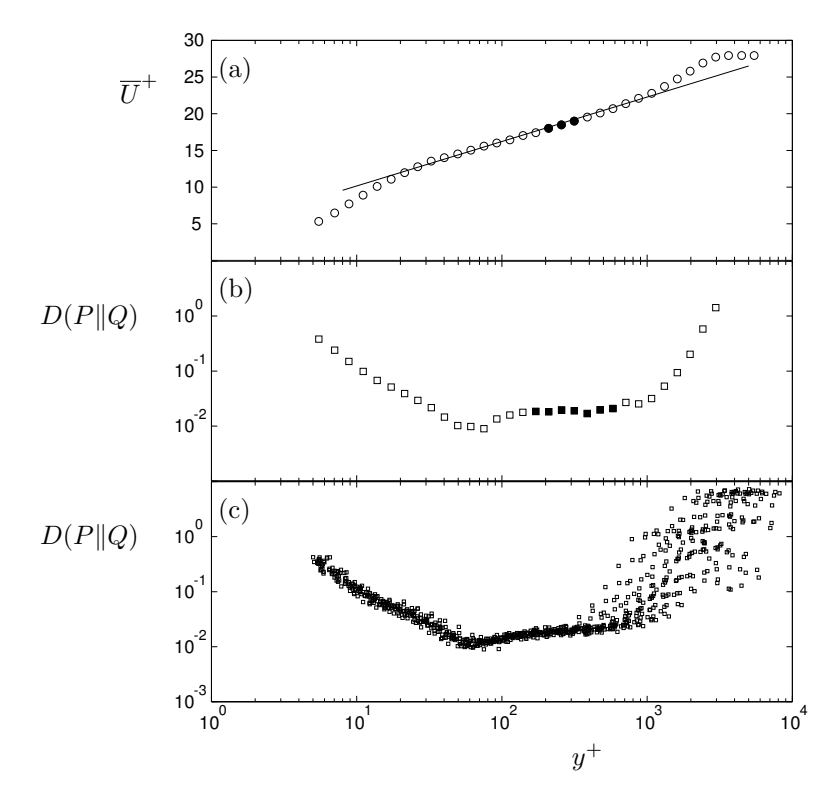


FIGURE 3.7. (Top) Mean velocity profile in inner scaling at $Re_{\theta} = 9707$. The filled markers correspond to the log-layer, $y^{+} > 200 \& y/\delta_{95} < 0.15$. The solid line represents the log law with $\varkappa = 0.38$ and B = 4.1. (Middle) The KLD of the streamwise velocity at $Re_{\theta} = 9707$. The filled markers correspond to the constant divergence region. (Bottom) The KLD for 18 velocity profiles with wire length $l^{+} < 15$ at $2532 < Re_{\theta} < 12633$.

where ζ is $u/u_{\rm rms}$, $H_n(\zeta)$ are Hermite functions and $\phi(\zeta)$ is the Gaussian distribution. The coefficients are given by: $c_0 = 1$, $c_1 = c_2 = 0$, $c_3 = -S$ and $c_4 = F - 3$ where S and F are the skewness and flatness factors respectively. Higher order coefficients are related to hyper skewness and hyper flatness in the following way

$$c_5 = -H_S + 10S, (3.39)$$

$$c_6 = H_F - 15F + 30, (3.40)$$

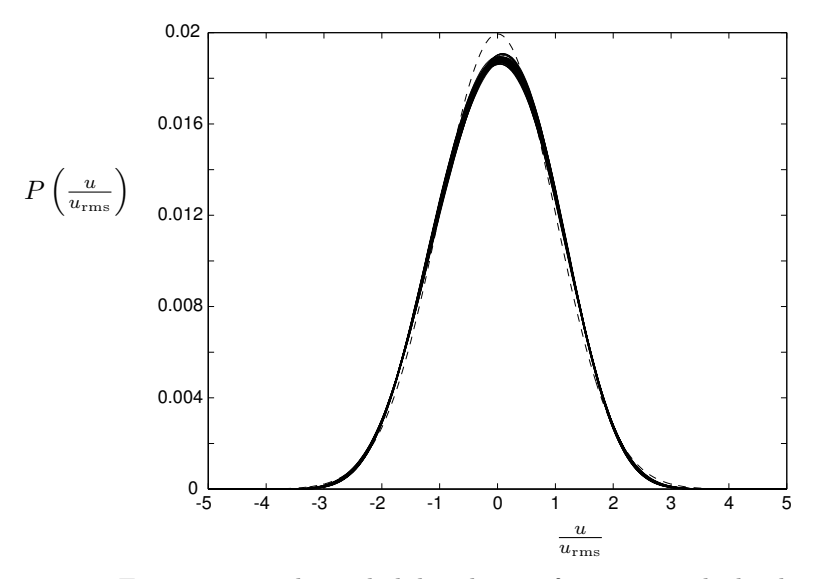


FIGURE 3.8. The probability density functions in the log-layer at $4312 < Re_{\theta} < 12633$ (57 density distributions). solid lines: Gram-Charlier expansion; dashed line: Gaussian distribution.

where H_S is the hyper skewness and H_F hyper flatness defined as the fifth moment normalized by u_{rms}^5 and the sixth moment normalized by u_{rms}^6 .

In figure 3.8 57 Gram-Charlier expanded probability density distributions are plotted together with the Gaussian distribution. The nice collapse further strengthens the hypothesis of self-similar PDFs in the overlap region. Furthermore, plotting the Gram-Charlier coefficients against Reynolds number shows that the variation is small for all moments and that there is no clear Reynolds number trend.

3.3. Plane asymmetric diffuser flow

The flow in an asymmetric plane diffuser with an opening angle of 8.5° was studied primarily using optical measurement techniques. The inlet condition was fully developed channel flow and the Reynolds number based on the friction velocity, u_{τ} , and the channel height was 2000. This flow case is, as mentioned in chapter 1, very useful for testing new turbulence models since it is a very demanding situation with separated flow, strong pressure-gradient and high turbulence intensity. The purpose of our measurements was to build up a database with all mean and fluctuating velocity components in a plane along the centerline of the diffuser to be used as reference data for turbulence modelers.

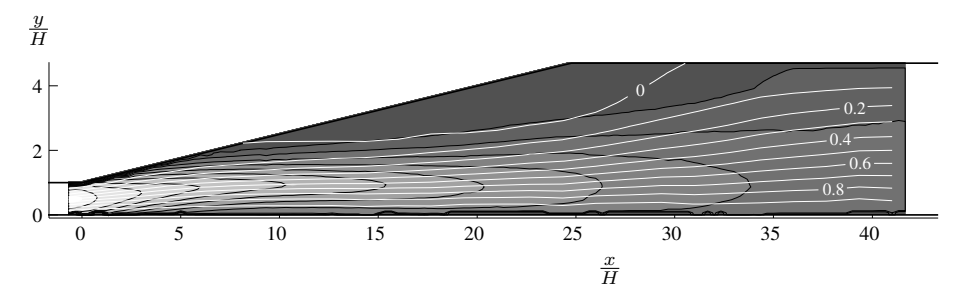


FIGURE 3.9. Streamlines shown as white curves. The stream function is integrated from the inclined wall. Gray-scale background with separating black curves show the speed, with a contour increment of 2 m/s.

Earlier experimental studies of this flow have been made by Obi et al. (1993a) and Buice & Eaton (2000) but with a slightly larger opening angle (10°). Their case has also been used for comparisons with simulations by e.g. Kaltenbach et al. (1999) who made a large eddy simulation and Gullman-Strand et al. (2002) who made a simulation based on an explicit algebraic Reynolds stress model. The results from a workshop where many turbulence models are tested are reported in Hellsten & Rautaheimo (1999). The results from these simulations are rather mixed. It appears that our case is even more demanding from a simulation point of view since the flow is closer to attached with a smaller opening angle.

In figure 3.9 the streamlines are shown as white curves. The streamline with a stream function value of $\Psi=0$ is the dividing streamline which separates the region with recirculating flow from the outer flow in a mean sense. The mean separation point is where the upstream end of this dividing streamline meets the wall and the mean reattachment point is where its downstream end meets the wall. In the experiments the separation and reattachment points were found to be at 9 and 31 inlet channel heights downstream of the diffuser inlet, respectively. The gray scale background shown is the speed, i.e. $\sqrt{\overline{U}^2 + \overline{V}^2}$ with an increment of 2 m/s between curves. As can be seen in the figure the flow turns towards the inclined wall just downstream of the diffuser inlet and it is deflected back towards the straight wall as soon as the separation bubble starts to develop.

The experimental results are also compared to the results from a simulation using an explicit algebraic Reynolds stress model developed by Wallin & Johansson (2000) with K and ω as the two transported turbulence quantities. These calculations are performed by Johan Gullman-Strand and the scheme

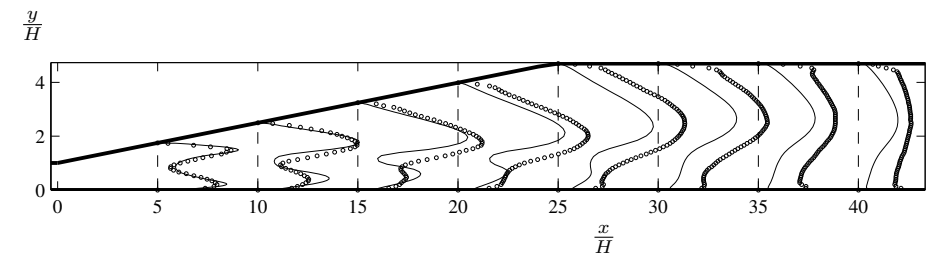


FIGURE 3.10. Turbulence kinetic energy, $K = 1/2(\overline{u}\overline{u} + \overline{v}\overline{v} + \overline{w}\overline{w})$. Solid curve: simulation data. Circles: experimental data.

used is a finite element method with linear base functions both for the velocities and the pressure on a single grid using pressure correction terms. The method is presented in Gullman-Strand (2002).

In figure 3.10 the calculated turbulence kinetic energy is compared to the experimental data. The agreement is very good in the upstream part of the diffuser but there are substantial differences in the downstream part. This is thought to mainly be the result of an under-prediction of the separation bubble size which leads to a less violent flow and thereby less production of turbulence. The mean separation point found in the simulation is 11 inlet channel heights downstream the diffuser inlet, which should be compared to 9 for the experiment and the mean reattachment point was located at x/H=27, which should be compared to 31 in the experiments.

CHAPTER 4

Concluding remark and outlook

Both the newly built and the MTL wind-tunnels have been thoroughly evaluated and although their overall performance was very good there is still room for some improvements. For instance, the settling time of the test section temperature is rather long in both tunnels which is caused by deficiencies in the control loops and the piping. The systems operating the tunnels can also be improved especially regarding their integration with measurement equipment and measurement computers. The flow quality in these tunnels also have to be checked from time to time and the screens have to be cleaned regularly especially now when there is an increase in use of measurement techniques using seeding particles that accumulate in screens and heat exchanger.

The zero pressure-gradient turbulent boundary layer data, measured in the MTL wind-tunnel by Jens M. Österlund, is stored in a data-base which to some extent is available on the internet (see Österlund (1999a)). Although the data-base has been extensively used during the last couple of years by Österlund (1999b) and others, it is still a useful source of experimental data that can be used for testing and verification of new ideas. During the completion of this thesis, the data-base has been used for testing new scaling laws in the overlap and wake regions, investigating similarity properties of probability density functions in the overlap region and studying near-wall structures in boundary layer flow.

When new scaling laws, derived using Lie group symmetry methods, were tested, it was found that the assumption of parallel flow was appropriate in the overlap region but not in the outer region of the boundary layer. It would certainly be interesting to derive new scaling laws using the same methods but without this assumption. It would also be interesting to include pressure-gradient effects which come in, in a way somewhat similar to non-parallel effects but they will be significant also close to the wall. In Skote & Henningsson (2002) scaling laws are proposed for the inner region for adverse pressure-gradient turbulent boundary layers. They also compared these laws with DNS data. Furthermore, Angele (2002) and Castillo & George (2001) propose scaling laws for the outer region in an adverse pressure gradient turbulent boundary layer. It would be desirable to, via the symmetry group method, find scaling laws for both these regions and compare them to the findings by Skote &

Henningsson (2002), Angele (2002) and Castillo & George (2001). It would also be interesting to make complementary measurements to the existing database with the attention directed towards two-point correlations. Especially the spanwise separation is interesting since this is a homogeneous direction and there is no interference between probes. With such measurements the Taylor's hypothesis used here can be omitted.

The diffuser flow has to be studied further with special attention to the near-wall regions where many features affecting the flow, also in the interior are generated. Capturing the flow in the near-wall regions is therefore essential for a turbulence model to also predict the interior flow field well. The EARSM turbulence model used for comparisons with the experimental data in paper 8 should also include the streamline curvature corrections introduced by Wallin & Johansson (2002). This is especially important in the upstream part of the diffuser where the wall-normal velocity and streamline curvature effects are large. It is plausible that differential Reynolds stress models are necessary to capture this very challenging flow case and with the automated code generation presented in Gullman-Strand (2002), it should be possible to include such models in the future.

The plane asymmetric diffuser project also incorporates control as an important part. This subject has only been touched upon yet with the vortex generator measurements presented in paper 7. There are nowadays many research groups, e.q. at the Department of Mechanics, KTH, developing useful control schemes with fast enough feedback to be applicable in a flow like this. The question of sensors and actuators are rather complicated here since the force needed to affect the flow and the wall area of the diffuser are both very large. Some suggestions on actuators are besides the common blowing and suction, piezo electrical flaps, tested in laminar flow by e.q. Fredrik Lundell (private communication), wall-jets, inclined vortex generating jets (see e.q.Wallis (1960)) and synthetic jets (see e.g. Glezer & Amitay (2002)). Another, perhaps more advanced option would be plasma jets (see e.g. Lorber et al. (2000)). Some of these options may be too complicated and demand too much power input to be feasible in a practical situation, but from a scientific point of view they may still be interesting. The sensor part is even more complicated but traditional wall-wires, and other wall shear-stress sensors based on varying techniques, and miniature speakers to capture pressure fluctuations are some suggestions. However, these aspects of control have to be analyzed further. A good understanding of the basic flow in the diffuser is the first essential step in making the correct choices for the future.

Acknowledgment

I would like to thank my supervisor, Prof. Arne V. Johansson, for accepting me as his student and guiding me through the challenging work facing a graduate student. I am grateful for the funds Arne provided that were necessary to complete this work. I would also like to thank him for critically reviewing this thesis and suggesting improvements to the manuscripts.

I am very thankful towards my friends, office mates and colleagues Jens Österlund and Olle Törnblom, with whom I have cooperated in some projects, for the joy and stimulation in sharing the labour in the otherwise sometimes lonely work situation of a graduate student. We have also shared interesting and exciting moments on regattas with mixed fortunes, above all, of course, due to the unpredictable weather.

I would also like to thank my present and former colleagues with whom I have spent many fun and interesting times both at work and off-work ours. Especially those playing indoor bandy and soccer with whom I have had many hard and challenging encounters.

I would like to thank Prof. Yoshiyuki Tsuji, with whom I worked on one of the papers, for providing interesting views on scaling of turbulent boundary layer flow, and Prof. P. Henrik Alfredsson for his views on the measurements performed in the MTL wind-tunnel.

I wish to thank Mr. Ulf Landén and Mr. Marcus Gällstedt for helping me in designing and manufacturing high quality measurement equipment and wind-tunnel parts that are critical in the achievement of good experimental data.

Finally the Swedish Research Council for Engineering Science (TFR), the Swedish National Board for Industrial and Technical Development (NUTEK) and the Swedish Research Council (VR) are gratefully acknowledged for financial support.

Bibliography

- ALFREDSSON, P. H. & JOHANSSON, A. V. 1984 Time scales in turbulent channel flow. Phys. Fluids A 27 (8), 1974–81.
- ANGELE, K. P. 2002 Pressure-based scaling in a separating APG boundary layer. In *Advances in Turbulence IX* (ed. I. P. Castro, P. E. Hancock & T. G. Thomas), pp. 639–642. CIMNE, Barcelona, Spain.
- Apsley, D. D. & Leschziner, M. A. 1999 Advanced turbulence modelling of separated flow in a diffuser. Flow, Turbulence and Combustion 63, 81—112.
- BARENBLATT, G. I. 1993 Scaling laws for fully developed turbulent shear flows. Part 1. Basic hypotheses and analysis. *J. Fluid Mech.* **248**, 513–520.
- Barenblatt, G. I. & Prostokishin, V. M. 1993 Scaling laws for fully developed turbulent shear flows. Part 2. Processing of experimental data. *J. Fluid Mech.* **248**, 521–529.
- Boussinesq, T. V. 1877 Essai sur la théorie des eaux courantes. Mém. Prés. Acad. Sci. p. 46.
- Buice, C. U. & Eaton, J. K. 2000 Experimental investigation of flow through an asymmetric plane diffuser. *Tech. Rep.* TSD-107. Thermo sciences Division, Dep. of Mechanical Eng. Stanford University, Stanford, Ca, USA, Report No.
- Castillo, L. & George, W. K. 2001 Similarity analysis for turbulent boundary layer with pressure gradient: Outer flow. AIAA J. 39 (1), 41–47.
- Chou, P. Y. 1945 On velocity correlations and the solutions of the equations of turbulent motion. *Quart. of Applied Math.* 3, 38–54.
- CLAUSER, F. H. 1956 The turbulent boundary layer. Advances Appl. Mech. 4, 1–51.
- COLES, D. E. 1956 The law of the wake in the turbulent boundary layer. J. Fluid Mech. 1, 191–226.
- Coles, D. E. 1962 The turbulent boundary layer in a compressible fluid. R 403-PR. The RAND Corporation, Santa Monica, CA.
- Collar, A. R. 1936 Some experiments with cascades of aerofoils. A.R.C. Technical Report 1768. Aeronautical Research Committee.
- VAN DRIEST, E. R. 1956 On turbulent flow near a wall. J. Aero. Sci. 23, 1007–1011.
- Fernholz, H. H. & Finley, P. J. 1996 The incompressible zero-pressure-gradient turbulent boundary layer: An assessment of the data. *Prog. Aerospace Sci.* 32, 245–311.

- FERNHOLZ, H. H., KRAUSE, E., NOCKEMANN, M. & SCHOBER, M. 1995 Comparative measurements in the canonical boundary layer at $Re_{\delta_2} < 6 \cdot 10^4$ on the wall of the german-dutch windtunnel. *Phys. Fluids* 7 (6), 1275–1281.
- FRIEDMAN, D. & WESTPHAL, W. R. 1952 Experimental investigation of a 90° cascade diffusing bend with an area ratio of 1.45:1 and with several inlet boundary layers. TN 2668. NACA.
- GATSKI, T. B. & SPEZIALE, C. G. 1993 On explicit algebraic stress models for complex turbulent flows. J. Fluid Mech. 254, 59–78.
- George, W. K. & Castillo, L. 1997 Zero-pressure-gradient turbulent boundary layer. Applied Mech. Reviews 50, 689–729.
- GLEZER, A. & AMITAY, M. 2002 Synthetic jets. Ann. Rev. Fluid Mech. 34, 503-529.
- Gullman-Strand, J. 2002 Turbulence modeling using automated code generation applied to asymmetric diffuser flow. *Tech. Rep.* 2002:06. Lic. thesis, Dept. of Mechanics, KTH, TRITA-MEK.
- Gullman-Strand, J., Amberg, G. & Johansson, A. V. 2002 Study of separated flow in an asymmetric diffuser. In *Advances in Turbulence IX*, pp. 643–646. Southampton, U.K.
- Gupta, A. K., Laufer, J. & Kaplan, R. E. 1971 Spatial structure in the viscous sublayer. J. Fluid Mech. 50, 493–512.
- Hellsten, A. & Rautaheimo, P., ed. 1999 Workshop on refined turbulence modelling. ERCOFTAC/IAHR/COST.
- HITES, M. H. 1997 Scaling of high-Reynolds number turbulent boundary layers in the National Diagnostic Facility. PhD thesis, Illinois Institute of Technology.
- Hydon, P. 2000 Symmetry Methods for Differential Equations A Beginner's Guide. Cambridge University Press Publisher.
- JIANG, F., TAI, Y.-C., GUPTA, B., GOODMAN, R., TUNG, S., HUANG, J. B. & HO, C.-M. 1996 A surface-micromachined shear stress imager. In 1996 IEEE Micro Electro Mechanical Systems Workshop (MEMS '96), pp. 110–115.
- JOHANSSON, A. V. 1992 A low speed wind-tunnel with extreme flow quality-design and tests. Proc. the 18:th ICAS Congress pp. 1603–1611.
- Jones, M. B., Nishizawa, N., Chong, M. S. & Marusic, I. 2002 Scaling of the turbulent boundary layer at high Reynolds numbers. In *IUTAM symposium on Reynolds number scaling in turbulent flow*. Princeton, University, NJ, USA.
- Kähler, C. J., Stanislas, M. & Kompenhans, J. 2002 Spatio-temporal flow structure investigation of near-wall turbulence by means of multiplane stereo particle image velocimetry. In 11th Int. Symp. on Applications of Laser Techniques to Fluid Mech.. Instituto superior técnico, Center for innovation, technology, and policy research, Lisbon, Portugal.
- Kaltenbach, H. J., Mittal, M., Fatica, R., Lund, T. S. & Moin, P. 1999 Study of flow in a planar asymmetric diffuser using large-eddy simulation. *J. Fluid Mech.* **390**, 151–185.
- VON KÁRMÁN, T. 1921 Ueber laminare un turbulente Reibung. Z. angew. Math. Mech. pp. 233–252, NACA TM 1092.
- VON KÁRMÁN, T. 1930 Mechanische Aehnlichkeit und Turbulenz. Nachr. Ges. Wiss. Göttingen, Math. Phys. Kl. pp. 58–68, NACA TM 611.

- Klebanoff, P. S. 1955 Characteristics of turbulence in a boundary layer with zero pressure gradient. TR 1247. NACA.
- KNOBLOCH, K. & FERNHOLZ, H. H. 2002 Statistics, correlations and scaling in a canonical, incompressible turbulent boundary layer with $Re_{\delta_2} \leq 1.15 \times 10^5$. In *IUTAM symposium on Reynolds number scaling in turbulent flow*. Princeton, University, NJ, USA.
- KRÖBER, G. 1932 Schaufelgitter zur umlenkung von flussigkeits-strömung. Ingenieur-Archiv ${f 3},\,516.$
- Kullback, S. 1959 Information theory and statistics. Wiley, London.
- LINDGREN, B. & JOHANSSON, A. V. 2002a Design and evaluation of a low-speed wind-tunnel with expanding corners. TRITA-MEK 2002:14. Department of Mechanics, KTH.
- LINDGREN, B. & JOHANSSON, A. V. 2002b Evaluation of the flow quality in the low-speed MTL wind-tunnel. TRITA-MEK 2002:13. Department of Mechanics, KTH.
- LINDGREN, B., ÖSTERLUND, J. M. & JOHANSSON, A. V. 1997 Measurement and calculation of guide vane performance in expanding bends for wind tunnels. TRITA-MEK 1997:6. Department of Mechanics, KTH.
- LINDGREN, B., ÖSTERLUND, J. M. & JOHANSSON, A. V. 1998 Measurement and calibration of guide-vane performance in expanding bends for wind-tunnels. *Experiments in Fluids* **24**, 265–272.
- Lorber, P., McCormick, D., Anderson, T., Wake, B., MacMartin, D., Pollack, M., Corke, T. & Breuer, K. 2000 Rotorcraft retreating blade stall control. In *Fluids 2000 conference and exhibit*, vol. AIAA 2000-2475. Denver, Colorado, USA.
- Ludwieg, H. & Tillman, W. 1950 Investigations of the wall shearing stress in turbulent boundary layers. TM 1285. NACA.
- MILLIKAN, C. B. 1938 A critical discussion of turbulent flows in channels and circular tubes. In *Proceedings of the Fifth International Congress of Applied Mechanics*.
- NA, Y. & Moin, P. 1998 Direct numerical simulation of a separated turbulent boundary layer. J. Fluid Mech. 374, 379–405.
- NAGANO, Y. & HOURA, T. 2002 Scaling of near-wall structures in turbulent boundary layers subjected to adverse pressure gradient. In *IUTAM symposium on Reynolds number scaling in turbulent flow*. Princeton, University, NJ, USA.
- NAGIB, H. M., CHRISTOPHOROU, C., MONKEWITZ, P. A. & ÖSTERLUND, J. M. 2002 Higher Reynolds number boundary layer data on a flat plate in the NDF. In *IUTAM symposium on Reynolds number scaling in turbulent flow*. Princeton, University, NJ, USA.
- NAGUIB, A. M. & WARK, C. E. 1992 An investigation of wall-layer dynamics using a combined temporal filtering and correlation technique. *J. Fluid Mech.* **243**, 541–560.
- OBERLACK, M. 2001a Lecture notes from CISM cource on Theories of Turbulence, Udine. To be published by Springer.
- OBERLACK, M. 2001b A unified approach for symmetries in plane parallel turbulent shear flows. J. Fluid Mech. 427, 299–328.

- OBERLACK, M. & PETERS, N. 1993 Closure of the two-point correlation as a basis of Reynolds stress models. In So, R., Speziale, C., Launder, B., eds., Near wall turbulent flows, 85–94. Elsevier Science Publisher.
- OBI, S., AOKI, K. & MASUDA, S. 1993a Experimental and computational study of turbulent separating flow in an asymmetric plane diffuser. In 9th Symp. on Turbulent Shear Flows, Kyoto, Japan, August 16-18, p. 305.
- Obi, S., Ishibashi, N. & Masuda, S. 1997 The mechanism of momentum transfer enhancement in periodically perturbed turbulent separated flow. In 2nd Int. Symp. on Turbulence, Heat and Mass Transfer, Delft, The Netherlands, pp. 835–844.
- OBI, S., OHIZUMI, K. & MASUDA, S. 1993b Turbulent separation control in a plane asymmetric diffuser by periodic perturbation. In *Engineering Turbulence Modeling and Experiments* 2, pp. 3633–642.
- ÖSTERLUND, J. M. 1999a http://www2.mech.kth.se/~jens/zpg/.
- ÖSTERLUND, J. M. 1999b Experimental studies of zero pressure-gradient turbulent boundary-layer flow. PhD thesis, Department of Mechanics, Royal Institute of Technology, Stockholm.
- ÖSTERLUND, J. M., JOHANSSON, A. V., NAGIB, H. M. & HITES, M. H. 2000 A note on the overlap region in turbulent boundary layers. *Phys. Fluids* 12, 1–4.
- Perry, A. E., Hafez, S. & Chong, M. S. 2001 A possible reinterpretation of the Princeton superpipe data. *J. Fluid Mech.* 439, 395–401.
- PRANDTL, L. 1904 Ueber die Flüssigkeitsbewegung bei sehr kliner Ribung. In Verhandlungen des III. Internationalen Mathematiker-Kongress, Heidelberg, pp. 484–491.
- Prandtl, L. 1927 Ueber den Reibungswiderstand strömender Luft. Ergebn. Aerodyn. Versuchsanst. Göttingen 3, 1–5.
- Prandtl, L. 1932 Zur turbulenten Strömung in Rohren und längs Platten. Ergebn. Aerodyn. Versuchsanst. Göttingen 4, 18–29.
- REYNOLDS, O. 1883 On the experimental investigation of the circumstances which determine whether the motion of water shall be direct or sinuous, and the law of resistance in parallel channels. *Phil. Trans. Roy. Soc. Lond.* **174**, 935–982.
- REYNOLDS, O. 1895 On the dynamical theory of incompressible viscous fluids and the determination of the criterion. *Phil. Trans. Roy. Soc. A* **186**, 123–164.
- ROTTA, J. C. 1950 Über die Theorie der Turbulenten Grenzschichten. Mitt. M.P.I. Ström. Forschung Nr 1, also available as NACA TM 1344.
- ROTTA, J. C. 1962 Turbulent boundary layers in incompressible flow. In *Progress in aeronautical sciences* (ed. A. Ferri, D. Küchemann & L. H. G. Sterne), vol. 2, pp. 1–219. Pergamon press.
- SAFFMAN, P. G. & WILCOX, D. C. 1974 Turbulence-model predictions for turbulent boundary layers. AIAA Journal 12, 541–546.
- Schultz-Grunow, F. 1940 Neues Reibungswiederstandsgesetz für glatte Platten. Tech. Rep. 8. Luftfahrtforschung, translated as New frictional resistance law for smooth plates, NACA TM-986, 1941.
- Skote, M. & Henningsson, D. S. 2002 Direct numerical simulation of a separated turbulent boundary layer. J. Fluid Mech. 471, 107–136.

- Skote, M., Henningsson, D. S. & Henkes, R. A. W. M. 1998 Direct numerical simulation of self-similar turbulent boundary layers in adverse pressure gradients. *Flow, Turbulence and Combustion* **60**, 47–85.
- SMITH, D. W. & WALKER, J. H. 1959 Skin-friction measurements in incompressible flow. NASA TR R-26.
- SPALART, P. R. 1988 Direct simulation of a turbulent boundary layer up to $Re_{\theta} = 1410$. J. Fluid Mech. 187, 61–98.
- Spalart, P. R. & Coleman, G. N. 1997 Numerical study of a separation bubble with heat transfer. *European J. of Mech. B/Fluids* 16, 169.
- TSUJI, Y. & NAKAMURA, I. 1999 Probability density function in the log-law region of low Reynolds number turbulent boundary layer. *Phys. Fluids* 11 (3), 647–658.
- Wallin, S. & Johansson, A. V. 2000 An explicit algebraic Reynolds stress modell for incompressible and compressible turbulent flows. J. Fluid Mech. 403, 89–132.
- WALLIN, S. & JOHANSSON, A. V. 2002 Modeling streamline curvature effects in explicit algebraic Reynolds stress turbulence models. Int. J. of Heat and Fluid Flow. 23, 721–730.
- Wallis, R. A. 1960 A preliminary note on a modified type of air jet for boundary layer control. *Tech. Rep.* C.P. No. 513. Aeronautical Research Council, A.R.C.
- WOLF, H. 1957 Messungen im nachlauf eines gleichdruckgitters für 90-umlenkung. Maschinenbautechnik 6 (10), 539.
- Wosnik, M., George, W. K., Karlsson, R. I. & Johansson, T. G. 2002 The Nordic Wind-Tunnel - proposal to build a large turbulence research facility. In Advances in turbulence IX, p. 899. СІМNЕ, Barcelona, Spain.
- YOUNGREN, H. & DRELA, M. 1991 Viscous/inviscid method for preliminary design of transonic cascades. In AIAA, SAE, ASME, and ASEE, Joint Propulsion, Conference, 27th..
- ZAGAROLA, M. V., PERRY, A. E. & SMITS, A. J. 1997 Log laws or power laws: The scaling in the overlap region. *Phys. Fluids* **9** (7), 2094–100.

Paper 1

Measurement and calibration of guide-vane performance in expanding bends for wind-tunnels

By Björn Lindgren, J. M. Österlund & Arne V. Johansson

Dept. of Mechanics, KTH, SE-100 44 Stockholm, Sweden

Published in Exp. in Fluids 1998

The design of guide vanes for use in expanding bends was investigated both experimentally and numerically. The primary application in mind is the use of expanding corners in wind-tunnels for the purpose of constructing compact circuits with low losses. To investigate the performance of guide vanes in realistic situations expansion ratios between 1 and 5/3 were tested in the experiments. These were carried out in an open wind-tunnel specially built for the present purpose. The experimental results demonstrated that suitably designed guide vanes give very low losses and retained flow quality even for quite substantial expansion ratios. For wind-tunnel applications expansion ratios around 1.3 seem appropriate. Optimization of a guide vane design was done using a two-dimensional cascade code, MISES. A new vane optimized for an expansion ratio of 4/3 gave a two-dimensional total pressure-loss coefficient as low as 0.041 for a chord Reynolds number of 200000.

1. Introduction

In closed wind-tunnels the requirement of attached flow in the diffusers is often a major factor in determining the total length of the circuit. In the present work we investigate the idea of using expanding corners equipped with guide vanes to reduce the need for diffusers in wind-tunnel applications. Actually, the use of expanding corners could also be of interest in various other applications, such as ventilation systems.

Expanding corners with low losses would both reduce the total losses and give the possibility of increasing the length of the test section for a given circuit length. Space restrictions are often a serious limiting factor when wind-tunnels are designed. Expanding corners offer a promising way to obtain a compact circuit if a good performance of the guide vanes can be guaranteed.

Many wind-tunnels use $\frac{1}{4}$ -circle-shaped vanes with prolongation at the trailing edge. Such vanes have a three-dimensional total pressure-loss coefficient of typically 0.20, see Klein *et al.* (1930). This is about 4 times as much

as for an optimized profile. It is not, however, always the lowest pressure-loss coefficient that is desirable. Also good flow quality is essential, especially in the corner upstream of the settling chamber.

The present work includes both an experimental and a numerical investigation of guide vane performance in expanding 90° bends. The experiments cover a range of Reynolds numbers, vane spacings and area ratios. The numerical calculations were done both for comparison with the experimental results and to optimize a new vane for expanding corners.

The experiments were performed in a small test tunnel built specifically for this purpose. It is an open tunnel, with a $300 \times 300 \text{ mm}^2$ straight section upstream the corner connected to the downstream variable area section. The tests covered a chord Reynolds number range up to 230000. The total pressureloss coefficient was determined and the behaviour of the flow was studied with the aid of smoke visualization.

During the construction of the MTL wind-tunnel at KTH a guide vane was developed and optimized for a non diffusing corner at low Reynolds numbers. A first part of this study is reported by, Sahlin & Johansson (1991), pertaining to vanes designed to have turbulent boundary layers. The ones finally used in the MTL-tunnel at KTH were designed to have laminar boundary layers. An already good understanding of its behaviour and the very low pressure-loss achieved in a corner using this vane made it suitable for the new application. The two-dimensional pressure loss coefficient is below 0.04 for this vane at a chord Reynolds number of 200000.

These vanes were tested in expanding corners and found to give quite satisfactory results. A new vane was also designed and optimized for the situation in an expanding corner.

The present results will be used in the construction of a new wind-tunnel at KTH, where the corner expansions are used to accommodate a total area expansion of a factor of three. Plane diffusers, with the expansion only in the direction normal to the plane of the tunnel circuit, are then used to give a further area increase by a factor of three. Hence, a total contraction ratio of nine is achieved with a quite moderate need of diffusers, yet with an expansion ratio of about 1.32 in each corner. The results presented in this work show that this can be achieved with very small losses in the corners, and a good quality of the flow exiting the corners.

2. Methods of calculating total pressure-loss coefficient and lift coefficient

When the flow passes through a sharp bend equipped with guide vanes, the pressure field is set up by the ensemble of vanes and the walls. Hence, instead of analyzing a single vane, one has to analyze a cascade of vanes.

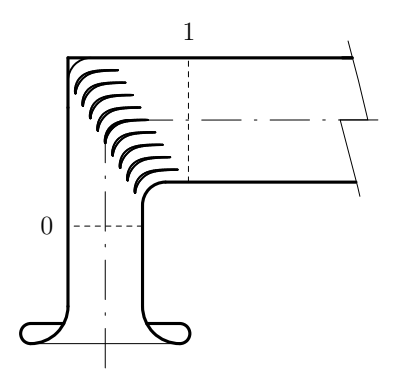


FIGURE 1. The guide-vane corner with the measurement positions 0 & 1.

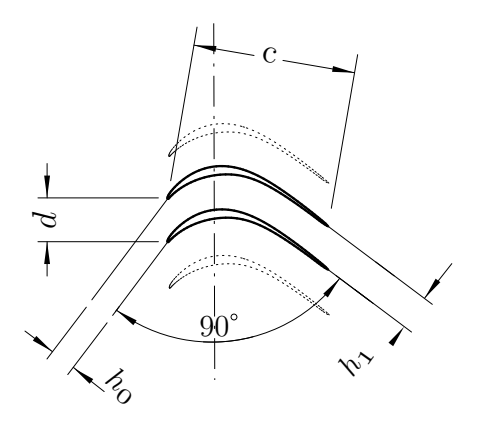


FIGURE 2. The cascade geometry.

2.1. The total pressure-loss coefficient

The quantities needed to be measured in the experiments are the difference between total and static pressure at position 1 and the difference between atmospheric pressure and static pressure at position 0 and 1 respectively. Position 0 is located upstream of the corner and position 1 is located downstream of the corner (see figure 1).

The total pressure-loss coefficient is defined as

$$\frac{\Delta H}{q_0} = \frac{p_{\text{t0}} - \overline{p_{\text{t1}}}}{q_0} \tag{41}$$

where p_{t0} is the total pressure at position 0 and $\overline{p_{t1}}$ is the mean value of the total pressure over the cross-section at position 1. ΔH is the average total pressure-loss in the corner and q_0 is the dynamic pressure at position 0. The dynamic pressure at position 0 is defined as

$$q_0 = \frac{1}{2}\rho U_0^2 \tag{42}$$

where U_0 is the flow velocity at position 0. The mean value of the total pressure at position 1 is

$$\overline{p_{t1}} = \frac{1}{nh_1} \int_0^{nh_1} p_{t1}(y) dy \tag{43}$$

where n is the number of vanes over which the integration is performed and h_1 is the spacing between the vanes perpendicular to the outflow direction, see figure 2.

If the frictional resistance in the inlet is neglected the Bernoulli's theorem gives that q_0 is the difference between the atmospheric pressure and the static pressure at position 0. Hence,

$$q_0 = p_{\text{atm}} - p_0 \tag{44}$$

The same reasoning yields that the total pressure at position 0, p_{t0} , is equal to the atmospheric pressure,

$$p_{\rm t0} = p_{\rm atm} \tag{45}$$

Combining equations 41, 43, 44 and 45 results in the following expression for the total pressure-loss coefficient written on a form displaying the pressure differences measured in the experiments,

$$\frac{\Delta H}{q_0} = \frac{p_{\text{atm}} - p_1 - \frac{1}{nh_1} \int_0^{nh_1} (p_{\text{t1}}(y) - p_1) \, dy}{p_{\text{atm}} - p_0} \tag{46}$$

2.2. Calculation of lift coefficient

From the momentum theorem, the following expression for the lift-force on a 90° expanding bend, can be derived.

$$L' = 2q_0 \frac{d}{e} \tag{47}$$

where L' is the lift force per unit length in the spanwise direction and d is the spacing between the vanes, see figure 2. The expansion ratio, e, is defined as

$$e = \frac{h_1}{h_0} \tag{48}$$

where h_0 and h_1 is the spacing between the vanes perpendicular to the inflow and outflow directions respectively, see figure 2.

The total pressure-loss over the cascade, ΔH , is

$$\Delta H = \frac{D'}{d} \tag{49}$$

where D' is the drag per unit length in the spanwise direction.

This results in the following expression for the total pressure-loss coefficient,

$$\frac{\Delta H}{q_0} = \frac{2}{e} \frac{D'}{L'} \tag{50}$$

Note that the lift-to-drag ratio in equation 50 refers to the entire corner and not just a single vane. In other words it is important not only to maximize the lift-to-drag ratio for a single vane but also to reduce the number of vanes needed in the cascade.

The dimension-less lift coefficient is defined as

$$c_{L'} = \frac{L'}{\frac{1}{2}\rho c u^2} \tag{51}$$

where c is the vane chord and u is the flow speed over the vanes. The question is now which flow speed is the most representative for this case. The most important factor affecting the flow characteristics is obviously separation, which normally will start at the trailing edge of the vane. Therefore the flow speed at the trailing edge is chosen for normalization in expression 51. It now reads

$$c_{L'} = \frac{L'}{\frac{1}{2}\rho c(\frac{U_0}{e})^2} \tag{52}$$

Introducing the dimension-less pitch, ϵ , defined as the vane spacing to chord ratio,

$$\epsilon = \frac{d}{c} \tag{53}$$

results, together with eq. 42, 47 and 52, in the following equation for the lift coefficient

$$c_{L'} = 2\epsilon e. (54)$$

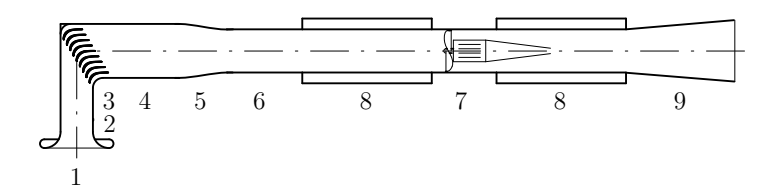


FIGURE 3. The wind-tunnel used in the experiments. Expansion ratio $e = \frac{5}{3}$.

3. Experimental apparatus

The wind tunnel, see figure 3, used in the experiments was constructed especially for this purpose, although the fan with upstream and downstream silencers existed as parts of an older test rig.

3.1. The wind-tunnel used in the experiments.

The tunnel is of open-suction-type with an inlet equipped with a contraction (1), (numbers referring to figure 3), with an area ratio of 9.

The straight section upstream the corner, (2), has an area of 300×300 mm² and a length of about 400 mm to ensure uniform inflow conditions for the corner vanes. In this section the static wall pressure is measured at a location 300 mm downstream of the inlet, at half tunnel height. Extra care has been taken to achieve good quality pressure taps. This is very important when measuring static pressure, see Shaw (1960).

The 90° corner, (3), has a constant inlet area, and is adaptable to the expansion ratios, 1, $\frac{4}{3}$, $\frac{3}{2}$, $\frac{5}{3}$ by varying the outlet width to 300, 400, 450 and 500 mm, respectively, keeping the tunnel height constant at 300 mm. The corner walls are given a radius of curvature of 77.5 mm.

The guide vanes (91L198) tested are of the same design, although somewhat smaller than those used in the MTL low turbulence wind-tunnel at KTH. They are optimized for a non-expanding corner with a pressure-loss coefficient for such a situation that has been shown to be very small. They are made of aluminum extruded at SAPA, Sweden. Their span is 282 mm and the chord is 196 mm. This gives an aspect ratio of about 1.44.

To minimize the secondary flow over the vanes at this low aspect ratio, the wall boundary layers have to be controlled. This is achieved by separating the vanes 8 mm from the wall boundary layers. Small $\frac{1}{4}$ -circle plates guides the boundary layer flow through the corner.

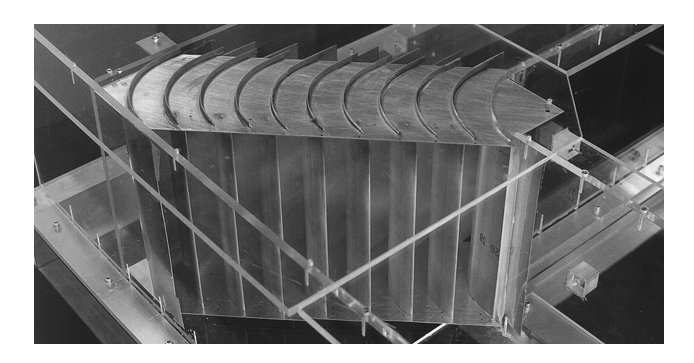


FIGURE 4. The guide vanes at expansion ratio 1

A mechanism enabled the angle of attack of the guide vanes to be easily adjustable in order to obtain the desired outflow angle which is achieved by measuring the static wall pressure 300 mm downstream from the corner.

The straight section downstream the corner, (4), is made with an adaptive wall that enables the desired expansion ratio to be set. A pair of static wall pressure sensors is located 110 mm downstream from the inner radius at half tunnel height.

Sections, (5), (6), (7), (8) and (9) include a diffuser, a transformation from a square to a circular cross section, silencers, a fan and another diffuser to increase the top speed of the wind-tunnel.

The speed range is from 0 to 25 m/s upstream of the corner giving a maximum chord Reynolds number of 325000.

3.2. Measurement equipment.

The measurements were made with a total pressure tube 2 mm in diameter and 100 mm long. It was attached to a 400 mm long tube 8 mm in diameter, which could be traversed in the cross-stream direction with a resolution of about 10 μ m.

A high accuracy (Furness Control FC012) micro-manometer was used for the pressure measurements.

4. Measurements of the total pressure-loss coefficient

Four series of measurements were carried out to investigate the dependence of the two-dimensional total pressure-loss coefficient on the key flow parameters. First, measurements with a pitch (spacing to chord ratio) of 0.27 were made at the expansion ratios 1, $\frac{4}{3}$, $\frac{3}{2}$ and $\frac{5}{3}$. Then, two different expansions, $\frac{4}{3}$ and $\frac{3}{2}$, were used to investigate the effects of the Reynolds numbers in the range from 25000 to 230000. In a third series of measurements the influence of the pitch was examined with the pitch ranging from 0.27 to 0.39. The aim was to find an optimum pitch for the expansion ratio $\frac{4}{3}$. The final type of comparative measurements studied the three expansion ratios, 1, $\frac{4}{3}$ and $\frac{3}{2}$, with the vanes having the same lift coefficient. The Reynolds number was 200000 in all measurements excluding the Reynolds number variation experiment.

4.1. Variation of expansion ratio for constant pitch.

The total pressure-loss coefficient increases with increasing expansion. There is reason to assume that the rate of increase becomes higher at large expansion ratios because of boundary layer separation on the vanes. In order to investigate this behaviour, expansion ratios as large as $\frac{5}{3}$ were tested.

A Reynolds number of 200000 was selected because it is high enough to make the pressure loss fairly independent of small variations, but still low enough to represent typical flow speeds of low-speed wind-tunnels. In this case, with a vane chord of 196 mm, the velocity is about 15 m/s.

The pitch chosen is the same as in the MTL low turbulence wind-tunnel at KTH which is motivated by the fact that the vanes used in the experiments are of the same type as in that tunnel. The MTL-tunnel does not have expanding corners though. This pitch (0.27) is not an optimized value for the total pressure-loss coefficient, but is instead optimized for low disturbances in the flow and the vanes are thus able to take higher loads, occurring in expanding corners.

The results for different expansion ratios indicate indeed that there is a possibility to successfully incorporate the expanding corner element into the design of wind-tunnels (see figure 5). The results were very encouraging even at rather large expansion ratios. A more dramatic increase of the two-dimensional total pressure-loss coefficient was found only between the two highest expansion ratios.

The pressure distribution at position 1 is shown in figure 6 for an expansion ratio of $\frac{4}{3}$. For this expansion ratio flow over the vanes is essentially attached and the loss is only marginally higher than for the non-expanding case. The wake profiles for the largest expansion, on the other hand, indicate substantial separation of the vane boundary layers.

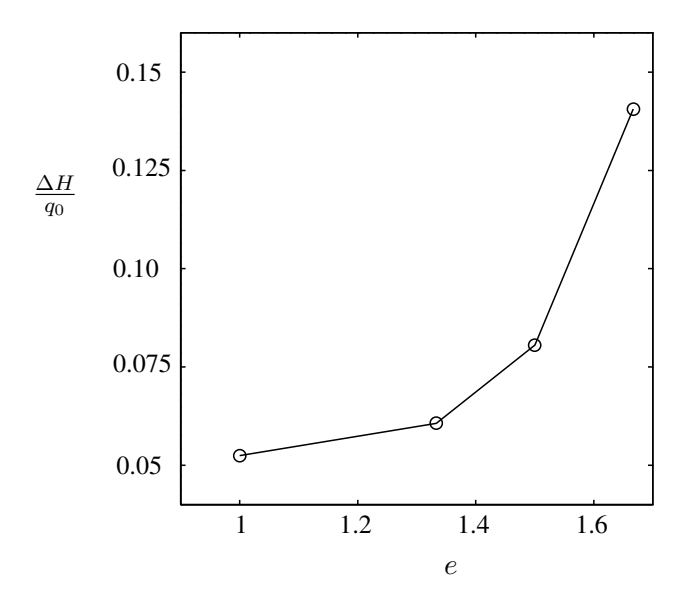


FIGURE 5. The total pressure-loss coefficient as a function of the expansion ratio. Re=200000 and $\epsilon=0.27$

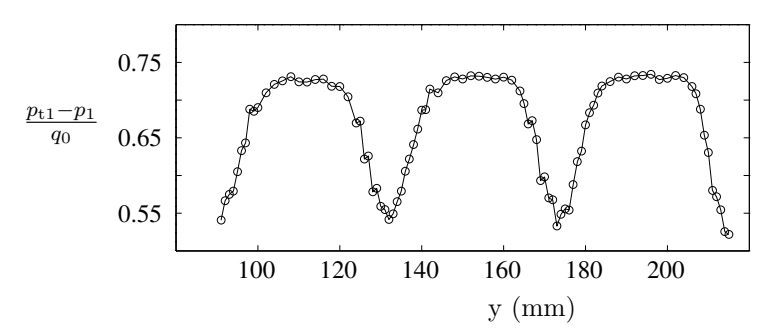


FIGURE 6. Typical wake pressure distribution. $e = \frac{4}{3}$, $\epsilon = 0.27$ and Re = 200000.

4.2. Variation of Reynolds number

The Reynolds number dependence of the total pressure-loss coefficient was studied at the two expansion ratios, $\frac{4}{3}$ and $\frac{3}{2}$. For non-diffusing corners with attached laminar flow on the vanes the normalized loss varies approximately as

$$\frac{\Delta H}{q_0} \sim \frac{1}{\sqrt{Re}} \tag{55}$$

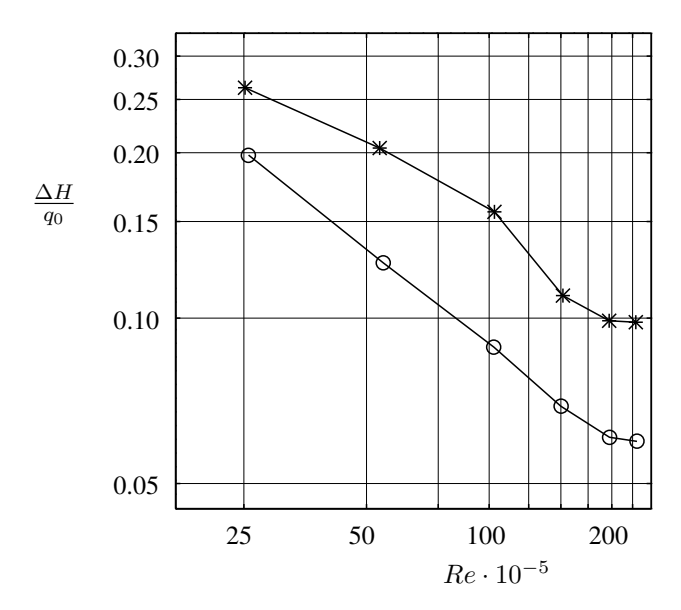


FIGURE 7. The total pressure-loss coefficient as a function of the Reynolds number. $*: e = \frac{3}{2}$ and $\epsilon = 0.24$, $\circ: e = \frac{4}{3}$ and $\epsilon = 0.27$.

The two measurement series with varying Reynolds numbers for expansion ratios of $\frac{4}{3}$ and $\frac{3}{2}$ gave similar results, although somewhat less favourable for the larger expansion, see figure 7. Hence, as might be expected, low-Reynolds number effects seem to be more severe at larger expansions.

At the lowest Reynolds number studied, about 25000, the flow speed is only 1 to 2 m/s which makes the measurements rather inaccurate and sensitive to disturbances caused by air movements in the laboratory outside the inlet of the open tunnel.

For the smaller expansion, $\frac{4}{3}$, we can observe a behaviour in figure 7 that is approximate in agreement with the expected from a completely laminar attached flow. Hence the slope is close to $-\frac{1}{2}$ in the log-log plot (cf eq. 55). At higher expansion ratio the slope is smaller at low Reynolds number. Thereafter the total pressure-loss coefficient first begins to decrease faster then at lower Reynolds numbers but with increasing Reynolds number the decrease in the value of the coefficient slows down again. An explanation for this behaviour could be that the flow is separated at low Reynolds numbers and at some higher value there is a reattachment creating a separation bubble. Downstream of the reattachment the flow is most probably turbulent and the relative increase seen at high Reynolds numbers may then be interpreted as being caused by turbulent skin friction over an increasing part of the vane as the separation bubble

becomes smaller. This behaviour would qualitatively explain the appearance of the curve for $\frac{3}{2}$ in figure 7 however this phenomenon has to be examined further.

4.3. Variation of pitch

The pressure-loss variation with pitch was investigated with the aim of finding an optimum at an expansion ratio in the range that would be of interest for wind-tunnel applications. This was here chosen as $\frac{4}{3}$. The optimum should be expected to vary somewhat with the expansion ratio. Actually a minimum of the total pressure-loss may not be the optimum solution in a more general sense since stability and flow quality also must be considered.

To find the vane spacing with the lowest value of the total pressure-loss coefficient, a series with the pitch ranging from 0.24 to 0.39 was performed. The results in figure 8 exhibit a minimum at a rather high value of the pitch, about 0.35. At this high value, the flow is most probably separated, but because of the thickness of the profiles and the frictional resistance they produce, a certain amount of separation leads to lower losses since fewer vanes are needed. The Reynolds number used here was 200000. At lower Reynolds numbers separation tends to occur more easily, and the optimum value for the pitch will then be somewhat lower. The behaviour of the total pressure-loss coefficient as a function of the pitch indicates a sharp increase for pitch-values higher than the optimum value.

4.4. Variation of expansion ratio for constant lift coefficient

To best illustrate how the total pressure-loss coefficient varies with varying expansion ratio, one should perhaps make the comparison for equal loading of the vanes. By choosing $\epsilon = 0.27$ for the expansion ratio $\frac{4}{3}$, we get a lift coefficient from eq. 54 of 0.72, which should not be too high for this type of vane. With equal lift coefficient for the expansion ratios 1, $\frac{4}{3}$ and $\frac{3}{2}$ we obtain pitch values of 0.24, 0.27 and 0.36 for each expansion ratio respectively.

Hence, in this measurement series the expansion ratio is varied under conditions such that the lift coefficient is held constant. This gives perhaps the most direct indication on how well every particular expansion functions. The increase in the total pressure-loss coefficient was found to be slightly stronger than in the case with the same pitch for every expansion, see figure 9. The Reynolds number was the same in both series, about 200000, which enables a direct comparison between the results in figures 5 and 9.

4.5. Summary of the experimental results

It is clear from the above that the idea of expanding wind-tunnel corners works well if the expansion is not too large and the Reynolds number is kept reasonably high. A good performance requires fairly well designed vanes but even

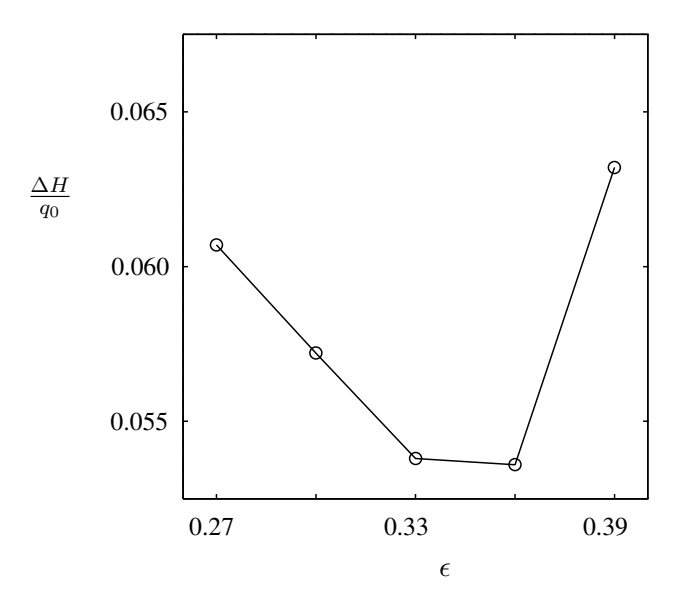


FIGURE 8. The total pressure-loss coefficient as a function of the pitch. $e = \frac{4}{3}$ and Re = 200000.

vanes optimized for non-expanding corners can work well if designed to accommodate the lift coefficients occurring in the expanding corner.

With vanes optimized for a particular expansion the results will obviously be better. In the present investigation the vanes used were originally designed for non-expanding corners. A configuration with these vanes for an expansion ratio of $\frac{4}{3}$ and a pitch between 0.33 and 0.36 gives a total pressure-loss coefficient of less than 0.054 at a Reynolds numbers of about 200000. A vane optimized for a non-diffusing corner was found by Sahlin & Johansson (1991) to give a two-dimensional total pressure-loss coefficient of about 0.036 at Re=154000. The increase in total pressure-loss is 50% for the expanding case.

If we choose to compare cases with equal lift coefficient, the $\frac{4}{3}$ expansion has a two-dimensional total pressure-loss coefficient of 0.061 to be compared with 0.048 for the non-expanding case, *i.e.* a 27% loss increase caused by the expansion.

We may also have in mind that typical vanes used today in wind-tunnels are designed as $\frac{1}{4}$ -circle-shaped vanes with prolongation at the trailing edge. For a non-expanding corner such vanes give a three-dimensional total pressure-loss coefficient of about 0.20, see Klein *et al.* (1930).

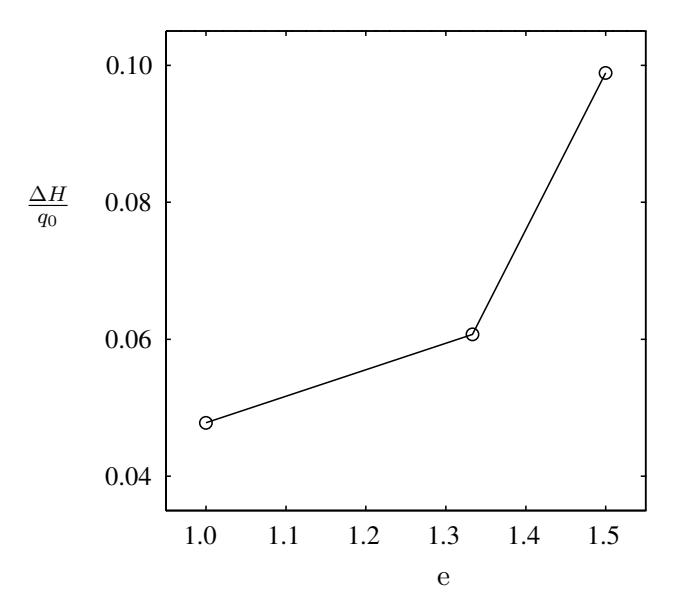


FIGURE 9. The total pressure-loss coefficient as a function of the expansion ratio. Re = 200000 and $c_{L'} = 0.72$

5. Calculations of infinite cascade with experimental vane and vane optimization

Numerical calculations matching the Reynolds numbers and the expansion ratios with those in the experiments, give an opportunity to further study the values of the losses and pressure distributions around the vanes. They also provide information on the level of accuracy of the measurements.

Since the tested vane is optimized for non-expanding flows there are cases where parts of the flow are separated when the vane is used in an expanding corner. Abrupt increases of the pressure coefficient, C_p , in the pressure distribution of the vane will indicate where the separations take place. A profile more optimized for an expansion ratio of $\frac{4}{3}$ is also developed.

5.1. The numerical code used in the calculations

The numerical calculations are made with the MISES code. MISES is a collection of programs for cascade analysis and design, including programs for grid generation and initialization, flow analysis, plotting and interpretation of results, and an interactive program to specify design conditions. MISES was developed by Harold Youngren and Mark Drela to analyze turbo-machinery design.

MISES first generates an incompressible 2-D panel solution to find the stagnation streamlines. It also locates iso-potentials at the vane edges. The streamlines and iso-potentials are used to generate the grid.

On the grid generated previously MISES solves steady Euler equations coupled with integral boundary layer equations using a Newton-Raphson method. This makes it possible to analyze flows with strong viscous/inviscid interactions like shock induced separation flows or separation bubbles. However, this requires the flow to be compressible. The minimum Mach number needed is in the range of 0.10-0.15. This is small enough not to significantly affect the results for incompressible cases.

Optimizations of vane shapes can be performed with the help of an inverse method. Two different inverse methods are available, one suited for large modifications and one suited for detail modifications. In these methods the pressure distribution of the vane can be altered at wish and a number of modified Chebyshev polynomials are used to change the shape of the vane to fit the specified pressure distribution. These polynomials can be modified according to the users requests. The changes in the pressure distribution, however, has to be moderate to achieve convergence. This means that the optimization process has to be repeated a considerable number of times before major improvements are reached. It is also possible to edit the blade shape in the blade editor. However, only basic editing modes like rotate, translate and scale are available.

For further information on the MISES code see Youngren & Drela (1991); Drela & Youngren (1995); Giles & Drela (1987)

5.2. Calculations of infinite cascades with the experimental vane

The losses calculated in the MISES code are matching the losses obtained in the experiments quite well at moderate expansion ratios (see figure 10). However at higher expansion ratios the agreement is not very good. The losses from the computations show only a slight increase with increasing expansion ratio. Hence, the computations do not capture the large effects of separation at large expansion ratios. Three-dimensional effects will also disturb the two-dimensional measurements resulting in a faster increase of the losses then in the numerically calculated solutions which are purely two-dimensional.

The pressure distribution around the vane at the expansion ratio $\frac{4}{3}$ clearly indicates that it was not designed for expanding corners (see figure 11). On the lower surface there is a small separation bubble near the leading edge and on the upper surface there is another but larger separation bubble about $\frac{1}{3}$ downstream of the leading edge. These features have a negative effect on the performance of the vane and the losses can be reduced substantially in an optimization process.

The vane is also quite sensitive to variations in the angle of attack. Especially the first corner in a wind-tunnel is exposed to significant variations in the

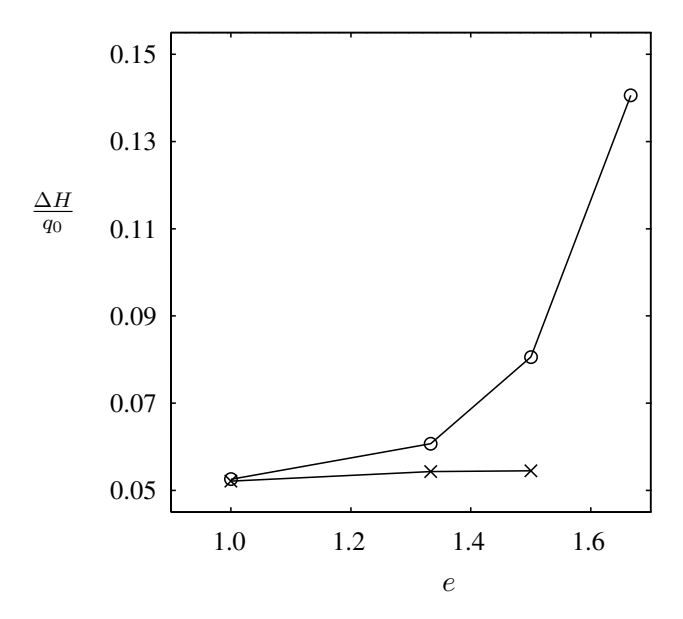


FIGURE 10. The total pressure-loss coefficient as a function of the expansion ratio. $\epsilon = 0.27$ and Re = 200000. ×: computations, \circ : experiments

angle of attack where the disturbances from the test section are of considerable strength.

Numerical calculations with variations in the Reynolds number indicates an increase in the size of the separation bubbles with decreasing Reynolds number. The separation bubble on the upper surface also tends to move downstream with decreasing Reynolds number. For sufficiently small Reynolds number (or high loads), the flow will separate entirely from the vane. The MISES code is not able to reproduce this behaviour since it only accepts small wakes.

As long as the expansion ratio is moderate, the numerical calculations and the experimental results agree well. This means that the numerical calculation method can be used in the optimization process which could lead to a new profile design that better suits the particular conditions of expanding corners.

5.3. Optimization of a vane for the $\frac{4}{3}$ expansion ratio

When a new vane, emerging from the inverse process, fulfills the requirements of the designer one has to bear in mind that the profile is only optimized for the given Reynolds number, pitch, angle of attack and expansion ratio. To create a vane, that can be used under other circumstances than those specified in the optimization process, it is normally not meaningful to push the optimization

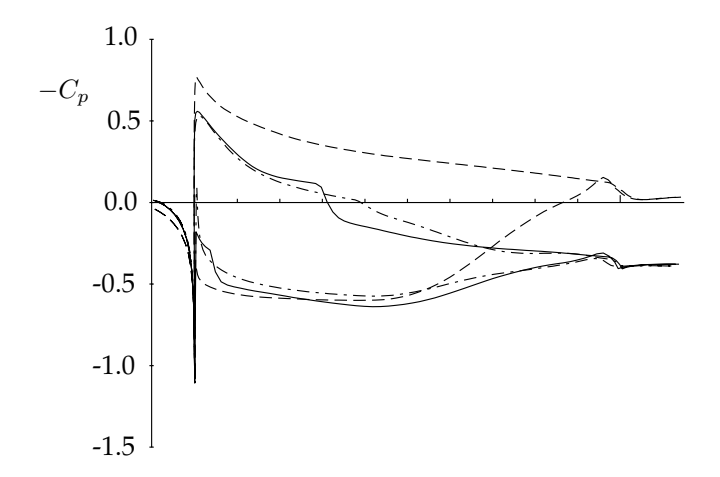


FIGURE 11. Pressure distribution for 91L198 at Re=200000. Solid line: $e=\frac{4}{3}$ and $\epsilon=0.27$. Dashed line: e=1 and $\epsilon=0.3$ (design point). Dash-dotted line: $e=\frac{4}{3}$ and $\epsilon=0.27$

too far for any given set of parameters. It is more important to assure that the vane can operate within a wide spectrum of flow conditions. This may lead to slightly larger losses but it will not have a major influence on e.g. the overall losses of the wind tunnel.

The main goal of this optimization was to minimize and, if possible, eliminate all separation bubbles. The separation bubbles generates both transition from laminar to turbulent boundary layers and rapid increase in the pressure. With the new vane the influence of separation bubbles has been substantially reduced. See figure 11.

To improve the tolerance to variations in angle of attack the leading edge radius was enlarged. This resulted in a slightly larger total pressure-loss but increased the ability to perform with up to 3 degrees of negative angle of attack, (see figure 12).

The new vane is designed for a Reynolds number of 200000 but it has been tested numerically for Reynolds numbers between 100000 and 600000. The total pressure-loss coefficient decreases rapidly with Reynolds number between 100000 and 200000 but for Reynolds numbers higher than 200000 the decrease in total pressure-loss coefficient is small.

The conditions under which the optimization was performed is essential when comparing the results with other calculations or experiments. The Reynolds number, pitch and expansion ratio all have a strong impact on the final results, both in terms of losses and optimum vane shape. This new vane has

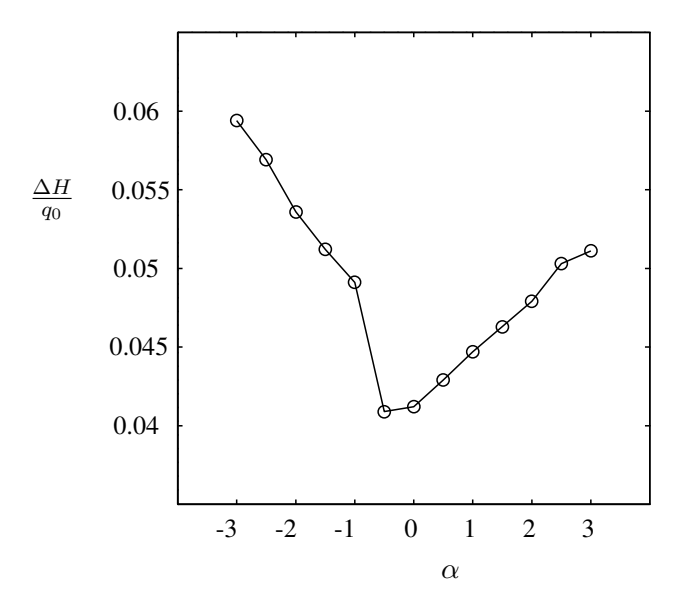


FIGURE 12. The total pressure-loss coefficient as a function of the angle of attack, α . $e=\frac{4}{3}$, $\epsilon=0.27$ and Re=200000.

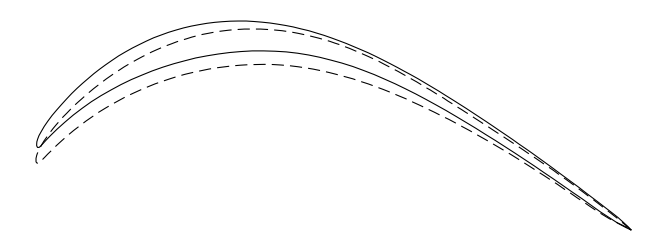


FIGURE 13. Solid line: 91L198 optimized for non-expanding corners, e=1 and $\epsilon=0.3$. Dashed line: L27132B the new vane optimized for expanding corners, $e=\frac{4}{3}$ and $\epsilon=0.27$.

a total pressure-loss coefficient of 0.041 with a Reynolds number of 200000, a pitch of 0.27 and an expansion ratio of $\frac{4}{3}$.

The differences in profiles of the experimentally tested vane and the new design, L27132B, suited for expanding corners are illustrated in figure 13. Coordinates representing the shape of the new vane can be found in Lindgren *et al.* (1997).

6. Discussion

The idea of using guide vane corners in wind-tunnels has been put forward by several earlier investigators, e. g. Collar (1936); Klein et al. (1930); Kröber (1932); Wolf (1957). An investigation of expanding corners that also include control of the boundary layers, was carried out by Friedman & Westphal (1952). They studied a 90° cascade expanding bend with an area ratio of 1.45: 1 and with several inlet boundary layers. Despite the rather simple design of the vanes used in that study quite promising results were obtained with a three-dimensional, but with thin boundary layers, total pressure-loss coefficient as low as 0.11. The total pressure-loss coefficient was almost independent of the Reynolds number that was varied between 330000 and 950000.

The present results show that a more sophisticated vane design can reduce this significantly and that indeed it is possible to construct expanding corners with small additional losses as compared to non-expanding ones.

This has several implications for the design of wind-tunnel circuits, but could also be used in a number of other applications, such as ventilation systems. For wind-tunnels it opens possibilities to substantially reduce the length of the return circuit without increasing the risk for separation in the diffusers. Actually, there are often conflicting requirements in connection with the construction of wind-tunnels to fit in the circuit within a given space and to have as large a test section as possible.

A possibility is also to reduce the total losses in the circuit by reducing wall friction losses and by enabling a larger cross sectional area at the second corner, thereby reducing the losses there. In normal situations the diffuser between the first and second corners is quite short so that the second corner will have a cross sectional area not much larger than the first, and thereby comparable losses.

For large expansion ratios large regions of the flow will be separated and the mean flow will be non-uniformly distributed with higher velocities near the inner radius. In the present study this phenomenon was visualized by smoke, which however was only possible at low Reynolds number (and may perhaps not be wholly representative for high Reynolds numbers). Also three-dimensional secondary flow effects increase with increasing expansion. These drawbacks were quite negligible though at moderate expansion ratios, such as 1.33.

The geometry in an expanding corner is also somewhat different from an ordinary corner. In contrast to non-expanding corners the imaginary line from the center of the inner radius to the center outer radius does not go through

the points where the straight walls meet. This means that the whole package of vanes is translated downstream in the tunnel. The relative position between the vanes also differs from the non-expanding case. This implies that there is room for significant improvements in the vane geometry from that optimized for the non-expanding situation. This was also clearly demonstrated by the new vane L27132B. Perhaps even better results can be achieved if the vane is designed to have a turbulent boundary layer on the upper surface. With the fast increase in pressure along the chord which is a result of the expansion in the corner it is very difficult to maintain a laminar boundary layer on the upper surface. A vane designed to have turbulent boundary layers may therefore in some respects be a better starting-point in the optimization process.

The lift force on the vanes changes direction with changing expansion. This called for adjustments in the profile geometry. The absolute value of the lift force decreases with increasing expansion. This improves the efficiency of the expanding corner solution.

A suitable methodology that one may adopt in wind-tunnel circuit design with expanding corners is the following. Let us first define the x-y plane as the plane defined by the circuit centerline. For a given contraction ratio, C_R , and a contraction section with equal distortions in the two lateral directions, we can then choose to take the total x-y plane expansion, $\sqrt{C_R}$, in the corners, and the z-expansion in the diffusers. The diffusers will hence be plane with this approach, and will have a total area increase of a factor $\sqrt{C_R}$, only. The expansion in each corner becomes $C_R^{1/8}$ if the expansion is chosen to be the same in all corners. For instance, with a contraction ratio of 9, the expansion in each corner becomes approximately 1.32. This value will vary only slightly over the range of interesting contraction ratios because of the small value of the exponent $(\frac{1}{8})$.

Many alternative approaches are, of course, possible, depending on the design requirements in the specific case.

Acknowledgments

The authors are grateful to Professor Mark Drela at MIT for supplying the MISES code. We wish to thank Mr. Alexander Sahlin and Mr. Per Åke Thorlund for valuable comments on the design of guide vanes. We are grateful to Mr. Ulf Landén and Mr. Marcus Gällstedt who helped with the manufacturing of the experimental apparatus. We also wish to thank NUTEK for the financial support.

References

Collar, A. R. 1936 Some experiments with cascades of aerofoils. A.R.C. Technical Report 1768. Aeronautical research committee.

- Drela, M. & Youngren, H. 1995 A users guide to MISES 2.1. MIT Computational Aerospace Sciences laboratory.
- FRIEDMAN, D. & WESTPHAL, W. R. 1952 Experimental investigation of a 90° cascade diffusing bend with an area ratio of 1.45:1 and with several inlet boundary layers. TN 2668. NACA.
- GILES, M. B. & DRELA, M. 1987 Two-dimensional transonic aerodynamic design method. AIAA Journal 25 (9), 1199.
- KLEIN, G. J., TUPPER, K. F. & GREEN, J. J. 1930 The design of corners in fluid channels. *Canadian J. of research* 3, 272.
- KRÖBER, G. 1932 Schaufelgitter zur umlenkung von flussigkeits-strömung. Ingenieur-Archiv 3, 516.
- LINDGREN, B., ÖSTERLUND, J. M. & JOHANSSON, A. V. 1997 Measurement and calculation of guide vane performance in expanding bends for wind tunnels. TRITA-MEK 1997:6. Department of Mechanics, KTH.
- SAHLIN, A. & JOHANSSON, A. V. 1991 Design of guide vanes for minimizing the pressure loss in sharp bends. Phys. Fluids A 3, 1934.
- Shaw, R. 1960 The influence of hole dimensions on static pressure measurements. J. Fluid Mech. 7, 550.
- Wolf, H. 1957 Messungen im nachlauf eines gleichdruckgitters für 90-umlenkung. Maschinenbautechnik 6 (10), 539.
- Youngren, H. & Drela, M. 1991 Viscous/inviscid method for preliminary design of transonic cascades. In AIAA, SAE, ASME, and ASEE, Joint Propulsion, Conference, 27th..

Paper 2

P2

Design and evaluation of a low-speed wind-tunnel with expanding corners

By Björn Lindgren and Arne V. Johansson

Dept. of Mechanics, KTH, SE-100 44 Stockholm, Sweden

Published as internal report. TRITA-MEK 2002:14

A new low-speed closed circuit wind-tunnel has been designed and built at the Royal Institute of Technology, Stockholm. It has a test section with a cross section area of 0.5×0.75 m² and a length of 4.2 m. The maximum speed is about 48 m/s with empty test section. The contraction ratio is 9. A heat exchanger, a honeycomb and 5 screens are included to minimize flow disturbances in the test section. The streamwise turbulence intensity in the test section is less than 0.04\% in the core with similar values for the cross stream turbulence intensities. The variation in total pressure is less than $\pm 0.1\%$ and the variation in temperature is less than $\pm 0.07^{\circ}$ C over the cross section area and ± 0.03 °C in time in the center of the test section. The concept of expanding corners, with a substantially larger outlet than inlet cross section area, (e = 1.316), has been implemented successfully with a total pressureloss coefficient in the first corner downstream the test section of 0.047 at a guide-vane chord Reynolds number of 205000. This value is a two-dimensional estimate obtained from measurements in a centre plane downstream the vanes. It compares favorably with the total pressure-loss coefficient in most windtunnels using non-expanding corners. Together with the good flow quality found in the test section this proves the usefulness of expanding corners in modern wind-tunnels to minimize the overall size for a given test section length.

1. Introduction

Wind-tunnels represent a useful tool for investigating various flow phenomena. An advantage of using wind-tunnels is that experiments there can be performed under well controlled flow circumstances compared to experiments in the open environment. The drawback is that small scale models often have to be used instead full scale ditto. To achieve the same Reynolds number as for the real application, the kinematic viscosity or flow velocity normally has to be changed. In most wind-tunnels air at atmospheric pressure is used, and the only option left is to increase the flow velocity. Often it is not possible to increase the velocity enough, so the results from wind-tunnel experiments fall in between

those achievable in most well resolved simulations and the real application on a Reynolds number scale. There are however some large wind-tunnels used in the auto and aircraft industries. These tunnels have test sections that can accommodate full scale vehicles and small aircraft.

There are many types of wind-tunnels and they can be classified by e.g. flow speed dividing them into four groups.

- subsonic or low-speed wind-tunnels
- transonic wind-tunnels
- supersonic wind-tunnels
- hypersonic wind-tunnels

Subsonic or low-speed wind-tunnels are the most common type and the wind-tunnel described in this paper is of this type. Transonic wind-tunnels are common in the aircraft industry since most commercial aircraft operate in this regime. Supersonic wind-tunnels can be used to investigate the behavior of jet engines and military aircraft. Hypersonic wind-tunnels find their applications in rockets and space vehicles. A further way to categorize low-speed tunnels is by dividing them into open circuit or closed circuit wind-tunnels. In open circuit wind-tunnels there is no use for corners and long diffusers but the power needed to drive the wind-tunnel is high because of the loss of energy in the outflowing air. Closed circuit wind-tunnels recirculate the air and thus normally need less power to achieve a given flow speed, see section 2, and, above all, facilitate the achievement of well controlled flow conditions in the test section. The present, and most low-speed tunnels used for research, are of the closed circuit type.

Wind-tunnel design is a complex field involving many fluid mechanics and engineering aspects and it is impossible to cover them all in just one paper. Some books and articles have been written about this topic and e.g. Rae & Pope (1984), Bradshaw & Pankhurst (1964) are useful references when designing and constructing low-speed wind-tunnels. See also the comprehensive report on the German-Dutch Wind-tunnel edited by Seidel (1982).

The first wind-tunnel at the Royal Institute of Technology was completed in the summer of 1932 at a newly constructed laboratory for aeronautical sciences. It had a closed circuit and an open jet test section, *i.e.* the test section had no walls. The test section was cylindrical in shape with a diameter of about 1.6 m and a similar length. It was primarily used for measuring forces on aircraft models and airfoils. It had an axial fan and corners with simple guide-vanes made of bent plates in the shape of $\frac{1}{4}$ -circles. The contraction ratio was about 5 and the maximum speed in the test section about 50 m/s, see Malmer (1933). It was later modified with, among other things *e.g.* a closed test section, and was in use until only a few years ago.

A number of other wind-tunnels for aeronautical research have existed over the years at KTH. Another low-speed tunnel, (formerly known as L2 now L2000), was built in 1963 and is still used for aeronautical research. It has a 3 m long test section of 2×2 m² cross section and a maximum speed of 62 m/s. A supersonic, a hypersonic and a ballistic wind-tunnel are also part of the early aeronautical research history at KTH. In 1991 the MTL low-turbulence low-speed tunnel was inaugurated.

The present tunnel complements the MTL-tunnel in several respects, both in research projects and in teaching. In particular it fulfills the need of a test section with very flexible design to allow e.g. strong pressure gradients etc.

The limited available space made it necessary to use innovative design ideas that could allow a large enough test section for research projects, such as high Reynolds number turbulent boundary layer studies, into a small size wind-tunnel. There are some possibilities to reduce the overall size of a closed circuit wind-tunnel without making the test section smaller. One obvious way is to decrease the contraction ratio, CR, i.e. the ratio between the largest cross section are, (found in the stagnation chamber), and smallest cross section area, (found in the test section). Most large wind-tunnels already have quite small contraction ratios though, $CR \leq 6$. One should keep in mind that a high contraction ratio is a key factor in achieving a good flow quality. Another way to reduce size is to use wide-angle diffusers. The use of wide-angle diffusers is a fairly common method to reduce the overall circuit length. The resulting losses, though, are rather high and accompanied by an increased level of flow disturbances. Finally there is also the possibility to use expanding corners which is used in this wind-tunnel.

Expanding corners have a larger outlet than inlet cross section area reducing the need for long diffusers, see section 2.3, and can thus reduce the total wind-tunnel circuit length by about 20% without a large increase in total pressure-loss. The idea of using expanding corners has been around for a long time, e.g. Friedman & Westphal (1952), Collar (1936), Wolf (1957) and Kröber (1932) made some interesting experiments on expanding bends. However, most of the early results were not too encouraging, so the idea was put aside until recently. One of the reasons for the unfavorable results were the use of simple guide-vane shapes. When there is a large expansion, (expansion ratio of e.g. 1.316), in such a short distance a lot of effort has to go into the design of the guide-vanes to avoid boundary layer separation and a large total pressure-loss. Today, some new or planned wind-tunnels use expanding corners both at universities and in the automobile industry. The concept of expanding corners is especially useful in large wind-tunnels, because of the reduction in the total wind-tunnel circuit length.

The design of the guide-vanes used in the present wind-tunnel has primarily been made using the MISES code developed by Harold Youngren and Mark Drela at MIT, see e.g. Drela & Youngren (1995). This code solves the coupled

Euler- boundary layer equations on an infinite array of guide-vanes to compute the two-dimensional flow field. This method allows for small boundary layer separation bubbles but cannot handle large separations. The code was developed for turbo machinery applications and some compressibility has to be introduced for convergence. The main advantage using the MISES code is that it has a built-in optimization tool which allows the user to specify the pressure field on the guide-vane surface and from that obtain the desired guide-vane shape to fit the specified pressure profile. This facilitates the optimization substantially. For more information on the code and its mathematical methods see e.g. Drela & Youngren (1995), Youngren & Drela (1991), Giles & Drela (1987), Drela & Giles (1987).

The use of expanding corners also has implications on other parts in the wind-tunnel circuit. The diffusers in this wind-tunnel are two-dimensional, or plane, *i.e.* the expansion is only in one plane. This type of diffusers are more sensitive to boundary layer separation than their three-dimensional counterparts leading to a smaller maximum opening angle and thus a longer diffuser for a given area increase. This removes a small part of the gains made in wind-tunnel circuit length by using expanding corners. There has been numerous investigations on two-dimensional diffusers and their optimum shape, *e.g.* Fox & Kline (1962), Reneau *et al.* (1976), Çabuk & Modi (1992), Ganesan *et al.* (1991). The diffusers here have straight walls for simple manufacturing.

2. The wind-tunnel design

In 1995 it was decided to build a new low-speed wind-tunnel as a complement to the larger MTL wind-tunnel already operating at the Department of Mechanics, KTH, Stockholm, see Johansson (1992) and Lindgren & Johansson (2002). Aside from reducing the user load on the larger MTL wind-tunnel the purpose of the new tunnel was also to give the undergraduate students the possibility to work with a new state of the art wind-tunnel. A primary aim was to here accommodate experiments that require a large degree of flexibility of the test section geometry. To meet these requirements it was necessary to specify design criteria that are close to those of the MTL wind-tunnel and thereby simplifying the transfer of projects between the two wind-tunnels. The main design criteria are listed in the table below,

- ① Closed circuit wind-tunnel.
- ② Good flow quality (mean flow variation, turbulence intensities & temperature variation).
- \odot Contraction ratio, CR, of 9.
- Test section aspect ratio of 1.5 and the maximum test section length possible in the available space.
- (5) Maximum flow speed in the test section of at least 40 m/s.
- 6 Low noise level.
- ② Low cost.

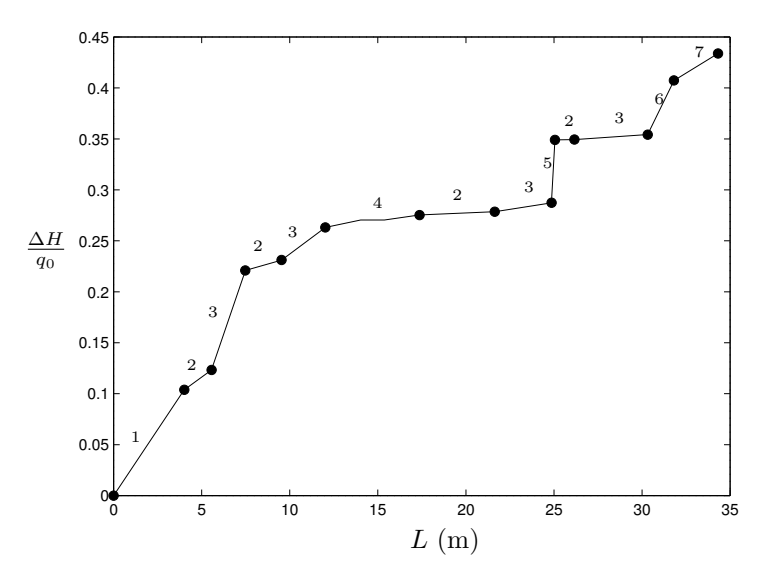


FIGURE 1. An estimate of the cumulative total pressure-loss coefficient for each part in the wind-tunnel at a test section speed of 40 m/s. See table 2 and figure 2 for numbering of wind-tunnel parts.

- ① A closed circuit wind-tunnel gives better control of the flow conditions such as temperature and pressure and it also reduces the necessary power to run the wind-tunnel at a given speed compared to an open wind-tunnel. In addition it improves the environment with lower noise levels and avoids air blowing around the laboratory.
- ② To achieve good flow quality it was decided that the stagnation chamber should have one honeycomb and five screens. It was also decided that the wind-tunnel should be equipped with a heat exchanger. This is the same configuration as in the MTL wind-tunnel, see Johansson (1992).
- ③ To improve the flow quality and to make use of the well-proved contraction shape of the MTL wind-tunnel it was decided that the contraction ratio, which is the ratio between the largest, (stagnation chamber), and the smallest, (test section), cross section area in the wind-tunnel circuit, should be equal to 9.
- 4 The test section aspect ratio was chosen to be identical to that in the larger MTL wind-tunnel to simplify the transfer of projects between the two wind-tunnels. The maximum possible cross section area in the test section with CR = 9 is 0.5×0.75 m² because of space limitations. The length of the test section was chosen to be around 4 m to be able to get a high enough Reynolds number on a flat plate. This size of test section was made possible by the use of expanding corners, see section 2.3 and Lindgren *et al.* (1998)

- \odot Most of the experiments planned for this wind-tunnel are aimed for speeds of about 25 m/s in the test section. To allow for increasing flow resistance due to measurement equipment such as flat plates, cylinders and traversing equipment the design goal for the maximum speed was set to 40 m/s.
- © A large fan running at low rpm and silencers around the fan were expected to be sufficient to achieve low noise levels in the tunnel and the surrounding laboratory.
- ② All the design and construction of the wind-tunnel parts were made inhouse, using the previously acquired knowledge from the construction of the MTL wind-tunnel keeping the total cost of the wind-tunnel to a minimum.

A computer program was written to calculate the size of the individual wind-tunnel parts, the pressure variation and pressure-loss variation around the wind-tunnel circuit. These calculations were made to decide the appropriate motor for the fan and the necessary cooling power to keep the temperature steady at full speed with a set temperature of about room temperature. The calculated total pressure loss coefficient around the wind-tunnel circuit is shown in figure 1. It can be seen that the parts contributing most to the overall loss are the test section, the first expanding corner downstream of the test section, (denoted as corner 1 in this paper), the heat exchanger and the stagnation chamber with the screens and the honeycomb. This illustrates the dilemma where increasing flow quality also means increasing total pressure-loss. Therefore when comparing the total pressure-loss coefficient for different wind-tunnels it is important to bear in mind the length of the test section and what flow quality improving devices are included, e.g. air cooler and number of screens.

By measuring the dynamic pressure in the test section, q_1 , for a variation of fan rpm the power factor, λ , of the wind-tunnel can be estimated. The power factor is a measure of the total pressure-loss of the wind-tunnel circuit and can be compared to the computed total pressure-loss shown in figure 1. It is defined as follows,

$$\lambda = \frac{\Delta p_{\text{tot}}}{\eta_{\text{f}} q_1} = \frac{P_{\text{m}} \eta_{\text{m}}}{A_1 U_1 q_1} \tag{1}$$

where $\Delta p_{\rm tot}$ is the total pressure-loss of the wind-tunnel circuit, $P_{\rm m}$ is the power input from the motor, A_1 is the test section cross section area, U_1 is the test section flow speed and $\eta_{\rm f}$, $\eta_{\rm m}$ are the fan and motor efficiency factors respectively. In table 1 the test section velocity, the power input and the power factor are presented for different fan rpm values. It can be seen that for low rpm the power factor is very high, indicating large losses in the wind-tunnel circuit, and for high rpm the power factor approaches a constant value, which in this case is about 0.45. It should be compared to the estimated value of the power factor of 0.44 at 40 m/s. One can also compare it with the value of the power factor for the MTL wind-tunnel which is about 0.39 at 69 m/s, see Johansson &

TABLE 1. The power input, $P_{\rm m}$, the test section speed, U, and the power factor, λ , for fan rpm values from 100 to 1000.

rpm	100	200	300	400	500	600	700	800	900	1000
$P_{\rm m}$ kW										
U m/s	3.5	8.1	12.7	17.4	22.2	27.1	32.0	36.9	41.8	46.6
λ	1.97	0.89	0.72	0.61	0.56	0.53	0.50	0.48	0.47	0.46

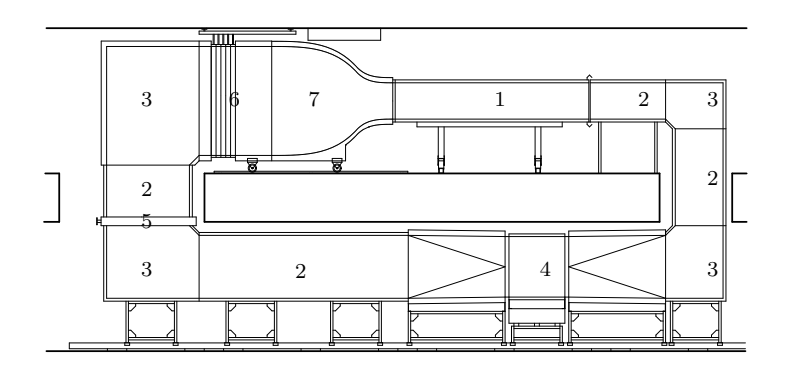


FIGURE 2. The wind-tunnel layout. For description of the numbered parts see table 2.

Alfredsson (1988). The comparison with the MTL wind-tunnel and the trend showing decreasing power factor with increasing test section speed, illustrate the two major influences on the power factor, namely the importance of the size of the wind-tunnel and at what test section speed the value of λ is calculated. A number of design features, especially the number of screens, the length of the test section and the presence of a heat exchanger also have a large influence on the value of λ , (see figure 1). Hence one should keep these effects in mind when comparing the power factor of different closed circuit wind-tunnels.

In the following sections a short description of the wind-tunnel parts is presented. They can be seen in figure 2.

2.1. Test section

The highest velocity in the tunnel circuit occurs in the test section resulting in a large contribution to the total pressure-loss from skin friction on the walls. Also disturbances from models, plates etc in the test section will substantially contribute to the pressure-losses. It is therefore important to remember this when choosing the length of the test section and when the test section accessories, such as traversing system etc are designed. Another effect of disturbances in

Table 2. A description of the wind-tunnel parts. See also figure 2. (A = cross-section area, L = length, e = expansion ratio, D = diameter, P = power, CR = contraction ratio.)

Part	Description
1.	Test section, $(A = 0.5 \times 0.75 \text{ m}^2, L = 4.2 \text{ m})$
2.	Two-dimensional diffuser
3.	Expanding corner, $\left(e = \sqrt[8]{CR} \approx 1.316\right)$
4.	Fan, $(D = 1.25 \text{ m}, P = 15 \text{ kW})$
5.	Cooler, $(P = 17 \text{ kW})$
6.	Honeycomb, screens & stagnation chamber
7.	Contraction, $(CR = 9)$

the test section is that it can lead to flow separation in the diffuser directly downstream of the test section, (referred to as diffuser 1 in this paper), and in corner 1. This is the reason for a somewhat conservative design of the first diffuser. The size of the test section is $0.5 \times 0.75 \text{ m}^2$ in cross section area and 4.2 m in length. This is the maximum possible length due to space restrictions. For a given cross section the length of the test section should not be made too large in order to avoid too much influence on the core flow from the wall boundary layers.

To be able to set the pressure gradient along the centerline of the test section one wall is adjustable to vary the cross section area in the downstream direction. Previous experience from the operation of the MTL wind-tunnel and the difficulty there to adjust the pressure gradient made us choose one adjustable wall instead of two as in MTL. With two opposite adjustable walls a movement of one wall affects the flow at the other wall leading to a time consuming iterative process before the desired pressure gradient is achieved with sufficient accuracy. The entire side of the test section containing the adjustable wall can be replaced making the test section more flexible and facilitating experiments that require major changes of the test section, see e.g Angele (2000). Two walls are also equipped with hatches to improve access to the interior of the test section. The test section is made of a steel frame for stiffness with plywood top and bottom, and the side walls, including the adjustable wall, made of Plexiglas[®].

2.2. Diffusers

In this wind-tunnel the diffusers are plane or two-dimensional. This is a result of using expanding corners where all the expansion in one plane around

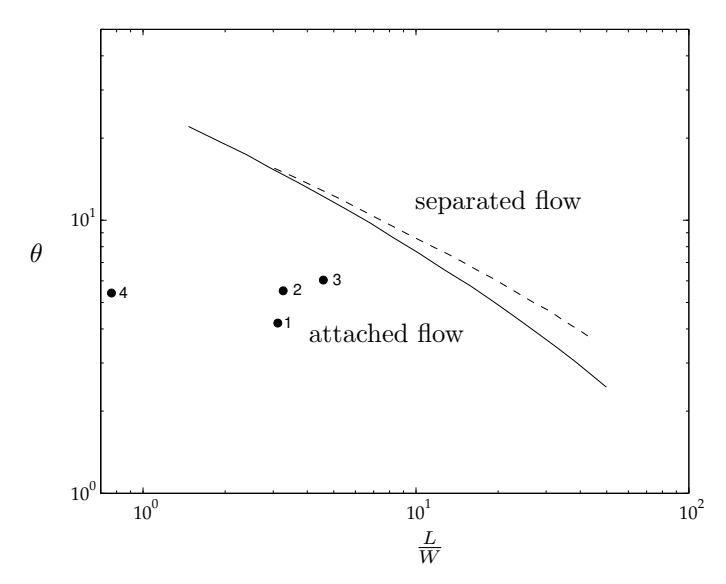


FIGURE 3. Separation of two-dimensional diffusers. —: Line of maximum pressure recovery, —: Line of separation, •: The diffusers in this wind-tunnel numbered from the test section following the flow. L=length, W=width and θ =total opening angle. The lines are taken from Fox & Kline (1962).

the wind-tunnel circuit is accommodated in the corners, see section 2.3. Twodimensional diffusers are less efficient in recovering static pressure and less resistant to boundary layer separation than three-dimensional diffusers. Therefore two dimensional diffusers have to have a smaller opening angle leading to a longer diffuser for a given expansion. Consequently, the reduction of the windtunnel circuit length achieved by the use of expanding corners is partly lost by the fact that it is accompanied by two-dimensional diffusers.

The thickness of the inlet boundary layers and non-uniformities of the inlet velocity profiles are also important factors, see Waitman et al. (1961) and Wolf (1969), when setting the diffuser opening angle. Thick diffuser wall boundary layers separate easier than thin boundary layers. In figure 3, the line of separation, (solid line), is plotted as a function of the ratio between diffuser length and width, (according to Fox & Kline (1962)). In that case, however, the boundary layer thickness at the diffuser inlet is small and in this wind-tunnel circuit they are usually quite thick. As an example the thickness of the inlet boundary layers in the diffuser following corner 1 is about 10 cm. Therefore it is important not to design diffusers with opening angles too close to the separation line. The diffusers in this wind-tunnel are represented in the figure as filled circles and they are numbered in the downstream direction. Diffuser number

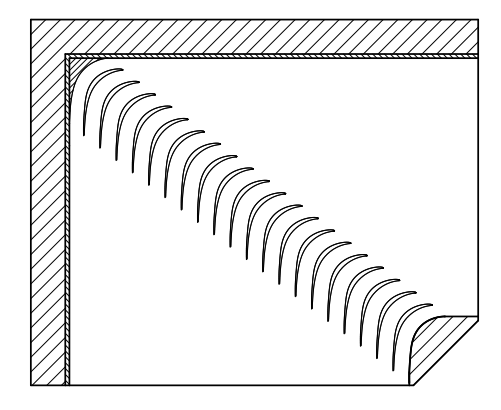


FIGURE 4. First corner in the flow direction from the test section. The flow is from right to bottom. $e = A_{\text{out}}/A_{\text{in}}$

4, located downstream the heat exchanger, see figure 2, is not as close to the line of separation as desired but other geometrical restrictions also influenced the design of the diffusers. The optimum wall shape of a diffuser has a larger opening angle at its entrance and a decreasing opening angle thereafter. Here, however, all diffusers have straight walls to simplify the manufacturing.

The dashed line in the figure is the line of maximum pressure recovery, (according to Fox & Kline (1962)). The reason for this line to be located into the regime with separation is that the friction-loss on the diffuser walls decreases and that the increase in pressure-loss due to a small separation is relatively small. For optimization of plane diffusers the reader may also wish to consult Reneau et al. (1976), Çabuk & Modi (1992) and Ganesan et al. (1991).

An extra benefit with plane diffusers is that they can easily have adjustable diffuser walls so that the expansion in the diffuser can be changed. This is especially useful in the diffuser following the test section. The test section has an adjustable wall so that the user can set the pressure gradient in the streamwise direction, see section 2.1. It is then useful to adjust the diffuser wall as well, which is possible in plane diffusers that have two parallel walls, to fit the cross section area to that of the test section. Hereby, it is possible to make measurements on e.g. a flat plate closer to the exit of the test section and in this way increase the maximum Reynolds number on e.g. a flat plate.

2.3. Corner

The idea of using expanding corners has been around for a long time, see e.g. Collar (1936) and Kröber (1932), but it was always discarded since the early

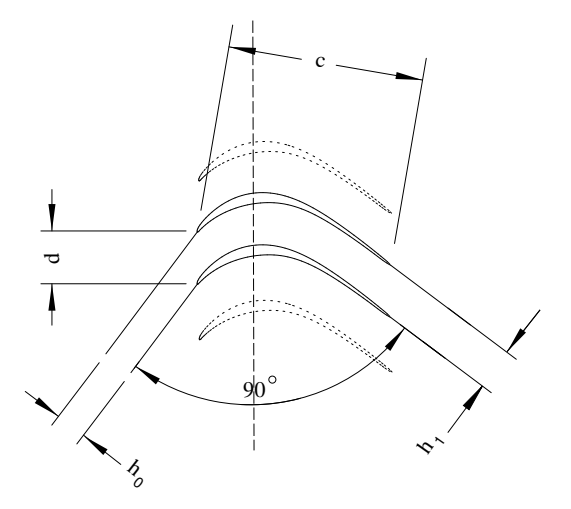


FIGURE 5. The geometry of a cascade of 90° turning guidevanes. c = vane chord, d = spacing between vanes, $h_0 = \text{inlet}$ distance between vanes, $h_1 = \text{outlet}$ distance between vanes & $e = h_1/h_0 = \text{is the expansion ratio}$.

experimental results were not too encouraging. One of the reasons for the discouraging results is the simple guide-vane shapes that were used then. The most common shape used in wind-tunnels for a long time has been the $\frac{1}{4}$ -circle with a constant thickness and with a straight prolongation at the trailing edge (sometimes also at the leading edge). In more recent investigations guide-vanes with varying thickness were used, although the shapes of the suction and pressure sides were still simple and often circular, see *e.g.* Friedman & Westphal (1952) and Wolf (1957).

The major benefit of using expanding corners is the larger size of the test section that can be fitted into a wind-tunnel for a given circuit length without an increase in total pressure-loss for the wind-tunnel circuit. Other benefits are reduced friction loss, the possibility to use diffusers with variable diffuser angle and the possibility to have a larger fan radius leading to lower fan rpm and thus lower blade tip speed and consequently less noise. The reason for the larger fan and the reduced friction loss is the rapid expansion achieved by the first two corners which are located fairly close to the test section in the downstream direction. With a compact design of the circuit we have a short first diffuser exposing corner 1 to the disturbed flow from the test section which emphasizes the importance of well designed guide-vanes optimized for the expansion ratio used.

In this case the guide-vane used in the MTL wind-tunnel developed by Sahlin & Johansson (1991) was used as a starting shape for the development of a new guide-vane optimized for the expansion ratio used in this wind-tunnel and a chord Reynolds number of 200000, see Lindgren et al. (1998). The procedure of developing the new guide-vane was to look at the pressure profile on the original vane. Its performance here was, as expected, not totally satisfying with e.g. laminar separation bubbles on each side of the guide-vane profile. In an iterative process, where the guide vane profile was altered gradually, a pressure profile was achieved which was free from separation bubbles and without transition to a turbulent boundary layer on the pressure side.

These calculations were made using the MISES cascade code and its inverse optimization tool, see Drela & Youngren (1995) and Lindgren et al. (1998). Inverse optimization means that a new pressure profile that is not too different from the pressure profile found in the previous iteration is specified and the guide-vane shape matching the new pressure profile is then calculated. Step by step a larger change in pressure profile and guide-vane shape are achieved.

The new guide-vane was then tested at varying Reynolds numbers and inlet flow conditions. These tests lead to some minor changes of the guide-vane shape such as increased nose radius and reduced camber. It also slightly increased the calculated cascade pressure-loss coefficient, which is a measure of the total pressure-loss in the corner, from 0.039 to 0.041. The value determined from experiments was found to be slightly higher, see section 4.5.

Figure 4 shows a cut through corner 1. The expansion ratio in all corners in this wind-tunnel is $\sqrt[8]{9} \approx 1.316$ where 9 is the contraction ratio, CR, of the wind-tunnel. Hence, the 4 corners account for a total expansion of $\left(\sqrt[8]{9}\right)^4 = 3$, leaving only a factor of 3 in expansion to be handled by the diffusers. Note that the shape of the corner inner and outer walls mimic the suction and pressure shapes of the guide-vane. This is important because the flow then sees the cascade as infinite. However, there is also a negative effect on the performance of the guide-vanes from the corner wall boundary layers. The rapid expansion in the corners lead to a very rapid increase in boundary layer thickness, see section 4.5. The influence of the wall boundary layers is neglected when the total pressure-loss coefficient of the guide-vane cascade is measured for comparison with the calculations.

The guide-vanes are separated by a distance, d, of 0.3 times their chord length, c, see figure 5. This is not the optimum spacing for maximum static pressure recovery, see Lindgren $et\ al.\ (1998)$, but it guarantees a satisfactory capability of avoiding boundary layer separation on the vanes if the inlet flow condition is poor. This is especially important in this wind-tunnel because of the short diffuser between the test section, where large disturbances can be generated by measurement equipment, and corner 1.

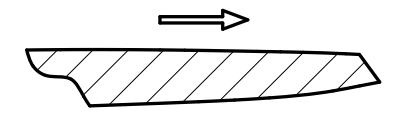


FIGURE 6. The shape of the guide-vane trailing edge. The flow tends to curl up from the lower side of the guide-vane with higher pressure towards the upper suction side which means that there should be a sharper angle at the corner closest to the lower side. The arrow indicates the flow direction.

The guide-vanes are made of extruded aluminum and they are mounted to the inside of the corner walls. Two expanding pins run through a laser cut plate into the short end of the guide-vane. A center screw then fixes the guide-vane to the plate. This way of fixing the guide-vanes in the corners ensures that their position and angle of attack is very accurate.

In the first three corners the guide-vane angle of attack is fixed, but in the fourth corner there is a possibility to adjust it by a few degrees to compensate for deviations in flow direction. The adjustment is made individually for each guide-vane. There are both pros and cons with this arrangement. There is an obvious advantage of being able to adjust the flow direction for compensating possible local flow misalignment. On the other hand it is difficult and time consuming to make these changes and once the wind-tunnel is calibrated the guide-vane angle of attack will probably never be altered.

To avoid an oscillating flow separation point at the trailing edge of the guide-vane causing high levels of noise at a distinct frequency, the trailing edge of the guide-vane should be cut as shown in figure 6. The noise is generated by the von Kármán vortex street behind a blunt trailing edge. There are also other mechanisms that can generate noise. One suggestion is that there is an interaction between Tollmien-Schlichting generated boundary layer instabilities that are strongly amplified on the pressure side close to the trailing edge. These instabilities then roll up to form a von Kármán type vortex street with the same frequency as the noise, see Nash et al. (1999). It is important that the trailing edge corner close to the pressure side of the guide-vane is sharper than the corner on the suction side since the flow wants to curl around the trailing edge from the pressure to the suction side.

2.4. Machinery

The control of the test section speed, *i.e.* fan rpm, and temperature is fully automated by the use of computers, current controlled valves and a fan control unit. A computer located near the test section is used to enter the desired values



FIGURE 7. The new guide-vane developed for an expansion ratio of 1.316. Observe that the trailing edge is not modified from calculations.

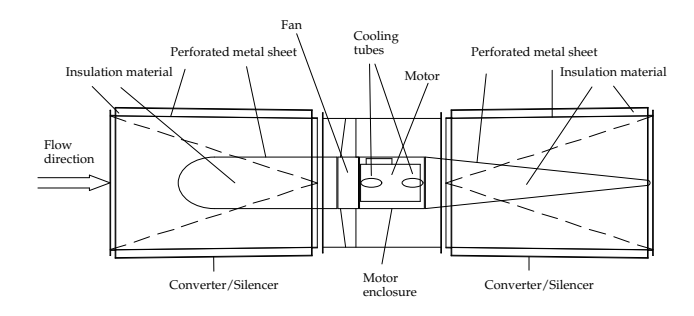


FIGURE 8. The fan located in between the two silencers.

for velocity and temperature. This can either be done manually, by using the keyboard, or from another computer through an Ethernet connection. The entered set values are then sent to a NI Field Point control system by serial RS 232 communication. This Field Point system consists of four modules. One for data communication and power supply, one for digital output signals, one for analog output signals and one for temperature input signals, (PT-100). The digital output is used to start and stop the fan and the cooling circuit pump and the analog output is used for automatic control of fan rpm and cooling system valves.

2.4.1. Driving unit

The fan configuration is shown in figure 8. It is located downstream the second corner, see figure 2. The fan is positioned between a pair of silencers. They also transform the cross section shape of the wind-tunnel circuit between circular, (the parts nearest to the fan), and rectangular. Some expansion is also taking

place in the silencers to keep the total wind-tunnel circuit length to a minimum. In the center of the silencers, cylinder shaped bodies made of perforated steel plate and filled with acoustic insulation material are mounted. In the upstream silencer the cylinder has a constant diameter and its nose is shaped as half an ellipsoid, see figure 8. The central body in the downstream silencer is shaped as a cone, see figure 8, to avoid flow separation. The central bodies improve the flow quality both upstream and downstream of the fan. They also improve the noise reduction capability of the silencers. The insulation material is (long-fibered) glass wool and it is separated from the air flow by a perforated steel plate. The sound waves can thus penetrate into the insulation material, through the holes in the steel plates, where they are absorbed. The thickness of the insulation layer is 10 cm.

The motor delivers 15 kW of power. It is mounted axially behind the fan and it is enclosed in a steel plate cylinder to minimize the disturbance on the flow. Therefore, extra air for cooling the motor is provided from outside the wind-tunnel circuit through two cylindrical pipes.

The fan diameter is 1.25 m and the hub diameter is 0.5 m. The fan has 8 blades with an angle of attack of 53°. With this angle of attack and an empty test section the fan efficiency is close to its maximum value of 75%. The blades do not enter the stall region even at considerably higher loads, making sure that the wind-tunnel efficiency and flow quality stays intact during the operation of the most common kinds of experiments. The adjustment of the blade angle of attack was done during the wind-tunnel calibration, see section 4.1.

The use of axial fans can, however, create some flow quality problems, if they are subjected to very high loads, but even with more moderate loads they can create a low frequency pulsating variation of the streamwise flow component. In the present tunnel this is essentially, but not completely, avoided by a relatively low fan blade load.

2.4.2. Cooling circuit

One of the primary measurement techniques used in this kind of wind-tunnel is the Constant Temperature Anemometry, CTA. Since the idea of this measurement technique is to keep the hot-wire at constant temperature, a change in the surrounding air flow temperature will affect the cooling of the wire and, will thus be interpreted as a change in velocity. Therefore it is very important to have a stable, well determined temperature in the test section. This is achieved by including a heat exchanger, *i.e.* an air cooler, into the wind-tunnel circuit. This heat exchanger consists of elliptical pipes with cooling flanges through which cold water is flowing at a constant rate. The air blows perpendicularly through the grid of cooling pipes.

The main problem with using a heat exchanger of this type is that it is one of the parts that contributes most to the total pressure-loss of the wind-tunnel circuit, see figure 1. Therefore it is important to install it where the cross section area of the wind-tunnel circuit is as large as possible. This would indicate an optimum position in the stagnation chamber, see figure 2. On the other hand it is important to give the flow time to even out spatial temperature variations and therefore the heat exchanger should be installed far away from the test section. The compromise between these goals resulted in the positioning of the heat exchanger between corner 3 and diffuser 4, see figure 2. Here the cross section area is sufficiently large to keep the pressure-loss at an acceptable level and it is far enough from the test section so that the spatial temperature variation has time to even out. There is also the option of using turbulence generators on the cooling pipes to improve the heat transfer but they increase the pressure-loss radically and the turbulence they generate deteriorates the flow quality significantly. This option was therefore rejected.

A schematic view of the cooling circuit is shown in figure 9 and the parts are described in table 3. As seen in figure 9 the system is divided into three parts. The first part is the wind-tunnel circuit with its flow of air. The air is cooled by water flowing through a heat exchanger in the second part. This part consists of a closed loop of piping where the water flows at a constant rate. The way of changing the heat flux from the air to the water is therefore by changing the water temperature. The reason for doing it this way, instead of changing the water flux, is that a high flow rate through the heat exchanger results in a better air temperature uniformity over the cross section. The final part is the external cooling water system of the building. It consists of a high pressure and a low pressure side with a water temperature of about 10°C on the high pressure side. This water cools the water in the closed loop, (second part), through another heat exchanger. The flow rate from the high to the low pressure side is controlled by a current-controlled valve. By keeping the closed loop circuit length to a minimum and using a high flow rate the response time of the whole system can be minimized resulting in small temporal air temperature variations in the test section and shorter transient times at changes in the set temperature and set velocity. Finally there is a shunt pipe bypassing the heat exchanger, see figure 9, in the closed loop circuit to be used in more advanced control techniques than the PID regulator system now in use.

2.5. Stagnation chamber & contraction

2.5.1. Stagnation chamber

The stagnation chamber, located downstream corner 4, is the part of the windtunnel circuit that has the largest cross section area. This part has a major influence on the flow quality in the test section. Because of the high local pressure drop generated by flow improving devices it is important to position them in the location with the lowest flow speed and thereby minimize their contribution to the total pressure drop of the wind-tunnel circuit. In the present

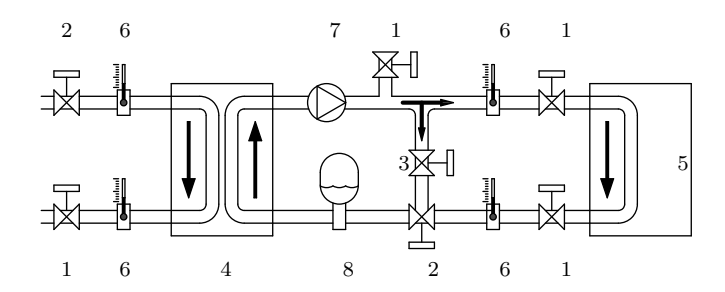


FIGURE 9. The water cooling circuit in the wind-tunnel. The outer, (left in figure) part is an in-house cold water system and the inner, (right in figure) part is a closed circuit loop with the flow controlled by the user. For numbering of parts see table 3.

Table 3. A description of the cooling circuit parts. See also figure 9

Part	Description
1.	Stop valve
2.	Current controlled regulator valve
3.	Throttle valve in shunt pipe
4.	Water to water heat exchanger
5.	Water to air heat exchanger
6.	Thermometer, (PT-100)
7.	Pump with maximum pressure rise of 35 m H ₂ O (0.35 MPa)
8.	Expansion tank

wind-tunnel the stagnation chamber is equipped with one honeycomb and five screens.

The honeycomb used here is 75 mm long and the hexagonally shaped cells have a diameter of a quarter of an inch or 6.4 mm, i.e. the length to diameter ratio of the cells is about 12. The primary reason to use a honeycomb is that, with a sufficient length of about 10 cell diameters, see Bradshaw & Pankhurst (1964), it is a very effective flow straightening device. The relatively low pressure drop of a honeycomb makes it rather ineffective in reducing non-uniformities or fluctuations in the streamwise component but it is very effective in reducing cross-stream components, see e.g. Scheiman & Brooks (1981). This is especially useful in wind-tunnels with expanding corners since the low guide-vane chord Reynolds number in the last corner increases the risk

of boundary layer separation on the suction side of the guide-vanes. A honeycomb also breaks up eddies larger than the cell size and reduce the free-stream turbulence level, see *e.g.* Loehrke & Nagib (1976).

The use of screens to improve the flow quality in wind-tunnels was first proposed by Prandtl (1932). The screens are very effective in breaking up larger eddies and acts primarily to reduce mean non-uniformities and fluctuations of the streamwise component. The screens also reduce cross-flow components but less effectively than honeycombs. Hence, the combination of honeycomb and screens provide, in a natural way, a good overall flow quality improvement.

By using a cascade of screens with subsequently finer mesh the turbulence and mean flow variation can be reduced substantially, see Groth (1991). In the wind-tunnel there are five screens with varying mesh size, see table 4, where M is the mesh size and d is the wire diameter, see also figure 10. Screens also reduce flow angle deviations. The relationship between the inflow angle, θ , and the out flow angle, ϕ , is,

$$\phi = \alpha \theta, \tag{2}$$

where α is a constant between 0 and 1. Empirically, see Laws & Livesey (1978), α is related to the local pressure-loss coefficient, K_0 , through the following expression,

$$\alpha = \frac{1.1}{\sqrt{1 + K_0}}.\tag{3}$$

The local pressure-loss coefficient, K_0 , is determined by the solidity of the screen, $\sigma = 1 - \beta$, and the wire diameter Reynolds number, Re_d ,

$$K_0 = f\left(Re_{\rm d}\right) \frac{1 - \beta^2}{\beta^2},\tag{4}$$

derived by Laws & Livesey (1978). The function $f(Re_d)$ in equation 4 has a strong Reynolds number dependence for low Reynolds numbers, $(Re_d < 100)$, but it is almost constant, with a value of about 0.5, for high Reynolds numbers, see Groth & Johansson (1988). The solidity, $1 - \beta$, is here between 0.3 and 0.4. At high Reynolds numbers, $(Re_d > 100)$, the flow over the screen wires is supercritical. This means that small scale turbulence is generated by the wires in the screen. Although the reduction in flow variation is less for supercritical than sub-critical screens it is preferable not to use sub-critical screens because of their very large pressure drop. A series of supercritical screens with consecutively smaller mesh is more effective in reducing flow variations and turbulence than a single sub-critical screen, and with a smaller pressure drop, see Groth (1991). The distance between the screens needs to be larger than about 30 mesh sizes, for the wire generated turbulence to decay sufficiently, see Groth & Johansson (1988).

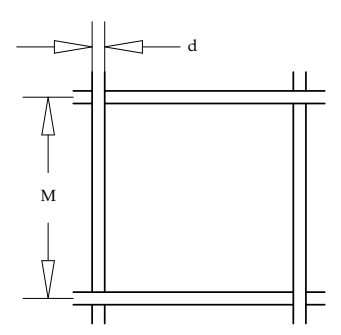


FIGURE 10. Definition of mesh width, M, and wire diameter, d.

The porosity, β , is defined as,

$$\beta = \left(1 - \frac{d}{M}\right)^2,\tag{5}$$

where M is the mesh size and d is the wire diameter, see figure 10. The values of M, d and β for the screens used in this wind-tunnel are presented in table 4.

The reduction in the streamwise mean flow variation can also be expressed in terms of α and K_0 . The expression derived by Taylor & Batchelor (1949) reads

$$\frac{\Delta u_2}{\Delta u_1} = \frac{1 + \alpha - \alpha K_0}{1 + \alpha + K_0},\tag{6}$$

where Δu_1 is the variation in streamwise velocity upstream the screen and Δu_2 is the variation in streamwise velocity downstream the screen.

The reader may notice that the expression in equation 6 equals zero for $K_0 = 1 + 1/\alpha$. It would be ideal to be able to eliminate the flow variation this way but equation 6 is only valid for solidities below 0.45 and the solidity required for equation 6 to be zero is 0.63. The reason for equation 6 to become invalid is a phenomenon called jet-collapse, see *e.g.* Baines & Petersen (1951). It occurs when the jets flowing out through the screen holes merge and form larger jets and structures. This leads to large variations in the flow and thus, must be avoided. The values of the porosity of the screens used in this wind-tunnel is presented in table 4.

When the flow has passed through the last screen it has been exposed to a substantial strain, which gives an anisotropic state with most of the turbulence energy in the cross-stream components. It is therefore important to allow it

Table 4. Data for the screens and the honeycomb used in the new tunnel at a test section flow speed of 40 m/s.

Screen	d [mm]	M [mm]	β	Re_d	K_0	f
1	0.71	3.2	0.61	210	0.80	0.50
2	0.56	2.4	0.58	165	0.99	0.55
3	0.56	2.4	0.58	165	0.99	0.55
4	0.16	0.7	0.61	47	1.71	0.75
5	0.16	0.7	0.61	47	1.71	0.75
honeycomb	0.075	6.35	0.97	29	-	-

to relax towards an isotropic state before entering the next part in the windtunnel circuit, which is the contraction. Just as the screens, the contraction is most effective in reducing streamwise fluctuations and in particular mean velocity variations.

The relaxation takes place in a straight part of the wind-tunnel circuit with constant cross section area (settling chamber), which is 0.75 m long in this wind-tunnel.

2.5.2. Contraction

The final, and for flow quality improvement, maybe most important, part in the wind-tunnel circuit is the contraction through which the flow passes before entering the test section. In the contraction the flow is accelerated rapidly. This results in a large streamwise strain, that reduces mean flow variations and the larger the contraction ratio, CR, the larger the strain and thus reduction. In this wind-tunnel the contraction ratio is 9.

The contraction can be divided into two parts. The first part has walls of concave shape and it is very important to elongate this part as much as possible to avoid wall boundary layer separation to occur here. The risk for separation is caused by the streamline curvature effects on the pressure gradient in the boundary layer. Along a fair part of this section there will be a positive pressure gradient see e.g. Seidel (1982). The generation of Görtler vortices decreases the risk for separation because the vortices inserts fluid with higher momentum into the boundary layers, see Görtler (1941) but they will not prevent separation completely if the contraction curvature is to sharp. The second part of the contraction has convex walls. Here, there is also a risk of separation close to the test section since there is a positive pressure gradient here as well, see e.q.Seidel (1982). It is easy to counteract a separation in this section by using some boundary layer tripping device such as tape with V-shaped roughness elements, (used in the MTL wind-tunnel). A separation in the first part is very difficult to eliminate though through tripping etc. The location of the contraction, just upstream of the test section, makes it very important to achieve a high quality

contraction design. The shape used in this wind-tunnel is taken from the MTL wind-tunnel and it was derived by Henrik Alfredsson and Alexander Sahlin at the department through inviscid/boundary layer calculations optimizing the pressure gradient along the contraction walls. It resulted in a shape described by:

$$f = A\left(\sinh\left(B\frac{x}{L}\right) - B\frac{x}{L}\right), \qquad \frac{x}{L} \le 0.7$$
 (7)

$$f = 1.0 - C\left(\sinh\left(D\left(1 - \frac{x}{L}\right)\right) - D\left(1 - \frac{x}{L}\right)\right), \qquad \frac{x}{L} > 0.7$$
 (8)

where A=0.205819, B=3.52918, C=0.08819 and D=8.23523. x is the downstream coordinate and L is the contraction length. Here L is 2.5 m. The height and width are given by

$$H = \pm h \left(\sqrt{CR} \left(1 - f \left(\frac{x}{L} \right) \right) + \frac{1}{2} f \left(\frac{x}{L} \right) \right) \tag{9}$$

$$B = \pm b \left(\sqrt{CR} \left(1 - f \left(\frac{x}{L} \right) \right) + \frac{1}{2} f \left(\frac{x}{L} \right) \right) \tag{10}$$

where h = 0.75 m is the test section height and b = 0.5 m is the test section width. Further information on design and optimization of contractions can be found in *e.g.* Downie *et al.* (1984), Borger (1976) and Mikhail & Rainbird (1978).

The reduction of the variation in mean flow velocity in the contraction is very large

$$\frac{\Delta u_1}{U_1} = \frac{\Delta u_0}{CR^2 U_0},\tag{11}$$

$$\frac{\Delta v_1}{U_1} = \frac{\Delta v_0}{\sqrt{CR}U_0},\tag{12}$$

where U is the mean velocity in the streamwise direction and Δu and Δv are the velocity variations in the streamwise and crosswise directions, respectively. Subscripts 0 and 1 indicate positions at the upstream and downstream ends of the contraction respectively. As seen in equations 11 and 12 the reduction is much larger for the streamwise component, as it scales with the contraction ratio squared, than for the crosswise component that scales with the square root of the contraction ratio. For a contraction ratio of 9, as in this wind-tunnel, the reduction of the streamwise velocity component is 81 times the initial variation and for the crosswise components it is 3 times the initial variation. This simple inviscid theory can also be used to give a first rough estimate of the reduction of turbulence, (by replacing Δu with $u_{\rm rms}$ etc). The basis for a better, but still

inviscid and linear, theory is the assumption that the strain-rates for the turbulent fluctuations are much smaller than those for the mean flow components, see Batchelor (1976). The relations 11 and 12 can then be modified for this, so called, rapid distortion theory as follows

$$\frac{\Delta u_{\rm rms1}}{U_1} = \frac{1}{CR^2} \sqrt{\frac{3}{4} \left(\ln \left(4CR^3 \right) - 1 \right)} \frac{u_{\rm rms0}}{U_0},\tag{13}$$

$$\frac{\Delta v_{\rm rms1}}{U_1} = \sqrt{\frac{4}{3CR}} \frac{v_{\rm rms0}}{U_0},\tag{14}$$

However, for geometries such as that of the present contraction effects of viscous dissipation are non-negligible. The formulas 13 and 14 would give reduction factors of 35.4 and 3.7, respectively, for $u_{\rm rms}/U$ and $v_{\rm rms}/U$. From the study of Sjögren & Johansson (1998) we find that realistic values of these factors should be 36.4 and 9.1. In this case the rapid distortion theory works quite well for the streamwise component but the error is large in the cross stream component. This can mainly be contributed to a large dissipation in the beginning of the contraction. This dissipation is present in both components but has a larger influence on the cross stream component. At the end of the contraction there is also a redistribution of energy from the cross stream component to the streamwise component.

3. Experimental setup

The experiments concerning flow quality in the test section, e.g. mean flow, temperature and turbulence intensity measurements, were performed at a position 250 mm from the inlet of the test section. A special traversing arm was built, see figure 11, made of three joints connected by two beams. The beams are made of extruded aluminum with a laminar airfoil profile. Trip tape was applied to the beams to eliminate flow instability induced noise, see e.g. Nash et al. (1999). The axes were all orientated in the streamwise direction allowing movements in the cross stream plane of the traversing arm. One joint was mounted on the test section wall, one joined the two beams and one was located at the far end of the outer beam allowing rotation of a 500 mm long sting. This was a necessary feature to allow control of the rotational direction of the probe. The sting is long enough to keep the probe upstream of the flow field influenced by the traversing arm.

All three axes were equipped with DC servo controlled motors that could be operated from a computer, automating the traversing process. On the inner axis there was also a balance weight mounted to counteract the gravitational force on the traversing arm.

Two coaxial cables and two pressure tubes that can be connected to a probe run inside the beams and the sting, thereby minimizing flow disturbances.

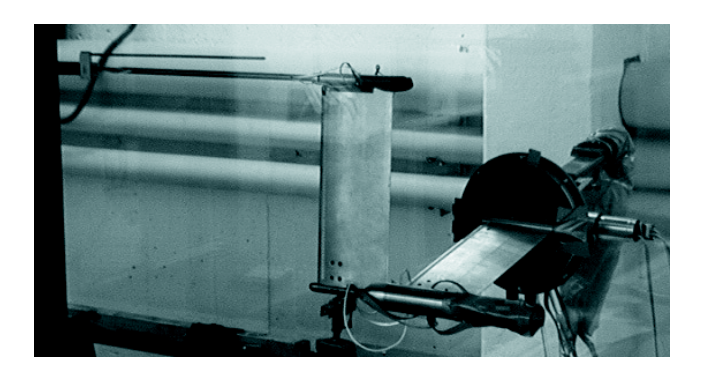


FIGURE 11. The traversing system used for measurements in the cross section of the test section at a position of 250 mm downstream the entrance of the test section.

Cables supplying power and encoder information for the motors also run inside the beams.

The probes used in the experiments at this location were single-wire and cross-wire probes for measuring the turbulence intensities and mean velocity components in the streamwise and the two cross-stream directions. A PT-100 probe for measuring the temperature fluctuations and a Prandtl tube for total pressure measurements were also used.

The single wire was calibrated in the free-stream over a large enough velocity range using King's law

$$U_0 = \left(\frac{E^2 - A}{B}\right)^{\frac{1}{n}} \tag{15}$$

where U_0 is the free-stream velocity, A, B and n are constants to be determined and E is the voltage output from the anemometer. The velocity was determined using a Prandtl tube measuring the dynamic pressure and by measuring the static pressure and the temperature of the air.

The cross-wire probe was calibrated in a similar way using a fifth order polynomial instead of King's law. In that case an extra device allowing variation of the probe angle was mounted onto the sting. The streamwise and cross stream velocities were determined by

$$U = U_0 \cos \alpha, \tag{16}$$

$$V = U_0 \sin \alpha, \tag{17}$$

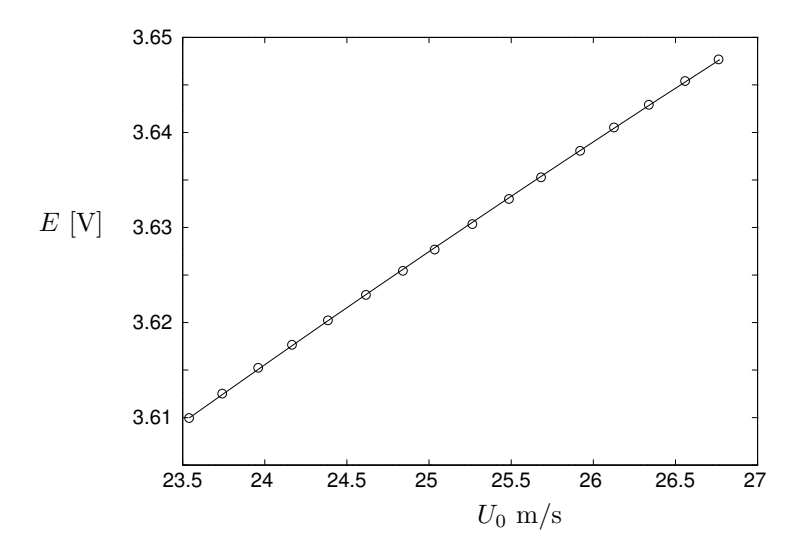


FIGURE 12. The calibration of a single-wire. The circles are measured points and the solid line is the King's law derived by a least square fit to the measured points.

where U and V are the streamwise and cross stream velocity components respectively and α is the probe angle. Two new variables, x and y were constructed from the wire voltages E_1 and E_2 as follows

$$x = E_1 + E_2, (18)$$

$$y = E_1 - E_2, (19)$$

The variables x and y were then used to construct two polynomials of fifth order, denoted M and N, for the two variables, U and $\tan \alpha$. By solving the equations

$$MA = U, (20)$$

$$NB = \tan \alpha,$$
 (21)

the coefficients in the vectors A and B can be determined. They are then used when the measurement data in form of voltages are converted to velocities.

Figures 12 and 13 show the results from one single wire and one cross-wire calibration. Note that all samples during a measurement have to be inside the end points of the calibration curve for the single-wire case and inside the area bounded by the solid lines for the cross-wire case.

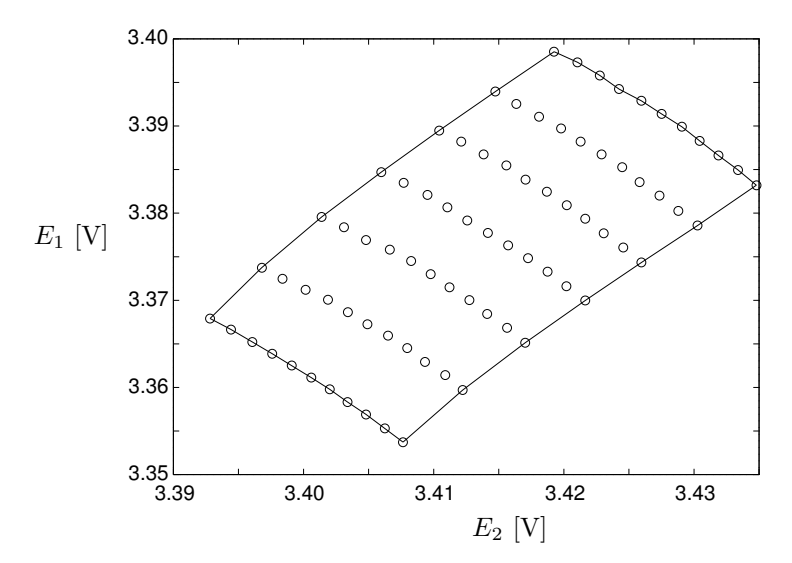


FIGURE 13. The calibration of a cross-wire. The circles are measured calibration points and the solid lines represent the area within which all measurement points must lie.

The error in U for the single-wire calibrations was less than $\pm 0.1\%$ and for the cross-wire calibration it was less than $\pm 0.1\%$ for the streamwise, U, component and the cross stream components V and W.

For the temperature measurements a PT-100 probe was mounted at the end of the sting. By using three of the four wires available for cross-wire measurements and connecting them to the NI Field Point temperature unit, described in section 2.4, with a built-in wire compensation the temperature could be measured across the cross section area. The temperature probe permanently mounted in the test section for controlling the wind-tunnel air temperature was used for the temporal variation measurements. The accuracy of the temperature sensors was about $0.4\,^{\circ}\mathrm{C}$ in absolute value but the relative accuracy is much higher.

For the pressure measurements a differential pressure transducer from Furness Controls was used. It communicated with the computer via an RS-232 serial port. It has a built in averaging function for up to 20 sec of averaging and the relative accuracy at low pressure differences is less than 0.1 Pa.

Some measurements were performed downstream of corner 1 to verify the results in earlier experiments and calculations of guide-vane performance, see Lindgren *et al.* (1998). In this setup a different traversing system was used. It consists of a bar running horizontally through the diffuser downstream of

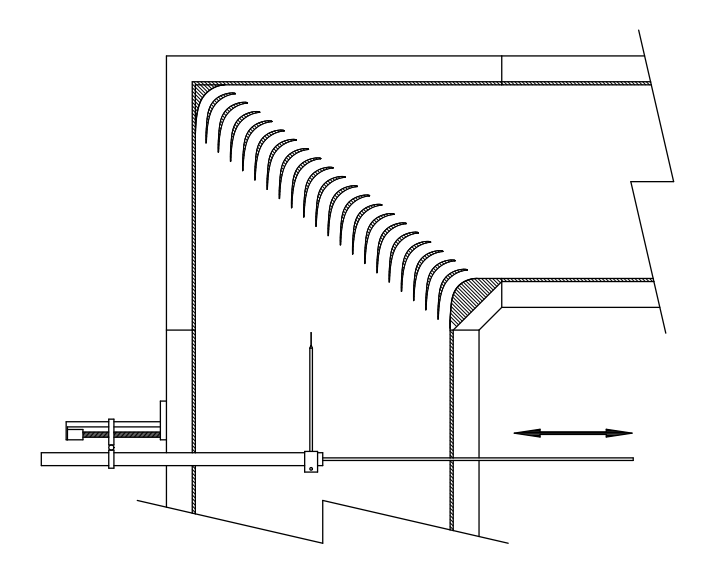


FIGURE 14. The traversing arm behind corner 1. The axis of motion is, as the arrow indicates, horizontal.

corner 1. The bar holds a sting with a Pitot tube pointing vertically at its end, see figure 14. The Pitot tube was positioned in the mid spanwise plan and it could be traversed across the array of guide-vanes using a servo controlled DC motor. This enabled quasi two-dimensional measurements of the guide-vane wakes behind the corner and calculation of the corresponding total pressure-loss of the corner. The static pressure upstream and downstream the corner also had to be measured. When measuring the static pressure at a wall it is very important that the pressure holes are not damaged in their edges. Therefore plugs were made containing the pressure holes and these were carefully flushmounted in the wall to avoid disturbances, see Shaw (1960).

Finally noise measurements outside the test section and the fan were performed with a hand held dB meter. It was done during a time of the day when outer noise disturbances were at a minimum. Still there is a fair contribution from other noise sources, such as ventilation etc, to the results at low test section speeds.

4. Results

When investigating the results of the design and construction of a wind-tunnel there are several key factors that have to be checked carefully. The most important factors concern mean flow variations in time and space over the test section cross section area, the turbulence fluctuation intensities, both in the streamwise and cross-stream directions, and temperature variations in time and over the same cross section area.

A mean flow variation in time would indicate problems with the fan or with static pressure changes. This kind of problems can be eliminated by changing e.g. fan blade angles or by increasing the flow through the pressure equalizing slit downstream the test section. Mean flow non-uniformities can originate from e.g. separation on some of the corner guide-vanes, diffuser separation or by flow blockage due to inefficient screens or honeycomb. If these deficiencies are small the problems can be taken care of by the contraction but larger deficiencies and problems generated in the contraction are difficult to eliminate, see section 2.5.2.

High turbulence levels often originate from small separations or deficient screen and honeycomb design, e.g. through jet collapse, see section 2.5.1.

Large temperature variations in time suggest an insufficient control system and large variations in space that the heat exchanger is located too close to the test section or that the water flow rate is not large enough.

All these factors were investigated and the results are presented in the following section.

Noise measurements were also performed outside the wind-tunnel. Static pressure variation measurements inside the test section are very difficult to perform without getting excessive influence from the dynamic pressure variations, see Johansson (1992). Static pressure fluctuations are present as sound waves traveling both in the upstream and downstream directions around the wind-tunnel circuit, see Michel & Froebel (1988). However, in low speed wind-tunnels the contribution to the streamwise velocity fluctuation from the static pressure fluctuations is small. Equation 22 shows an estimate of the contribution from static pressure variations.

$$\left(\frac{u_{\rm rms}}{U}\right)_{\rm p_{\rm rms}} = \frac{C_{\rm p_{\rm rms}}M}{2} \tag{22}$$

The Mach number, M, is small and the pressure coefficient, $C_{\rm p_{rms}} = p_{\rm rms}/q$ is usually also small for low-speed wind-tunnels making the contribution small, (q is the dynamic pressure, p is static pressure and u is the streamwise velocity component). In the MTL wind-tunnel efforts were made to measure the static pressure fluctuation intensity and it was found to be below 0.00015q, see Johansson (1992). With $C_{\rm p_{rms}} < 0.00015$ and M = 0.072 it results in a contribution of less than 5×10^{-4} % to the total velocity fluctuation.

The measurements in the test section in this article are confined to the core region of the test section. For the case of *e.g.* boundary layer experiments on a flat plate it will also be relevant to investigate the velocity variation in the streamwise direction along the test section length and the two-dimensionality of

the flat plate boundary layer, see e.g. Mehta & Hoffmann (1987) and Österlund & Johansson (1999).

Aside from measurements in the test section an investigation of the performance of the expanding corners was made. Here, the velocity in the test section was chosen so that the vane chord Reynolds number was about 200000 to enable comparisons with the calculations and experiments earlier performed by Lindgren *et al.* (1998).

4.1. Total pressure measurement

The total pressure variation in the test section is a measure of the uniformity of the flow. It is defined as

$$\frac{\Delta p_{\rm t}(y,z)}{q_1} = \frac{p_{\rm t1}(y,z) - p_{\rm t0}}{q_1} \tag{23}$$

where $p_{t1}(y, z)$ is the total pressure in the test section, p_{t0} is the total pressure in the stagnation chamber at a fixed position and q_1 is the dynamic pressure in the test section at a fixed position, (e.g. the centerline). The reason for choosing the total pressure in the stagnation chamber as a reference pressure is that it is very stable in time.

The results at a free-stream velocity of about 25 m/s is shown in figure 15. The maximum variation was found to be less than $\pm 0.1\%$ which is satisfactorily low. It can be compared to the total pressure variation in the MTL wind-tunnel which also has a peak to peak variation of $\pm 0.1\%$, see Johansson (1992) and Lindgren & Johansson (2002). It is interesting to note that a total pressure variation of $\pm 0.1\%$ corresponds to a velocity variation of $\pm 0.05\%$. The location of the contours shown in figure 15 has a fair uncertainty because of the difficulty in measuring these extremely small pressure differences.

The small variation in the mean flow is here achieved by the use of screens and a contraction ratio as high as 9. As explained in section 2.5 a careful choice of mesh sizes and solidities for the screens and a contraction with high contraction ratio reduce the mean flow variation to a very low level. The results here and the design of these parts are similar to those in the MTL wind-tunnel for which the flow quality has been shown to be very good, see Johansson (1992) and Lindgren & Johansson (2002).

As part of the tuning of the wind-tunnel the angle of attack of the fan blades was adjusted to achieve a suitable loading on the blades, and to ensure that boundary layer separation does not occur on them. This is crucial in order to achieve a good flow uniformity. A separation pattern can vary in time and with blade, leading to a pulsating flow in the test section. The load on the fan blades is also determined by the total pressure-loss of the wind-tunnel circuit. An increasing pressure-loss increases the blade load. The adjustment of the blades and the corresponding variation in flow behavior is described in some

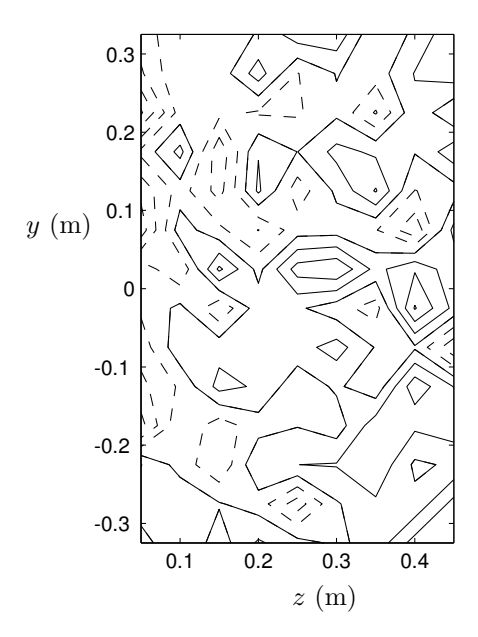


FIGURE 15. The total pressure variation in a cross section area of the test section located 0.25 m from its entrance. Each line represents an increment of 0.025%. Dashed lines are negative values and solid lines positive values.

detail in Lindgren (1999). With a blade angle of attack of 53° a separation free flow was achieved and the fan efficiency factor, η_f , was about 75%.

4.2. Temperature measurement

When using measurement techniques depending on heat transfer, such as hotwire anemometry, it is very important that the temperature in the test section is well controlled and uniform over the entire cross section area, and stable in time. To investigate these variations in the new wind-tunnel a Pt-100 temperature probe was traversed over the cross section area at the same position as where the total pressure measurements were made, see section 3. The variation in time was measured at the test section centerline for a test section velocity of about 25 m/s and a set temperature of about 1°C below ambient temperature.

The temperature variation over the cross section area is presented in figure 16. The maximum variation is $\pm 0.07^{\circ}$ C. The location of the contours has a fair amount of uncertainty due to the difficulties in measuring the temperature with very high accuracy. The variation in time has a non-negligible effect on the spatial variation. However, there is a clear distinction between two areas with higher temperatures in the lower and left parts of figure 16 and lower

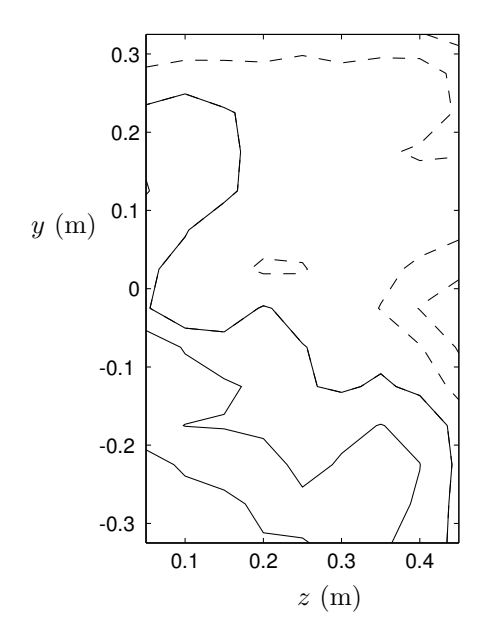


FIGURE 16. The temperature variation in a cross section area of the test section located 0.25 m from the entrance of the test section. The increment of each line is 0.025°C. Dashed lines represents negative values and solid lines positive values.

temperature in the upper and right parts of the cross section. This can be explained by the fact that the water enters the heat exchanger in the upper right corner of the cross section and exits at the lower right corner with a temperature difference between entering and exiting water of a few tenths of a degree leading to a colder right part of the cross section area. The small variation of temperature in the cross section indicates that the positioning of the heat exchanger is adequate and the flow rate through the heat exchanger is large enough, see section 2.4.2. The MTL wind-tunnel had originally, as a comparison, a temperature variation across the test section area of $\pm 0.2^{\circ}$ C, (Johansson (1992)), although significantly better results are now achieved ($\pm 0.05^{\circ}$ C) with an improved temperature control system (Lindgren & Johansson (2002)).

Some types of measurements in the wind-tunnel can take many hours and it is normally important to maintain a constant temperature. It is important not only that the temperature is stable during long times, but also that the short time variation is small. The control loop used in the new wind-tunnel for all measurements was of PI type. The D, (derivative part), in the PID-regulator was not used, although it shortens the transient time when *e.g.* the wind-tunnel speed is changed, because it leads to a larger short time variation.

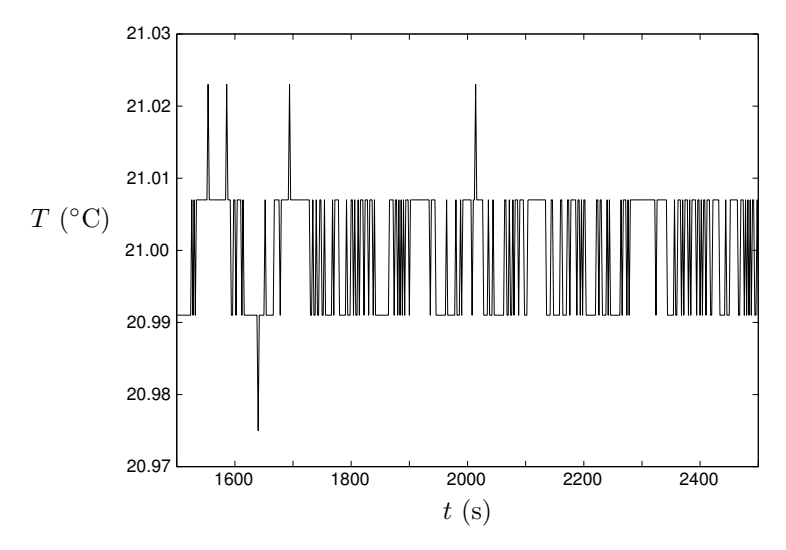


FIGURE 17. The temperature variation in time in the center of the test section 0.25 m from the its entrance.

The temperature was monitored for more than 4 hours and a window of 1500 s is shown in figure 17. The rest of the measurement shows a similar behavior. The 16 bit AD-converter gives a resolution of 0.016° C and as seen in figure 17 the variation is less than $\pm 0.03^{\circ}$ C or 3 bits.

4.3. Turbulence intensity measurement

One of the most important aspects of the flow quality in a wind-tunnel is the level of turbulence intensity. During the design of the wind-tunnel, a lot of work was devoted to ensure that the parts used for turbulence damping, such as screens, honeycomb and contraction would work well, see section 2.5. The measurement of the turbulence intensity in both the streamwise and cross-stream directions were made to verify the quality of the design of these parts.

The turbulence intensity is defined as

$$I_{\rm x} = \frac{u_{\rm rms}}{U},\tag{24}$$

$$I_{\rm y} = \frac{v_{\rm rms}}{U},\tag{25}$$

$$I_{\rm z} = \frac{w_{\rm rms}}{II},\tag{26}$$

where I_x , I_y and I_z are the turbulence intensities in the streamwise, the cross-stream vertical and the cross-stream horizontal directions, respectively, and U is the streamwise mean velocity.

One important aspect is to define what turbulence is in this case. There will always be flow variations with wave lengths of several meters containing a substantial part of the total turbulent kinetic energy. In this case we decided to include only flow structures with smaller wave length than 1.25 m. These measurements were made at a test section speed of about 25 m/s and the cut-off frequency, $f_{\rm c}$, is 20 Hz using,

$$f_{\rm c} = \frac{U}{\lambda_{\rm c}} \tag{27}$$

where λ_c is the cut-off wave length. The choice of cut-off frequency is of course somewhat subjective. Here we chose the limiting wave length to be twice the mean of the vertical and horizontal side lengths.

The rms values can be calculated by summing up the square of the absolute value of the Fourier transforms of the time signal. The high-pass filtering then consists of summing only over the frequencies above the cut-off frequency. The expressions for the three velocity components reads

$$u_{\rm rms} = \left(2\sum_{k=N_c}^{N/2} |X_i|^2\right)^{\frac{1}{2}},\tag{28}$$

$$v_{\rm rms} = \left(2\sum_{k=N_{\rm c}}^{N/2} |Y_i|^2\right)^{\frac{1}{2}},$$
 (29)

$$w_{\rm rms} = \left(2\sum_{k=N_{\rm c}}^{N/2} |Z_i|^2\right)^{\frac{1}{2}},\tag{30}$$

where X, Y and Z are the Fourier transforms corresponding to the velocity time signals u(x,y;t) - U(x,y), v(x,y;t) - V(x,y) and w(x,y;t) - W(x,y) respectively (with U, V, W denoting the time averaged values). N is the total number of samples and N_c is the summation index, k, corresponding to the frequency f_c .

To illustrate the distribution of kinetic energy over the frequencies the energy density function is calculated according to the following expression

$$\Phi(f_k) = 2N\Delta t |X_i(f_k)|^2 \quad k = 0, 1, \dots, \frac{N}{2}$$
(31)

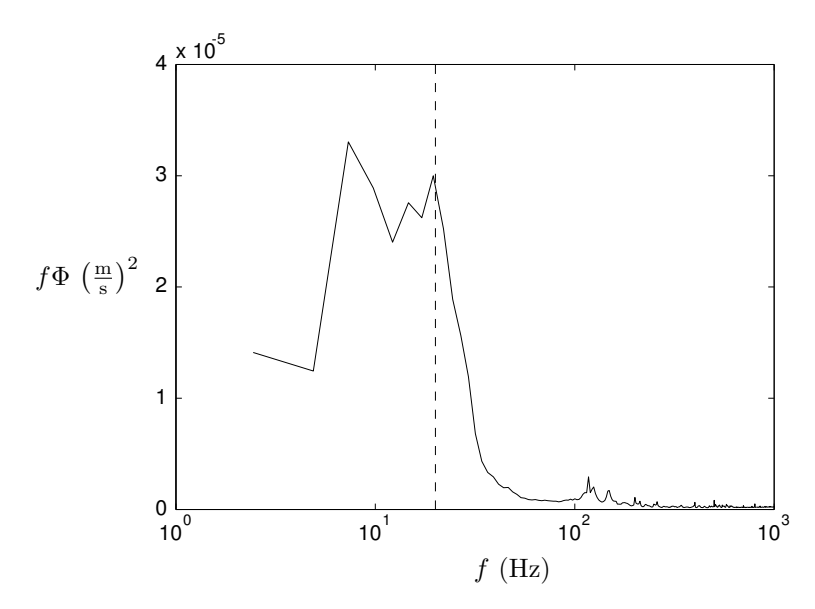


FIGURE 18. A typical power spectrum for the u velocity component in the core region of the test section. the dashed vertical line illustrates the cut-off frequency for the high-pass filter.

where $f_k = k/(N\Delta t)$. In figure 18 an example of a power spectrum for the streamwise velocity in the core region of the test section is shown. Note that most of the energy is located at very low frequencies. For the streamwise component the filtering removes about 50% of the energy as can be seen in figure 18 where the area under the curve to the left of the cut-off frequency is about similar in size to the area to the right. For the cross-stream components the effect of filtering is much smaller since less energy is located at low frequencies here. The cross-stream components are not affected by the waves traveling around the wind-tunnel circuit. This illustrates the purpose of the filtering which is to remove the influence of the traveling waves on the results. For comparison results for both filtered and unfiltered data are given in this paper. A comparison between the maximum values of the turbulence intensity for unfiltered and filtered data is shown in table 5.

The streamwise turbulence intensity over the measurement area for both unfiltered and filtered data is shown in figure 19. In the case of filtering the turbulence intensity is less than 0.04%, (see also table 5). In the center of the measurement area the turbulence intensity is less than 0.02%. This is very low especially considering the novel feature of expanding corners and the small cross section area of the test section. Most future experiments will be performed in this region of the test section cross section area. It is also comparable

Table 5. A comparison between filtered and unfiltered turbulence intensities in the core region of the test section.

Turb. Int.	filtered (20 Hz)	non-filtered
I_{x}	< 0.04 %	< 0.08 %
$I_{ m y}$	< 0.06 %	< 0.08 %
$I_{ m z}$	< 0.04 %	< 0.05 %

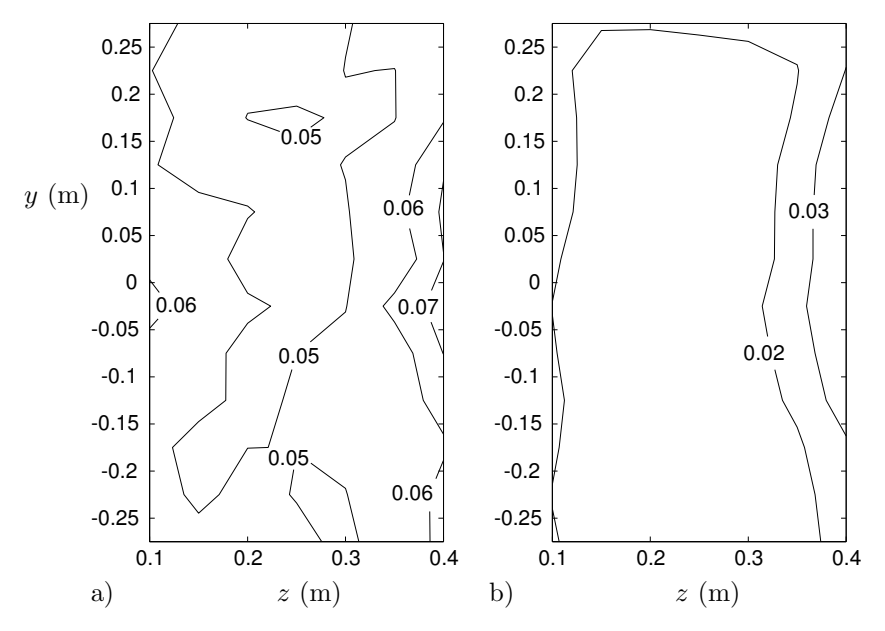


FIGURE 19. The streamwise turbulence intensity in a cross section area of the test section located 0.25 m from its entrance. a) non-filtered data, b) high-pass filtered data with cut-off frequency 20 Hz.

to the turbulence intensity measured in the MTL wind-tunnel under similar conditions, see Johansson (1992) and Lindgren & Johansson (2002).

For the unfiltered data the corresponding maximum intensity reaches 0.08% towards the right vertical wall but there is also an increase towards the left wall. (The flow is in the positive x-direction). In general the influence from the side walls is larger than the influence from the top and bottom walls. This can partly be explained by the shorter distance between the vertical walls compared to the horizontal walls. The more irregular pattern of the contours in the figure showing unfiltered data can be explained by the fact that the measurement time of each point is slightly too small to give good statistics for the low frequencies.

For the filtered vertical cross-stream component the turbulence intensity is 50% higher than for the streamwise component, *i.e.* less than 0.06% which is still very low compared to most wind-tunnels. The most noticeable feature of figure 20b is the strong gradient at the right wall. (The flow is in the positive x-direction). The gradient was also larger at this wall for the streamwise component but not as pronounced as here. The high turbulence level was first thought to be the result of a separation bubble at this wall located in the contraction. An investigation was performed using tufts to detect the separation. The result of the investigation was however that no separation bubble could be detected. Other possible reasons could be e.g. rough joints between wind-tunnel parts or vertical vibrations of the probe at these positions. As will be seen below the contribution from low frequency structures to the high turbulence intensity is substantial in this region.

The contours of the unfiltered vertical cross-stream intensity in figure 20a have a similar pattern to those in figure 20b. The effect of the filtering is not as pronounced for this component as for the streamwise one. There is, however, a larger filtering effect close to the right vertical wall indicating that the contribution to the high turbulence level encountered here is mainly from low frequency components. The maximum value of the unfiltered intensity is less than 0.8% which is comparable to the streamwise case, see table 5. In the central region of the measurement area the level of turbulence intensity is less than 0.03% which is very low, although this region is fairly small.

The horizontal component of the cross-stream turbulence intensity is in the filtered case less than 0.04%. The turbulence intensity is fairly evenly spread out over the measurement area with only a slight increase towards the edges and a very small central region where the intensity is less than 0.02%. For most of the measurement area the level is below 0.03%, see figure 21b. There is no large gradient at the right vertical wall as was the case for the vertical cross-stream component indicating that probe vibrations could be the cause for the strong gradient since it effects the streamwise and vertical components but not the horizontal component. (The flow direction is as before into the paper).

The unfiltered intensity for the horizontal component is also evenly distributed over the measurement area with slightly lower values in the central region and higher towards the wall as is expected. The value of the turbulence intensity is less than 0.05% over the entire region and less than 0.03% in a fairly large core region.

The filtered values of the cross-stream components is comparable to the values found in the MTL wind-tunnel, excluding the high values of vertical component at the right wall. This is somewhat surprising since the size of this wind-tunnel is substantially smaller, which makes it more difficult to achieve low values, because the walls influence a relatively speaking larger part of the cross section area. One could also expect some separation on the guide vanes

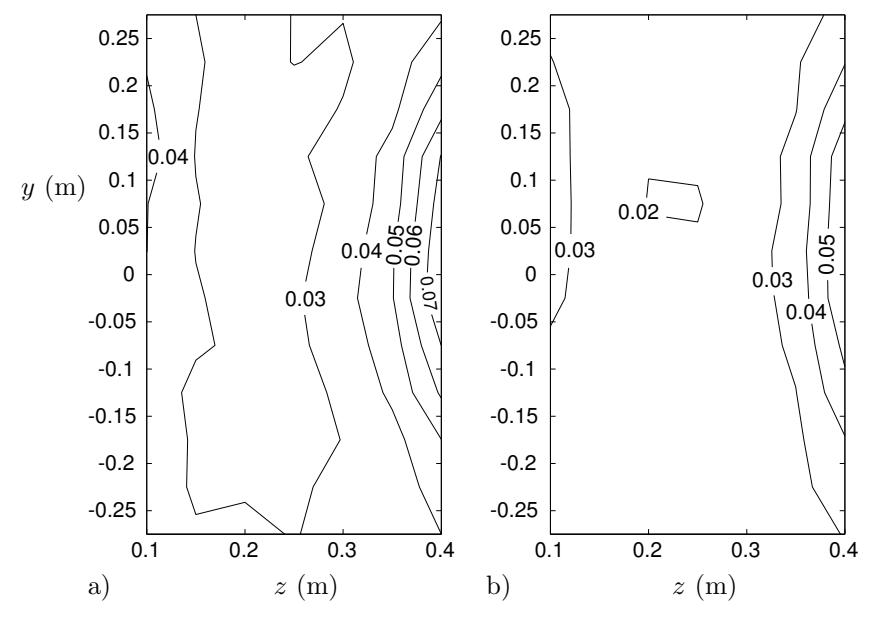


FIGURE 20. The vertical crosswise turbulence intensity in a cross section area of the test section located 0.25 m from its entrance. a) non-filtered data, b) high-pass filtered data with cut-off frequency 20 Hz.

in the fourth corner due to the very low chord Reynolds numbers found there, which could have a negative influence on the turbulence levels. However one should keep in mind that the data presented for the MTL wind-tunnel spans tunnel velocities between 10 and 60 m/s while this tunnel was only tested at 25 m/s which is the design tunnel velocity for which the wind-tunnel is optimized.

4.4. Noise measurement

The lack of insulation material in the wind-tunnel circuit except in the two silencers surrounding the fan made it particularly important to check the noise level in the wind-tunnel lab. As a comparison it can be noted that the MTL wind-tunnel has insulated walls throughout most of the wind-tunnel circuit. As seen in figure 22, the noise level outside the test section is very low. Actually it is impossible to hear the wind-tunnel running at a speed of 25 m/s if it is not totally quiet elsewhere in the room. The noise level outside the fan is slightly higher but the machinery is located on a lower level and the sound is effectively blocked by the floor. The reason for the somewhat irregular behavior of the curves in figure 22, especially that representing the position outside the fan, is that the load on the fan bearings varies with rpm leading to a mechanically induced noise increment at some fan speeds.

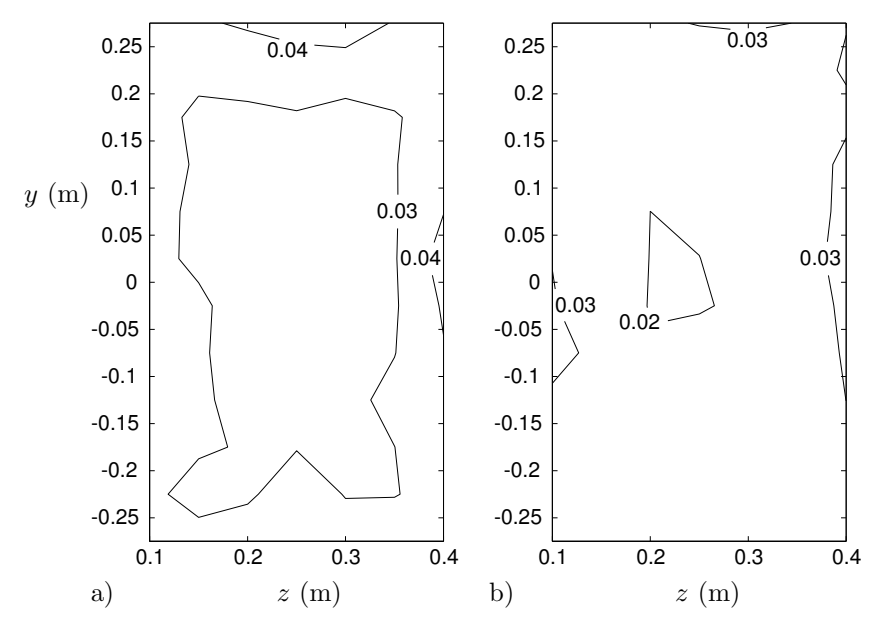


FIGURE 21. The horizontal crosswise turbulence intensity in a cross section area of the test section located 0.25 m from its entrance. a) non-filtered data, b) high-pass filtered data with cut-off frequency 20 Hz.

4.5. Guide-vane performance

A central design aspect for this wind-tunnel is the use of expanding corners, see section 2.3. To get a good comparison with the experiments and calculations presented in Lindgren et al. (1998), the chord Reynolds number was chosen to be around 200000. The most critical corner in terms of pressure-loss and flow quality is corner 1, located closely behind the test section, see figure 2. This is due to the disturbances often generated in the test section from measurement equipment, such as traversing arms, boundary layer plates or cylinders. The measurement consisted in traversing a pitot tube across the guide-vanes at the center of their span and also to measure the static pressures upstream and downstream of corner 1. This way of setting up the experiment should give close to two-dimensional results. The measurements in Lindgren et al. (1998) were performed in a similar way. The calculations in Lindgren et al. (1998) were purely two-dimensional on an infinite cascade with undisturbed incoming flow. Therefore the wall side boundary layers were excluded when calculating the

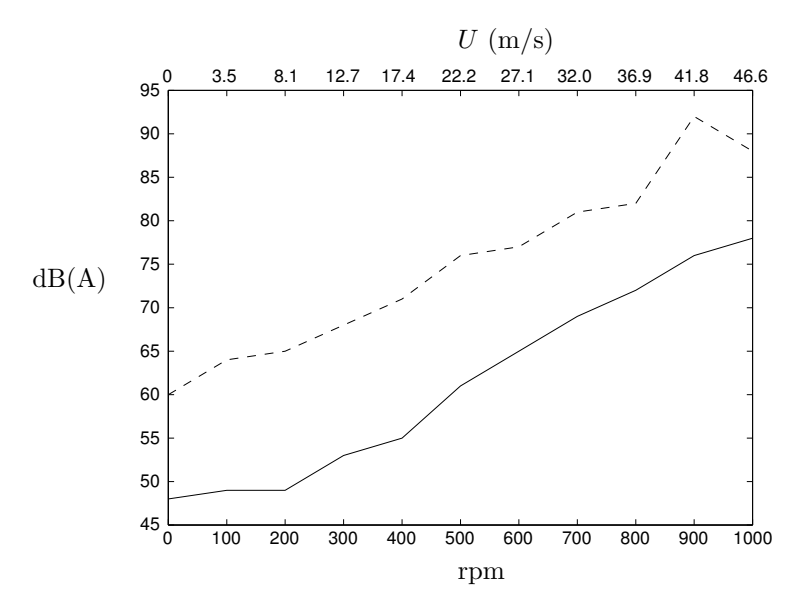


FIGURE 22. The Noise level outside the test section, —, and outside the fan, —. Fan rpm scale (bottom) Test section velocity scale (top)

total pressure-loss coefficient in the new experiment. The total pressure-loss coefficient is defined as

$$\frac{\Delta H}{q_0} = \frac{p_{\text{t0}} - \overline{p_{\text{t1}}}}{q_0} \tag{32}$$

where p_{t0} is the total pressure upstream the corner and $\overline{p_{t1}}$ is the mean total pressure downstream the corner. Expressed in the three measured pressure differences, $(p_{t0} - p_1, p_{t1}(y) - p_1)$ and $p_{t0} - p_0$, the equation reads

$$\frac{\Delta H}{q_0} = \frac{p_{t0} - p_1 - \frac{1}{nh_1} \int_0^{nh_1} (p_{t1}(y) - p_1) dy}{p_{t0} - p_0}$$
(33)

where p_0 and p_1 are the static pressure upstream and downstream the corner, n is the number of vanes over which the integration is performed and h_1 is the outlet distance between the vanes, see figure 5. The results show good agreement between calculations and experiments with a total pressure-loss coefficient for the calculations in Lindgren *et al.* (1998) of 0.041 and this experiment with a total pressure-loss coefficient of 0.047. Remember that the calculations are performed on a non-disturbed purely two-dimensional flow completely free of the three-dimensional effects which influences the measurements and leads to higher pressure-loss. The value of the total pressure-loss coefficient of 0.047

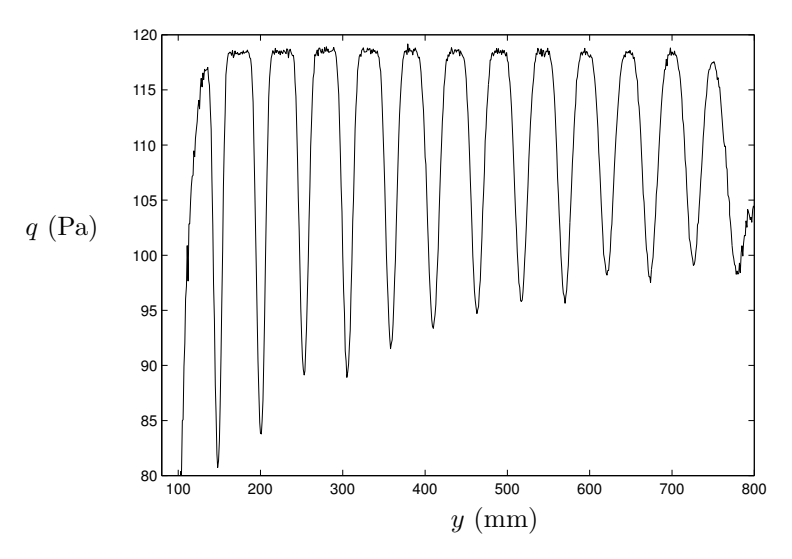


FIGURE 23. The variation of the dynamic pressure across the guide-vanes at their spanwise center position, $Re_c = 205000$.

is very good even when compared to most non-expanding guide-vane corners which often have values of the total pressure-loss coefficient above 0.1.

In figure 23 the wakes behind the guide-vanes can be seen with the trailing edges of the vanes located at a y position coinciding with the minimum values of dynamic pressure, q. To the right in figure 23 the wakes are wider but not so deep. This is because the distance between the traversed pitot tube and the guide-vanes is larger there, see figure 14.

Note also the thickness of the boundary layers. It can be seen in the left part of the figure 14 that the boundary layer here is about 15 cm thick. The guide-vanes, however, still seem to cope well with these adverse conditions.

5. Concluding remarks

The design of the new wind-tunnel is a success. All considered flow quality factors, such as mean flow variations, turbulence intensities, temperature variations and noise are well within the expected levels. It is proved that it is possible to include expanding corners into the wind-tunnel design without deteriorating the flow quality or increasing the wind-tunnel circuit total pressure-loss. The use of a standard industrial fan/motor solution with an AC motor and frequency converter has not had a negative effect on the flow quality but some disturbances on the electrical mains affecting e.g. temperature and hot-wire anemometry measurements have been detected. It was also possible to

eliminate these disturbances by improved cabling. The maximum speed is 48 m/s with an empty test section, but it can be increased further by over-riding the maximum rpm allowed for the fan, without over-heating the motor. This can be done for shorter periods of time, (up to a few hours), without risk of damaging the fan bearings.

The total pressure-loss of the wind-tunnel circuit represents a moderately high power factor value of 0.46, see section 4.1, but it is important here to consider the size and length of the wind-tunnel test section and the flow quality improving devices implemented leading to a higher total pressure-loss.

The variation of total pressure in the test section at a test section velocity of 25 m/s is below $\pm 0.1\%$. This is equivalent to a velocity variation of less than $\pm 0.05\%$. No clear trend in the variation over the test section cross section can be seen. The small variations present are irregularly distributed and the amplitude is of the same order of magnitude as the accuracy of the measurements.

The temperature variation in the test section at a test section speed of 25 m/s is very small. Over the cross section in the test section the variation is less than $\pm 0.07^{\circ}$ C and the variation over a time period of 4 hours is less than $\pm 0.03^{\circ}$ C in the center of the cross section. A clear trend of the temperature variation over the cross section can be seen.

The turbulence levels at a test section speed of 25 m/s are very low, see section 4.3. All components of the turbulence intensity are below 0.04% in the core region of the test section cross section area. These values are calculated with a high-pass filter at 20 Hz eliminating flow structures larger than 1.25 m. Without filtering, the values of the turbulence intensities are slightly higher with a streamwise turbulence intensity of less than 0.06% and for the cross flow directions it is less than 0.08%. These levels are still very low proving that the honeycomb, screen package and contraction are complying fully to our expectations.

The noise level outside the fan and outside the test section pressure equalizing slit is satisfactorily low, see section 4.4. Outside the test section the noise level is about 63 dB(A) at a speed of 25 m/s and about 74 db(A) at maximum speed. This low noise level is achieved by a low rpm fan of relatively large size. The larger diameter of the fan is made possible by the use of expanding corners that leads to a fast increase in the wind-tunnel cross section area.

In the experiments and calculations of Lindgren *et al.* (1998) it was found that expanding corners represent a good design concept for obtaining a compact tunnel circuit with low pressure losses. The measurements on the expanding corners in the new wind-tunnel shows that this is indeed the case with a quasi two-dimensional total pressure-loss coefficient of 0.047 at a chord Reynolds number of about 200000. The earlier experiments with a slightly different guide-vane had a total pressure-loss coefficient of 0.057 at the same Reynolds

number and the two-dimensional calculations on an infinite cascade pointed to a total pressure-loss coefficient of 0.041 at the same Reynolds number, see Lindgren et al. (1998). The slightly higher value for the experiment than the calculation with the new guide-vane is expected because the flow condition in reality is never as good as the disturbance free, purely two-dimensional flow condition in the calculation. However, the new experimental result is clearly better than the earlier result with the other guide-vane proving that the optimization of a new guide-vane for expanding corners was successful. The good flow quality in the test section also indicates that the new guide-vane is able to perform also at the very low chord Reynolds number encountered in corner 4. These results prove that the use of expanding corners can be implemented in wind-tunnel constructions saving space and money without sacrificing flow quality or increasing the total pressure-loss of the wind-tunnel circuit noticeably.

6. Acknowledgment

The authors would like to thank Jens Österlund for his support and suggestions during the work and Ulf Landén and Marcus Gällstedt for their help in assembling of the wind-tunnel parts and manufacture measurement equipment. Finally we wish to thank The Göran Gustafsson Foundation and The Swedish Research Council for financial support.

References

- ANGELE, K. P. 2000 PIV measurements in a separating turbulent APG boundary layer. TRITA-MEK 2000:15. Lic. Thesis, Department of Mechanics, KTH.
- Baines, W. D. & Petersen, E. G. 1951 An investigation of flow through screens. Trans. ASME 73, 467–480.
- BATCHELOR, G. K. 1976 The theory of homogeneous turbulence. Camebridge University Press.
- BORGER, G. G. 1976 The optimization of wind tunnel contractions for the subsonic range. *Tech. Rep.* TTF 16899. NASA.
- Bradshaw, P. & Pankhurst, R. C. 1964 The design of low-speed wind tunnels. Progress in aeronautical sciences 6, 1–69.
- Çabuk, H. & Modi, V. 1992 Optimum plane diffusers in laminar flow. J. Fluid Mech. 237, 373–393.
- COLLAR, A. R. 1936 Some experiments with cascades of aerofoils. A.R.C. Technical Report 1768. Aeronautical research committee.
- DOWNIE, J. H., JORDINSON, R. & BARNES, F. H. 1984 On the design of threedimensional wind tunnel contractions. J. Royal Aeronautical Society pp. 287– 295.
- DRELA, M. & GILES, M. B. 1987 Viscous-inviscid analysis of transonic and low Reynolds number airfoils. AIAA 25 (10), 1347.

- Drela, M. & Youngren, H. 1995 A users guide to MISES 2.1. MIT Computational Aerospace Sciences laboratory.
- FOX, R. W. & KLINE, S. J. 1962 Flow regime data and design methods for curved subsonic diffusers. Trans. ASME, J. Basic Engineering, Ser. D 84, 303–312.
- FRIEDMAN, D. & WESTPHAL, W. R. 1952 Experimental investigation of a 90° cascade diffusing bend with an area ratio of 1.45:1 and with several inlet boundary layers. TN 2668. NACA.
- Ganesan, V., Suzuki, K., Narayana, P. A. & Chithambaran, V. K. 1991 Investigations of mean and turbulent flow characteristics of a two dimensional plane diffuser. *Experiments in Fluids* **10**, 205–212.
- GILES, M. B. & DRELA, M. 1987 Two-dimensional transonic aerodynamic design method. AIAA Journal 25 (9), 1199.
- GÖRTLER, H. 1941 Instabilität laminarer Grenzschichten an konkaven Wänden gegenüber dreidimensionalen Störungen. ZAMM 21, 250–252.
- Groth, J. 1991 On the modelling of homogeneous turbulence. *Tech. Rep.*. Dep. of Mechanics, KTH, SE-100 44 Stckholm.
- Groth, J. & Johansson, A. V. 1988 Turbulence reduction by screens. J. Fluid Mech 197, 139–155.
- Johansson, A. V. 1992 A low speed wind-tunnel with extreme flow quality-design and tests. *Proc. the 18:th ICAS Congress* pp. 1603–1611.
- Johansson, A. V. & Alfredsson, P. H. 1988 Experimentella metoder i strömningsmekaniken. Department of Mechanics, Royal Institute of Technology.
- Kröber, G. 1932 Schaufelgitter zur Umlenkung von Flussigkeits-Strömung. Ingenieur-Archiv 3, 516.
- LAWS, E. & LIVESEY, J. 1978 Flow through screens. Ann rev Fluid Mech. 10, 247–266.
- LINDGREN, B. 1999 Development of guide-vanes for expanding corners with application in wind-tunnel design. TRITA-MEK 1999:8. Department of Mechanics, KTH.
- LINDGREN, B. & JOHANSSON, A. V. 2002 Evaluation of the flow quality in the low-speed MTL wind-tunnel. TRITA-MEK 2002:13. Department of Mechanics, KTH.
- LINDGREN, B., ÖSTERLUND, J. M. & JOHANSSON, A. V. 1998 Measurement and calibration of guide-vane performance in expanding bends for wind-tunnels. *Experiments in Fluids* **24**, 265–272.
- LOEHRKE, R. I. & NAGIB, H. M. 1976 Control of free-stream turbulence by means of honeycombs: A balence between suppression and generation. J. Fluids Engineering pp. 342–353.
- Malmer, I. 1933 Tekniska högskolans flygtekniska laboratorium. Teknisk Tidskrift .
- MEHTA, R. D. & HOFFMANN, P. H. 1987 Boundary layer two-dimensionality in wind tunnels. *Experiments in Fluids* 5, 358–360.
- MICHEL, U. & FROEBEL, E. 1988 Lower limit for the velocity fluctuation level in wind tunnels. *Experiments in Fluids* **6**, 49–54.
- MIKHAIL, M. N. & RAINBIRD, W. J. 1978 Optimum design of wind tunnel contractions, paper 78-819. In AIAA 10th Aerodynamic Testing Conference.

- NASH, E. C., LOWSON, M. V. & MCALPINE, A. 1999 Boundary-layer instability noise on airfoils. *J. Fluid Mech.* **382**, 27–61.
- ÖSTERLUND, J. M. & JOHANSSON, A. V. 1999 Turbulent boundary layer experiments in the MTL wind-tunnel. TRITA-MEK 1999:16. Department of Mechanics, KTH.
- Prandtl, L. 1932 Herstellung einwandfreier Lufstöme (Windkanäle). Handbuch der Experimentalphysik, Leipzig, Germany, vol 4, part 2,p.73. *Naca Tech. Mem.* 726
- RAE, W. H. & POPE, A. 1984 Low-speed wind tunnel testing., 2nd edn. John Wiley & sons.
- Reneau, L. R., Johnson, J. P. & Kline, S. J. 1976 Performance and design of straight, two-dimensional diffusers. *Trans. ASME, J. Basic Engineering* 89, 141–156.
- Sahlin, A. & Johansson, A. V. 1991 Design of guide vanes for minimizing the pressure loss in sharp bends. *Phys. Fluids A* 3, 1934–1940.
- Scheiman, J. & Brooks, J. D. 1981 Comparison of experimental and theoretical turbulence reduction from screens, honeycomb and honeycomb-screen combinations. *JAS* 18, 638–643.
- Seidel, M. 1982 Construction 1976-1980. Design, manufacturing, calibration of the German-Dutch wind tunnel (DNW). *Tech. Rep.*. Duits-Nederlandese Windtunnel (DNW).
- Shaw, R. 1960 The influence of hole dimensions on static pressure measurements. *J. Fluid Mech.* **7**, 550.
- SJÖGREN, T. & JOHANSSON, A. V. 1998 Measurement and modelling of homogeneous axisymmetric turbulence. J. Fluid Mech 374, 59–90.
- Taylor, G. & Batchelor, G. K. 1949 The effect of wire gauze on small disturbances in a uniform stream. *Quart. J. Mech. and App. Math.* 2, part 1,1.
- Waitman, B. A., Reneau, L. R. & Kline, S. J. 1961 Effect of inlet conditions on performance of two-dimensional subsonic diffusers. *Trans. ASME, J. Basic Engineering* 83, 349–360.
- Wolf, H. 1957 Messungen im Nachlauf eines Gleichdruckgitters für 90°-umlenkung. Maschinenbautechnik $\bf 6$ (10), 539.
- Wolf, S. 1969 Effects of nonuniform inlet velocity profiles on flow regimes and performance in two-dimensional diffusers. Trans. ASME, J. Basic Engineering 91, 462–474.
- Youngren, H. & Drela, M. 1991 Viscous/inviscid method for preliminary design of transonic cascades. In AIAA, SAE, ASME, and ASEE, Joint Propulsion, Conference, 27th..

Paper 3

P3

Evaluation of the flow quality in the MTL wind-tunnel

By Björn Lindgren and Arne V. Johansson

Dept. of Mechanics, KTH, SE-100 44 Stockholm, Sweden

Published as internal report. TRITA-MEK 2002:13

The flow characteristics of the MTL wind-tunnel at the Department of Mechanics, KTH, have been evaluated 10 years after its completion. The wind-tunnel is of closed circuit type with a 7 m long test section that has a cross section area of $1.2 \times 0.8 \text{ m}^2$. The contraction ratio is 9 and the maximum speed is approximately 70 m/s. The experiments performed included measurements of total pressure variation, temperature variation, flow angle variation and turbulence intensity variation. The measurements were carried out in the test section over a cross flow measurement area of $0.9 \times 0.5 \text{ m}^2$ located 0.4 m downstream the inlet. The temperature variation in time was also measured at the center of the measurement area. The experiments were performed at three different wind-tunnel speeds, 10, 25 and 40 m/s. The present results confirm the high flow quality of the MTL wind-tunnel. The flow quality measurements carried out soon after the completion of the tunnel are here repeated and extended. For instance, at 25 m/s the streamwise turbulence intensity is less than 0.025% and both the cross flow turbulence intensities are less than 0.035% at the same speed. The total pressure variation is less than $\pm 0.06\%$ and the temperature variation is less than ± 0.05 °C.

1. Introduction

The Minimum Turbulence Level or Mårten Theodore Landahl (MTL), wind-tunnel, named after its late initiator, was designed in the mid 80s to suit experiments in basic transition and turbulence research. The wind-tunnel that was completed in 1991 has now been in operation for 10 years and it was decided to re-confirm the early flow quality measurements and to extend them with the aid of the accurate and automated traversing equipment now in use. The French company Sessia was contracted for the wind-tunnel construction, although the responsibility for the aerodynamic design remained with the Department of Mechanics. The primary aim of the early tunnel calibration study was to perform experiments that could confirm that the design requirements in the contract were fulfilled. The main results were reported in Johansson (1992).

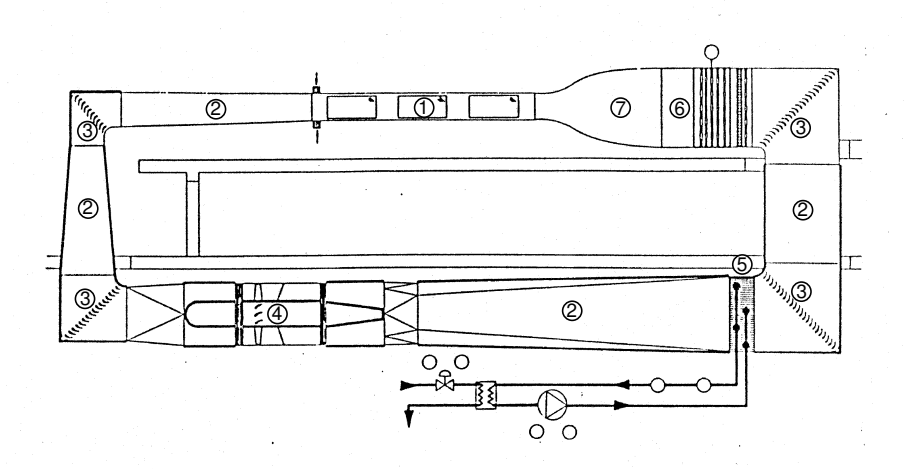


FIGURE 1. The MTL wind-tunnel layout.

At that time no automated traversing system existed and the manual system used only allowed for measurements with coarse spatial resolution. Experiments similar to those in the early study have been performed allowing for direct comparisons. This is important not just from the point of view of establishing the current status of the flow quality but also to analyze the effect of the wear on the wind-tunnel parts. It is commonly known that *e.g.* the maximum speed of a wind-tunnel is usually decreasing with time but is there also a negative effect on the flow quality from possible deterioration of screens, honeycomb and machinery? Answering questions like these helps planning for future maintenance of the wind-tunnel circuit.

In the MTL wind-tunnel many landmark experiments have been performed over the years. A complete list of the doctoral and licentiate theses where the MTL wind-tunnel was used is given in the appendix together with a short description of the main findings in these works. Other landmark papers with measurements performed in the MTL wind-tunnel are also described and listed in the appendix.

1.1. Description of the MTL wind-tunnel

The MTL wind-tunnel is a closed loop circuit wind-tunnel. The advantages of a closed loop tunnel is that less energy is needed to operate the tunnel at a given speed and that disturbances in the tunnel surroundings do not interfere with the flow inside the tunnel making it easier to control the mean flow characteristics during measurements. A small gap between the test section and the first diffuser ensures that the static pressure in the test section is close to the

atmospheric pressure. The overall length of the MTL tunnel is about 25 m and the height is 9 m.

Its design is optimized for very good flow quality rather than low total pressure drop, see Johansson (1992). The efficiency factor, λ , is a measure of the losses in the wind-tunnel circuit, defined as

$$\lambda = \frac{\Delta p_{\text{tot}}}{q_{\text{test}}\eta_{\text{fan}}},\tag{1}$$

where $\Delta p_{\rm tot}$ is the total pressure-loss, $q_{\rm test}$ is the dynamic pressure in the test section and $\eta_{\rm fan}$ is the efficiency factor of the fan. For the MTL tunnel the efficiency factor is about 0.4. In figure 1 a side view of the tunnel circuit is presented with the numbers referring to different parts of the wind-tunnel.

1.1.1. Test section

The test section, item ① in figure 1, is 7 m long and it has a cross section area of $1.2 \times 0.8 \text{ m}^2$ (at the inlet). The dimensions of the test section ensures that e.g. experiments on a flat plate at fairly high Reynolds numbers can be achieved without a very high free stream velocity, see e.q. Osterlund & Johansson (1999). The cross section area is large enough to enable measurements at the downstream end of the test section without interference from the test section wall boundary layers. The top and bottom walls are adjustable so that the streamwise pressure gradient can be modified between moderate negative to moderate positive values. Most importantly, a zero streamwise pressure gradient can be achieved by compensating for the boundary layer growth on the test section walls. This can be achieved to within a variation of 0.2% of the free stream velocity, see Osterlund (1999). A traversing arm penetrates the top wall of the test section. The traversing system has 5-axes making it possible for a measurement probe to be translated in the three spatial directions and to be rotated along the streamwise axis and along one cross flow axis free of choice. An extra long sting facilitates measurements in the contraction, see Sjögren & Johansson (1998). The maximum free-stream velocity in the (empty) test section is approximately 69 m/s.

1.1.2. Diffusers

The diffusers, items ② in figure 1, are conservatively designed so that wall boundary layer separation is avoided at any time, see e.g. Seidel (1982). For very large flow disturbances, vortex generators, see e.g. Lin et al. (1991), can be mounted in the first diffuser downstream of the test section. Calculations have been made to find the optimum shape of the diffuser downstream the fan. The calculations combined the potential theory with boundary layer equations. Model experiments were also performed using a 2 m long diffuser. Various shapes and inlet conditions were investigated to achieve an efficient diffuser

without wall boundary layer separation. The conservative design of the diffusers leads to a longer wind-tunnel return circuit and is one contributing factor to the relatively large total pressure-loss in this wind-tunnel circuit compared to wind-tunnels used for commercial testing.

1.1.3. Corners

One wind tunnel part that could cause flow disturbances, and especially noise is the corner, item 3 in figure 1. The corner, which turns the flow 90°, are equipped with a cascade of airfoils, here called guide-vanes. If the guide-vanes are not properly designed they could be exposed to large boundary layer separations leading to poor flow uniformity, large turbulence levels as well as high total pressure-loss. In the design of the MTL tunnel, special care was given to this detail with experiments and calculations performed by Sahlin & Johansson (1991). In addition to the published results for profiles with turbulent boundary layers, a very efficient guide-vane with laminar boundary layers and a two-dimensional total guide-vane pressure-loss coefficient as low as 0.036, measured at the first corner downstream the test section, was designed for use in the MTL-tunnel. Despite the very low pressure-loss the guide-vanes allows for moderate $(\pm 2^{\circ})$ changes in angle of attack without separating. It is important to design a guide-vane that will perform well under adverse flow conditions especially in the first corner where measurement equipment may disturb the flow substantially.

1.1.4. Driving unit

Item \oplus in figure 1 is the fan and motor. The fan used in the MTL tunnel is of axial type with 12 blades and the motor mounted directly onto the fan axis. The motor is of DC current type and it is enclosed in a cylinder with the same diameter as the fan hub for reasons of improved aerodynamics. It is cooled separately by a fan outside the tunnel circuit and cooling air is supplied to the enclosed cylinder through elliptical pipes. This means that the heat generated by losses in the motor does not need to be removed by the wind-tunnel heat exchanger. The power of the motor is 85 kW and the speed of the fan is controlled by a thyristor control unit.

In-front of and behind the fan there are silencers with central bodies to minimize noise disturbances from the fan. The upstream central body has the diameter of the fan hub and an ellipsoidal shaped nose cone. The central body of the downstream silencer is shaped as a cone with the base diameter equaling the upstream central body diameter. The upstream silencer also converts the tunnel circuit cross section from square to circular and the downstream silencer converts the cross section from circular to octagonal shape, which is the shape of the following diffuser, see figure 1. The walls of the silencers and their central bodies are made of perforated plates with a thick sound absorbing material (long fibered glass-wool covered by a woven glass-fiber material) for good

efficiency. The wind-tunnel parts located between the first and forth corners have sound insulated walls, resulting in a very quiet wind-tunnel. Measurement of the noise level inside the test section was performed and are reported in Johansson (1992).

1.1.5. Heat exchanger

The tunnel circuit heat exchanger, item ⑤ in figure 1, is located at the lower part of the wind-tunnel just in-front of the third corner counting from the test section in the downstream direction. This positioning of the heat exchanger is conservative in some sense ensuring that the temperature variation in the test section cross section is small. A small drawback of this positioning is that the cross section area is slightly smaller here than in the stagnation chamber, see 1.1.6, leading to a small increase in local pressure drop.

The tubes of the heat exchanger are of elliptical cross section shape which decreases the local pressure drop slightly compared to standard circular pipes. Cooling flanges are mounted onto the pipes to increase the cooling area of the heat exchanger. Extra turbulence generators can also be added to the cooling flanges to enhance the heat transfer, but such items are not used here because of the very high pressure drop and the increase of the turbulence level caused by these turbulence generators.

The water flowing through the heat exchanger has a high and constant flow rate. It is cooled through an additional heat exchanger by water from an external, in-house, cooling system. A valve regulates the flow rate in the external system thereby controlling the temperature of the water passing through the wind-tunnel heat exchanger. This valve is regulated by a commercial PID regulator.

The temperature in the wind-tunnel test section is measured by a PT-100 sensor and is used as input into the PID regulator. The set, (chosen), wind-tunnel temperature is entered manually from the regulator front panel.

1.1.6. Stagnation chamber

The stagnation chamber, or settling chamber as it is often called, item 6 in figure 1, has the largest cross section area, and thereby also the lowest flow velocity, in the wind tunnel circuit. This is where items used for flow quality improvements are located such as screens and honeycomb. Sometimes the heat exchanger is also located here, see e.g. Seidel (1982), to minimize the local pressure-drop. This positioning was here rejected because of the ambition to achieve a high degree of temperature uniformity in the test section.

The MTL stagnation chamber consists of three different parts, the honeycomb, the screens and the relaxation duct, in that order of location relative to the flow direction. The purpose of the honeycomb is to break up large eddies into smaller ones and, more importantly, to rectify the flow coming from the fourth corner. A screen also rectifies the flow to some extent but the honeycomb is more efficient in this respect and it has a lower cost in pressure drop. The ratio between the length, (in the streamwise direction), and the cell diameter of the honeycomb is the most important parameter influencing the degree of flow rectification, see e.g. Lumley (1964); Loehrke & Nagib (1976); Scheiman & Brooks (1981). The honeycomb is 100 mm long and the cell diameter is about 10 mm in the MTL tunnel.

The screens on the other hand are more efficient than the honeycomb in reducing the turbulence by breaking down larger eddies into smaller ones with a size of the mesh width, see e.g. Laws & Livesey (1978) and Groth & Johansson (1988). The screens are also very effective in reducing mean flow variations over the cross section area. This ability is related to the solidity, i.e. the ratio of blockage generated by the screen wire front area, and the pressure drop coefficient of the screens, see Taylor & Batchelor (1949). It has been found that a combination of screens with decreasing mesh sizes in the downstream direction is very efficient in reducing mean flow variations, see e.g. Groth & Johansson (1988). The distance between the screens has to be more than about 30 mesh sizes to let the screen wire induced turbulence die out sufficiently before it hits the next screen. The porosity of the screens must also be larger than about 55% to avoid a phenomenon called jet collapse, see Baines & Peterson (1951). Jet collapse leads to a strong mean flow variation and must be avoided. In the MTL tunnel there are 5 screens with decreasing mesh size in the streamwise direction between 3.1 mm and 0.75 mm. These values were chosen carefully after a study made by Groth & Johansson (1988) for maximum screen efficiency.

The effect of turbulence reduction of the screens is much larger in the streamwise component than in the cross stream components of the flow. This is especially true for under-critical screens where up to 90% of the reduction is in the streamwise component, see Groth & Johansson (1988); Tan-Atichat et al. (1982). This means that the flow is very non-isotropic just downstream of the screens making it important to allow the flow to relax towards a state of isotropy before it enters the contraction where it again will be subjected to high strains. This is achieved at the downstream end of the non-diverging stagnation chamber. The length of this section is 750 mm in the MTL tunnel, which is a long enough distance for the flow to reach an approximately isotropic state.

1.1.7. Contraction

The final part in the wind-tunnel return circuit is the contraction, item $\overline{\mathcal{O}}$ in figure 1. It transform the wind-tunnel cross section area back to that of the test section. The contraction also reduces the relative mean flow velocity variation and turbulence intensity. These reductions are much larger in the streamwise

direction than in the cross stream directions. They are also highly dependent on the contraction ratio with increased reduction for increasing contraction ratio, see e.g. Johansson & Alfredsson (1988). The contraction ratio in the MTL tunnel is 9, i.e. the area ratio between the stagnation chamber and test section cross section areas. This value is rather high compared to most other wind-tunnels but there are occasional examples of even higher contraction ratios. The drawback of a high contraction ratio is the relative increase in tunnel return circuit length, highly non-isotropic flow in the test section inlet and an increased risk for separating boundary layers on the contraction walls.

The shape of the contraction has to be designed very carefully to avoid wall boundary layer separation. A contraction can be divided into one upstream concave part and one downstream convex part. Separation can occur in both these parts. A boundary layer separation is induced by a positive pressure gradient along the contraction wall and is caused by the curvature of the wall. It is present even though the mean flow in general is accelerating due to the decrease in cross section area. Positive pressure gradients are found both in the concave part close to the inflection point, where the shape of the walls become convex, and at the downstream end of the convex part. A separation occurring in the concave part is very difficult to eliminate once the contraction is built which means that it has to be avoided already at the design stage. A separation bubble in the convex part, however, can be eliminated by tripping the laminar boundary layer achieving transition to a turbulent boundary layer that is more resistant to separation. This kind of boundary layer tripping is implemented in the MTL tunnel using V-shaped dymo-tape as roughness elements.

The shape of the contraction used in the MTL wind-tunnel was optimized using flow calculations. These calculations were based on a combination of potential theory and boundary layer equations. They were performed using a code that was provided by Downie *et al.* (1984). The aim was to minimize the contraction length keeping a wall pressure gradient distribution without risk for wall boundary layer separation. For further information on optimization of three dimensional wind-tunnel contractions see *e.g.* Borger (1976); Mikhail & Rainbird (1978).

The final shape chosen for the MTL-tunnel can be expressed as a combination of sinus-hyperbolic functions where the concave part covers the first 70% of the contraction length and the convex part the remaining 30%.

2. Experimental setup

The present measurements were performed in a cross section of the test section at a position 400 mm downstream the test section entry. The area covered by the measurement probes was 900×500 mm² and located around the center, see figure 2. This area is here referred to as the measurement region. The area ratio between the measurement region and the test section is 0.47, thus almost half the total area is covered in the experiments. The reason for excluding the

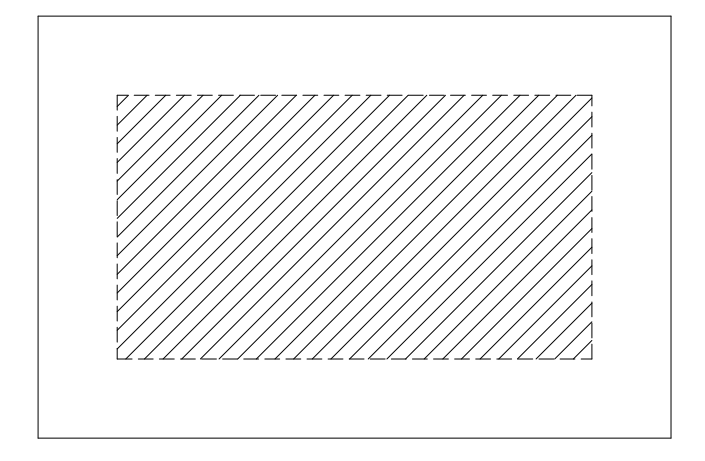


FIGURE 2. The cross section of the test section. The hatched area is the area covered in the measurements.

150 mm wide rim closest to the walls is that the flow is here disturbed by the tunnel circuit walls and it is usually not included when figures of wind-tunnel flow qualities are compared. The velocity variation is stronger in the rim than in the core region (measurement region). Therefore most experiments occurring in the MTL tunnel are performed in the core region. Also by excluding the rim the calibration range of the probes can be minimized increasing the resolution of the measurements in the core region. The measurements were performed at three different test section free stream velocities covering a large part of the wind-tunnel velocity range. The three velocities are 10 m/s, 25 m/s, and 40 m/s. These velocities were chosen because they are representative for many of the experiments performed so far in the MTL tunnel. 10 m/s is a typical velocity for experiments on transition phenomena, 25 m/s is a typical velocity for medium Reynolds number experiments and 40 m/s is a typical velocity for higher Reynolds number experiments. The fan blade angles are not easily changed and they are positioned for maximum performance at around 25 m/s. Therefore we expect the results of these measurements to be most favourable at 25 m/s free-stream velocity.

The traversing system used is a 5-axes system, see section 1.1.4. This system can traverse a probe in the streamwise and cross stream directions. It can rotate the probe around its own axis and it can also change the angle of attack. The last feature makes it possible to calibrate a cross wire probe or a flow angle probe without removing them from the test section, making the calibration more accurate. The traversing system and the wind-tunnel velocity are controlled from a computer.

2.1. Measurement instrumentation

For the hot-wire measurements we used a two-channel anemometer, (AN-1003), from AA Labs (Israel). For further amplification of the hot-wire signal a stereo amplifier, (AX-490), from Yamaha was used. This amplifier was also used to filter the signal, removing contributions from noise at very high frequencies. The signal was then sampled into a computer by a 12 bit AD board.

The measurement of the dynamic pressure was achieved through a differential pressure transducer, (FCO510) from Furness Control, (Great Britain). The absolute accuracy of the pressure transducer is 0.25% of full scale, (± 2000 Pa). The sampled data are transferred to the measurement computer through the serial bus.

The temperatures were measured using Pt-100 sensors. The absolute accuracy of these sensors is in the order of 0.056°C per °C. A 6 digit accurate multimeter (HP-34401A) from Hewlett Packard with a built in 4-wire compensation resistance meter was used to measure the probe resistance. The 4-wire compensation eliminates any contribution from the inherent resistance in the connecting cables. The measured data was then transferred to the measurement computer through GPIB communication and then converted into temperatures using the following equation

$$R_{\rm t} = R_0 \left(1 + AT + BT^2 \right),$$
 (2)

where $R_{\rm t}$ is the probe resistance, R_0 is the resistance at 0°C, T is the temperature and A and B are constants.

2.2. Probe calibrations

The probes used were single- and cross- hot-wire probes and a flow angle probe. Calibrations of the hot-wire probes were performed immediately before every new measurement. The flow angle probe was calibrated using several runs to verify the calibration accuracy.

2.2.1. Single-wire probe calibration

The exclusion of the near wall region allows the velocity range over which the calibration is made to be very small. This means that the calibration can be made with high accurately. The error in streamwise velocity for the single-wire calibrations was less than $\pm 0.05\%$. The single wire was calibrated in the free stream using King's law

$$U_0 = \left(\frac{E^2 - A}{B}\right)^{\frac{1}{n}} \tag{3}$$

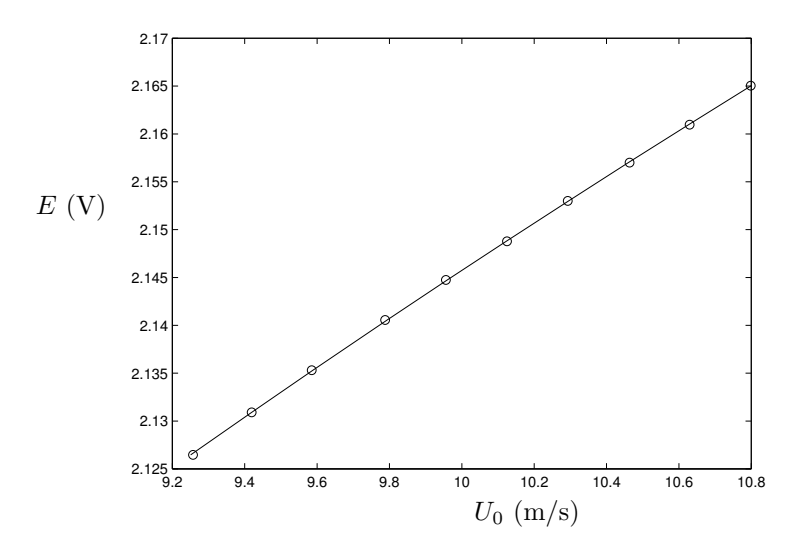


FIGURE 3. A typical calibration of a single-wire. The circles are measured points and the solid line is the King's law derived by a least square fit to the measured points.

where U_0 is the free-stream velocity, A, B and n are constants to be determined and E is the voltage output from the anemometer. The mean velocity, U_0 , was determined through the relationship

$$p_{\rm tot} - p = \frac{1}{2}\rho U_0^2 \tag{4}$$

using a Prandtl tube to measure the dynamic pressure. The density and viscosity of the air could be determined accurately by measuring the static pressure and the temperature. In equation 4, $p_{\rm tot}$ is the total pressure, p is the static pressure and ρ is the air density. A typical single-wire calibration curve is seen in figure 3.

2.2.2. Cross-wire probe calibration

Calibrating the cross-wire probe includes variations both in the velocity and probe angle of attack. A surface is then fitted to the measured data points using a fifth order polynomial. The use of a polynomial that lacks any relevant physical information makes it extra important not to allow any data points outside the calibration range during measurements. This may lead to strongly erroneous results.

The streamwise and cross stream velocities were determined by the equations

$$U = U_0 \cos \alpha, \tag{5}$$

$$V = U_0 \sin \alpha, \tag{6}$$

where U and V are the streamwise and cross stream velocity components respectively and α is the probe angle of attack. Two help variables, x and y representing the streamwise and the cross stream velocity components, are calculated from the wire voltages E_1 and E_2 as follows

$$x = E_1 + E_2, (7)$$

$$y = E_1 - E_2, (8)$$

These variables are then used to construct two two-dimensional fifth order polynomials, here denoted by M and N, for the two variables, U and $\tan \alpha$. By solving the following equations in a least square sense

$$MA = U, (9)$$

$$NB = \tan \alpha,$$
 (10)

the coefficients in the vectors A and B can be determined. These coefficients are then stored and used later in the experiments to determine the instantaneous velocities, u and v.

In figure 4 the results from a typical cross-wire calibration is shown. The area inside the solid lines is the calibration area where all measurement points must lie. The error of the cross-wire calibration was less than $\pm 0.05\%$ for the streamwise, U, component and the cross stream components V and W.

2.2.3. Flow angle probe calibration

The flow angle probe was calibrated by altering the probe angle of attack in the center of the measurement area. The shape of the probe makes it very sensitive to flow angle variations. There are two pressure holes, one on each side of the probe close the bottom of the V-shaped cut, see figure 5. When the stagnation point at the bottom of the V cut moves towards one side a pressure difference can be measured between the holes. The inclined edges of the V cut accentuates this pressure difference. The pressure difference is measured for different angles of attack and a least square fit of a third order polynomial is then made to the measured data points. In figure 6 a typical calibration of a flow angle probe is shown. The error in the flow angle calibrations is less than $\pm 0.02^{\circ}$.

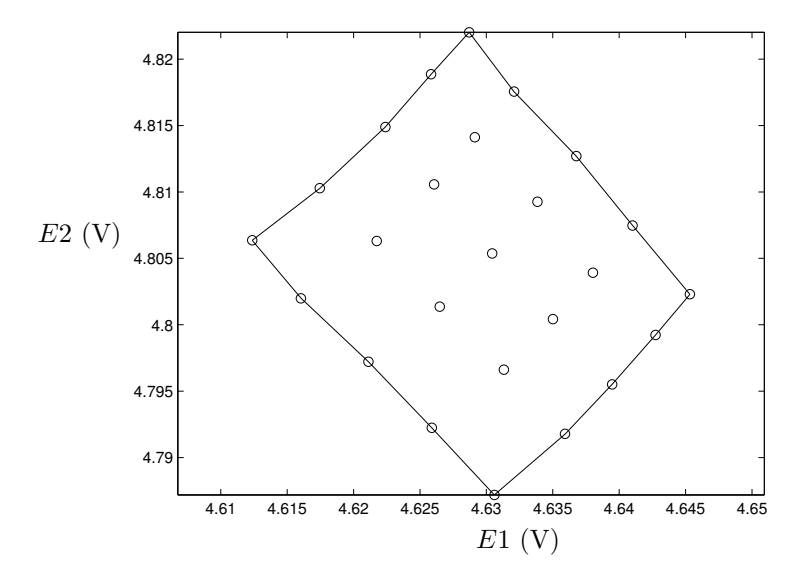


FIGURE 4. A typical calibration of a cross-wire. The circles are measured points and the solid lines represent the border of the calibration area.



FIGURE 5. The flow angle probe. The horizontal direction is sensitive to flow angle of attack.

3. Results

In this section we will present results for some important measures of flow quality. The quantities presented are, in order of appearance, the total pressure variation, which is a measure of the streamwise flow uniformity over the measurement area, the temperature variation, the flow angularity, which is a measure of how parallel the flow is and the turbulence intensities in both the streamwise and the two cross stream directions.

The measurement area $(900 \times 500 \text{ mm}^2)$ leaves out a rim of 150 mm along the test section walls where the flow is affected by the proximity of the walls. The streamwise position of the measurements is 400 mm downstream of the test section inlet. This position was chosen because it is far enough upstream to minimize disturbances from the test section walls and far enough downstream to allow the flow to relax after the high strain encountered in the contraction.

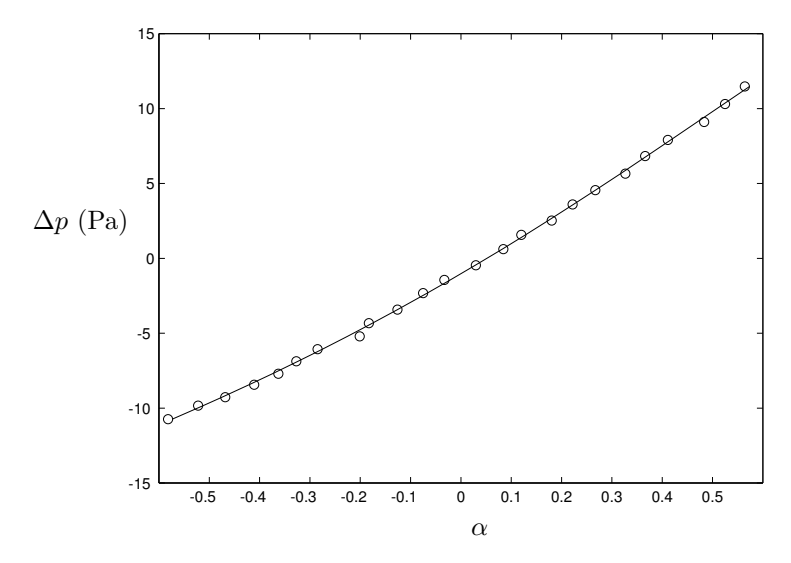


FIGURE 6. A typical calibration of a flow angle probe. The circles are measured points and the solid line is the fitted curve.

Most results are presented as contour plots with solid lines indicating positive values and dashed lines negative values. These figures are orientated so that the flow is into the paper sheet, i.e. we are looking in the downstream direction.

In measurements of this kind with very low fluctuations and very small mean variations it is very difficult to achieve accurate absolute and relative measures. This is partly because of the limitations in accuracy and resolution of the instrumentation such as pressure transducers, anemometers, multimeters and sensors. Measurement noise problems associated with high gains are also encountered. The accuracy of the location of the contours in the figures presented below are varying slightly between repeated measurements but the trends and the average values given in the figures were found to be the same.

3.1. Total pressure

The total pressure variation over the cross section area of the test section is a good measure of the mean velocity variation. A variation of e.g.~0.1% in total pressure corresponds to a variation of 0.05% in streamwise velocity. From the total pressure in the test section, $p_{\rm test}$, the total pressure in the stagnation chamber, $p_{\rm stag}$, is subtracted to form the pressure difference measured by the differential pressure transducer in the experiments. The measured pressure is

then divided by the dynamic pressure at the center of the measurement area, q_{test} , to form the dimensionless measure of the total pressure variation,

$$\frac{\Delta p_{\text{test}}(y, z)}{q_{\text{test}}} = \frac{p_{\text{test}}(y, z) - p_{\text{stag}}}{q_{\text{test}}}$$
(11)

where y and z are the vertical and horizontal directions.

The variation in total pressure was measured at three different test section velocities, 10 m/s, 25 m/s and 40 m/s. The results are shown in figure 7 with dashed lines corresponding to negative values and solid lines positive values.

At a test section speed of 10 m/s, (figure 7a), the variation of the total pressure is less than $\pm 0.10\%$. All contour curves here represent negative values contrasting with figures corresponding for the higher free-stream velocities. One reason for this could be that the accuracy of the absolute pressure measured by the pressure transducer is not high enough resulting in a constant pressure error. Another reason might also be that the pressure-loss in the contraction is relatively speaking higher in this case than at the other test section velocities. This is however contradicted by the fact that there is more positive contours for the 25 m/s case (figure 7b) than at the 40 m/s case (figure 7c).

At a test section speed of 25 m/s, (figure 7b), the variation in total pressure is less than $\pm 0.06\%$ over the measurement region. Note that the total pressure is higher in the left hand side and lower in the right hand side of the figure indicating that there is a velocity gradient in the horizontal direction over the cross section area. Although the gradient is small it is seen in repeated measurements. The maximum variation in total pressure variation is well within the expected limits.

At a test section speed of 40 m/s, (figure 7c), the variation in total pressure is very similar but slightly higher than for the 25 m/s case with a maximum variation of $\pm 0.09\%$. The gradient in the horizontal direction found for the 25 m/s case is also found at 40 m/s.

The overall results for the total pressure variation is very good with a maximum variation of less than $\pm 0.1\%$ over the velocity range studied. The results compare well with the findings in Johansson (1992) where the maximum variation was reported to be less than $\pm 0.1\%$. The flow uniformity does not seem to have been affected in a negative way by the 10 years of operation of the wind-tunnel.

3.2. Temperature

The variation of temperature in the test section is of importance when temperature sensitive measurement techniques, such as hot-wire and hot-film anemometry, are used. The temperature in the MTL wind-tunnel varies with the same order of magnitude in both time and space. Long measurement times were used at each point in space for good averages and several measurements under

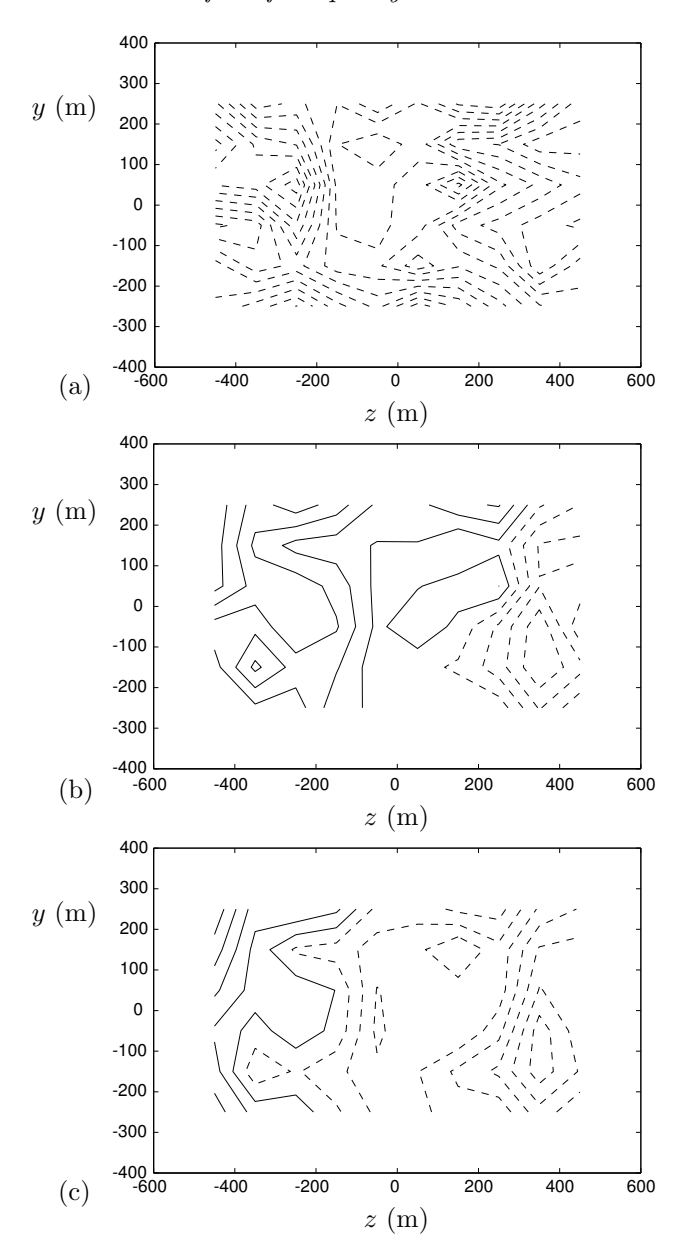


FIGURE 7. The total pressure variation over the cross section area of the test section at a free stream velocity of 10~m/s (top), 25~m/s (middle) and 40~m/s (bottom). Each line represents an increment of 0.01% with dashed lines representing negative values and solid lines positive values.

the same conditions were made to confirm the results. Although the position of each curve in the contour plots in figure 9 varies slightly between the measurements the trends are always similar confirming repeatability. The temperature contours presented in figure 9 are calculated as the temperature deviation from the mid-range value normalized by the mean temperature (in ${}^{\circ}$ C), *i.e.*

$$\Delta T = \frac{T(y,z) - \frac{1}{2} (T_{\text{max}}(y,z) + T_{\text{min}}(y,z))}{\overline{T(y,z)}},$$
(12)

where T is the temperature and y and z is the vertical and horizontal coordinates. The mid-range value is subtracted to give a clearer picture of the temperature variation in the figure. The mean temperature in the measurements is about $20^{\circ}\mathrm{C}$.

The temperature variation over the measurement area in the test section was measured at 10 m/s, 25 m/s and 40 m/s. The flow direction in the contour plots in figure 9 is into the paper sheet.

At 10 m/s the variation in temperature was less than $\pm 0.2\%$ or $\pm 0.04^{\circ}$ C, see figure 9a. This is a very small difference with the maximum temperature peak at about z=-250 mm and y=50. This peak is also found at the other two tunnel speeds at a similar position. As was the case for the total pressure measurements the variation of the temperature over the cross section area at this low velocity differs from the higher velocity cases. The trend in figure 9 was confirmed by repeated measurements.

The variation in time is for the same test section velocity $\pm 0.04^{\circ}$ C, see figure 8a. This variation is of the same magnitude as the variation over the cross section area. The variation in time has a typical period of 300 s sometimes interrupted by longer periods of more constant temperature. A hot-wire sampling time seldom exceeds 30 s which is one tenth of a period. A measurement can therefore occur at any time in the period. A hot-wire usually has a temperature of almost two hundred degrees making the errors small even between samples taken at times coinciding with the high and low extreme points in the temperature oscillation.

At a test section speed of 25 m/s the temperature variation in space over the measurement area was $\pm 0.25\%$, or $\pm 0.05^{\circ}\mathrm{C}$ see figure 9b. Here we find the peak also present in the 10 m/s case at z=-350 mm and y=50. Furthermore, it can be seen that the upper right corner is cooler than the lower left corner. A possible reason could be that the cooling water enters in the top right corner and at the middle right side and that it exits at the lower right corner and the middle right side.

The variation in time over a period of 3 hours was ± 0.05 °C, see figure 8b, which is slightly higher than at the test section velocity of 10 m/s. The higher temperature at the beginning in figure 8b is ignored because it is remains from

the settling time of the cooling system. The period of the fluctuation is about 170 s which is almost half the period found at 10 m/s.

At the highest test section speed of 40 m/s the variation in space increased further to a value of $\pm 0.35\%$, see figure 9c, or $\pm 0.07^{\circ}$ C. The pattern of variation is very similar to the one found at 25 m/s and the peak at z=-350 mm and y=50 is still present.

The variation in time was about $\pm 0.05^{\circ}$ C which is slightly higher than for the 25 m/s case, see figure 8c. The fluctuation period is here also 170 s. Overall the similarity between the 25 m/s and the 40 m/s cases are strong. One difference however is the increasing amplitude in the short time fluctuations seen as a thickening of the line with increasing speed in figure 8. This is caused by the slow response time of the cooling system and it is the result of too long piping between the heat exchangers and the constant flow rate of the cooling water.

Comparing with the first study by Johansson (1992), that found a temperature variation of $\pm 0.2^{\circ}$ C, the variation has improved mainly due to a better system regulator. It is important to notice that the regulator, in this case, was not calibrated for each speed separately. This means that it probably is possible to get a slightly steadier temperature in time than what is presented here. However, the process of finding the best calibration constants for the regulator is rather time consuming. Therefore we did not do it here making our results a better representation for the temperature variations found in a typical MTL wind-tunnel experiment.

The settling time for the temperature, *i.e.* the time it takes to reach the desired temperature in the test section with minimum fluctuations in time from a new start of the wind-tunnel is fairly long. *E.g.* at a test section velocity of 25 m/s it takes approximately 30 minutes to stabilize the temperature. The reason for these long settling times is the simple type of regulator used at the moment in the tunnel, (PID) and the long piping between the regulator valve and the heat exchanger. There have been a discussion of improving this system in the future. A software based regulator with increased input information and improved piping is used in a newly built wind-tunnel at the department, see Lindgren & Johansson (2002), and it has the potential to shorten the settling time and decrease the temperature variation from the values found here in the MTL wind-tunnel.

3.3. Flow angularity

The flow angularity is a measure of the straightness of the flow *i.e.* the ratio between the two cross flow velocities and the streamwise velocity. The flow angle is calculated by measuring the pressure difference of two symmetrically placed holes on a special probe, see section 2.2.3. By rotating the probe 90°

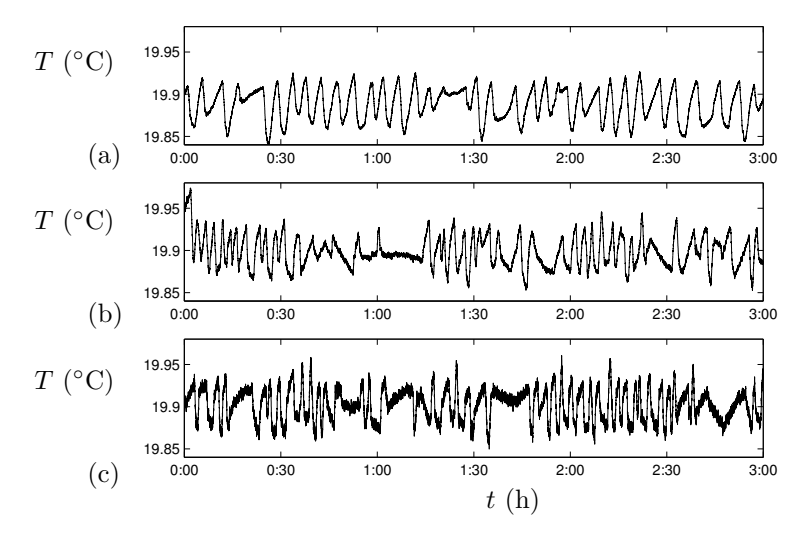


FIGURE 8. The temperature variation in time in the center of the test section cross section area at a free stream velocity of 10 m/s (top), 25 m/s (middle) and 40 m/s (bottom).

both cross stream components, α in the vertical direction and β in the horizontal direction, could be measured at the same position. The mean flow angle was then subtracted from the measured values giving a relative measure of the flow angularity. It is very difficult to exactly define which direction should give zero flow angularity since the test section walls are not completely parallel. Through the subtraction however we find important information on vortices and the flow pattern over the measurement area. The flow angularity is here defined as

$$\alpha(y,z) = \alpha_{\rm m}(y,z) - \overline{\alpha_{\rm m}(y,z)} \tag{13}$$

$$\beta(y,z) = \beta_{\rm m}(y,z) - \overline{\beta_{\rm m}(y,z)} \tag{14}$$

where the index m indicates measured values.

The flow angularity was measured at the three test section speeds 10 m/s, 25 m/s and 40 m/s. The pattern and magnitude of the arrows are similar at all three velocities indicating that the flow pattern is fairly independent of the velocity, see figure 10. The maximum magnitude of the arrows is about 0.25° at the edge of the measurement area and close to zero at the center. The measurements clearly reveals a flow pattern where the fluid expands from the center towards the test section walls.

Note that the probe was calibrated in the center of the test section with zero angularity in a direction that by eye sight was thought to be the mean

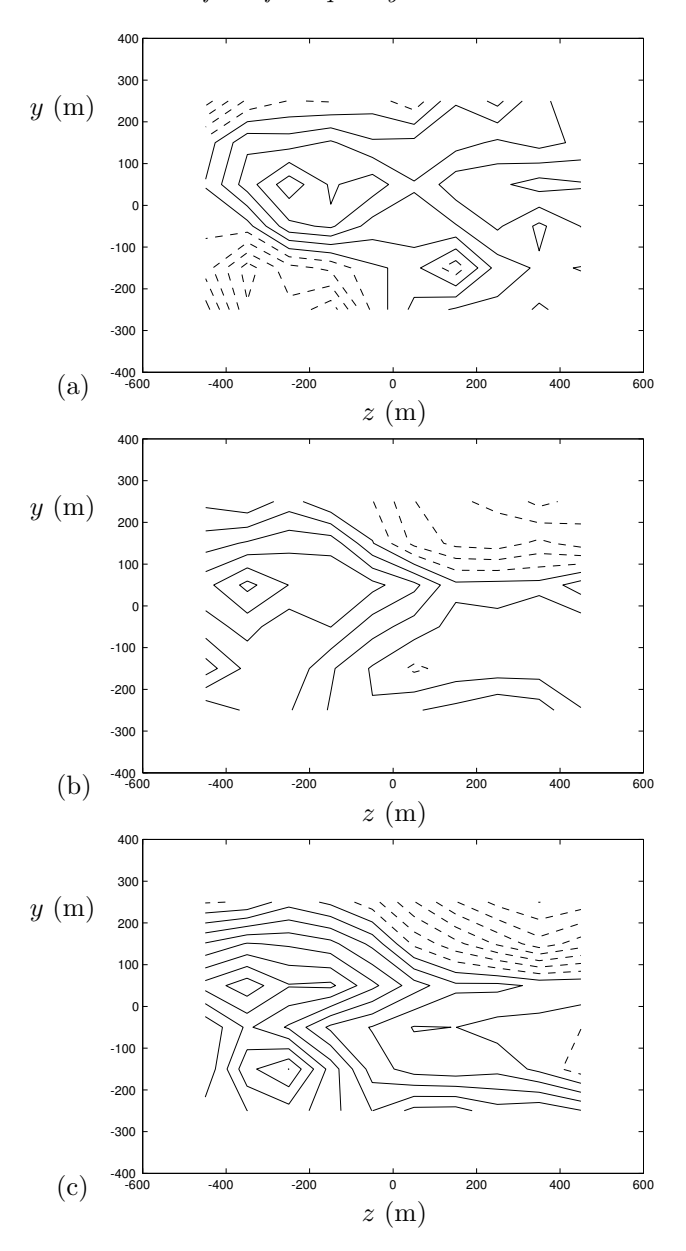


FIGURE 9. The temperature variation over the measurement area of the test section at a free stream velocity of $10~\mathrm{m/s}$ (top), $25~\mathrm{m/s}$ (middle) and $40~\mathrm{m/s}$ (bottom). Each line represents an increment of 0.05% with dashed lines representing negative values and solid lines positive values.

flow direction. However, from the calibration curve, see figure 6, it can be seen that this direction does not represent zero pressure difference.

There are several possible reasons for this result. First there is an actual expansion of the width of the test section, equal to 5 mm in 500 mm length or 0.06°, at the streamwise position where the measurements were performed. However this is partly compensated for by the boundary layer growth which is between 1.4 mm and 1.8 mm on each wall in the velocity range used here. There is also a slight variation in the height of the test section since the upper and lower walls are adjustable to compensate for wall boundary layer growth making it difficult to position them absolutely parallel. The slit in the roof, allowing the traversing sword to enter the test section, is not sealed allowing air to exit the test section due to the positive pressure encountered over the slit.

Johansson (1992) encountered flow angularities well below 0.1° . This value is much lower than the ones found in this study. The main reason for the large increase in flow angularity is probably that the slit in the Johansson (1992) study was completely sealed. During our measurements we opted for an open slit since this is the case for most experiments taking place in the MTL wind-tunnel. The rather large expansion of the width of the test section, 5 mm from the inlet to the measurement position, has not been reported earlier and it will also contribute to an outwards directed flow. This expansion could be caused by swelling of the plywood test section walls as wood is a material that easily changes shape and size with e.q. moisture and temperature.

3.4. Turbulence intensity

A very important aspect of wind-tunnel flow quality is the level of turbulence intensity in the test section. Low free stream turbulence levels are essential in transition related experiments where all flow disturbances should be created and controlled by the experimentalist. Also in other types of flow experiments the level of free stream turbulence could be of importance. The turbulence intensities in the three spatial directions are simply defined as

$$I_{\rm x} = \frac{u_{\rm rms}}{U},\tag{15}$$

$$I_{\rm y} = \frac{v_{\rm rms}}{II},\tag{16}$$

$$I_{\rm z} = \frac{w_{\rm rms}}{U},\tag{17}$$

where the streamwise mean velocity, U, is used for normalization of the rms data.

When comparing the level of turbulence intensity from different windtunnel studies it is important to consider the amount of high-pass filtering of the data. Normally high-pass filters are applied to remove contributions to

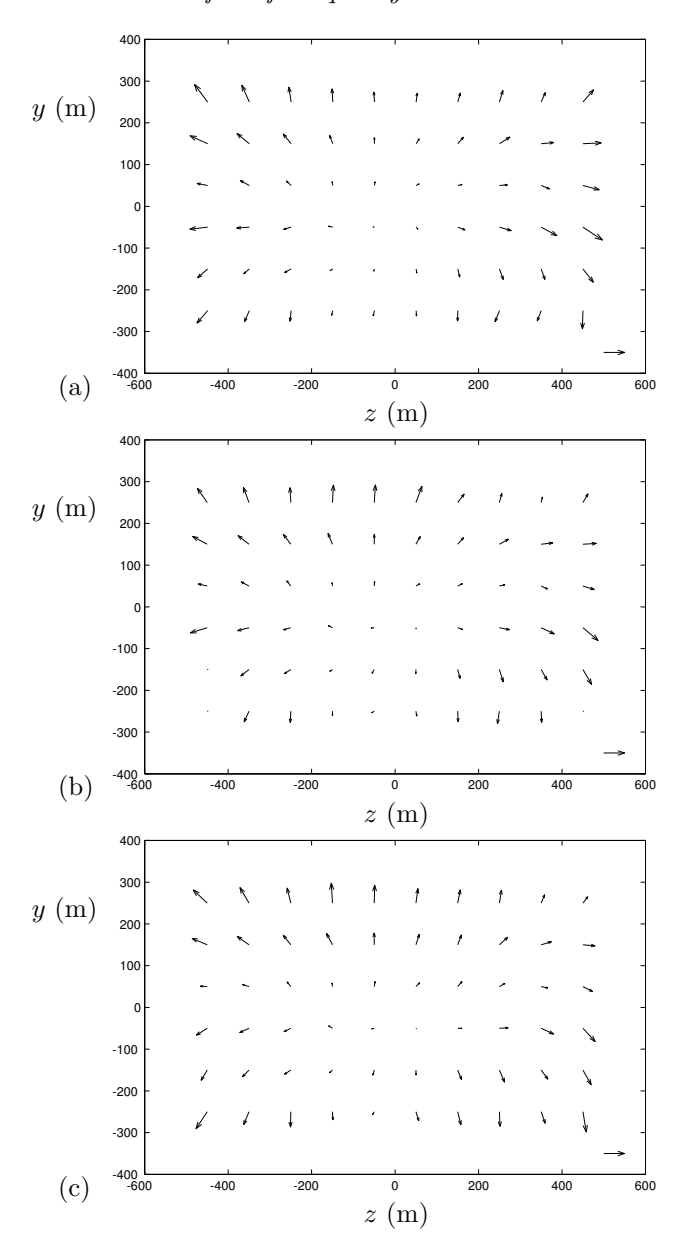


FIGURE 10. The cross flow direction over the cross section area of the test section at a free stream velocity of 10 m/s (top), 25 m/s (middle) and 40 m/s (bottom). The horizontal arrows at the lower right corner of the figures represents an angle of 0.25° .

the turbulence intensity from low frequency waves traveling the wind-tunnel circuit. The cut-off frequency is always chosen in a somewhat arbitrary manner. In this case we wanted all disturbances with wave lengths fitting in the test section cross section area to be conserved. Allowing for some margin we chose the wave length as the sum of the two test section side lengths, *i.e.* the cut-off wave length was chosen to be 2.0 m. A large part of the fluctuating energy is found at low frequencies which means that the filter can easily reduce the rms value by 50%. In this section the results will be provided for both unfiltered and high-pass filtered data, to simplify comparisons with results from other wind-tunnels and to visualize the impact of the filtering.

The cut-off frequency, f_c , is calculated from the free stream mean velocity, U and the cut-off wave length, λ_c as follows

$$f_{\rm c} = \frac{U}{\lambda_{\rm c}}.\tag{18}$$

The rms values are calculated by summation of the square of the absolute value of the Fourier transforms from the time signal. The high-pass filtering is applied by summing only over the frequencies above the cut-off frequency. The rms values for the three velocity components thus read

$$u_{\rm rms} = \left(2\sum_{k=N_{\rm c}}^{N/2} |X_i|^2\right)^{\frac{1}{2}},\tag{19}$$

$$v_{\rm rms} = \left(2\sum_{k=N_c}^{N/2} |Y_i|^2\right)^{\frac{1}{2}},$$
 (20)

$$w_{\rm rms} = \left(2\sum_{k=N_{\rm c}}^{N/2} |Z_i|^2\right)^{\frac{1}{2}},\tag{21}$$

where X, Y and Z are the Fourier transforms corresponding to the velocity time signals u(x,y;t)-U(x,y), v(x,y;t)-V(x,y) and w(x,y;t)-W(x,y). N is the total number of samples and N_c is the summation index, k, corresponding to the frequency f_c .

The turbulence intensities were measured at the three different wind-tunnel speeds, 10 m/s, 25 m/s and 35 m/s. Note the change in velocity from 40 m/s to 35 m/s for the highest test section speed case compared to the previous results presented in this section. The reason for this is the influence from vibrations and acoustic noise from the probe holder devices at high speeds. The flow disturbances are very small and have much of their energy at low frequencies, typical also of vibrating stings, making it increasingly important to avoid these

vibrations. The high-pass filtering could help removing vibrations. However, there is no guarantee that these measurements are fully free from unwanted disturbances.

In the earlier study by Johansson (1992), measurements up to 60 m/s were obtained using another more rigid traversing arm. The increased flexibility and maneuverability of the traversing arm has here been exchanged with a lower maximum test section speed. The cut-off wave length in the Johansson (1992) study was 2.5 m which is slightly different from the one used in this study. This will have some effect on the results in the streamwise direction and less in the other two directions.

3.4.1. Streamwise turbulence intensity

The streamwise turbulence intensity varies with tunnel speed being higher at low velocities.

At 10 m/s the level of turbulence intensity is less than 0.04% (figure 11a), when high-pass filtering is applied in the manner described above. The turbulence intensity is in general low over the measurement area but some increase can as expected be found towards the walls where the wall generated turbulence influences the results. These values are slightly higher than those found in the Johansson (1992) study, where the streamwise turbulence intensity was reported to be below 0.03% at all speeds between 5 m/s and 60 m/s. A ridge of slightly higher turbulence intensity is found just right of the vertical centerline in figure 11a. This ridge of unknown origin only appears at 10 m/s but can be found also for the two cross stream components. The total, unfiltered intensity is found to be less than 0.1% at 10 m/s (figure 11b) for this case.

At 25 m/s the streamwise turbulence intensity is less than 0.025% with higher values found towards the corners of the measurement region (figure 11c). This value compares well with the one found by Johansson (1992). The total unfiltered intensity is less than 0.08% (figure 11c).

At a tunnel speed of 35 m/s the streamwise turbulence intensity is less than 0.025%, see figure 11e. As in the 25 m/s case it is in one corner of the measurement area that the turbulence intensity exceeds 0.02%. At this velocity the results also compare well with the results found by Johansson (1992). The unfiltered intensity is less than 0.1%, see figure 11f, although it is very similar to the 25 m/s case in most of the measurement area except for one peak reaching above 0.08%.

As can be seen in the unfiltered data, (figures 11 b, d, f), the contours are not very smooth. The reason for this might be that the low frequency disturbances are not averaged over long enough time to give smoothly varying results. The sampling time of one minute at each point was set long enough to resolve the structures of the filtered signal.

No unfiltered data are available in the Johansson (1992) paper leaving us without comparisons here. However it seems that the unfiltered streamwise turbulence intensity has increased somewhat over the years. This can be the result of dirt accumulation in honeycomb, screens and heat exchanger. Partly due to the increase in the usage of smoke recently for LDV, PIV and visualization measurements and to changes in fan blade angles for high pressure-loss experiments. After these measurements were completed it was found that there was an error in the manufacturing of the fan bearings leading to their destruction. The bearings have now been changed making the fan run more smoothly. A thorough cleaning of the tunnel and tuning of the fan blade angles would probably improve the unfiltered turbulence intensity results.

3.4.2. Cross-stream turbulence intensity

The cross-stream turbulence intensities are expected to be slightly higher than the streamwise turbulence intensity because the damping of disturbances are much higher in the streamwise direction through the screens and contraction. This is also observed if only filtered data is considered. The low frequency disturbances related to the traveling waves in the wind-tunnel circuit appears only in the streamwise component and constitute a considerable contribution making the unfiltered streamwise turbulence intensity higher than its unfiltered cross flow counterparts. At low test section speeds ($< 10 \, \text{m/s}$) the filtered cross flow turbulence intensity is of the same magnitude as the streamwise turbulence intensity. At higher test section speeds the cross-flow components are slightly higher than the streamwise one.

At 10 m/s the filtered vertical and horizontal turbulence intensities are less than 0.04% and 0.05% respectively, see figures 12a and 13a. The vertical ridge slightly to right of the centerline found in the filtered streamwise case is also present for both the vertical and the horizontal turbulence intensities. For the unfiltered case, the cross-stream turbulence intensities are less than 0.05%, see figures 12b and 13b. The effect of the high-pass filter is here almost negligible indicating that most disturbances are contained in higher frequencies than the cut-off frequency. This was expected from the reasoning above about low frequency traveling waves around the wind-tunnel circuit. An enlargement of the center region of very low turbulence intensity is the only difference between filtered and unfiltered data.

At 25 m/s the filtered vertical and horizontal turbulence intensities are less than 0.035% and 0.03% respectively, see figures 12c and 13c. The corresponding unfiltered values are both 0.04%, see figures 12d and 13d. Here, as for the 10 m/s case the difference between filtering and non-filtering is very small. Apart from the values in the corners the horizontal and vertical turbulence intensities are even lower than the numbers stated above.

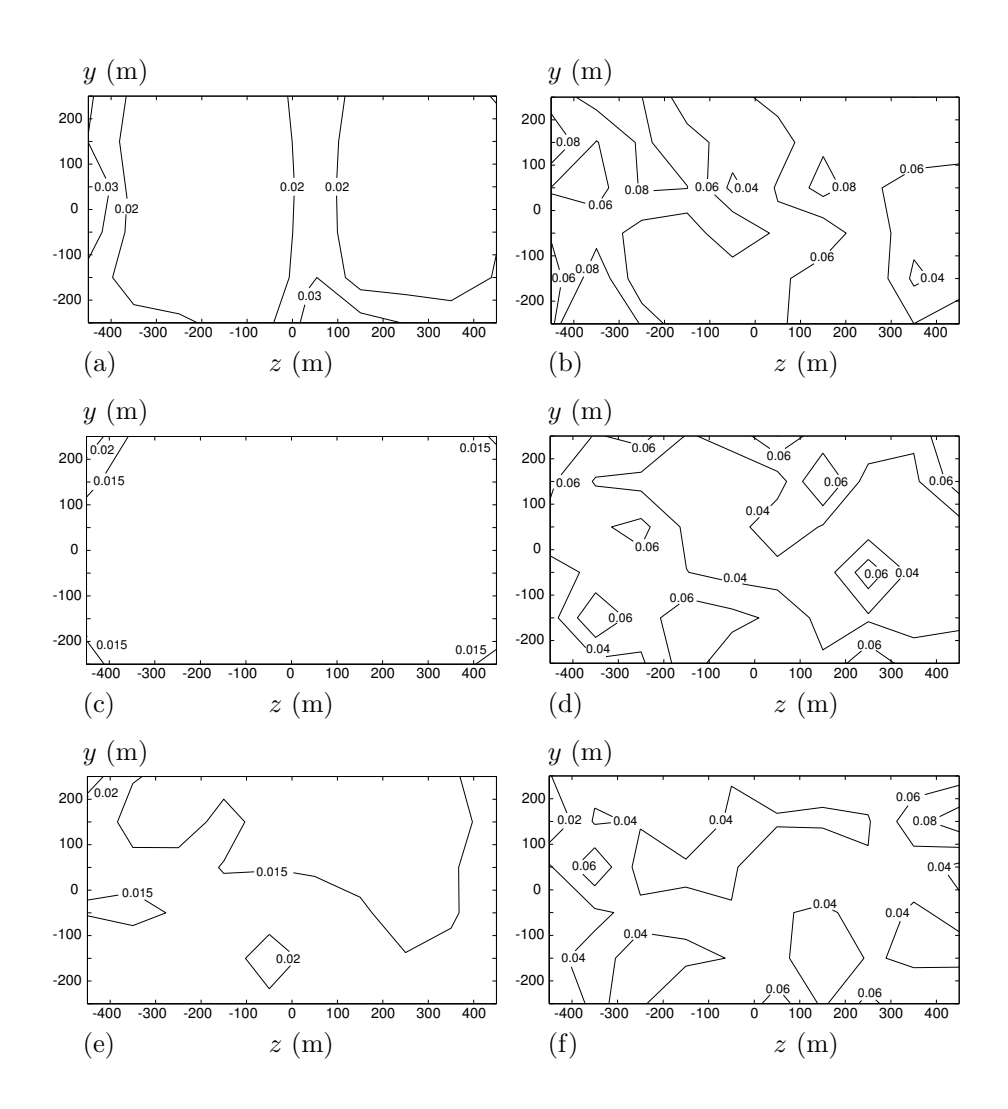


FIGURE 11. The streamwise turbulence intensity variation in % over the cross section area of the test section at a free stream velocity of 10 m/s (top), 25 m/s (middle) and 35 m/s (bottom). The left column represents the high pass filtered data with $U/f_{\rm c}=2.0$ m and the right column represents unfiltered data.

At 35 m/s the filtered results for the vertical and horizontal turbulence intensity components are less than 0.04% and 0.03% respectively, see figures 12e and 13e. Their unfiltered counterparts are less than 0.04% and 0.05%, see also figures 12f and 13f. The larger difference between filtered and unfiltered values for the horizontal component is the result of high unfiltered turbulence intensity in the upper left corner. Neglecting this corner reduces the difference to the values found for the other velocity cases.

In general the results for the cross flow turbulence intensities are well below the design criteria specified to the manufacturer of 0.09% also cited in Johansson (1992). There, the filtered cross-stream components were reported to be less than 0.06% in the velocity span of 5 to 60 m/s which is larger than the results presented here. The cross flow turbulence intensities increased also with increasing speed. This was not confirmed by this study where the cross flow turbulence intensities were more or less independent of test section speed. However the limited maximum velocity of 35 m/s used here is far from the 60 m/s maximum velocity reported by Johansson (1992) and the cross flow turbulence intensities might well increase with higher test section speeds.

The cross-stream turbulence intensity does not seem to have changed much over the years This is natural since wear on the driving unit and dirt deposition in screens etc mostly effects the pressure-loss and pressure waves which are directly related to the streamwise component.

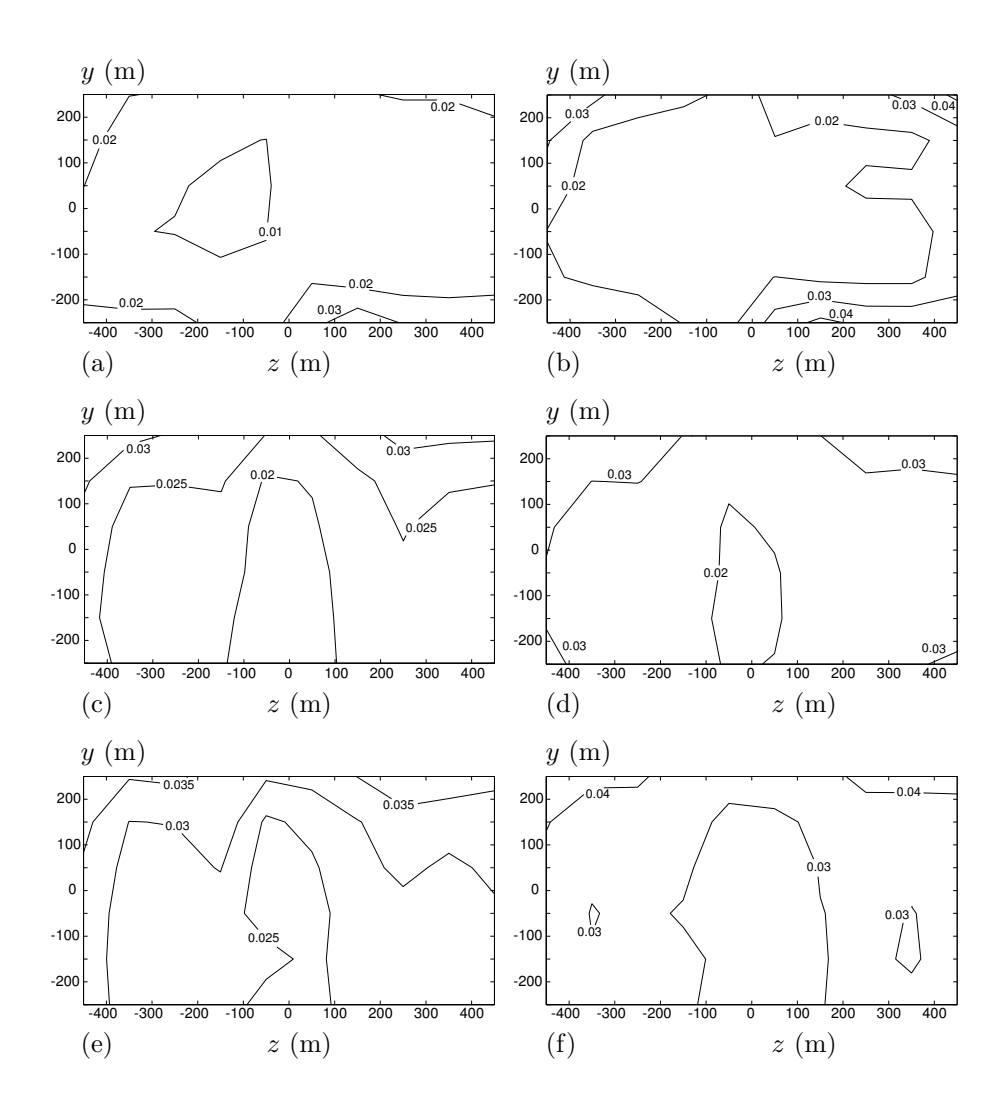


FIGURE 12. The vertical cross-stream turbulence intensity variation over the cross section area of the test section at a free stream velocity of 10 m/s (top), 25 m/s (middle) and 35 m/s (bottom). The left column represents the high pass filtered data with $U/f_{\rm c}=2.0$ m and the right column represents unfiltered data.

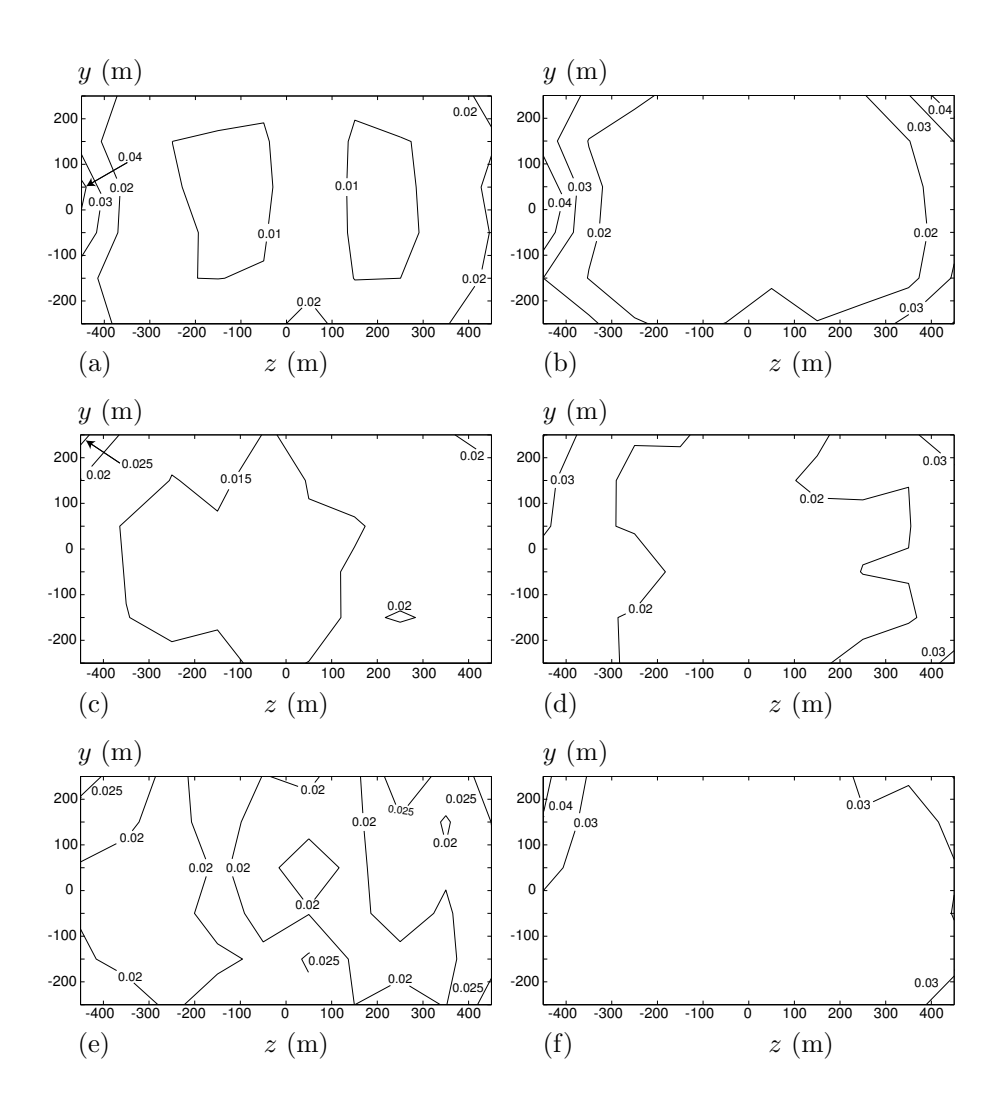


FIGURE 13. The horizontal cross-stream turbulence intensity variation over the cross section area of the test section at a free stream velocity of 10 m/s (top), 25 m/s (middle) and 35 m/s (bottom). The left column represents the high pass filtered data with $U/f_{\rm c}=2.0$ m and the right column represents unfiltered data.

4. Concluding remarks

The flow quality in the MTL wind-tunnel at the Department of Mechanics, KTH has been investigated. It was also studied in connection with the construction of the wind-tunnel. The results from these early measurements are reported in Johansson (1992). The reason for performing new measurements were both to improve the documentation of the flow quality and to investigate how the flow quality has changed after 10 years of extensive use of the facility. In the new experiments the same quantities as in the early experiment have been measured except for static pressure variations over the test section measurement area. It was measured in the early experiment but left out here due to the high difficulty in achieving results not influenced by changes in dynamic pressure.

The total pressure variation over the test section cross section area is less than $\pm 0.06\%$ at a test section speed of 25 m/s and slightly larger at 10 m/s and 40 m/s. These results are well in line with those found earlier by Johansson (1992) that reported a total pressure variation of less than $\pm 0.1\%$ over a test section velocity range of 5 to 60 m/s. The variation in total pressure variation has not been severely effected by time.

The temperature variation over the measurement area was found to be less than ± 0.05 °C, (at 25 m/s), which is substantially smaller than the initial findings by Johansson (1992) of ± 0.2 °C, due to a better control of the cooling system.

The temporal variation of the temperature is less than ± 0.04 °C at a test section speed of 10 m/s and ± 0.05 °C at test section speeds of 25 m/s and 40 m/s. The temperature variation in time is thus similar to the variation in space.

The flow angularity was measured over the measurement area using a special probe that is very sensitive to a change in position of the stagnation point. The results show a maximum deviation of 0.25° at the edges of the measurement area at all test section velocities. The flow is directed outwards towards the test section walls around the measurement area edge. The reason for this outwards directed flow is an increase in the cross section area of the test section in the vicinity of the downstream measurement position, partly compensated for by boundary layer growth, and the unsealed slit in the upper wall allowing air to flow out from the test section where the static pressure is slightly larger than the atmospheric pressure outside. A comparison with the earlier measurements by Johansson (1992) shows that the flow angle variation observed in the present investigation is substantially larger, partly because of the introduction of the traversing system. The maximum flow angularity was in the early study below 0.1° .

The turbulence intensity has been measured in the streamwise and the vertical and horizontal cross-stream directions. At a test section velocity of 25

m/s the streamwise turbulence intensity was found to be less than 0.025% and the vertical and horizontal cross-stream turbulence intensity components was less than 0.035% and 0.03% respectively. Here, the data was high-pass filtered removing structures with wave lengths longer than 2.0 m. At the other speeds investigated (10 and 35 m/s) the intensities were found to be somewhat higher.

These results compares well with those found by Johansson (1992) and they are within the original design criteria. The unfiltered streamwise turbulence intensity is higher than what was expected but it can probably be lowered by adjusting the fan blade angles and cleaning the wind-tunnel screens, guide vanes and heat exchanger.

In general the MTL wind-tunnel still has an overall flow quality to well justify the name, Minimum Turbulence Level. Some deterioration has been noticed mainly in flow angularity and unfiltered turbulence levels. These problems are though thought to be of such nature that a minor overhaul could well be enough to restore the initial performance. The general flow quality indicates a good potential for the MTL wind-tunnel to be a high-quality tool in transition and turbulence research also for the coming ten years. The increased use of optical measurement methods, such as LDV and PIV requiring seeding, implies an increased need for regular cleaning of the interior of the tunnel.

5. Acknowledgment

The authors would like to thank Valeria Durañona from the Technical University of Uruguay, Montevideo, Uruguay, for assistance in some of the measurements. Further thanks goes to Ulf Landén for his aid in manufacturing the measurement equipment. Henrik Alfredsson is gratefully acknowledged for many comments on the manuscript and for sharing the main responsibility of the planning and design of the MTL wind-tunnel with the second author. Finally financial support from the Swedish Research Council for the first author is gratefully acknowledged.

References

- Baines, W. & Peterson, E. 1951 An investigation of flow through screens. *Trans.* ASME 73, 467–480.
- BOIKO, A. V., WESTIN, K. J. A., KLINGMANN, B. G. B., KOZLOV, V. V. & ALFREDSSON, P. H. 1994 Experiments in a boundary layer subjected to free-stream turbulence. Part 2. The role of TS-waves in the transition process. *J. Fluid Mech* **281**, 219–245.
- BORGER, G. G. 1976 The optimization of wind tunnel contractions for the subsonic range. *Tech. Rep.* TTF 16899. NASA.

- DOWNIE, J. H., JORDINSON, R. & BARNES, F. H. 1984 On the design of threedimensional wind tunnel contractions. J. Royal Aeronautical Society pp. 287– 295.
- ELOFSSON, P. A. & ALFREDSSON, P. H. 1998 An experimental study of oblique transition in plane poiseuille flow. *J. Fluid Mech* **358**, 177–202.
- Groth, J. & Johansson, A. V. 1988 Turbulence reduction by screens. J. Fluid Mech 197, 139–155.
- HÄGGMARK, C. P., BAKCHINOV, A. A. & ALFREDSSON, P. H. 2000 Experiments on a two-dimensional laminar separation bubble. *Phil. Trans. R. Soc. Lond. A* 28.
- Johansson, A. V. 1992 A low speed wind-tunnel with extreme flow quality-design and tests. *Proc. the 18:th ICAS Congress* pp. 1603–1611.
- Johansson, A. V. & Alfredsson, P. H. 1988 Experimentella metoder i strömningsmekaniken. Department of Mechanics, Royal Institute of Technology.
- LAWS, E. & LIVESEY, J. 1978 Flow through screens. Ann rev Fluid Mech. 10, 247–266.
- LIN, J. C., SELBY, G. V. & HOWARD, F. G. 1991 Exploratory study of vortexgenerating devices for turbulent flow separation control. In 29th AIAA Aerospace Sciences Meeting, Reno, Nevada. AIAA paper 91-0042.
- LINDGREN, B. & JOHANSSON, A. V. 2002 Design and calibration of a low-speed windtunnel with expanding corners. TRITA-MEK 2002:14. Department of Mechanics, KTH.
- LOEHRKE, R. I. & NAGIB, H. M. 1976 Control of free-stream turbulence by means of honeycombs: A balence between suppression and generation. *J. Fluids Engineering* pp. 342–353.
- Lumley, J. L. 1964 Passage of turbulent stream through honeycombs of large length-to-diameter ratio. *Trans. ASME, J. Basic Engineering* **86**, 218–220.
- MATSUBARA, M. & ALFREDSSON, P. H. 2001 Disturbance growth in boundary layers subjected to free stream turbulence. *J. Fluid Mech.* **430**, 149–168.
- MIKHAIL, M. N. & RAINBIRD, W. J. 1978 Optimum design of wind tunnel contractions, paper 78-819. In AIAA 10th Aerodynamic Testing Conference.
- ÖSTERLUND, J. M. 1999 Experimental studies of zero pressure-gradient turbulent boundary-layer flow. PhD thesis, Department of Mechanics, Royal Institute of Technology, Stockholm.
- ÖSTERLUND, J. M. & JOHANSSON, A. V. 1999 Turbulent boundary layer experiments in the MTL wind-tunnel. TRITA-MEK 1999:16. Department of Mechanics, KTH.
- ÖSTERLUND, J. M., JOHANSSON, A. V., NAGIB, H. M. & HITES, M. H. 2000 A note on the overlap region in turbulent boundary layers. *Phys. Fluids* 12, 1–4.
- Sahlin, A. & Johansson, A. V. 1991 Design of guide vanes for minimizing the pressure loss in sharp bends. *Phys. Fluids A* 3, 1934–1940.
- Scheiman, J. & Brooks, J. D. 1981 Comparison of experimental and theoretical turbulence reduction from screens, honeycomb and honeycomb-screen combinations. *JAS* 18, 638–643.
- SEIDEL, M. 1982 Construction 1976-1980. Design, manufacturing, calibration of the

- German-Dutch wind tunnel (DNW). Tech. Rep.. Duits-Nederlandese Windtunnel (DNW).
- SJÖGREN, T. & JOHANSSON, A. V. 1998 Measurement and modelling of homogeneous axisymmetric turbulence. J. Fluid Mech 374, 59–90.
- Tan-Atichat, J., Nagib, H. M. & Loehrke, R. I. 1982 Interaction of free-stream turbulence with screens and grids: a balance between tubulence scales. *J. Fluid Mech.* 114, 501–528.
- Taylor, G. & Batchelor, G. K. 1949 The effect of wire gauze on small disturbances in a uniform stream. *Quart. J. Mech. and App. Math.* 2, part 1,1.
- WESTIN, K. J. A., BOIKO, A. V., KLINGMANN, B. G. B., KOZLOV, V. & ALFREDSSON, P. H. 1994 Experiments in a boundary layer subjected to freestream turbulence. Part 1. Boundary layer structure and receptivity. J. Fluid Mech 281, 193–218.
- Wikström, P. M., Hallbäck, M. & Johansson, A. V. 1998 Measurements and heat-flux transport modelling in a heated cylinder wake. *Int. J. Heat and Fluid Flow* 19, 556–562.

Appendix

Here follows a list of the Doctoral and Licentiate theses so far produced at the Department of Mechanics, KTH, where experiments performed in the MTL wind-tunnel are included. There is also a list of selected papers, not included in a thesis, based on experiments in the MTL tunnel.

Doctoral theses in chronological order

- 1. JOHAN GROTH, On the modeling of homogeneous turbulence, 1991, ISRN KTH/MEK/TR-91/00-SE.
 - Groth's thesis includes work on screen turbulence which was used in determining the size and number of screens to have in the MTL wind-tunnel. These results are also published in Groth & Johansson (1988).
- TORBJÖRN SJÖGREN, Development and calibration of turbulence models through experiment and computation, 1997,

ISRN KTH/MEK/TR-97/05-SE.

- Torbjörn Sjögren performed the first experiment where the pressurestrain rate term in (statistically) axisymmetric turbulence was directly measured. These results are also presented in Sjögren & Johansson (1998).
- 3. JOHAN WESTIN, Laminar turbulent boundary layer transition influenced by free stream turbulence, 1997,

ISRN KTH/MEK/TR-97/10-SE.

- Results concerning non-parallel effects on boundary-layer stability were found and these results are reported in Westin $et\ al.\ (1994)$ and Boiko $et\ al.\ (1994)$.
- 4. PER ELOFSSON, Experiments on oblique transition in wall bounded shear flows, 1998, ISRN KTH/MEK/TR–98/05–SE.
 - Per Elofsson made investigations of the role of oblique transition in Poiseuille and Blasius flows which are reported in Elofsson & Alfredsson (1998).
- PETRA WIKSTRÖM, Measurements, direct numerical simulation and modeling of passive scalar transport in turbulent flows, 1998, ISRN KTH/MEK/TR-98/11-SE.
 - Experiments on passive scalars (temperature) in a cylinder wake were performed. Special care was taken to measure the Reynolds fluxes. See also Wikström *et al.* (1998).
- 6. JENS ÖSTERLUND, Experimental studies of zero pressure-gradient turbulent boundary layer flow, 1999, ISRN KTH/MEK/TR-99/16-SE. Jens Österlund established the log-law for z.p.g. turbulent boundary layer flow and determined new values for the Kármán and additive constants. These findings are reported in Österlund et al. (2000).

 CARL HÄGGMARK, Investigations of disturbances developing in a laminar separation bubble flow, 2000, ISRN KTH/MEK/TR-00/03-SE.

Investigations were made on highly instable high frequency two-dimensional waves in a laminar separation bubble, see Häggmark et al. (2000).

Licentiate theses in chronological order

- KRISTIAN ANGELE, PIV measurements in a separating turbulent APG boundary layer, 2000, ISRN KTH/MEK/TR-00/15-SE.
 This work focuses on scaling and structures of in a turbulent separation bubble.
- JENS FRANSSON, Investigations of the asymptotic suction boundary layer, 2001, ISRN KTH/MEK/TR-01/11-SE.
 This work is mainly focused on the study of the asymptotic suction boundary layer.

Selected papers in chronological order

Other papers, not included in a thesis from the Department of Mechanics, involving measurements in the MTL wind-tunnel are listed below.

- 1. Sahlin & Johansson (1991)
 Alexander Sahlin was part of the MTL aerodynamic design team. Among other things he developed the guide-vanes used in the present tunnel. He was also heavily involved in the calibration of the wind-tunnel.
- Matsubara & Alfredsson (2001)
 Matsubara has made experiments on instabilities and their growth in laminar boundary layers. Some of which are reported in the above cited paper.

Ongoing theses/post doc work

There are still work in process in the MTL wind-tunnel that will be published in the future. In the list below, the people currently involved in measurements in the MTL wind-tunnel, are listed in alphabetical order.

- 1. Kristian Angele, (Dr. thesis work) Title: Turbulent flow separation.
- 2. Jens H. M. Fransson, (Dr. thesis work)
 Title: Investigations of the asymptotic suction boundary layer.
- 3. Björn Lindgren, (Dr. thesis work)
 Title: Flow facility design and experimental studies of wall bounded turbulent shear-flows
- 4. Fredrik Lundell, (Dr. thesis work)
 Title: An experimental study of by-pass transition and its control.

- 5. Davide Medici, (Dr. thesis work)
 Title: Non-axisymmetric wakes and the possibility to optimize the power output of wind-turbine farms.
- 6. Shuya Yoshioka, (Post. Doc. work)
 Title: Boundary layer suction for reduction of friction drag.

Paper 4

 $\mathbf{P4}$

Flow structures in zero pressure-gradient turbulent boundary layers at high Reynolds numbers

By Jens M. Österlund, Björn Lindgren & Arne V. Johansson

Dept. of Mechanics, KTH, SE-100 44 Stockholm, Sweden

Submitted to Eur. J. of Mech. B/ Fluids

The near-wall region of zero-pressure gradient turbulent boundary layers was studied through correlation- and other two-point measurements over a wide range of Reynolds numbers. The requirements of high spatial resolution were met by use of a MEMS-type of hot-film sensor array together with a small, inhouse built hot-wire probe. Streak-spacing and characteristics of buffer region shear-layer events were studied. At high Reynolds numbers the motions that are of substantially larger scale than the streaks have a significant influence on the near-wall dynamics. By removing such scales through high-pass filtering a streak spacing was recovered that is close to that found in low Reynolds number flows. The frequency of occurrence of shear-layer events was found to scale with a mixed time scale, in analogy with earlier findings in channel flow, again indicating the increasing relative influence of large scales with increasing Reynolds number.

1. Introduction

The statistical, Reynolds averaged, description of turbulent boundary layers hides a wealth of structure-related phenomena with e.g. a quite intermittent character of the turbulence production. This has been illustrated in flow visualizations, measurements and from DNS-generated data in a large number of papers, see e.g. the landmark paper of Kline et~al.~(1967), who showed that a significant part of the turbulence could be described in terms of deterministic events. These studies showed that in the close proximity of the wall the flow is characterized by elongated regions of low and high speed fluid of fairly regular spanwise spacing of about $\lambda^+ = 100$. Sequences of ordered motion occur randomly in space and time where the low-speed streaks begin to oscillate and to suddenly break-up into a violent motion, a "burst". Kim et~al.~(1971) found the intermittent bursting process to be closely related to shear-layer like flow structures in the buffer region, and also roughly 70% of the total turbulence production to be associated with the bursting process. The "bursts" were further

investigated by Corino & Brodkey (1969) who divided the turbulence producing events into two kinds. The ejection: involving rapid outflow of low speed fluid from the wall and sweeps: large scale motions originating in the outer region approaching the wall. Smith & Metzler (1983) investigated the characteristics of low-speed streaks using hydrogen bubble-flow and a high-speed video system. They found that the streak spacing increases with the distance from the wall. Furthermore, they found the persistence of the streaks to be one order of magnitude larger than the observed bursting times associated with the near-wall region turbulence producing events.

Many different schemes have been proposed for the structure identification, using one or more components of the velocity or the wall-shear stress. The qualitative and quantitative features of the structures are then normally found through conditional averaging of the detected events as was first employed by Kovasznay et al. (1970). One should keep in mind, though, the unavoidable subjectivity inferred by the choice of detection. A comprehensive comparison between different schemes and the kind of events they identify can be found in Yuan & Mokhtarzadeh-Dehghan (1994). Wallace et al. (1972) and Willmart & Lu (1972) introduced the uv quadrant splitting scheme. Blackwelder & Kaplan (1976) developed the VITA technique to form a localized measure of the turbulent kinetic energy and used it to detect shear-layer events. The detected events were studied using conditional averaging. Chen & Blackwelder (1978) added a slope condition to the VITA technique to detect only events corresponding to rapid acceleration. The behavior of the conditionally averaged streamwise velocity detected on strong accelerating events may be explained by tilted shear-layers that are convected past the sensor. Kreplin & Eckelmann (1979) measured the angle of the shear-layer front from the wall and found that it was about 5° in the immediate vicinity of the wall. In the buffer region the inclination angle of the shear layer has been found to be about 15-20°. This angle is much smaller than that of typical outer-layer flow structures. Head & Bandyopadhyay (1981) found that angle to be about 45°.

Gupta et al. (1971) investigated the spatial structure in the viscous sublayer using an array of hot-wires distributed in the spanwise direction. They used a VITA correlation technique to determine the spanwise separations between streaks in the viscous-sub layer. The evolution of shear layers was studied by Johansson et al. (1987a) in the Göttingen oil channel by use of two-probe measurements in the buffer region of the turbulent channel flow. Wark & Nagib (1991) studied coherent structures in turbulent boundary layers at moderate Reynolds number using a quadrant detection technique. They found that a large part of the events are relatively large in scale. They also found that there is a hierarchy of sizes and that the outer flow influences the bursting process. The bursting frequency in turbulent boundary layers was first investigated by Rao et al. (1971), their experiments indicated that outer scaling gave the best collapse of the data. Later, Blackwelder & Haritonidis (1983) carried out experiments on the bursting frequency in turbulent boundary layers. They found the non-dimensional bursting frequency was independent of Reynolds number when scaled with the inner time scale and found a strong effect of spatial averaging for sensors larger than 20 viscous length scales. Alfredsson & V. (1984) studied the frequency of occurrence for bursts in turbulent channel flow, where they found the governing time scale to be a mixture (the geometric mean) of the inner and outer time scales. Johansson et al. (1991) analyzed near-wall flow structures obtained from direct numerical simulation of channel flow (Kim et al. 1987) using conditional sampling techniques. They also analyzed the space-time evolution of structures and asymmetry in the spanwise direction was found to be an important characteristic of near-wall structures, and for shear-layers in particular.

There seems to be no consensus on how to define a coherent structure and several definitions exist. In a review article on the subject Robinson (1991) defines a coherent structure as

...a three-dimensional region of the flow over which at least one fundamental flow variable (velocity component, density, temperature, etc.) exhibits significant correlation with itself or with another variable over a range of space and/or time that is significantly larger than the smallest local scales of the flow.

Other more restricted definitions are given by e.g. Hussain (1986) and Fiedler (1986). Here we will deal mainly with the streaks found in the viscous sub-layer and the connected shear-layer type structures that are believed to be important contributors to the turbulence generation.

The majority of the experimental studies on structures in zero pressure gradient turbulent boundary layers have been conducted at low Reynolds numbers ($Re_{\theta} < 5000$), where flow visualization and high resolution velocity measurements are relatively easy to obtain. One of the objectives with this study was therefore to extend the knowledge about turbulence structures to high Reynolds numbers, in particular the issue of the relative importance on outer scale motions on the near-wall dynamics.

Three types of investigations were carried out. First, we investigate the mean streak spacing by measurements of the instantaneous wall-shear stress in two points with different spanwise separations. Secondly, the scaling of the "bursting frequency" was investigated by detection of the frequency of VITA events in the buffer region. Thirdly, a single wire probe was traversed in a streamwise wall-normal (x,y)-plane above the hot-film sensor, with the aim to detect and characterize shear-layer type events and to determine their spatial structure and local propagation velocity.

2. Experimental facility

The flow field of a zero pressure-gradient turbulent boundary layer was established on a 7 meter long flat plate mounted in the test section of the MTL wind-tunnel at KTH. The MTL wind tunnel is of closed-return type designed with low disturbance level as the primary design goal.

The flow quality of the MTL wind-tunnel was reported by Johansson (1992). For instance, the streamwise turbulence intensity was found to be less than 0.02%. The air temperature can be controlled to within $\pm 0.05^{\circ}$ C, which is very important for this study since the primary measurement technique was hot-wire/hot-film anemometry, where a constant air temperature during the measurement is a key issue. The test section has a cross sectional area of 0.8 m \times 1.2 m (height \times width) and is 7 m long. The upper and lower walls of the test section can be moved to adjust the pressure distribution. The maximum variation in mean velocity distribution along the boundary layer plate was $\pm 0.15\%$.

The first 5.5 m of the plate was used for the experiment. One of the plate sections was equipped with two circular inserts, one for a Plexiglas plug where the measurements were done, and one for the traversing system. The traversing system was fixed to the plate to minimize any vibrations and possible deflections. The distance to the wall from the probe was determined by a high magnification microscope. The absolute error in the determination of the wall distance was within $\pm 5\mu$ m.

The boundary layer was tripped using several rows of tape with raised V-shapes at the beginning of the plate and the two-dimensionality of the boundary layer was checked by measuring the spanwise variation of the wall shear stress $\tau_{\rm w}$. The maximum spanwise variation in friction velocity $u_{\tau} = \sqrt{\tau_{\rm w}/\rho}$ was found to be less than $\pm 0.7\%$.

The reference conditions used in the calibration of the probes were determined using a Prandtl tube in the free-stream directly above the measurement station. The accuracy of the pressure measurement was 0.25~% and the accuracy of the temperature measurement was $0.02~^{\circ}\mathrm{C}$.

Constant temperature hot-wire an emometry was used in all velocity measurements. All hot-wire probes were designed and built at the lab. Three sizes of single-wire probes were used in the experiments with wire diameters of: 2.5, 1.27 and 0.63 μ m and a length to diameter ratio always larger than 200.

The MEMS hot-film (figure 1) used in the wall-shear stress measurements was designed by the MEMS group at UCLA/Caltech (Jiang et al. 1996, 1997; Ho & Tai 1998). It was flush-mounted with a printed circuit board for electrical connections which in turn was flush-mounted into a Plexiglas plug fitting into the instrumentation insert of the measurement plate-section. The MEMS sensor chip has four rows of 25 sensors with a spanwise separation of 300 μ m, see figure 1. The length of each hot-film is 150μ m and the width 3μ m. It is placed

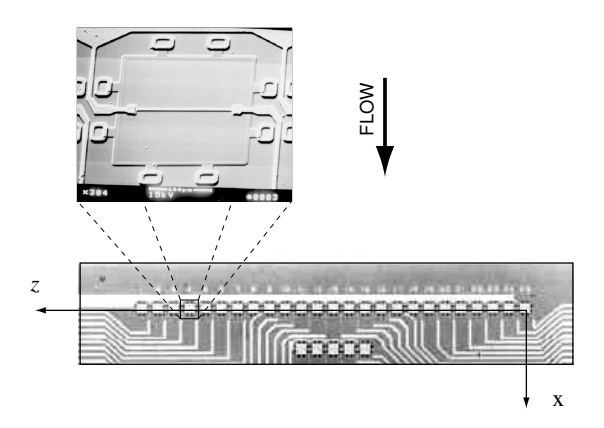


FIGURE 1. Enlargement of the MEMS hot-film wall-shear stress sensor chip from UCLA/Caltech (Jiang $et\ al.\ 1996$) showing the array of 25 sensors used, seen as the row of white squares on the z-axis. A blow-up of one of the hot-films is also shown.

on a $1.2\mu\mathrm{m}$ thick silicon-nitrite diaphragm with dimensions $200\mu\mathrm{m} \times 200\mu\mathrm{m}$. Thermal insulation of the hot-film to the substrate is provided by a $2\mu\mathrm{m}$ deep vacuum cavity underneath the diaphragm.

The anemometer system (AN1003 from AA lab systems, Israel) has a built-in signal conditioner and the signals from the anemometer were digitized using an A/D converter board (A2000 from National Instruments, USA) in the measurement computer. The A/D converter has 12 bit resolution and four channels which could be sampled simultaneously at rates up to 1 MHz divided by the number of channels used.

3. Experimental procedure

3.1. Probe calibration

The hot-wires were calibrated in the free-stream against the velocity obtained from a Prandtl tube at 10 different speeds ranging from about 5% to 100% of the free-stream velocity of the actual experiment. A least-squares fit of the anemometer voltage versus the velocity was formed using King's law.

The hot-films were calibrated in situ in the turbulent boundary layer against the mean skin-friction obtained from oil-film interferometry, here denoted $\tau_{\rm w}^*$.

The principle of oil-film interferometry is to register the temporal deformation of a thin film of oil, due to the shear stress, from the flow, on its upper surface. From the deformation velocity the wall-shear stress can be determined

accurately, knowing the viscosity of the oil. The oil-film deformation velocity was determined by measuring the thickness of the oil-film by interferometry, see Fernholz *et al.* (1996). A least-squares fit of a variant of the logarithmic skin-friction law of the type

$$c_f = 2\left[\frac{1}{\kappa}\ln(Re_\theta) + C\right]^{-2} \tag{1}$$

was made to the obtained wall-shear stress, with the resulting values of the constants $\kappa = 0.384$ and C = 4.08, see figure 2. Comparisons with other methods and also other experiments are made in Österlund *et al.* (2000).

After the mean wall-shear stress relation was determined the anemometer voltage signals, from the two wall-shear stress sensors to be calibrated, were recorded for eight different mean wall-shear stress values in the range $0.3 < \tau_{\rm w}^* < 3$ times the mean value of interest. This large range was necessary, due to the long tails of the probability density function for $\tau_{\rm w}$, to avoid extrapolation of the calibration function (2). Kings law was used to relate the anemometer output voltage E to the instantaneous skin-friction $\tau_{\rm w}$,

$$\tau_{\rm w} = \left[\frac{1}{B}(E^2 - A)\right]^{1/n},\tag{2}$$

where A, B and n are constants. The constants in equation 2 were determined minimizing the sum of the mean-square-error, for all calibration points, between the measured mean skin-friction, $\tau_{\rm w}^*$, and the mean value, $\overline{\tau_{\rm w}}$, obtained applying relation 2 to the anemometer voltage signal E:

$$\min\left(\sum (\tau_{\rm w}^* - \overline{\tau_{\rm w}})^2\right). \tag{3}$$

The MEMS hot-film was found to give a relative fluctuation intensity of 0.35 (at $Re_{\theta} \approx 12400$), *i.e.* somewhat lower than the commonly reported value of 0.41, see Österlund (1999). This deviation reflects a limitation of the sensor technique but should not be of significant influence for the present correlation measurements.

3.2. Mean Flow Characteristics

Velocity profiles at five different streamwise positions (x = 1.5, 2.5, ...5.5m) were taken over a large span in Reynolds number ($2530 < Re_{\theta} < 27300$), see figure 2. The behavior of the boundary layer was found to confirm the traditional two layer theory with a logarithmic overlap region for $200\nu/u_{\tau} < y < 0.15\delta_{95}$ existing for $Re_{\theta} > 6000$. δ_{95} is the boundary layer thickness where the mean streamwise velocity is 95% of the free-stream velocity. It is here used instead of the more common δ_{99} because it can be determined experimentally much more accurately. This difference does not affect the scaling of the boundary layer, see Österlund (1999). The values of the von Kármán constant and the additive constants were found to be $\kappa = 0.38$, B = 4.1 and $B_1 = 3.6$, see Österlund

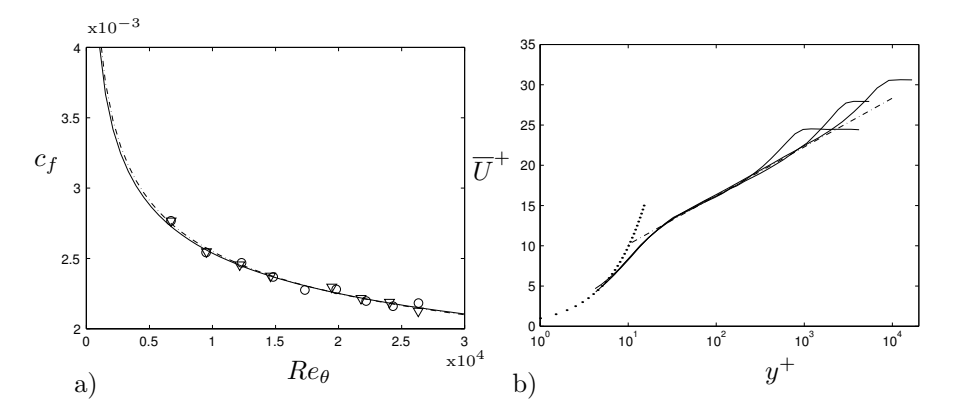


FIGURE 2. Mean flow characteristics of the boundary layer. $2530 < Re_{\theta} < 27300$.

- a) Skin-friction coefficient. o and ∇: oil-film interferometry. —: best-fit of logarithmic friction law (equation 1) to the oil-film data. —: Skin-friction law from Fernholz & Finley (1996).
- b) Mean velocity profiles for $Re_{\theta}=2530,\ 9700$ and 27300. Dotted and dashed curves represent $U^+=y^+$ and $U^+=\frac{1}{0.38}\ln y^++4.1.$

et al. (2000). (This slightly lower value of the von Kármán constant than the standard value of 0.4 has also been found by others, see e.g. the reevaluation of the superpipe data by Perry et al. (2001)).

3.3. Detection of events

In the detection of shear layer structures the variable-interval time average (VITA) was used. The VITA of a fluctuating quantity $Q(x_i, t)$ is defined by

$$\widehat{Q}(x_i, t, T) = \frac{1}{T} \int_{t - \frac{1}{2}T}^{t + \frac{1}{2}T} Q(s) ds, \tag{4}$$

where T is the averaging time. The conventional time average results when T becomes large, i.e.

$$\overline{Q}(x_i) = \lim_{T \to \infty} \widehat{Q}(x_i, t, T). \tag{5}$$

Blackwelder & Kaplan (1976) used the VITA technique to form a localized measure of the turbulent energy

$$var(x_i, t, T) = \frac{1}{T} \int_{t - \frac{1}{2}T}^{t + \frac{1}{2}T} u^2(s) ds - \left(\frac{1}{T} \int_{t - \frac{1}{2}T}^{t + \frac{1}{2}T} u(s) ds\right)^2.$$
 (6)

This quantity is also known as the short-time variance of the signal. The VITA variance can be used to detect shear-layer type events. An event is considered to occur when the amplitude of the VITA variance exceeds a certain threshold level. A detection function is defined as

$$D_u(t,T) = \begin{cases} 1 & var > k\overline{u^2} & \text{and} & \frac{\partial u}{\partial t} > 0\\ 0 & \text{otherwise} \end{cases}, \tag{7}$$

where k is the detection threshold level. The correspondence between shearlayers and VITA events was substantiated by e.g. Johansson & Alfredsson (1982) and Johansson $et\ al.\ (1987b)$.

A set of events $E_u = \{t_1, t_2, \dots, t_N\}$ was formed from the midpoints of the peaks in the detection function D_u . Conditional averages of a quantity Q can then be constructed as

$$\langle Q(\tau) \rangle = \frac{1}{N} \sum_{j=1}^{N} Q(t_j + \tau), \tag{8}$$

where τ is the time relative to the detection time and N is the total number of detected events.

In addition to detecting events using the VITA variance technique, events were detected on the amplitude of the fluctuating quantity itself, e.g. detection of peaks of the fluctuating wall-shear stress,

$$D_{\tau_{\mathbf{w}}}(t,T) = \begin{cases} 1 & \tau_{\mathbf{w}} > k\sqrt{\overline{\tau_{\mathbf{w}}^2}} \\ 0 & \text{otherwise} \end{cases}$$
 (9)

4. Results

4.1. Streak spacing

The mean spanwise separation between low-speed streaks in the viscous sublayer was investigated using the MEMS array of hot-films, see figure 1. It gave us 18 spanwise separations in the range $0 \le \Delta z^+ \le 210$. The spanwise length of the hot-films was $l^+ = 5.6$, at the Reynolds number $Re_\theta = 9500$ $(Re_\tau \equiv \delta_{95}u_\tau/\nu = 2300)$. The spanwise cross correlation coefficient between the wall-shear stress signals obtained from two hot-films separated a distance Δz^+ in the spanwise direction is defined by

$$R_{\tau_{\mathbf{w}}\tau_{\mathbf{w}}}(\Delta z) = \frac{\overline{\tau_{\mathbf{w}}(z)\tau_{\mathbf{w}}(z+\Delta z)}}{{\tau'_{\mathbf{w}}^2}},$$
(10)

where prime denotes r.m.s. value. The cross-correlation coefficient was used to estimate the mean streak spacing.

At low Reynolds numbers the low-speed streaks, and their associated liftup and ejection outwards, represent a dominant feature in the near-wall turbulence. An interesting issue is to what extent this also holds as the Reynolds

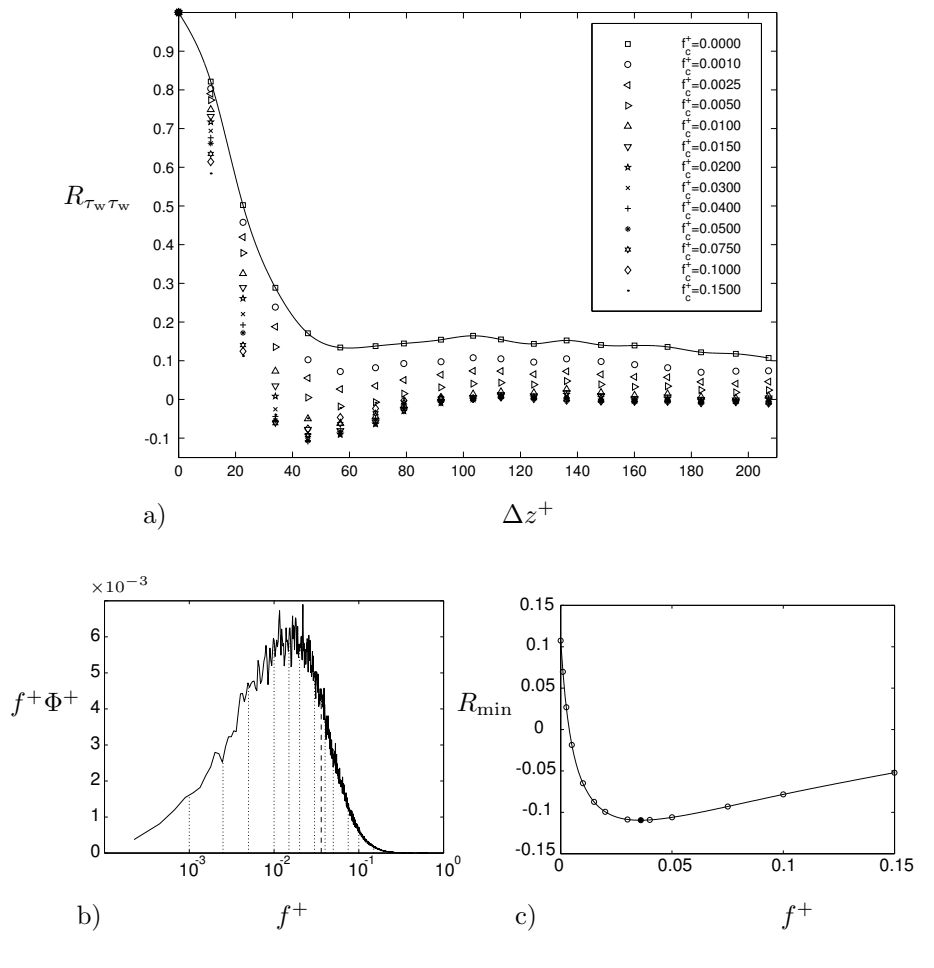


FIGURE 3. Determination of the optimum high-pass filter at $Re_{\theta} = 9500$.

- a) Two-point correlation function $R_{\tau_{\rm w}\tau_{\rm w}}(\Delta z^+)$ for various degrees of high-pass filtering, (cut-off frequencies given in diagram). The solid line is a spline fit to the unfiltered case.
- b) Spectrum from wall shear-stress measurement. Vertical dotted lines indicates the high-pass filter cut-off frequencies in diagram a. Dashed vertical line is the cut-off frequency that minimizes the correlation function, $f_c^+ = 0.036$.
- c) Minimum values of the correlation function for varying cutoff frequency (\circ) . Solid line: spline fit to data. \bullet : Absolute minimum found from spline.

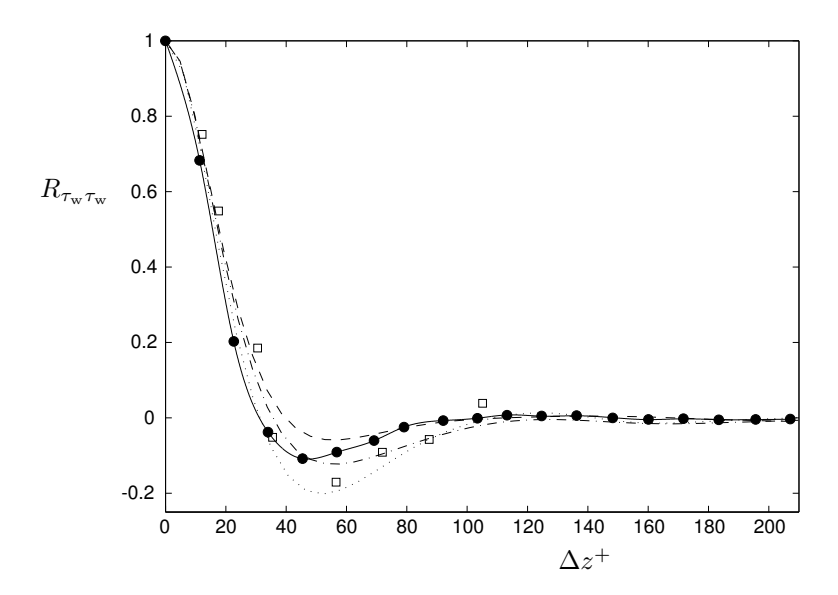


FIGURE 4. Streak spacing comparison with other data from experiments and DNS. •: Present data with $f_c^+ = 0.036$, —: spline fit to present data. DNS of channel flow, correlations of u at $y^+ = 5$, —: $Re_{\tau} = 590$, —·—: $Re_{\tau} = 395$, ···: $Re_{\tau} = 180$ (Kim et al. 1987; Moser et al. 1999). Measurement in channel flow, correlations of u at $y^+ = 5$, \square : $Re_{\tau} = 200$ (Kreplin & Eckelmann 1979)

number is increased. The answer to this question should give an important indication about the relative importance of outer scale motions for near-wall dynamics. For instance, we will later return to the issue of the scaling of the frequency of occurrence of buffer region shear-layer structures.

At low Reynolds numbers the dominance of the streaks in the viscous sublayer gives a distinct negative minimum in the spanwise correlation function for a spanwise separation of about 50 viscous length units. This is in accordance with the, from flow visualizations, observed mean streak spacing of about $100\nu/u_{\tau}$. In figure 3a the correlation function $R_{\tau_w\tau_w}(\Delta z^+)$ is shown for a momentum loss Reynolds number of 9500, and we can observe that no clear minimum is visible without filtering of the time signal. This indicates that, at this relatively high Reynolds number outer scale motions and dynamics become of importance even in the immediate vicinity of the wall. Similar observations have also been found by others, see e.g. Gupta et al. (1971) and Naguib & Wark (1992). In the later paper the authors filtered the time signal using a band-pass filter with varying frequency to identify the scaling of the correlation function between a wall-wire and a single-wire traversed from the buffer region outwards at Reynolds numbers based on the momentum loss thickness between 1579 and 5961.

A trend is clearly visible in the relatively low Reynolds number simulations by Kim et al. (1987) and Moser et al. (1999) where at their highest Reynolds number the minimum is less pronounced. One could hypothesize that the pattern of streaky sub-layer structures at high Reynolds numbers still exists but becomes increasingly concealed by contributions from large scale motions, as the range of scales increases. In an attempt to reveal and possibly obtain the streak spacing also from the high Reynolds number data in the present experiment we applied a high-pass (Chebyshev phase-preserving) digital filter to the wall-shear stress signals before calculating the correlation coefficient. This procedure emphasizes the contribution from the near-wall streaks and enhances the variation in the correlation coefficient.

With increasing cut-off frequency the minimum in the correlation function first becomes more pronounced but at very large cut-off frequencies the minimum tends to disappear again (see figure 3a). An investigation was performed to find the cut-off frequency that gives the most pronounced minimum in the correlation function. Since the streaks are responsible for the negative correlation values the optimum filtering cut-off should be high enough to remove the influence from larger flow structures. In figure 3c the minimum value of the correlation function is plotted against the cut-off frequency. The filled circle indicates the minimum and the value of the cut-off frequency here was found to be 0.036 in inner scaling. A calculation of the correlation function was performed with this particular cut-off frequency. The result is shown as filled circles in figure 4. It is interesting to notice that the minimum cut-off frequency of 0.036 can be translated to a length scale in inner variables, l^+ , of approximately 400. This is very close to the expected length of a streak.

The broad minimum in figure 3c is consistent with the fact that the streaks vary significantly in size. Note that also band-pass filtering was tested to remove influence of high frequency contributions to the correlation function but no significant effect could be found above that from the high-pass filtering. An explanation of this is that the energy content above, say $f^+ = 0.1$, is very small, as can be seen in figure 3b. The dotted vertical lines in figure 3b represent the cut-off frequencies used in figure 3a. The dashed vertical line is the chosen cut-off frequency of 0.036.

When plotted as in figure 3b the area under the curve directly represents the kinetic energy content. We may notice the large amount of energy located at lower frequencies than the chosen cut-off frequency. This points to the fact that the streaks play a less important role in the near-wall dynamics at high Reynolds number. This fact may also have an impact on control strategies for high Reynolds number flows.

The value of the separation, Δz^+ , for which correlation attains a minimum, was found to vary (decrease) only slightly with increasing cut-off frequency. The location of the minimum of the correlation function was at $\Delta z^+ = 48$ for a cut-off frequency of $f_c^+ = 0.036$. This corresponds to a streak spacing of 96, which lies in the range of values from other experiments and direct numerical simulations. The typical value for the streak spacing given is 100.

The filtered correlation function, see figure 4, is close to zero for separations $\Delta z^+ > 100$. This result agrees well with other experiments and simulations at low Reynolds numbers, see e.g. Kline et al. (1967), Kreplin & Eckelmann (1979), Smith & Metzler (1983), Kim et al. (1987) and Moser et al. (1999), some of which are included in figure 4 for comparison. Gupta et al. (1971) computed two-point correlations with spanwise separation in the near-wall region. They show results mostly from $Re_{\theta} = 3300$ where the (unfiltered) correlation function is of similar character to that shown in figure 3a. They noted the lack of a clear minimum in the correlation function, and instead used the VITA technique to extract some information on characteristic spanwise scales.

4.2. Propagation velocities

The space-time correlation of the wall-shear stress and the streamwise velocity was measured using one hot-film sensor and one hot-wire traversed in the (x, y)-plane. The time-shift of the peaks of the correlation coefficient,

$$R_{\tau_{\mathbf{w}}u}(\Delta x, \Delta y, \Delta t) = \frac{\overline{\tau_{\mathbf{w}}(x, y, t)u(x + \Delta x, y + \Delta y, t + \Delta t)}}{\tau'_{w}u'}, \tag{11}$$

for different Δx and Δy separations are shown in figure 5a. The peak in the correlation moves to negative time-shifts for increasing wall distances, *i.e.* the structures are seen earlier away from the wall. This indicates a forward leaning structure. The propagation velocity of the structure at different distances from the wall is defined by the slopes

$$C_p^+ = \frac{\Delta x^+}{\Delta t^+} \tag{12}$$

of lines fitted to the time-shifts at constant wall-distance in figure 5a. The resulting propagation velocities are plotted in figure 5b as filled circles and was found to be approximately constant $(C_p^+ \approx 13)$ up to about $y^+ = 30$. Further out it was found to be close to the local mean velocity. This means that the structure becomes stretched by the mean shear above $y^+ = 30$. It can also be seen from the variation of the shear layer angle with wall distance as we will return to later, see figure 8. In figure 5b results from other experiments and simulations are shown as open symbols. The results from channel flow at $Re_{\tau} \approx 180$ by Johansson $et\ al.\ (1987a)$ are shown in figure 5b as squares,

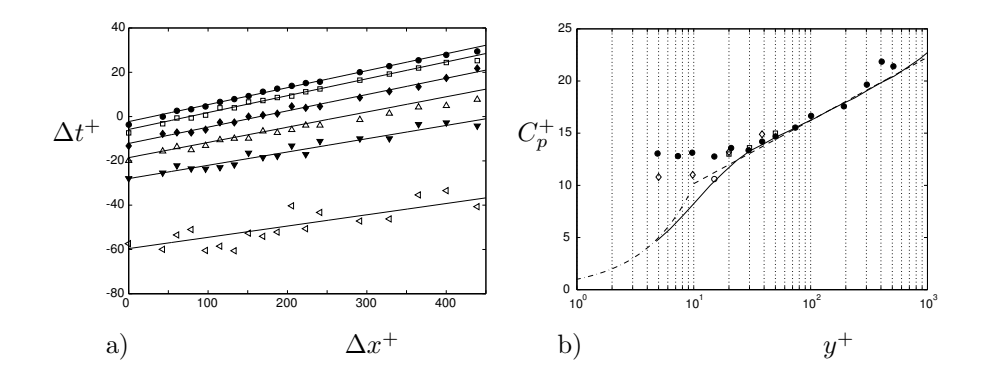


FIGURE 5. Propagation velocity in the boundary layer. a) Time-shift of maximum correlation, $\max(R_{u\tau_{\rm w}}). \bullet : y^+ = 5.$ $\Box : y^+ = 10. \quad \bullet : y^+ = 20. \quad \triangle : y^+ = 50. \quad \blacktriangledown : y^+ = 100.$ $\lhd : y^+ = 300.$ b) Propagation velocity C_p^+, \bullet : Present data $Re_\theta = 9500, \Box$: (Johansson *et al.* 1987*a*) at $Re_\tau = 180 \circ$: (Johansson *et al.*

(Johansson et al. 1987a) at $Re_{\tau} = 180$ \circ : (Johansson et al. 1991) at $Re_{\tau} = 180$, \diamond : (Krogstad et al. 1998) at $Re_{\theta} = 1409$. —: log-law, $\kappa = 0.38$ and B = 4.1. — : linear profile and —: mean velocity profile at $Re_{\theta} = 9700$.

and agree well with the present findings. Johansson et al. (1991) analyzed DNS data for channel flow at the same Reynolds number with a spatial counterpart to the VITA technique and found the propagation velocity to be 10.6 at $y^+=15$. Krogstad et al. (1998) investigated the importance of probe separation for the estimation of the propagation velocity. They found a slight variation with increasing measured propagation velocity with increasing separation. The values from their experiment shown in figure 5b as diamonds are taken at a separation of $\Delta x/\delta$ of 0.1 which corresponds to a value of Δx^+ of about 400. This corresponds well to the range of our least square fit, see figure 5a. Their results are similar to ours although at $y^+=38$ it is slightly higher than the expected value of the mean velocity and at $y^+\leq 10$ they found the propagation velocity to be around 11. This value is close to the value found by Johansson et al. (1991) although at a smaller y^+ .

4.3. Shear-layer events

Shear-layer events were detected from peaks in the short time variance as described in section 3.3 using the velocity signal from a hot-wire in the buffer layer. In table 1 an overview is given of the hot-wire measurements used for VITA detection. The detection times are taken as the midpoints of the peaks

	. —	∇		+	0
Re_{θ}	6700	8200	9700	12600 12.8	15200
l^+	6.6	8.2	9.7	12.8	15.8
y^+	14.3	13.8	14.5	14.8	15.2

TABLE 1. Hot-wire experiments used for VITA detection in the buffer layer.

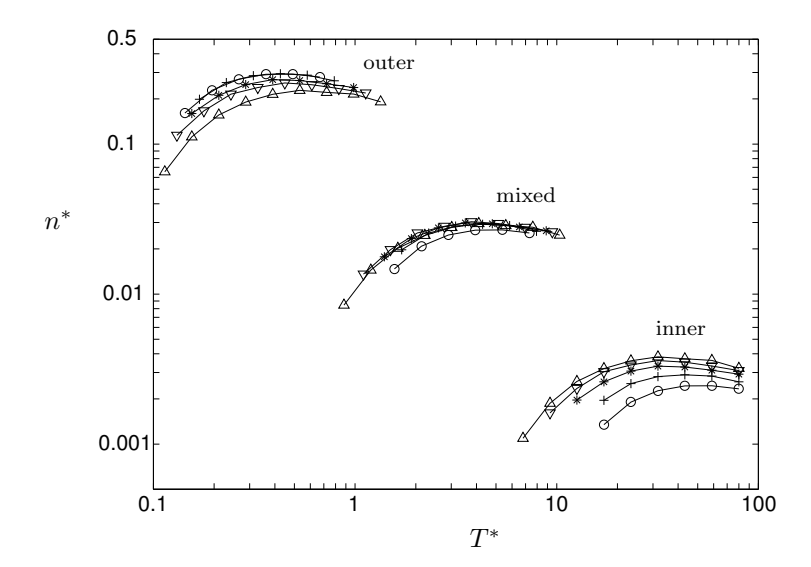


FIGURE 6. Frequency of occurrence of VITA events (k=1) as a function of the averaging time with outer, mixed and inner scaling (* denotes non-dimensional quantities). $y^+ = 15$, k = 1.0. For symbols see table 1.

of the detection function and an ensemble average is formed according to equation 8. The accelerating events considered here dominate in number over the decelerating events, and correspond to a forward leaning shear layer structure. Conditional averages for accelerating and decelerating events can be found in e.g. figure 2 in Johansson & Alfredsson (1982).

Alfredsson & V. (1984) investigated the scaling laws for turbulent channel flow and found that the governing time scale for the near-wall region was a mixture of the inner and outer time scales defined as follows,

$$t_{\rm m} = \sqrt{t_{\rm i} t_{\rm o}}. (13)$$

For further discussion of the interpretation of this timescale, see Alfredsson & V. (1984). The frequency of occurrence of the VITA events is shown in figure 6 against the averaging time for normalization with the outer, mixed and inner time scales defined as $t_{\rm o} = \delta_{95}/U_{\infty}$, $t_{\rm m} = (t_{\rm i}t_{\rm o})^{0.5}$ and $t_{\rm i} = \nu/u_{\tau}^2$, respectively. The choices of definition of the outer and mixed time scales in boundary layer flow are not evident. The most straightforward choice was made here, but an alternative possibility would e.g. be to use the Clauser-Rotta boundary layer thickness instead of δ_{95} in the expression for the outer timescale $t_{\rm o}$. This would however have a negligible influence on the appearance of the collapse in figure 6.

The chosen mixed scaling collapses the data also for the boundary layer flow, see figure 6, in a satisfactory manner. The important region to look at for collapse is around the peak of the curves. Also for the boundary layer situation the mixed scaling appears significantly better than inner and outer scaling. For very small averaging times one should keep in mind the non-negligible influence of finite probe size for the highest Reynolds numbers. One could argue that a minimum requirement for detecting a shear-layer structure is that the probe size, l^+ , should be less than half the width of the shear-layer. As illustrated in figure 1 of Johansson et al. (1991) the aspect ratio, A, of the shear-layer structure in the streamwise-spanwise plane at $y^+ = 15$ is about 5 - 6. Earlier in this paper it was also shown that the propagation velocity, C_p^+ is about 13 at $y^+ = 15$. We can now form a criteria on the minimum averaging time, T^+ , as

$$T^{+} > \frac{2Al^{+}}{C_{p}^{+}}.$$
 (14)

The minimum required time averaging window is thus equal to a time based on the probe size which is shown in table 1 for each Reynolds number used in figure 6. At very small time averaging windows, T^+ , the number of events is so small that they have a negligible impact on the near-wall dynamics.

In figure 6 the outer scaling shows significant spread near the peak, (around $T_0 = 0.3$). Outer scaling has been proposed by e.g. Rao et~al. (1971), based on the observation that the mean time between bursts multiplied by u_{τ}^2 was only weakly dependent on the viscosity. They also tried different outer scalings using, (δ^*/U_{∞}) , (δ/U_{∞}) and (δ/u_{τ}) , where δ^* is the displacement thickness, and found that scaling with the free-stream velocity and the displacement thickness gave the best collapse for Reynolds numbers, Re_{θ} between 600 and 9000. Antonia & Krogstad (1993) found that the scaling of the mean time between ejections or sweeps on a rough surface boundary layer was Reynolds number independent using outer variables for Reynolds numbers, Re_{θ} between 12000 and 22000. For lower Reynolds numbers they found that the outer scaling was not appropriate. Blackwelder & Haritonidis (1983) reported inner scaling for the 'bursting frequency' obtained by the VITA technique. However, their values for the friction velocities (obtained from the near-wall linear profile) deviate substantially from the present correlation for c_f and their mean velocity

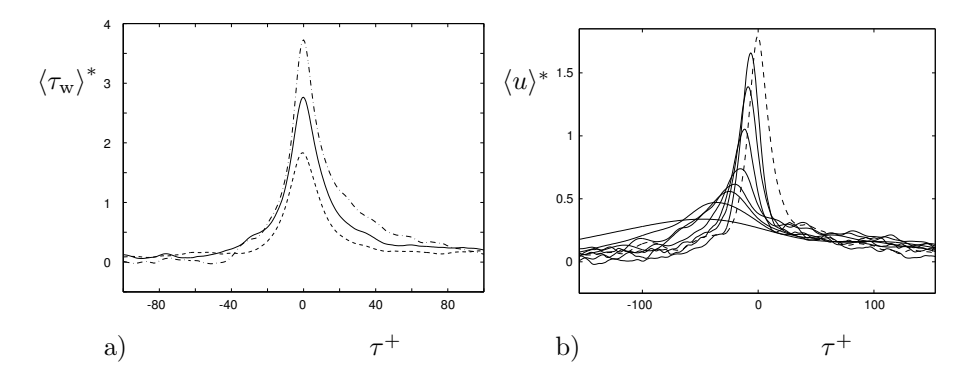


FIGURE 7. Conditional averages with detection on positive peaks of τ_{wrms} (* denotes normalization with local rms value). $Re_{\theta} = 9500$.

- a) Conditionally averaged wall-shear stress signal, $\langle \tau_{\rm w} \rangle^*$. Detection levels, $-\cdot -: k = 3, -: k = 2, --: k = 1$.
- b) Conditionally averaged streamwise velocity, $\langle u \rangle^*$. Detection level k=1. $\Delta x=0$. $y^+=\{5.7,\ 9.6,\ 16.6,\ 29.2,\ 51.7,\ 92.1,\ 164,\ 294\}$. —: detection signal.

profiles for different Reynolds numbers show a wide spread in the log-region. This severely affects the conclusions drawn in their study. Our results, in figure 6, indicate that inner scaling is not appropriate for the bursting frequency. With the mixed scaling used in figure 6 the collapse is good for a large span of Reynolds numbers.

4.4. Wall shear-stress events

The wall shear stress signal is highly intermittent (flatness factor ≈ 4.9) and peaks in the wall-shear stress was used to detect events. In figure 7a the conditionally averaged wall-shear stress events are shown for different detection threshold levels $k = \{1, 2, 3\}$. Broad peaks are seen that are largely symmetric. Negative events (not considered in this paper) are slightly wider and less pointed as compared to the positive events. Otherwise their shape is similar. The trace of the time signal has the characteristics of a low stable, (with small variation), level for extended periods of time mixed with short intermittent peaks in the wall shear-stress, see figure 7a. In this case detecting on high levels of the time signal itself means that these events are predominantly associated with sweep-like motions of fluid with high velocity from the outer part of the boundary layer that penetrates down to the viscous sublayer. Detection on peaks in the wall-shear stress was used to form conditional averages

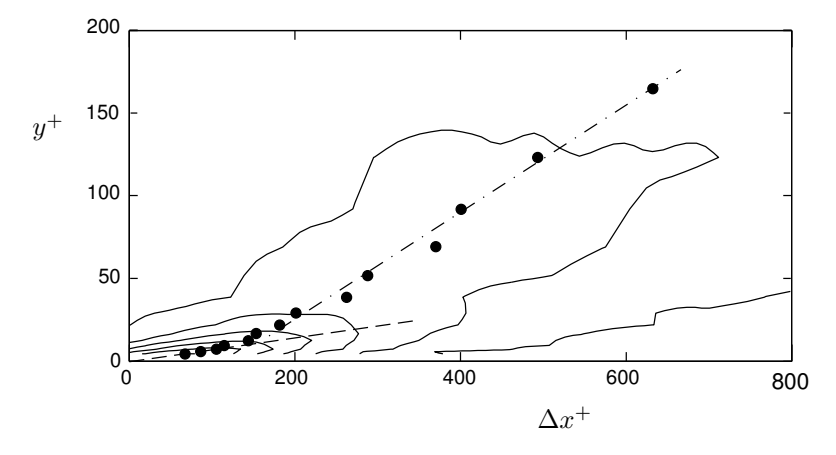


FIGURE 8. Conditionally averaged streamwise velocity. Detection of events where $\tau_{\rm w} > k\tau_{w_{r.m.s.}}$. k=1. •: locations of maximum correlation. $-\cdot$ -: slope of 18° . --: slope of 4° .

for the streamwise velocity obtained at a wall-normal separation Δy^+ . Conditional averages for the streamwise velocity are shown in figure 7b for different wall-normal separations above the hot-film used as detector. For increasing wall-distance the conditionally averaged velocity peak is shifted towards negative times indicating a forward leaning structure. In figure 8 the data in figure 7b are re-plotted into lines of constant disturbance velocity (normalized with the local r.m.s.-level) in the (x, y)-plane using the measured propagation velocities (figure 5) to transform the time to an x-coordinate. An elongated and forward leaning high-velocity structure is visible above the high wall-shear event detected at x = 0. The peaks of the conditionally averaged velocity in figure 7b are shown as filled circles and agree well with a shear layer angle above $y^+ = 40$ of about 15° found in many investigations, see e.g. Johansson et al. (1987a). The outermost points are here disregarded because they are very far from the wall. Closest to the wall, i.e. $y^+ < 15$ they reported shear-layer angles of about 7° . In this study it was found to be somewhat smaller, (4°) . The overall impression from figure 8 is that there is a gradual change in the shear angle out to y^+ of about 40 where it becomes constant.

5. Concluding remarks

Near-wall structures in a zero-pressure gradient turbulent boundary layer were studied at high Reynolds numbers. A MEMS-type of hot-film sensor array was used for this purpose together with a hot-wire probe. The small dimension of the hot-film and hot-wire sensors was a necessity for these measurements.

The streak spacing at high Reynolds numbers was studied through filtering of the wall-shear stress signals before constructing the two-point correlation $R_{\tau_w\tau_w}(\Delta z^+)$. While DNS results at low Reynolds number show a distinct negative minimum for separations around $\Delta z^+ = 50$, the correlation (without filtering) for a momentum loss Reynolds number of 9500 indicate a much stronger influence of large scale motions and no real sign of a minimum. By removing contributions from large-scale motions through high-pass filtering, a correlation function similar to that for low Reynolds number flows was recovered, indicating a streak spacing just below 100. It is interesting to note that the optimum cut-off filter frequency corresponds to about 400 viscous units, which is in the range of the typical streak-lengths. At this filter choice close to 90% of the energy (see figure 3b) is removed before calculation of the correlation, again signifying the influence of large-scale motions for the near-wall dynamics at high Reynolds numbers.

The streak-spacing obtained after filtering, as well as buffer region shearlayer angles and propagation velocities were found to be close to those typically found for low Reynolds number flows.

The frequency of occurrence of shear-layer events and their duration was found to scale with a mixed time scale for a wide range of Reynolds numbers. The mixed scale was taken as the geometric mean of the inner and outer time scales, *i.e.* the same type of scale as that found by Alfredsson & V. (1984) to collapse this type of data in turbulent channel flow. One may interpret also this finding as an increasing influence of large scale motions on the near-wall dynamics with increasing Reynolds number.

6. Acknowledgments

The authors wish to thank Professor Chih-Ming Ho at UCLA for providing us with the MEMS hot-film probe. We would like to thank Professor Henrik Alfredsson for many helpful discussions. We also wish to thank Mr. Ulf Landen and Mr. Marcus Gällstedt who helped with the manufacturing of the experimental set-up. Financial support from NUTEK and The Swedish Research Council is gratefully acknowledged.

References

Alfredsson, P. H. & V., J. A. 1984 Time scales in turbulent channel flow. *Phys. Fluids A* 27 (8), 1974–81.

ANTONIA, R. A. & KROGSTAD, P.-A. 1993 Scaling of the bursting period in turbulent rough wall boundary layers. *Experiments in Fluids* **15** (1), 82–84.

BLACKWELDER, R. F. & HARITONIDIS, J. H. 1983 The bursting frequency in turbulent boundary layers. J. Fluid Mech. 132, 87–103.

- Blackwelder, R. F. & Kaplan, R. E. 1976 On the wall structure of the turbulent boundary layer. J. Fluid Mech. 76, 89–112.
- Chen, K. K. & Blackwelder, R. F. 1978 Large-scale motion in a turbulent boundary layer. *J. Fluid Mech.* 89, 1–31.
- CORINO, E. R. & BRODKEY, R. S. 1969 A visual investigation of the wall region turbulent flow. *J. Fluid Mech.* 37, 1–30.
- Fernholz, H. H. & Finley, P. J. 1996 The incompressible zero-pressure-gradient turbulent boundary layer: An assessment of the data. *Prog. Aerospace Sci.* 32, 245–311.
- Fernholz, H. H., Janke, G., Schober, M., Wagner, P. M. & Warnack, D. 1996 New developments and applications of skin-friction measuring techniques. *Meas. Sci. Technol.* 7, 1396–1409.
- FIEDLER, H. E. 1986 Coherent structures. In $Advances\ in\ turbulence$, , vol. 32, pp. 320–336. Berlin: Springer-Verlag.
- Gupta, A. K., Laufer, J. & Kaplan, R. E. 1971 Spatial structure in the viscous sublayer. J. Fluid Mech. 50, 493–512.
- Head, M. R. & Bandyopadhyay, P. 1981 New aspects of turbulent boundary layer structure. *J. Fluid Mech.* **107**, 297–338.
- Ho, C.-M. & TAI, Y.-C. 1998 Micro-electro-mechanical-systems (MEMS) and fluid flows. Ann. Rev. Fluid Mech. 30, 579–612.
- Hussain, A. K. M. F. 1986 Coherent structures and turbulence. J. Fluid Mech. 173, 303–56.
- JIANG, F., TAI, Y.-C., GUPTA, B., GOODMAN, R., TUNG, S., HUANG, J. B. & HO, C.-M. 1996 A surface-micromachined shear stress imager. In 1996 IEEE Micro Electro Mechanical Systems Workshop (MEMS '96), pp. 110–115.
- JIANG, F., TAI, Y.-C., WALSH, K., TSAO, T., LEE, G. B. & Ho, C.-H. 1997 A flexible mems technology and its first application to shear stress sensor skin. In 1997 IEEE Micro Electro Mechanical Systems Workshop (MEMS '97), pp. 465–470.
- JOHANSSON, A. V. 1992 A low speed wind-tunnel with extreme flow quality design and tests. In *Prog. ICAS congress* 1992, pp. 1603–1611. Beijing, P. R. of China, iCAS-92-3.8.1.
- JOHANSSON, A. V. & ALFREDSSON, P. H. 1982 On the structure of turbulent channel flow. J. Fluid Mech. 122, 295–314.
- JOHANSSON, A. V., ALFREDSSON, P. H. & ECKELMANN, H. 1987a On the evolution of shear layer structures in near wall turbulence. In *Advances in Turbulence* (ed. G. Compte-Bellot & J. Mathieu), pp. 383–390. Springer-Verlag.
- JOHANSSON, A. V., ALFREDSSON, P. H. & KIM, J. 1991 Evolution and dynamics of shear-layer structures in near-wall turbulence. J. Fluid Mech. 224, 579–599.
- JOHANSSON, A. V., HER, J.-Y. & HARITONIDIS, J. H. 1987b On the generation of high-amplitude wall-pressure peaks in turbulent boundary layers and spots. J. Fluid Mech. 175, 119–142.
- KIM, H. T., KLINE, S. J. & REYNOLDS, W. C. 1971 The production of turbulence near a smooth wall in a turbulent boundary layer. J. Fluid Mech. 50, 133–160.

- KIM, J., MOIN, P. & MOSER, R. 1987 Turbulence statistics in fully developed channel flow. J. Fluid Mech. 177, 133–166.
- KLINE, S. J., REYNOLDS, W. C., SCHRAUB, F. A. & RUNSTADLER, P. W. 1967 The structure of turbulent boundary layers. *J. Fluid Mech.* **30**, 741.
- KOVASZNAY, L. G., KIBENS, V. & BLACKWELDER, R. S. 1970 Large-scale motion in the intermittent region of a turbulent boundary layer. J. Fluid Mech. 41, 283–325.
- KREPLIN, H.-P. & ECKELMANN, H. 1979 Propagation of pertubations in the viscous sublayer and adjacent wall region. J. Fluid Mech. 95, 305–322.
- KROGSTAD, P.-A., KASPERSEN, J. H. & RIMESTAD, S. 1998 Convection velocities in a turbulent boundary layer. Phys. Fluids 10 (4), 949–957.
- Moser, R. D., Kim, J. & Mansour, N. N. 1999 Direct numerical simulation of turbulent channel flow up to $Re_{\tau} = 590$. Phys. Fluids 11 (4), 943–945.
- Naguib, A. M. & Wark, C. E. 1992 An investigation of wall-layer dynamics using a combined temporal filtering and correlation technique. *J. Fluid Mech.* **243**, 541–560.
- OSTERLUND, J. M. 1999 Experimental studies of zero pressure-gradient turbulent boundary-layer flow. PhD thesis, Department of Mechanics, Royal Institute of Technology, Stockholm.
- ÖSTERLUND, J. M., JOHANSSON, A. V., NAGIB, H. M. & HITES, M. H. 2000 A note on the overlap region in turbulent boundary layers. *Phys. Fluids* **12**, 1–4.
- Perry, A. E., Hafez, S. & Chong, M. S. 2001 A possible reinterpretation of the Princeton superpipe data. *J. Fluid Mech.* 439, 395–401.
- RAO, K. N., NARASIMA, R. & BADRI NARAYANAN, M. 1971 The "bursting" phenomenon in a turbulent boundary layer. J. Fluid Mech. 48, 339–352.
- ROBINSON, S. K. 1991 Coherent motions in the turbulent boundary layer. *Ann. Rev. Fluid Mech.* 23, 601–639.
- SMITH, C. R. & METZLER, S. P. 1983 The characteristics of low-speed streaks in the near-wall region of a turbulent boundary layer. J. Fluid Mech. 129, 27–54.
- WALLACE, J. M., ECKELMANN, H. & BRODKEY, R. 1972 The wall region in turbulent shear flow. J. Fluid Mech. 54, 39–48.
- WARK, C. E. & NAGIB, H. M. 1991 Experimental investigation of coherent structures in turbulent boundary layers. *J. Fluid Mech.* 230, 183–208.
- WILLMART, W. W. & Lu, S. S. 1972 Structure of the Reynolds stress near the wall. J. Fluid Mech. 55, 65–92.
- Yuan, Y. M. & Mokhtarzadeh-Dehghan, M. R. 1994 A comparison study of conditional-sampling methods used to detect coherent structures in turbulent boundary layers. *Phys. Fluids* **6** (6), 2038–2057.

Paper 5

P5

Evaluation of scaling laws derived from Lie group symmetry methods in zero pressure-gradient turbulent boundary layers

By Björn Lindgren¹, Jens M. Österlund² and Arne V. Johansson¹

¹Dept. of Mechanics, KTH, SE-100 44 Stockholm, Sweden ²Swedish Defence Research Agency, Aeronautics FFA, SE-172 90 Stockholm, Sweden

Submitted to J. of Fluid Mech.

New scaling laws for turbulent boundary layers recently derived (see Oberlack (2000)) using Lie group symmetry methods have been tested against experimental data from the KTH data-base for zero-pressure-gradient turbulent boundary layers. The most significant new law gives an exponential variation of the mean velocity defect in the outer (wake) region. It was shown to fit very well the experimental data over a large part of the boundary layer, from the outer part of the overlap region to about two thirds of the boundary layer thickness (δ_{99}). In the outermost part of the boundary layer the velocity defect falls more rapidly than what is described by the exponential law. This can partly be contributed to intermittency in the outermost part of the boundary layer but the main contribution cause for this stems from non-parallel effects that are not accounted for in the derivation of the exponential law. The scaling law behaviour in the overlap region, derived from Lie group methods, for the two-point correlation functions could be verified by the experimental data. The two-point correlation function behaviour in the outer region, where an exponential velocity defect law is observed, was observed to be very different from that derived under the assumption of parallel flow. It is here made plausible that this indeed can be attributed to non-parallel effects. A small modification of the innermost part of the log-layer is predicted by the same method, in the form of an additive constant within the log-function. A qualitative agreement with such a behaviour just below the overlap region was found.

1. Introduction and theoretical considerations

Scaling issues in turbulent wall-bounded shear-flows have been a topic of much debate since the two-layer hypothesis was introduced by Millikan and von Kármán (see von Kármán (1930) and Millikan (1938)). In this paper the idea of using continuous transformation group (Lie group) symmetries to identify

scaling laws in different regions of zero pressure-gradient turbulent boundary layer flow is evaluated using data from experiments and direct numerical simulations. The use of Lie group symmetries is a very general tool for identification of possible similarity solutions to the flow equations. The scaling laws tested here have been obtained by Oberlack et al. (see Oberlack (1999), Oberlack (2000), Oberlack (2001b)). The description of the Lie group algebra here follows that of Oberlack (2001a). In the recent book of Cantwell (2002) the Lie group symmetry methods for fluid flows is described in detail, and free turbulent shear-flows are given particular attention.

The approach of obtaining scaling laws by means of Lie group symmetry methods offers a high degree of generality and allows study of the influence of *e.g.* boundary conditions in a systematic manner. An important feature is also that similarity type of solutions found by means of symmetry methods are guaranteed to be admitted by the underlying equations.

In recent years there has been a large number of papers published on the issue of the functional form of the mean velocity distribution in the overlap region between the inner (near-wall) and outer regions. Alternatives to the traditional log-law have been proposed by e.g. Barenblatt (1993), George & Castillo (1997) and others. Österlund $et\ al.\ (2000b,a)$ tested these competing theories using highly accurate measurements in high Reynolds number turbulent boundary layer flow with zero pressure-gradient and found that the classical theory still seemed to give the most accurate description of the data.

In the two-layer description of wall-bounded shear-flows the mean velocity is given by

$$\overline{u}_1^+ \equiv \frac{\overline{u}_1}{u_\tau} = f(x_2^+)$$
 in the inner region (1)

$$\frac{\overline{u}_{\infty} - \overline{u}_{1}}{u_{\tau}} = F(\eta) \quad \text{in the outer region}$$
 (2)

where \overline{u}_1 is the streamwise velocity, u_{τ} is the friction velocity, $\overline{u}_1^+ = \overline{u}_1/u_{\tau}$, \overline{u}_{∞} is the free-stream velocity, x_2 is the wall-normal coordinate, $x_2^+ = x_2 u_{\tau}/\nu$, and $\eta = x_2/\Delta$ where Δ is a measure of the boundary layer thickness.

The classical description of the overlap region can be given as

$$\overline{u}_1^+ = \frac{1}{\varkappa} \ln x_2^+ + B \tag{3}$$

or equivalently

$$\frac{\overline{u}_{\infty} - \overline{u}_{1}}{u_{\tau}} = -\frac{1}{\varkappa} \ln \eta + C. \tag{4}$$

A short description of the Lie group symmetry method is given in Appendix A. This description essentially follows that of Oberlack (2001a). We there consider flows (without system rotation) that depend only on one independent coordinate, the wall-normal distance x_2 . The inviscid dynamics are studied by

Evaluation of scaling laws derived from Lie group symmetry methods 171

considering the equation for the steady two-point correlation tensor,

$$R_{ij}(\mathbf{x}, \mathbf{r}) = \overline{u_i'(\mathbf{x}, t)u_j'(\mathbf{x} + \mathbf{r}, t)},$$
(5)

for positions, \mathbf{x} , where influence from viscous stresses etc is negligible, and for separations, \mathbf{r} , associated with length scales that are negligibly influenced by viscosity.

The approach of studying the evolution equation for the two-point correlation function is particularly interesting since it offers this possibility of studying essentially inviscid dynamics. Under these specified conditions the evolution equation for R_{ij} can readily be derived from the Euler equations, giving the inviscid equation for the fluctuating part of the velocity. The resulting evolution equation for R_{ij} inherits the symmetries from the Euler equations, which yields an interesting possibility for new insights into turbulence dynamics through the transferred Lie group symmetries.

Under the assumption of parallel flow where the mean velocity can be described by $\overline{u}_i = \overline{u}_1(x_2)\delta_{i1}$, the admitted symmetries can (see Appendix A) be described by an equation of characteristics in the following manner

$$\frac{\mathrm{d}x_2}{k_{s_1}x_2 + k_{x_2}} = \frac{\mathrm{d}r_{[k]}}{k_{s_1}r_{[k]}} = \frac{\mathrm{d}\overline{u}_1}{(k_{s_1} - k_{s_2})\overline{u}_1 + k_{\overline{u}_1}} = \frac{\mathrm{d}R_{[ij]}}{2(k_{s_1} - k_{s_2})R_{[ij]}} , \quad (6)$$

where brackets mean that summation over repeated indices should not be made. It can also be seen as a four parameter symmetry group, where the four parameters are $k_{s_1}, k_{x_2}, k_{s_2}, k_{\overline{u}_1}$. The symmetry can be seen as a scaling and translation transformation of the wall distance and the mean velocity and a resulting scaling symmetry of the Reynolds stress.

By specification of the values of the two scaling symmetry constants, k_{s_1} and k_{s_2} , scaling laws for different planar shear-flows can be obtained.

1.1. Plane wall-bounded shear-flows

Sufficiently close to the solid boundary in wall-bounded flows such as a zero pressure-gradient boundary layer or channel flow, we have a region of constant total shear stress. This can be described by

$$u_{\tau}^{2} = \nu \frac{\partial \overline{u}_{1}}{\partial x_{2}} - \overline{u'_{1}u'_{2}}.$$
 (7)

Obviously the symmetries described above can only be compatible with this equation in the part of this layer where the viscous influence is negligible.

In the region of strong viscous influence we must have $k_{s_2}=2k_{s_1}$ (and $k_{x_2}=k_{\overline{u}_1}=0$ near a boundary) and we simply retrieve the linear profile near the wall.

1.2. The overlap region

We note that in the region where equation 7 is valid, the friction velocity, u_{τ} , can be seen as an external parameter or boundary condition which inhibits the scaling of the streamwise velocity, \overline{u}_1 .

Let us now consider a region where equation 7 is valid, but restrict our attention to the part sufficiently far from the wall such that the viscous influence is negligible. Since no scaling of the streamwise velocity is admitted, we see from equation 6 that $k_{s_1} - k_{s_2}$ must be equal to zero, i.e. $k_{s_1} = k_{s_2}$. Inserting this into equation 6 and integrating we find the following expression for the streamwise velocity,

$$\overline{u}_1 = \frac{k_{\overline{u}_1}}{k_{s_1}} \ln \left(x_2 + \frac{k_{x_2}}{k_{s_1}} \right) + B. \tag{8}$$

In this form, that was derived by Oberlack (see e.g. Oberlack (2001b)) we recognize the classical log-law but with an extra constant $A = k_{x_2}/k_{s_1}$ inside the logarithm. We also recognize the Kármán constant $\varkappa = k_{s_1}/k_{\overline{u}_1}$. To understand the influence of the new constant A we scale the equation 8 in inner variables and make a series expansion with respect to x_2^+ ,

$$\overline{u}_1^+ = \frac{1}{\varkappa} \ln x_2^+ + B + \frac{A^+}{\varkappa} \frac{1}{x_2^+} + \text{h.o.t.}$$
 (9)

Hence, the extra term associated with the new constant A can be regarded as a small, higher-order, term in the overlap. Compatibility with the fixed location of the wall this parameter must be of negligible influence in the overlap region. Hence, A^+ must be small in comparison with the x_2^+ -values for the region where the symmetry should be valid (where viscous influence is negligible). We will in the results-section investigate whether an influence from such a term can be detected just below the overlap region.

Afzal & Yajnik (1973) have proposed similar forms of the log-law using a series expansion. Also Buschmann & Gad-el Hak (2002) have investigated this form. Wosnik *et al.* (2000) investigated this form for the pipe flow case.

When free scaling of the mean velocity, \overline{u}_1 , is inhibited we readily see from the characteristic equation 6, that the solution, \tilde{r}_k , for the separation becomes $\tilde{r}_k = r_k/x_2$, and that

$$R_{ij} = \tilde{R}_{ij}(\mathbf{r}/x_2) \tag{10}$$

(see also Oberlack (2001b))

1.3. The outer region

In the outer region of the flow we consider wall-distances of the order of the outer lengthscale, *i.e.* a scale that is of the order of the boundary layer thickness. In this region the flow is, hence, influenced by the outer geometrical

restriction. This acts as a boundary condition and is thereby a symmetry breaking condition that prohibits a free scaling of the wall-normal coordinate. In the symmetry group described by equation 6 we must, hence, put $k_{s_1} = 0$, which implies that

$$\frac{\mathrm{d}\overline{u}_1}{\mathrm{d}x_2} = -\frac{k_{s_2}}{k_{x_2}}\overline{u}_1 + \frac{k_{\overline{u}_1}}{k_{x_2}} \tag{11}$$

Integration gives that

$$\overline{u}_1 = C_{\text{exp}} \exp\left(-\frac{k_{s_2}}{k_{x_2}}x_2\right) + \frac{k_{\overline{u}_1}}{k_{s_2}}.$$
 (12)

This velocity law derived by Oberlack (2001b) is the first one that has been obtained from first principles for (parts of) the outer region. This is a remarkable finding and will be tested against experimental data in section 2.

If k_{s_2}/k_{x_2} is positive we find that \overline{u}_1 approaches a constant value as $x_2 \to \infty$. This is compatible with a boundary-layer situation in a semi infinite domain. In particular, we will consider zero pressure-gradient turbulent boundary layers. The free stream boundary condition implies that

$$\frac{k_{\overline{u}_1}}{k_{s_2}} = \overline{u}_{\infty} \tag{13}$$

The outer region is sometimes referred to as the wake region (see Coles (1956)) or velocity defect region. There has been some successful efforts to find a universal expression for the wake region, see *e.g.* Schultz-Grunow (1940) and Lewkowicz (1982). They are mostly fits to experimental data without any deeper physical background.

The velocity profile is usually written as a velocity defect law (see equation 2) in this region. To enable similarity type of descriptions the scaling of the wall-normal coordinate in the outer region must be done with a lengthscale that is characteristic for the boundary layer thickness. Here we will choose to use the Clauser-Rotta length scale ($\Delta = \delta_* \overline{u}_{\infty}/u_{\tau}$, where δ_* is the displacement thickness).

We can now rewrite equation 12 (using the boundary condition 13) as

$$\frac{\overline{u}_{\infty} - \overline{u}_1}{u_{\tau}} = F(\eta) = C_1 \exp\left(-C_2 \frac{x_2}{\Delta}\right) \tag{14}$$

where C_1 and C_2 are constants. The validity of the exponential velocity law in the outer region will here be tested against experimental data, and the constants C_1 and C_2 will be determined from the KTH database for zero pressure-gradient turbulent boundary layers (Österlund (1999)), which covers a Reynolds number range of about $2500 < Re_{\theta} < 27000$ (based on momentum-loss thickness, θ).

1.3.1. Derivation of the Reynolds shear-stress in the exponential velocity defect region

The Reynolds shear-stress profile in the region where the velocity defect exhibits an exponential variation, can be derived from the mean streamwise momentum equation neglecting the influence of viscosity, along with the continuity equation

$$\overline{u}_1 \frac{\partial \overline{u}_1}{\partial x_1} + \overline{u}_2 \frac{\partial \overline{u}_1}{\partial x_2} = -\frac{\partial \overline{u'_1 u'_2}}{\partial x_2}$$
 (15)

$$\frac{\partial \overline{u}_1}{\partial x_1} + \frac{\partial \overline{u}_2}{\partial x_2} = 0. \tag{16}$$

(17)

The velocity defect in the outer region is suitably expressed as a function of $\eta = x_2/\Delta$,

$$\frac{\overline{u}_{\infty} - \overline{u}_1}{u_{\tau}} = F(\eta) \tag{18}$$

The wall-normal velocity component is calculated using the continuity equation, (16), assuming a logarithmic velocity profile in the boundary layer below the exponential velocity defect region. This gives an overestimation of the wall-normal velocity but it is still accurate to first order in $\gamma = u_{\tau}/\overline{u}_{\infty}$. Assuming that the normalized turbulent shear-stress is a function of η ,

$$-\frac{\overline{u_1'u_2'}}{u_\tau^2} = g(\eta) \tag{19}$$

we get the following momentum equation to zeroth order in γ ,

$$g'(\eta) = H_{12}\eta F'(\eta), \tag{20}$$

where prime denotes differentiation with respect to η and $H_{12} = \delta_*/\theta$ is the shape factor.

We also note from the form of equation 20 that the normalization of the velocity defect with u_{τ} together with the scaling of the wall-normal distance with Δ gives a consistent similarity form of the momentum equation. We may expand $g(\eta)$ in the parameter γ , so that

$$g(\eta) = g_0(\eta) + \gamma g_1(\eta) + O(\gamma^2). \tag{21}$$

The zeroth order solution is found by inserting $g(\eta) = g_0(\eta)$ and the exponential velocity defect law into equation 20. The resulting equation has the following solution,

$$g_0(\eta) - g_0(\eta_0) = H_{12} \frac{C_1}{C_2} \left[(C_2 \eta + 1) \exp(-C_2 \eta) - (C_2 \eta_0 + 1) \exp(-C_2 \eta_0) \right].$$
(22)

The derivation of the equation for $g(\eta)$, and its solution are described in some detail in Appendix B.

1.3.2. Two-point correlation functions in the exponential velocity defect region

A further step in the investigation of the new scaling laws derived from Lie group symmetry methods is to look at the two-point correlation functions in the wake region. The equation for the two-point correlation function, neglecting viscosity, in a zero pressure-gradient turbulent boundary layer can be expressed as

$$\frac{\mathrm{D}R_{ij}}{\mathrm{D}t} = -R_{kj}\frac{\partial \overline{u}_{i}}{\partial x_{k}} - R_{ik}\left.\frac{\partial \overline{u}_{j}}{\partial x_{k}}\right|_{\mathbf{x}+\mathbf{r}} - (\overline{u}_{k}(\mathbf{x}+\mathbf{r}) - \overline{u}_{k}(\mathbf{x}))\frac{\partial R_{ij}}{\partial r_{k}} + (\text{terms containing press.vel. corr. \& triple corr.})$$
(23)

Under the assumption of parallel shear-flow, i.e. $\overline{u}_i = \delta_{i1}\overline{u}_1(x_2)$, the above equation reduces to

$$0 = -\delta_{i1}R_{2j}\frac{\partial \overline{u}_1}{\partial x_2} - \delta_{j1}R_{i2}\left.\frac{\partial \overline{u}_1}{\partial x_2}\right|_{x_2 + r_2} - (\overline{u}_1(x_2 + r_2) - \overline{u}_1(x_2))\frac{\partial R_{ij}}{\partial r_1} + (\text{terms containing press.vel. corr. \& triple corr.})$$
(24)

Note here that if the wall-normal separation, r_2 , is zero the streamwise-streamwise correlation component, R_{11} , does not appear in the equation, *i.e.* this equation yields no information regarding the scaling of the R_{11} component if parallel shear-flow is assumed.

Returning to the characteristic equation 6 we can see that the two-point correlation function, assuming inhibited scaling of x_2 in the outer region, giving $k_{s_1} = 0$, yields the following expressions for r_i and R_{ij}

$$\tilde{r}_i = r_i \tag{25}$$

$$\frac{\mathrm{d}R_{ij}}{\mathrm{d}x_2} = -2\frac{k_{s_2}}{k_{r_2}}R_{ij}.\tag{26}$$

Solving the equation for R_{ij} gives an exponential behaviour of the correlation functions with twice the exponent as compared to that for the velocity defect (equation 14) *i.e.*

$$R_{ij} = \tilde{R}_{ij}(\mathbf{r}) \exp\left(-2C_2 \frac{x_2}{\Delta}\right). \tag{27}$$

Modifications of this form due to non-parallel flow and other effects are discussed in conjunction with the presentation of experimental data in section 2.5.

2. Results

We will here test the scaling laws derived in the previous section against experimental data. Also, some DNS data will be analyzed for the same purpose. The focus is on the zero pressure-gradient turbulent boundary layer. Scaling laws for other flows and flow quantities can also be derived with the Lie group symmetry method (see Oberlack (2001b) and Cantwell (2002)).

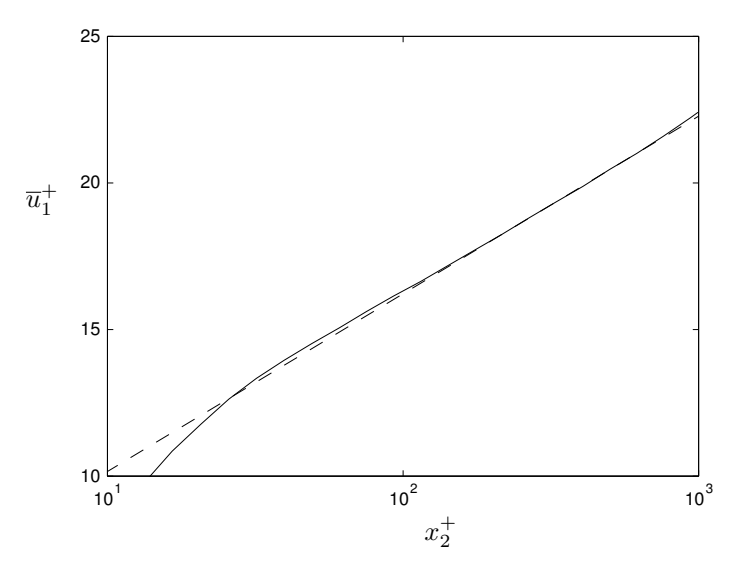


FIGURE 1. Streamwise mean velocity profile in inner scaling from Österlund (1999). Note the "hump" in the inner part of the log region. (Dashed line: log-law with $\varkappa = 0.38, B = 4.1$) $Re_{\theta} = 14300$

2.1. A modified log-law just below the overlap region in a zero pressure-gradient boundary layer

The form of the velocity distribution in the region inside the overlap region but sufficiently far from from the wall for the viscous stress to be negligible, is predicted to take the form

$$\overline{u}_1^+ = \frac{1}{\varkappa} \ln \left(x_2^+ + A^+ \right) + B$$
 (28)

With a positive value of A^+ , such a form should give a small overshoot (relative to the standard log-law) in the innermost part of (or just below) the overlap region. Such a behaviour has been observed in many experimentally obtained mean velocity profiles for turbulent boundary layers. A sample profile from the KTH data-base is shown in figure 1.

A small overshoot around (or just below) $x_2^+ = 100$ is clearly seen. Similar results can be found in other experiments and simulations. See *e.g.* figure 1 in Zagarola *et al.* (1997) and figure 1 in Perry *et al.* (2001) with data from pipe flow. See also figure 3.3 in the introduction of the Österlund (1999) thesis and the earlier work by *e.g.* Smith & Walker (1959). The data is here from boundary layer flow, but it can also be seen in some direct numerical simulations of turbulent channel flow, *e.g.* Moser *et al.* (1999). There are (at least) three possible explanations to this observation in experimental data.

An inaccuracy in the probe position relative to the wall can give an offset in x_2 that comes into the log-law exactly in the same way as the constant A in this case. However, it seems unlikely that all investigators would over-estimate the distance between the probe and the wall. Another explanation is that if the mean profile is determined using a pitot tube, the streamwise velocity is over-predicted in this region. Compensation for this phenomenon is included in many pitot tube calibration functions. A third possibility is that it is coupled to the A-constant in the law 28. The accuracy of the hot-wire data of Österlund (1999) has been analyzed in detail and the magnitude of the overshoot is larger than any possible inaccuracy of the measurements. For instance, the distance to the wall was there determined to within a few plus units.

A sensitive measure to test the possibility of a modified log-law is the diagnostic function Ξ

$$\Xi = \left(x_2^+ \frac{\mathrm{d}\overline{u}_1^+}{\mathrm{d}x_2^+}\right)^{-1}.\tag{29}$$

This quantity was evaluated from the ensemble of velocity profiles of the KTH data-base, that covers momentum loss Reynolds numbers from about 2500 to 27000. The details of the evaluation of this quantity are described in Österlund et al. (2000b). It is plotted in figure 2. It should be constant and equal to the Kármán constant if the log-law is valid. As we can see the classical log-law is valid down to about $x_2^+ = 200$. With the addition of the constant A^+ the modified log-law should give a diagnostic function that follows the function $\varkappa(1 + A^+/x_2^+)$. As is seen in figure 2 this may be said to be valid down to about $x_2^+ = 100$.

Österlund *et al.* (2000*b*) define the inner limit of the universal overlap region to be about $x_2^+ = 200$. We see that the influence of the additive constant is essentially below that limit.

We should note that the modified log-law cannot be part of the actual overlap region since it has a form that cannot be matched with the formulation in outer scaling. This is consistent with the finding that it only influences the mean profile below the inside limit of the universal overlap region as defined by Österlund $et\ al.\ (2000\ b)$.

In direct numerical simulations of channel flow by Moser *et al.* (1999) the diagnostic function Ξ has a similar behavior as the experimental data in figure 2 but without a proper log region due to the low Reynolds number. Similar trends in the behavior of Ξ is also found in data from the super-pipe experiment by Zagarola *et al.* (1997).

As can be seen in equation 28 the influence of the constant A^+ decreases outwards as the inverse x_2^+ and in figure 2 this decay is shown with the constant A^+ set to 5. This value is indeed negligible in comparison with typical x_2^+ -values in the overlap region.

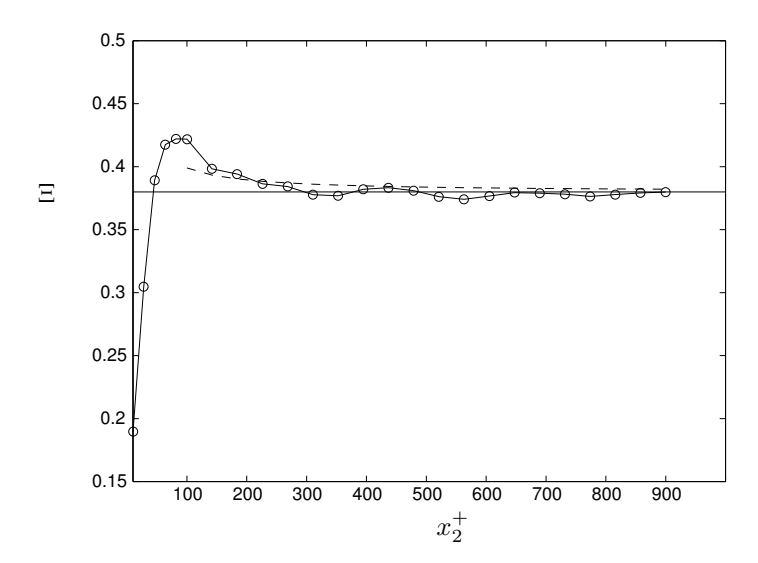


FIGURE 2. The diagnostic function, Ξ , data averaged from experiments by Österlund (1999) (circles), $\Xi = \varkappa$, (solid line) and the modified law $\Xi = \varkappa(1 + A^+/x_2^+)$ (dashed line), with $\varkappa = 0.38$ and $A^+ = 5$.

The difference between the modified and the standard log-law is seen in figure 2 where the solid straight line represents the classical theory and the dashed line represents the modified law.

2.2. The two-point correlation function, R_{12} , in the overlap region in a zero pressure-gradient boundary layer

The streamwise-wall-normal component of the two-point correlation function normalized with the friction velocity squared, i.e.

$$R_{12}^*(\mathbf{x}, \mathbf{r}) = \frac{\overline{u_1'(\mathbf{x}, t)u_2'(\mathbf{x} + \mathbf{r}, t)}}{u^2},$$
(30)

where * denotes normalization with u_{τ}^2 , was calculated for a number of separations in the streamwise direction using Taylor's hypothesis. Taylor's hypothesis of frozen turbulence $(\Delta x_1 = \overline{u}_1 \Delta t)$ is used throughout this paper whenever correlation functions are calculated. The use of Taylor's hypothesis to achieve a chosen separation between the points in the correlation function calculations will of course be a limiting factor in some parts of the flow where the fluctuating velocity is large compared to the mean velocity. In the log-layer $u_{2_{\rm rms}}/\overline{u}_1$, is fairly small (about 5-8%) and Taylor's hypothesis should be expected to work well.

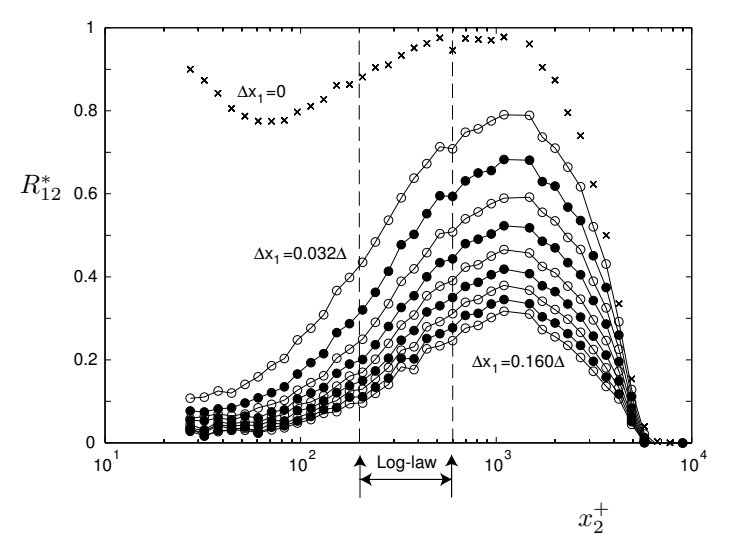


FIGURE 3. The R_{12}^* correlation function plotted against wall distance in inner scaling for varying separation. Non-zero separations, ($\Delta x_1/\Delta = 0.032$, 0.048, 0.064, 0.080, 0.096, 0.112, 0.128, 0.144 & 0.160) are estimated by use of Taylor's hypothesis. $Re_{\theta} = 17600$.

From the characteristic equation 6, we saw in the previous section that the two-point correlation should depend on the variable, r_k/x_2 , alone. With a separation vector $r_k = \Delta x_1 \delta_{k1}$ this becomes

$$R_{ij}^{*}(x_2; \Delta x_1) = R_{ij}^{*}\left(\frac{\Delta x_1}{x_2}\right)$$
 (31)

In figure 3, the R_{12}^* correlation function is plotted against the normalized wall-normal distance. As we can see the correlation function for large separations behaves in a functional manner similar to that for zero separation $(\overline{u_1'u_2'}/u_\tau^2)$ although the magnitude in the inner near-wall region decreases rapidly as the wall is approached for the case of large separations. This is a natural consequence of the fact that the large scale structures predominantly are found away from the wall, in the outer region. Furthermore since the separations are large and the information associated with R_{12}^* thereby is of large scale the accuracy of the experimentally determined curves should be very good since the problems with spatial resolution are negligible in this case.

When plotting R_{12}^* against $\Delta x_1/x_2$, as suggested by Lie group symmetry scaling (equation 31), the data collapses for the points from the logarithmic

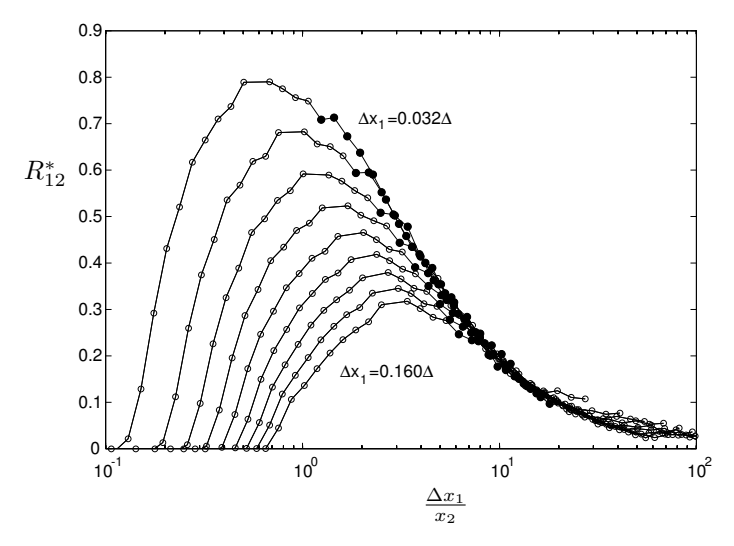


FIGURE 4. The R_{12}^* correlation plotted against separation scaled with wall distance. Filled symbols (circles) represent points within the log-layer ($x_2^+ > 200 \& x_2/\delta_{95} < 0.15$). Separations ($\Delta x_1/\Delta = 0.032$, 0.048, 0.064, 0.080, 0.096, 0.112, 0.128, 0.144 & 0.160) are estimated by use of Taylor's hypothesis. $Re_\theta = 17600$.

overlap region. This is shown in figure 4 where the filled circles represent experimental data points within the overlap region. The good agreement between the theory, developed using the parallel flow assumption, and the experimental data strongly supports that this assumption is valid in the logarithmic overlap region. In the overlap region the parallel flow assumption should be expected to be a good approximation. This is, however, not so in the entire boundary layer, however, as will be shown later in this paper.

2.3. An exponential mean velocity defect variation in the wake region of a zero pressure-gradient turbulent boundary layer

The mean streamwise velocity profiles from the KTH data-base (Österlund (1999)) used here cover a wide range of Reynolds numbers. In figure 5, 70 of these profiles, with Reynolds number based on the momentum-loss thickness ranging from 2500 to 27000, are plotted in outer scaling, *i.e.* as the velocity defect against the wall-distance normalized by the Clauser-Rotta boundary layer thickness. Despite the large number of profiles we can observe a very good collapse of the data. In the log-lin plot we can observe a substantial range where the data fall onto a straight line, *i.e.* where the velocity defect

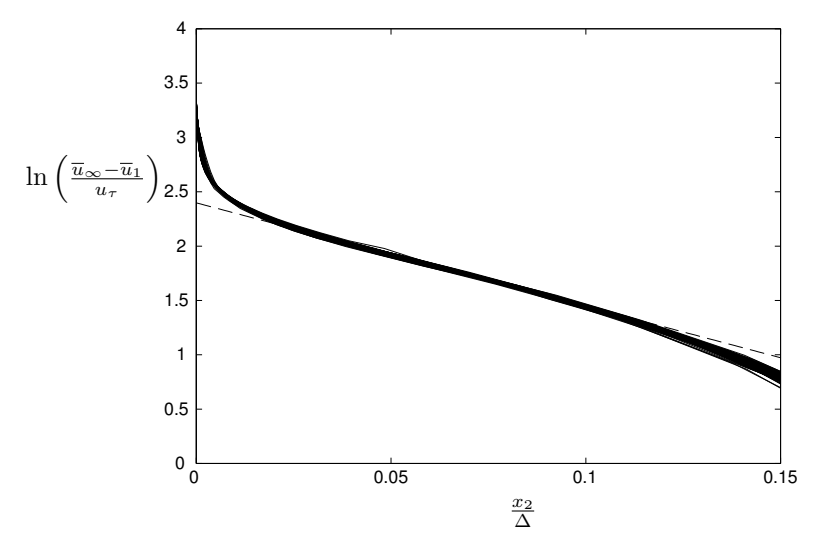


FIGURE 5. 70 mean velocity profiles from Österlund (1999) with $2530 < Re_{\theta} < 27300$ and the exponential wake law (dashed line)

exhibits an exponential variation with wall-distance. The exponential velocity law 14 closely fits the data in the range of about $0.025 \le x_2/\Delta \le 0.10$ with the constants determined as

$$C_1 = 11 \quad C_2 = 9.5.$$
 (32)

One should keep in mind that to translate the wall-distances normalized by the Clauser-Rotta boundary layer thickness to x_2/δ_{99} one should multiply by a factor of roughly 6, which means that the close fit covers a range of about $0.15 \le x_2/\delta_{99} \le 0.6$. Hence, this range corresponds to almost half the boundary layer thickness. It is thereby substantially larger than the region with a logarithmic velocity law.

The innermost part with an exponential velocity-defect variation corresponds approximately to the end of the overlap region, where the velocity defect has a logarithmic variation. It may seem surprising that these two rather different types of velocity laws can meet. There is no strict matching between the two, but to illustrate the situation the logarithmic velocity defect law found by Österlund $et\ al.\ (2000\ b)$ is plotted together with the exponential law 14 in figure 6. On should note that the exponential law is not located in an overlap region in the matching between the inner and outer flow regions. It is completely contained within the outer region. There it can be seen that the solid line representing the log-law and the dashed line representing the wake law

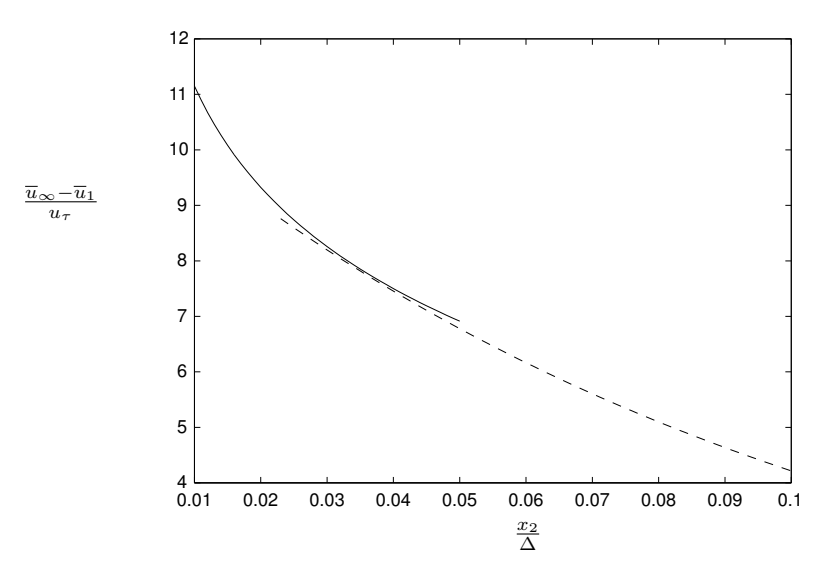


FIGURE 6. The log-law, (solid line), with $\varkappa = 0.38$ and B = -0.97 and the exponential wake law, (dashed line), with $C_1 = 10.9$ and $C_2 = 9.5$, versus wall-distance in outer scaling.

meet at an x_2/Δ of about 0.035. The derivative of the functions is the same here as well. The transition between the two forms is, hence, smooth, although some adjustment region must exist to match higher order derivatives between the two forms. The location of the transition is also consistent with the outer limit of the log-layer as determined by Österlund *et al.* (2000*b*).

As seen in figure 5, this set of experimental data with moderate to high Reynolds numbers closely follow the exponential law. In figure 7 data from Skote (2001) from a direct numerical simulation of a zero pressure-gradient turbulent boundary layer flow is plotted together with the new exponential law. The Reynolds number based on the momentum-loss thickness varies from 380 to 710. The data approaches the exponential law with increasing Reynolds number, but the curves are not quite straight at these low Reynolds numbers.

In the outermost part of the wake region the velocity defect decreases more rapidly than what is predicted by the exponential law. A possible reason for this behaviour is that the relative influence of viscosity may be higher in this region than otherwise in the outer region. In this paper we will attempt to investigate this possibility further. Another possible explanation is that undisturbed free-stream fluid penetrates the boundary layer to give an intermittent behaviour. Since this fluid has a higher velocity than the local mean of the turbulent flow, the mean velocity increases and thereby the velocity defect decreases. The region of the boundary layer affected by the intermittency can be identified by

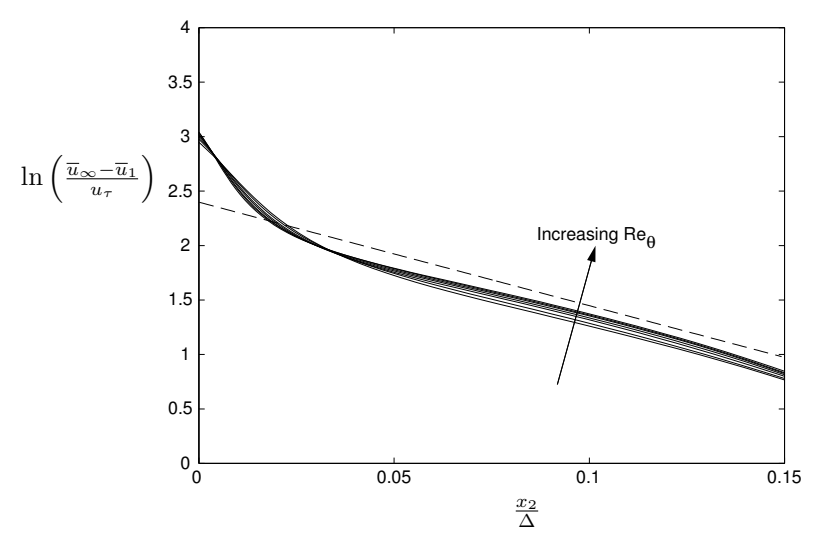


FIGURE 7. Direct numerical simulation data (7 profiles) from Skote (2001) for the velocity defect in boundary layer flow with $380 < Re_{\theta} < 710$ compared to the exponential wake law (dashed line)

the high flatness factor found there. The influence of intermittency is in this paper checked using experimental boundary layer data from the KTH database.

In figure 8 a short time trace of a hot-wire signal in a turbulent boundary layer at $x_2/\Delta=0.272$ is shown together with the short time variance of the same signal. The free-stream parts of the signal can clearly be seen here as flat regions where also the mean velocity is higher than in the turbulent parts. The flatness at this wall-normal position is about ten times higher than in the log-layer which indicates a very high degree of intermittency.

The influence of the intermittency on the velocity defect was investigated through the removal of the free-stream parts of the velocity time signal using a short time variance scheme. The idea is to locate the parts of the time signal with free-stream behaviour, using a running variance window, since the free-stream parts of the time signal have very low variance compared to the turbulent parts. A threshold, k, determines whether the given sample is kept or sorted out. The short time variance is defined as

$$var = \frac{1}{T} \int_{t-\frac{1}{2}T}^{t+\frac{1}{2}T} u_1^2(s) ds - \left(\frac{1}{T} \int_{t-\frac{1}{2}T}^{t+\frac{1}{2}T} u_1(s) ds\right)^2.$$
 (33)

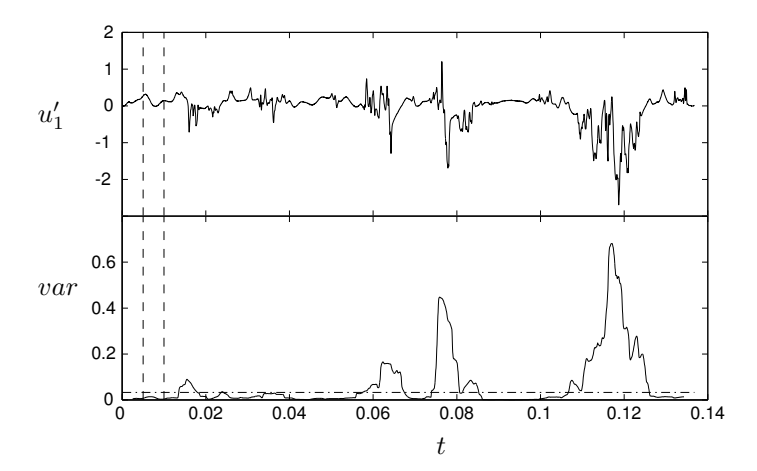


FIGURE 8. Top: Time-series of the streamwise velocity signal. Bottom: Short time variance of the velocity time series in the top figure. The vertical dashed lines show the size of the short time variance time window, T. The horizontal dashed line is the short time variance threshold, $k = 0.1u_{1_{rms}}^2$.

where T is the time window over which the variance is calculated. The parts where the variance is lower than $0.1u_{1_{\rm rms}}^2$, were removed when the new mean value of the streamwise velocity was calculated. In figure 8 the threshold level is shown as a horizontal dash-dotted line. The two vertical dashed lines indicate the size of the time window, T, used to calculate the short time variance.

As expected from the short sample in figure 8 the removal of the free-stream parts from the velocity time series decreases the streamwise velocity and thus increases the velocity defect at the wall-normal positions with high flatness, see figure 9. Otherwise the changes are small. The intermittency phenomenon does not, however, seem to be the major factor to explain the rapid decrease of the velocity defect.

It has been suggested that the relative influence of viscosity in the outer part of the boundary layer is high and that this could contribute to the fast approach of the velocity profile towards the free-stream value. A first check is to evaluate whether the viscous stresses can be neglected compared to the Reynolds stresses in the outermost region. If this would not be the case the inviscid approximation used to derive the scaling laws would be inappropriate, and it could be a contributing factor to the experimental data deviation from the exponential velocity defect law. In figure 10 we have calculated the ratio of the Reynolds shear-stress, $-\rho \overline{u_1 u_2}$, and the viscous stress, $\mu d\overline{u}_1/dx_2$ for a number of different Reynolds numbers, (6900 < Re_{θ} < 22600). The result

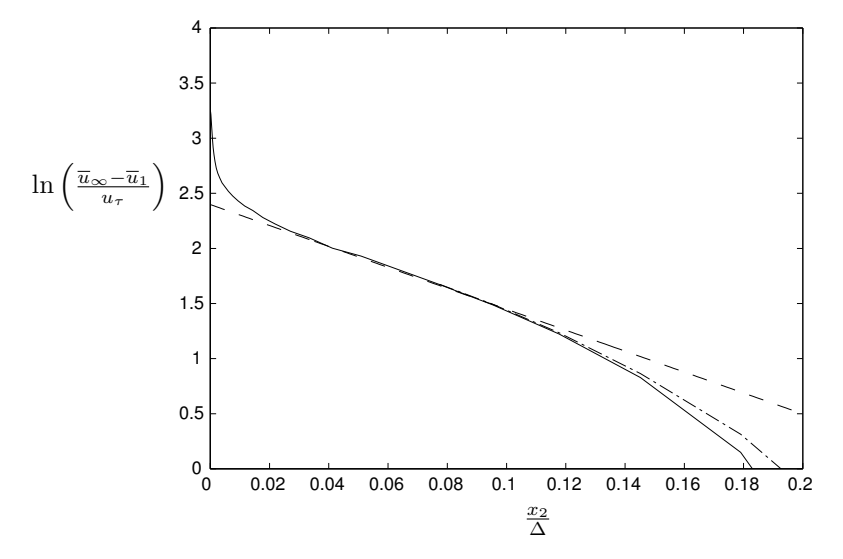


FIGURE 9. A mean velocity defect profile from Österlund (1999) at $Re_{\theta} = 9600$, (solid line), ditto compensated for intermittency, (dash-dotted line), and the exponential velocity defect law (dashed line)

indicates that the viscous stress is much smaller than the Reynolds shear-stress in the wake outside the region with an exponential velocity defect. The conclusion is therefore that the reason for the exponential defect law to fail outside $x_2/\Delta=0.12$ has to be found elsewhere, and most probably, in effects of non-parallel flow. In the section 2.5, this will be discussed further in connection with the evaluation of two-point correlation data.

2.4. Reynolds shear-stress in the exponential velocity defect region

The Reynolds shear-stress profile corresponding to the exponential form of the velocity defect law was derived in section 1.3.1 (and Appendix B). The solution to zeroth order in γ for the normalized shear-stress $(-\overline{u_1'u_2'}/u_\tau^2)$

$$g_0(\eta) = g_0(\eta_0) + H_{12} \frac{C_1}{C_2} \left[(C_2 \eta + 1) \exp(-C_2 \eta) - (C_2 \eta_0 + 1) \exp(-C_2 \eta_0) \right].$$
(34)

is shown for two different Reynolds numbers ($Re_{\theta} = 6930$ and $Re_{\theta} = 22530$) in figure 11. We see that this solution has the correct functional behaviour in the region with exponential velocity defect but that the error in magnitude is of order γ .

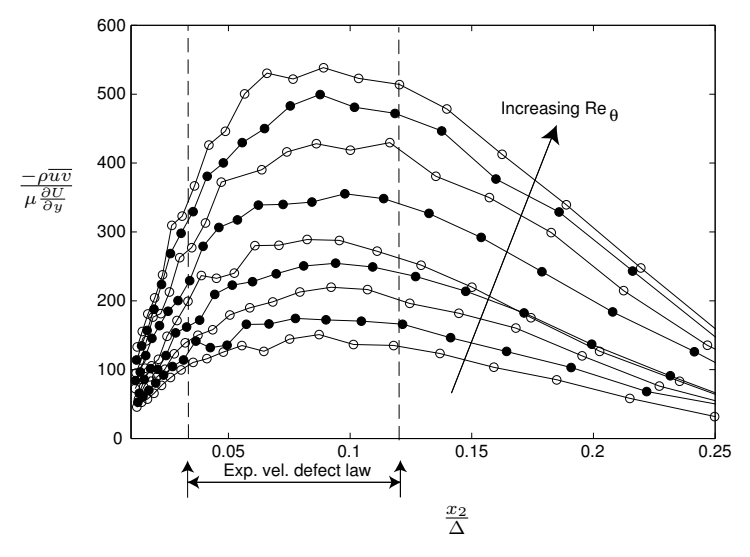


FIGURE 10. The ratio between the Reynolds stress and the viscous stress at $6900 < Re_{\theta} < 22600$. The open and filled markers are used to facilitate the interpretation of the figure.

The solution for $g(\eta)$ that is accurate to first order in γ (see Appendix B) is of similar form to $g_0(\eta)$. As seen in figure 11, it represents the Reynolds shear-stress accurately in the region where an exponential behaviour of the velocity defect can be observed.

2.5. Testing of theoretical predictions for two-point correlation functions in the exponential velocity defect region

As described in section 1.3.2 the form of the two-point correlation tensor, R_{ij} , that corresponds to the exponential velocity defect law is given by

$$R_{ij} = \tilde{R}_{ij}(\mathbf{r}) \exp\left(-2C_2\eta\right). \tag{35}$$

where $\eta = x_2/\Delta$. One should keep in mind that both are derived under the assumption of parallel shear-flow. This also means that the evolution equation for R_{ij} does not give any information regarding the scaling of R_{11} . Hence, the prediction regarding the spatial variation as given by equation 35 does not concern R_{11} . It may still be interesting to study its behaviour. Normalized by u_{τ}^2 it is plotted in figure 12 as function of wall-distance, η , for various (large) separations. Hence, here as well as in the following figures the streamwise separation is calculated by use of Taylor's hypothesis. The analyzed separations are chosen to be similar in size to typical wall-normal distances in the region investigated, namely the exponential defect region. In this region, we can observe a variation that is close to an exponential one. A closer look at the

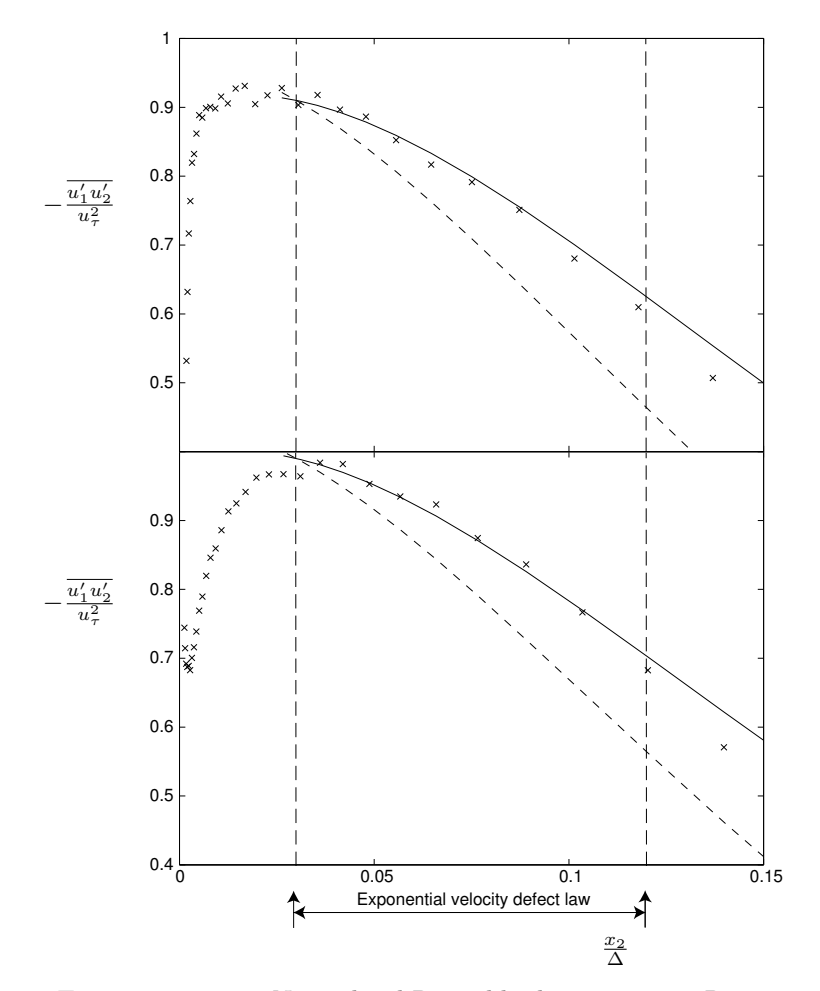


FIGURE 11. Top: Normalized Reynolds shear-stress at $Re_{\theta} = 6930$. Bottom: Normalized Reynolds shear-stress at $Re_{\theta} = 22530$. Solid and dashed curves represent the derived expressions for the Normalized Reynolds shear-stress that are accurate to first and zeroth order in γ , respectively. The integration constants $g_0(\eta_0)$ and $g_1(\eta_0)$ have been chosen to give the best fit to the experimental data.

slope of the straight lines in figure 12 shows (see figure 13) that the slope is far from constant and far from the value $2C_2 \approx 19$ in equation 35.

For the other two measured components of the two-point correlation function the exponential behaviour as written in equation 27 is expected to describe

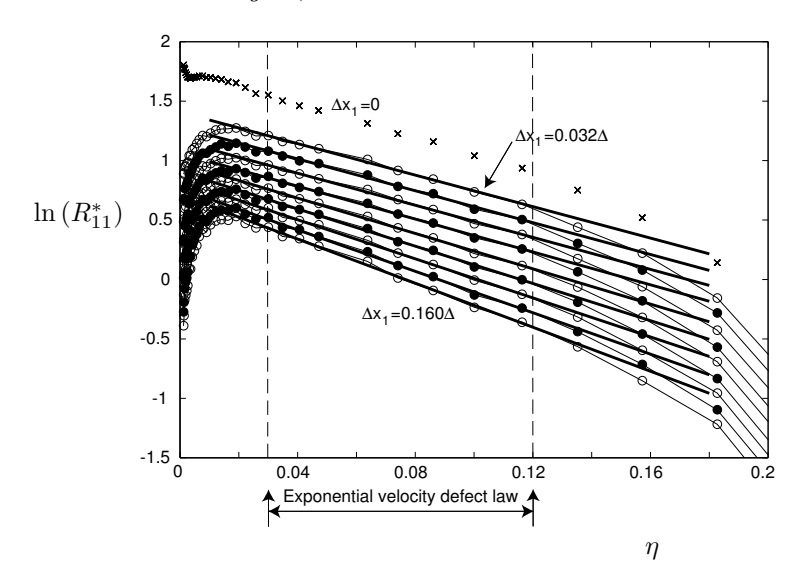


FIGURE 12. R_{11}^* in the wake region. Solid lines are least square fits to the data within the exponential wake region $(0.03 < x_2/\Delta < 0.12)$. ×: zero separation $(\overline{u_1u_1}/u_\tau^2)$. Nonzero separations, $(\Delta x_1/\Delta = 0.032, 0.048, 0.064, 0.080, 0.096, 0.112, 0.128, 0.144 & 0.160)$ are estimated by use of Taylor's hypothesis. $Re_\theta = 17300$

the spatial variation of the experimental data. Figures 14 and 15 show that this expectation does not hold. The predicted behaviour is a rapid exponential decrease (with a $-2C_2$ slope) with increasing distance from the wall. This is certainly not observed. In fact neither of them show any tendency towards an exponential form in the velocity defect region. As mentioned above some reasons for the deviation from exponential variation of the velocity defect in the outermost part of the boundary layer were tested but they could not explain the deviation found. It may be plausible to think that the same reason for deviation in the velocity defect behaviour affects the correlation function even closer to the wall. The most plausible candidate for the cause of error in both the velocity defect and the correlation function is the effect of deviation from parallel flow in the wake region of a boundary layer flow.

The effect of non-parallel flow in a boundary layer increases with wall-distance. In the overlap region the degree of non-parallel flow is very small which is supported by the fact that the theoretically predicted dependence of the Reynolds shear-stress correlation was shown to agree well with experimental data. However, in the outermost part of the boundary layer the relative importance of non-parallel effects grows. Therefore, the left hand side in the

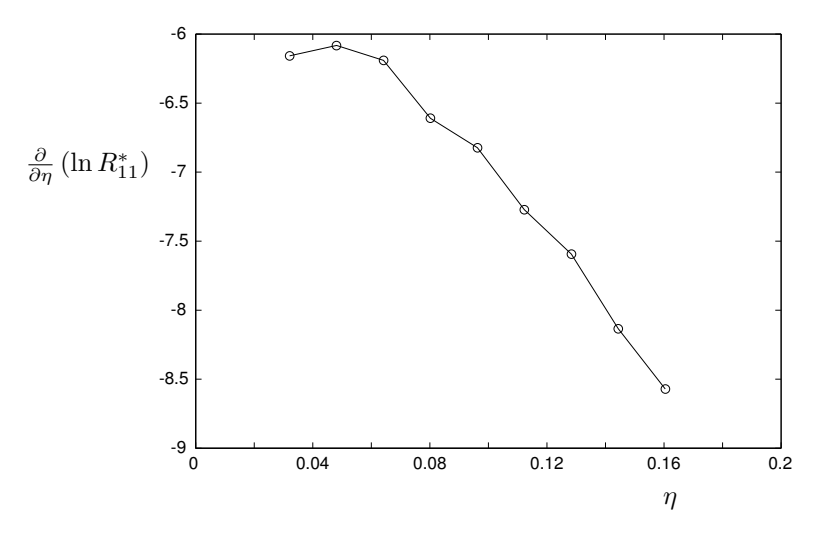


FIGURE 13. The variation of the slope of the least square fitted solid lines in figure 12 with wall-distance.

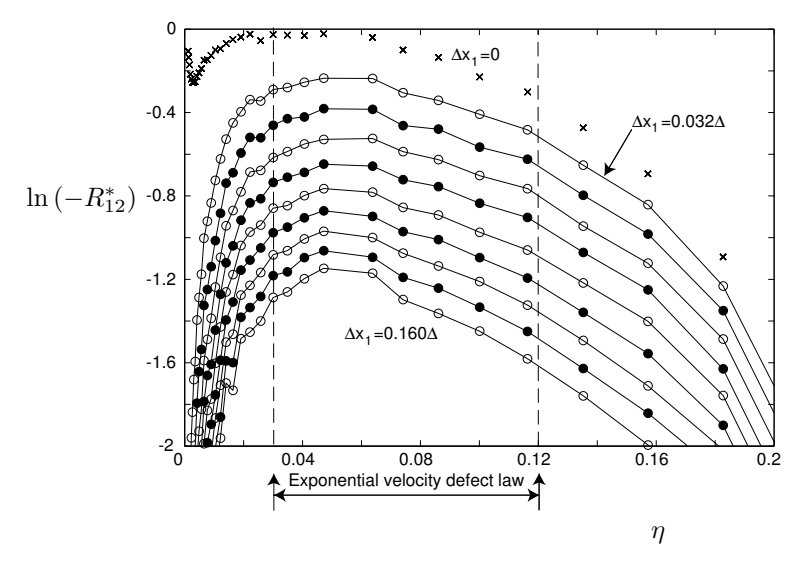


FIGURE 14. R_{12}^* in the wake region. ×: zero separation $(\overline{u_1u_2}/u_\tau^2)$. Non-zero separations, $(\Delta x_1/\Delta = 0.032, 0.048, 0.064, 0.080, 0.096, 0.112, 0.128, 0.144 & 0.160)$ are estimated by use of Taylor's hypothesis. $Re_\theta = 17300$

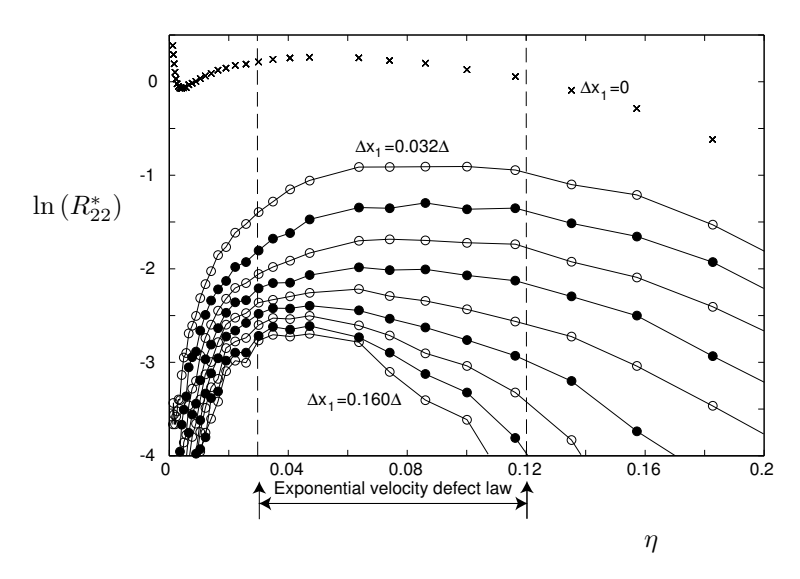


FIGURE 15. R_{22}^* in the wake region. ×: zero separation $(\overline{u_2u_2}/u_{\tau}^2)$. Non-zero separations, $(\Delta x_1/\Delta = 0.032, 0.048, 0.064, 0.080, 0.096, 0.112, 0.128, 0.144 & 0.160)$ are estimated by use of Taylor's hypothesis. $Re_{\theta} = 17300$

equation for the correlations, (23), can no longer be neglected as is the case when the parallel flow assumption is valid.

Now assume that the correlation function is a function of η and \mathbf{r} i.e.

$$R_{ij} = R_{ij}(\eta, \mathbf{r}). \tag{36}$$

The validity of the assumption of this form can be discussed, and we will return to its consequences later. We here use this form to simplify the analysis and it is probably sufficient to yield useful information about the importance of non-parallel effects in the outer part of the wake region. We can now rewrite equation 23 with the above assumption, also assuming steady state and a velocity defect form of the mean velocity description. The resulting equation (to zeroth order in γ) reads

$$\eta \frac{\partial R_{ij}}{\partial \eta} = -\delta_{i1}R_{2j}F'(\eta) - \delta_{j1}R_{i2}F'(\eta + \frac{r_2}{\Delta}) - \left(F(\eta + \frac{r_2}{\Delta}) - F(\eta)\right)\frac{1}{\Delta}\frac{\partial R_{ij}}{\partial r_1} + + (\text{terms containing press.vel. corr. \& triple corr.})$$
(37)

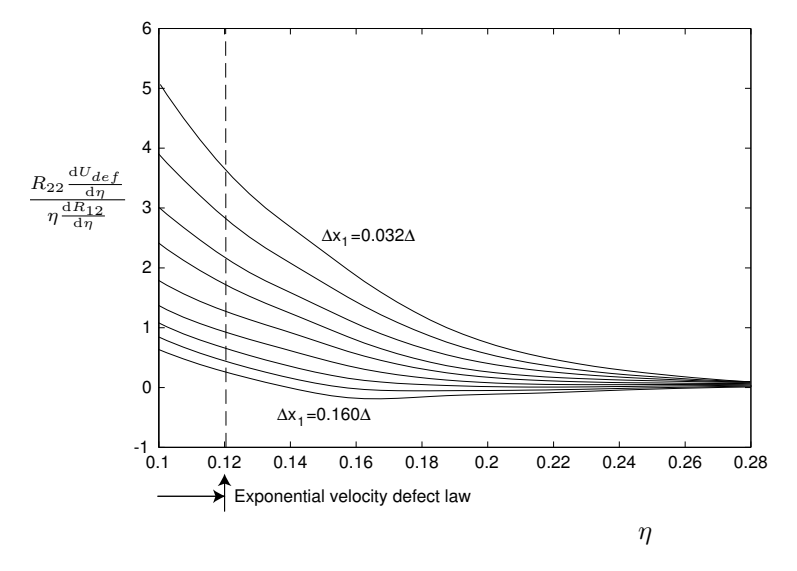


FIGURE 16. Ratio between advection and production term in the transport equation for R_{12} . The velocity defect and the correlation functions have here been smoothed and interpolated to facilitate differentiation. $Re_{\theta} = 17300$

Considering the case when the wall-normal separation is zero, i.e. $r_2 = 0$ we get the following equations for the correlation functions

$$\eta \frac{\partial R_{11}}{\partial \eta} = -2R_{12}F'(\eta) + (\text{terms containing}
\text{press.vel. corr. & triple corr.})$$
(38)

$$\eta \frac{\partial R_{12}}{\partial \eta} = -R_{22}F'(\eta) + \text{(terms containing press.vel. corr. & triple corr.)}$$
(39)

$$\eta \frac{\partial R_{22}}{\partial \eta} = 0 + \text{(terms containing press.vel. corr. \& triple corr.)}$$
(40)

Note here that $R_{12} = R_{21}$ in equation 38 because the separation in the wall-normal direction is zero.

To test the influence of non-parallel flow the ratio of the production term on the right hand side in equation 39 and the advection term is calculated from experimental data for various separations. The result is shown in figure 16. For the non-parallel effects to be important this ratio should be of order unity (or smaller). We see in the figure that the advection term rapidly becomes increasingly important as the boundary layer edge is approached. The influence of the advection term also increases with increasing separation. Note that the curves in figure 16 are made from curve fits to the experimental correlation function data. This was done to get a smoother and clearer picture of the relationship between the terms. It was, however, thoroughly investigated that the gradients calculated using the curve fitted data were similar to gradients calculated from the original data.

Under different assumptions of the form of R_{ij} , e.g. as $R_{ij}(\eta, \mathbf{r}/\Delta)$, the resulting equations would be somewhat different. This may indeed be a more natural choice. To equation 39 there will then be contributions from other terms related to the new scaling of \mathbf{r} that will be more important than the advection term based entirely on η derivatives. These terms are large enough to balance the production term on the right hand side in at least parts of the exponential velocity defect region. For both types of R_{ij} forms it seems clear that non-parallel flow effects give a drastically different behaviour of R_{ij} than predicted under the parallel flow assumption.

3. Concluding remarks

The new scaling laws for turbulent boundary layers derived by Oberlack (2001b) using Lie group symmetry methods have been tested against the experimental data of the KTH data-base for turbulent boundary layers with a wide range of Reynolds numbers. A modification of the log-law in the innermost part of the overlap region could be identified with a constant added to the wall-distance in the logarithmic function. With this constant, $A^+\approx 5$, added, the modified log-law described the experimental data down to $x_2^+\approx 100$ instead of $x_2^+\approx 200$ with the standard log-law (where $x_2^+\approx 200$ was found by Österlund et al. (2000b) as the lower limit of the universal overlap region).

The influence from the new constant decreases rapidly away from the wall and is negligible in the universal overlap region. This is consistent with the possibility of matching with the velocity law in outer scaling.

The two-point correlation function in the logarithmic overlap region is predicted by the Lie group symmetry method to be a function of $\Delta x_1/x_2$. This scaling of the wall-normal distance was tested for the R_{12} component using experimental data and it was found that the data collapsed well for points in the overlap region. The good collapse of the data also strongly supports that the assumption of parallel flow is in fact valid in the overlap region.

The new exponential velocity defect law fits data remarkably well over a large part (roughly half) of the boundary layer thickness. This supports the earlier testing of this law in the work of Oberlack (2001b).

In the outermost part, however, it deviates substantially from experimental data. This may in part be explained by the high intermittency factor here. High velocity free-stream parts of the streamwise velocity penetrating the boundary layer from outside makes the mean velocity approach the free-stream value

faster than the exponential law. The relative influence of viscosity was also tested but its influence was found to be negligible.

An expression for the Reynolds shear-stress in the wake region was derived using the exponential velocity defect law. It was found that in the region where this law is valid there was good agreement between the experimental data and the theory if terms of order $u_{\tau}/\overline{u}_{\infty}$ are included.

The two-point correlation function in the wake region was calculated from experimental data. The result did not agree with the, from Lie group theory, expected exponential behaviour with twice the exponent compared to the velocity defect. The main reason for the discrepancy between experimental results and theory was found to be the assumption of parallel flow. The relative influence of non-parallel effects increases with wall-distance. The non-parallel flow effects are also the most probable cause for the velocity defect to deviate from the exponential behaviour in the outermost part of the boundary layer.

4. Acknowledgment

The authors would like to thank Professor Martin Oberlack for sharing his knowledge on Lie group symmetry methods and discussing the various results in this investigation. Finally, financial support from the Swedish Research Council for the first author is gratefully acknowledged.

References

- Afzal, N. & Yajnik, J. 1973 Analysis of turbulent pipe and channel flows at moderately large reynolds number. J. Fluid Mech. 61, 23–31.
- BARENBLATT, G. I. 1993 Scaling laws for fully developed turbulent shear flows. Part 1. Basic hypotheses and analysis. *J. Fluid Mech.* **248**, 513–520.
- Buschmann, M. H. & Gad-el Hak, M. 2002 Reynolds-number-dependent scaling law for turbulent boundary layers. In *IUTAM symposium on Reynolds number scaling in turbulent flow*. Princeton University, NJ, USA.
- Cantwell, B. J. 2002 Introduction to Symmetry Analysis. Cambridge Press.
- Coles, D. E. 1956 The law of the wake in the turbulent boundary layer. *J. Fluid Mech.* 1, 191–226.
- George, W. K. & Castillo, L. 1997 Zero-pressure-gradient turbulent boundary layer. Applied Mech. Reviews 50, 689–729.
- Hydon, P. 2000 Symmetry Methods for Differential Equations A Beginner's Guide. Cambridge University Press.
- VON KÁRMÁN, T. 1930 Mechanische Aehnlichkeit und Turbulenz. Nachr. Ges. Wiss. Göttingen, Math. Phys. Kl. pp. 58–68, NACA TM 611.
- Lewkowicz, A. K. 1982 An improved universal wake function for turbulent boundary layers and some of its consequences. *Z. Flugwiss. Weltraumforsch* **9** (Heft 4), 513–520.

- MILLIKAN, C. B. 1938 A critical discussion of turbulent flows in channels and circular tubes. In *Proceedings of the Fifth International Congress of applied Mechanics*.
- Moser, R. D., Kim, J. & Mansour, N. N. 1999 Direct numerical simulation of turbulent channel flow up to $Re_{\tau} = 590$. Phys. Fluids 11 (4), 943–945.
- OBERLACK, M. 1999 Similarity in non-rotating and rotating turbulent pipe flows. J. Fluid Mech. 379, 1–22.
- OBERLACK, M. 2000 On symmetries on invarient solutions of laminar and turbulent wall-bounded flows. Zeitschrift für Angewandte Mathematik und Mechanik 80 (11–12), 791–800.
- OBERLACK, M. 2001a Lecture notes from CISM cource on Theories of Turbulence, Udine. To be published by Springer.
- OBERLACK, M. 2001b A unified approach for symmetries in plane parallel turbulent shear flows. J. Fluid Mech. 427, 299–328.
- OBERLACK, M. & Peters, N. 1993 Closure of the two-point correlation as a basis of Reynolds stress models. In So, R., Speziale, C., Launder, B., eds., Near wall turbulent flows, 85–94. Elsevier Science Publisher.
- OSTERLUND, J. M. 1999 Experimental studies of zero pressure-gradient turbulent boundary-layer flow. PhD thesis, Department of Mechanics, Royal Institute of Technology, Stockholm.
- ÖSTERLUND, J. M., JOHANSSON, A. V. & NAGIB, H. M. 2000a Comment on 'a note on the intermediate region in turbulent boundary layers' [Phys. Fluids 12, 2159]. *Phys. Fluids* 12, 2360–2363.
- ÖSTERLUND, J. M., JOHANSSON, A. V., NAGIB, H. M. & HITES, M. H. 2000b A note on the overlap region in turbulent boundary layers. *Phys. Fluids* **12** (1), 1–4.
- Perry, A. E., Hafez, S. & S., C. M. 2001 A possible reinterpretation of the Princeton superpipe data. *J. Fluid Mech.* 439, 395–401.
- Schultz-Grunow, F. 1940 Neues Reibungswiederstandsgesetz für glatte Platten. Tech. Rep. 8. Luftfahrtforschung, translated as New frictional resistance law for smooth plates, NACA TM-986, 1941.
- Skote, M. 2001 Studies of turbulent boundary layer flow through direct numerical simulation. PhD thesis, Department of Mechanics, Royal Institute of Technology, Stockholm.
- SMITH, D. & WALKER, J. 1959 Skin-friction measurements in incompressible flow. NASA TR R-26.
- Wosnik, M., Castillo, L. & George, W. K. 2000 A theory for pipe and channel flows. J. Fluid Mech. 421, 115–145.
- ZAGAROLA, M. V., PERRY, A. E. & SMITS, A. J. 1997 Log laws or power laws: The scaling in the overlap region. Phys. Fluids 9 (7), 2094–2100.

5. Appendix A: Lie group symmetry methods for differential equations

Basic descriptions of symmetry methods for differential equations are given by e.g. Hydon (2000), Oberlack (2001a), Oberlack (2001b) and Cantwell (2002). These methods can be viewed as a very general tool of obtaining similarity solutions, or invariants, of differential equations. We will below give a brief description of some of the key elements of such symmetry methods based on continuous Lie groups. An example is similarity type of solutions to partial differential equations, that effectively reduce the number of independent variables. The description below follows that of Oberlack (2001a). It is given here to illustrate the foundation of the ideas, in form of scaling laws, explored in the present paper.

The basic idea of symmetry methods for differential equations is to construct methods of finding transformations of the (ordinary or partial) differential equation that does not change its functional form with the change of variables.

$$\mathbf{F}(\mathbf{x}, \mathbf{y}, \mathbf{y}_i) = 0 \Leftrightarrow \mathbf{F}(\mathbf{x}^*, \mathbf{y}^*, \mathbf{y}_i^*) = 0 \tag{41}$$

where \mathbf{x} is the vector of independent variables, \mathbf{y} is the vector of dependent variables, index i denotes all derivatives of order i on \mathbf{y} and * denotes the transformed variables. Concentrating our efforts on Lie group symmetries we have analytic transformations that depend on a continuous parameter, ϵ . We write

$$S_{\epsilon}: \mathbf{x}^* = \phi(\mathbf{x}, \mathbf{y}; \epsilon) \quad \text{and} \quad \mathbf{y}^* = \psi(\mathbf{x}, \mathbf{y}; \epsilon).$$
 (42)

From a Taylor expansion with respect to ϵ we can derive the transformation groups in infinitesimal form,

$$S_{\epsilon} : \mathbf{x}^* = \mathbf{x} + \epsilon \xi(\mathbf{x}, \mathbf{y}) + O(\epsilon^2)$$

and $\mathbf{y}^* = \mathbf{y} + \epsilon \eta(\mathbf{x}, \mathbf{y}) + O(\epsilon^2)$ (43)

where $\xi = \frac{\partial \phi}{\partial \epsilon}\big|_{\epsilon=0}$ and $\eta = \frac{\partial \psi}{\partial \epsilon}\big|_{\epsilon=0}$ are the so called infinitesimals.

The striking feature about the Lie group method is that the transformation in infinitesimal form (only terms of order ϵ kept) is fully equivalent to the transformation in global form (as given by 42). The continuous form can hence be determined from the infinitesimals by integrating the first order system

$$\frac{\mathrm{d}\mathbf{x}^*}{\mathrm{d}\epsilon} = \xi(\mathbf{x}^*, \mathbf{y}^*), \quad \frac{\mathrm{d}\mathbf{y}^*}{\mathrm{d}\epsilon} = \eta(\mathbf{x}^*, \mathbf{y}^*)$$
(44)

with initial conditions $\mathbf{x}^* = \mathbf{x}$, $\mathbf{y}^* = \mathbf{y}$ at $\epsilon = 0$.

Furthermore, an important property of the Lie groups is that all linear combinations of distinct symmetry groups, $S_{\epsilon}^{(i)}$ also are symmetry groups. This property is also inherited by the infinitesimal form. The superposition property plays a central role in the determination of the scaling laws given in the results section.

To find all symmetries of a differential equation in a rigorous manner, the symmetry condition in equation 41 should be written in infinitesimal form. This is achieved by Taylor expanding equation 41 with respect to ϵ to first order in the same way as was done in equation 43. If we restrict ourselves (for algebraic simplicity) to a system of first order differential equations we may write this as

$$\mathbf{F}(\mathbf{x}, \mathbf{y}, \mathbf{y}_1) + \epsilon X \mathbf{F}(\mathbf{x}, \mathbf{y}, \mathbf{y}_1) + O(\epsilon^2) = 0. \tag{45}$$

We may note that the first term in equation 45 is equal to zero, according to equation 41, and we can write the symmetry condition in infinitesimal form as follows,

$$X\mathbf{F}\Big|_{\mathbf{F}=0} = 0. \tag{46}$$

X in equations 45 and 46 is (for a system of first order differential equations) defined as

$$X = \xi_i \frac{\partial}{\partial x_i} + \eta_j \frac{\partial}{\partial y_i} + \cdots$$
 (47)

The first terms given in equation 47 are together called the generator. In a somewhat simplified way we might say that to find the symmetry groups for a particular differential equation one introduces unknown infinitesimals ξ and η into equation 46. The result is an over-determined set of linear homogeneous differential equations that is solved for ξ and η . The infinitesimals are then transformed to global form through the Lie differential equation 44 with the initial condition given in connection with that equation.

We can define an invariant solution for a partial differential equation like the second equation in 41. If this equation admits a symmetry given in the form of a generator, X, $\mathbf{y} = \Theta(\mathbf{x})$ is an <u>invariant</u> solution to the partial differential equation if $\mathbf{y} - \Theta(\mathbf{x})$ is invariant under X, and $\mathbf{y} = \Theta(\mathbf{x})$ is a solution to the partial differential equation. Using the definition of a generator X from equation 47 a hyperbolic system is obtained

$$\xi_k(\mathbf{x}, \Theta) \frac{\partial \Theta_l}{\partial x_k} = \eta_l(\mathbf{x}, \Theta),$$
 (48)

Evaluation of scaling laws derived from Lie group symmetry methods 197 and the corresponding characteristic equation reads

$$\frac{\mathrm{d}x_1}{\xi_1(\mathbf{x}, \mathbf{y})} = \dots = \frac{\mathrm{d}x_m}{\xi_m(\mathbf{x}, \mathbf{y})} = \frac{\mathrm{d}y_1}{\eta_1(\mathbf{x}, \mathbf{y})} = \dots = \frac{\mathrm{d}y_m}{\eta_m(\mathbf{x}, \mathbf{y})}.$$
 (49)

Note that Θ is here replaced by \mathbf{y} .

Oberlack (2001a) identifies the symmetries of the Navier-Stokes and Euler equations, and analyzes further also the symmetries of the differential equation (derived e.g. by Oberlack & Peters (1993)) for the two-point correlation tensor. The two-point correlation tensor is defined as,

$$R_{ij}\left(\mathbf{x},\mathbf{r};t\right) = \overline{u_i'\left(\mathbf{x};t\right)u_j'\left(\mathbf{x}+\mathbf{r};t\right)}$$
(50)

where \mathbf{r} is the separation vector.

The Euler equations admit a ten parameter symmetry group, whereas the viscosity in the Navier-Stokes equations implies a symmetry-breaking that reduces this to a nine-parameter group. The elements can be qualitatively described as

- one group that describes translation in time (for which the Euler and Navier-Stokes equations obviously are invariant)
- three rotation groups that simply signify rotation of the coordinate system around each of the three axes (along with corresponding redefinition of the velocity components)
- three groups signifying extended Galilean invariance (in each of the three coordinate directions)
- pressure invariance (under addition of an arbitrary pressure term that is solely a function of time, or constant)
- two groups for the Euler equations and one for the Navier-Stokes equations, describing scaling invariance.

An important feature of analyzing the equation for the two-point correlation tensor, is that we can study essentially inviscid dynamics by restricting attention to separations that give length scales that are negligibly influenced by viscosity, and at the same time, restricting attention to positions in space where the influence of viscosity (e.g. through viscous stresses) is negligible. This means that all symmetries from the Euler equations carry over to this equation.

Note that this is not the case for the Reynolds stress transport equation, *i.e.* the single-point limit of the R_{ij} -equation, even if we restrict attention to positions where viscous stresses are negligible.

Hence, the equation for the two-point correlation tensor, admits a tenparameter symmetry group for length-scales (and positions) where the viscous influence is negligible. (The possibility for further symmetry groups of this equation has been investigated by Oberlack and coworkers.) However, restricting ourselves to plane turbulent shear-flow with all mean quantities dependent only on the wall-normal coordinate, x_2 , leaves us with only four of the original ten symmetries. These symmetries are the two scaling symmetries, \overline{X}_{s_1} and \overline{X}_{s_2} , here reduced due to the one-dimensional mean flow, $\overline{u}_1 = \overline{u}_1(x_2)$, the traditional Galilean invariance in the streamwise direction, $\overline{X}_{\overline{u}_1}$, and the spatial translation symmetry $\overline{X}_{\overline{u}_2}$ (which is the only part left of the extended Galilean invariance in the wall-normal direction).

The symmetry group for the R_{ij} -equation, with the above described restrictions, can then be written as

$$\overline{X}_{s_1} = x_2 \frac{\partial}{\partial x_2} + \overline{u}_1 \frac{\partial}{\partial \overline{u}_1} + 2\overline{p} \frac{\partial}{\partial \overline{p}} + r_i \frac{\partial}{\partial r_i} + 2R_{ij} \frac{\partial}{\partial R_{ij}} , \qquad (51)$$

$$\overline{X}_{s_2} = -\overline{u}_1 \frac{\partial}{\partial \overline{u}_1} - 2\overline{p} \frac{\partial}{\partial \overline{p}} - 2R_{ij} \frac{\partial}{\partial R_{ij}}.$$
 (52)

$$\overline{X}_{\overline{u}_1} = \frac{\partial}{\partial \overline{u}_1} \tag{53}$$

$$\overline{X}_{\overline{u}_2} = \frac{\partial}{\partial r_2} \tag{54}$$

Remembering the superposition property of Lie group algebra, we can combine the four symmetries into ,

$$\overline{X} = k_{s_1} \overline{X}_{s_1} + k_{s_2} \overline{X}_{s_2} + k_{\overline{u}_1} \overline{X}_{\overline{u}_1} + k_{x_2} \overline{X}_{\overline{u}_2}. \tag{55}$$

where $k_{s_1}, k_{s_2}, k_{\overline{u}_1}$ and k_{x_2} are constants (parameters).

We should keep in mind that the above with k_{s_1} , k_{s_2} being independent is only valid in situations where viscous influence is negligible. For cases with significant influence of viscosity it is straightforward to derive the symmetry breaking relation that requires that $k_{s_2} = 2k_{s_1}$.

The characteristic form of the hyperbolic equation 48 for the inviscid case reads

$$\frac{\mathrm{d}x_2}{k_{s_1}x_2 + k_{x_2}} = \frac{\mathrm{d}r_{[k]}}{k_{s_1}r_{[k]}} = \frac{\mathrm{d}\overline{u}_1}{(k_{s_1} - k_{s_2})\overline{u}_1 + k_{\overline{u}_1}} = \frac{\mathrm{d}R_{[ij]}}{2(k_{s_1} - k_{s_2})R_{[ij]}} , \qquad (56)$$

where [] means that there is no summation over the indices. By changing the values of the two scaling symmetry constants, k_{s_1} and k_{s_2} , scaling laws for different shear-flow situations can be derived.

6. Appendix B: Derivation of an expression for the Reynolds shear-stress in the wake region

Using the exponential velocity defect law, derived by use of Lie group symmetry methods, an expression for the corresponding Reynolds shear-stress profile is here derived, which is accurate to first order in $\gamma = u_{\tau}/\overline{u}_{\infty}$. The streamwise momentum equation for a zero pressure-gradient boundary layer, neglecting the viscous stress, and the continuity equation read

$$\overline{u}_1 \frac{\partial \overline{u}_1}{\partial x_1} + \overline{u}_2 \frac{\partial \overline{u}_1}{\partial x_2} = -\frac{\partial \overline{u}_1' u_2'}{\partial x_2}$$
(57)

$$\frac{\partial \overline{u}_1}{\partial x_1} + \frac{\partial \overline{u}_2}{\partial x_2} = 0 (58)$$

The velocity defect is defined as,

$$\frac{\overline{u}_{\infty} - \overline{u}_{1}}{u_{\pi}} = F(\eta) \tag{59}$$

where $\eta = y/\Delta$ and $\Delta = \delta_*/\gamma$ is the Clauser-Rotta boundary layer thickness. Differentiating \overline{u}_1 with respect to x_1 and x_2 , making use of equation 59, yields

$$\frac{\partial \overline{u}_1}{\partial x_1} = -u_\tau \frac{\partial \eta}{\partial x_1} F'(\eta) - \frac{\mathrm{d}u_\tau}{\mathrm{d}x_1} F(\eta) \tag{60}$$

for the x_1 derivative and

$$\frac{\partial \overline{u}_1}{\partial x_2} = -\frac{u_\tau}{\Delta} F'(\eta) \tag{61}$$

for the x_2 derivative. Prime here denotes differentiation with respect to η . The expression for the x_1 derivative of u_{τ} can be found from the logarithmic friction law, which, by Österlund *et al.* (2000*b*), was found to agree very well with experimental data. It reads

$$\frac{u_{\tau}}{\overline{u}_{\infty}} = \left(\frac{1}{\varkappa} \ln Re_{\theta} + C\right)^{-1} \tag{62}$$

Differentiating equation 62 with respect to x_1 and multiplying with θ gives

$$\frac{\theta}{\overline{u}_{\infty}} \frac{\mathrm{d}u_{\tau}}{\mathrm{d}x_{1}} = -\theta \left(\frac{1}{\varkappa} \ln Re_{\theta} + C \right)^{-2} \frac{1}{\varkappa \theta} \frac{\mathrm{d}\theta}{\mathrm{d}x_{1}} = -\frac{\gamma^{4}}{\varkappa}$$
 (63)

since

$$\frac{\mathrm{d}\theta}{\mathrm{d}x_1} = \gamma^2 \tag{64}$$

for a zero pressure-gradient boundary layer.

We will below also need $\frac{d\delta_*}{dx_1}$, which we can write as

$$\frac{d\delta_*}{dx_1} = \frac{d(H_{12}\theta)}{dx_1} = H_{12}\gamma^2 + \theta \frac{dH_{12}}{dx_1}.$$
 (65)

By inserting the definition 59 into the expressions for δ_* and θ we readily obtain

$$H_{12} = \int_0^\infty F(\eta) d\eta / \left(\int_0^\infty F(\eta) d\eta - \gamma \int_0^\infty F^2(\eta) d\eta \right) = 1 / \left(1 - \gamma \int_0^\infty F^2(\eta) d\eta \right)$$

$$(66)$$

where the second identity follows from the definition of Δ . Hence we obtain (by use of equation 63),

$$\frac{\mathrm{d}H_{12}}{\mathrm{d}x_1} = -\frac{H_{12}^2}{\varkappa\theta}\gamma^4 \int_0^\infty F^2(\eta)\mathrm{d}\eta \tag{67}$$

and thereby

$$\frac{\mathrm{d}\delta_*}{\mathrm{d}x_1} = H_{12}\gamma^2 + O(\gamma^4). \tag{68}$$

We can now compute the derivatives of η as

$$\frac{\partial \eta}{\partial x_1} = -\frac{\eta}{\Delta} \frac{d\Delta}{dx_1} = -\frac{\eta}{\Delta} \left(\frac{1}{\gamma} \frac{d\delta_*}{dx_1} - \frac{\delta_* \overline{u}_\infty}{u_\tau^2} \frac{du_\tau}{dx_1} \right) = -\frac{\eta}{\Delta} H_{12} \gamma \left(1 + \frac{1}{\varkappa} \gamma + O(\gamma^2) \right)$$
(69)

and

$$\frac{\partial \eta}{\partial x_2} = \frac{1}{\Delta}.\tag{70}$$

Multiplying with Δ/u_{τ} and making use of equations 69 and 63 we can rewrite expression 60 as

$$\frac{\Delta}{u_{\tau}} \frac{\partial \overline{u}_{1}}{\partial x_{1}} = H_{12} \gamma \left(\eta F'(\eta) + \frac{1}{\varkappa} \gamma (\eta F(\eta))' + O(\gamma^{2}) \right)$$
 (71)

and 61 as

$$\frac{\Delta}{u_{\tau}} \frac{\partial \overline{u}_{1}}{\partial x_{2}} = -F'(\eta). \tag{72}$$

Finally, to complete the left hand side of equation 57 it also necessary to calculate \overline{u}_2 . Using the continuity equation 58 and equation 71 we can express \overline{u}_2 as

$$\overline{u}_2 - \overline{u}_{2_0} = -u_\tau H_{12} \gamma \left\{ \int_{\eta_0}^{\eta} \xi F'(\xi) d\xi + O(\gamma) \right\}, \tag{73}$$

where η_0 , here is chosen as the outer limit of the log-layer. To estimate \overline{u}_{2_0} we assume a logarithmic velocity defect law, $F_{log}(\eta)$, in the region $0 < \eta < \eta_0$,

$$F_{log}(\eta) = -\frac{1}{\varkappa} \ln \eta + C, \ \eta \le \eta_0. \tag{74}$$

This assumption will overestimate \overline{u}_{2_0} with an error in \overline{u}_{2_0} of order γ^2 . Introducing equation 74 into the continuity equation, 58, and integrating gives the following expression for \overline{u}_{2_0}

$$\overline{u}_{2_0} = H_{12} \frac{u_\tau \gamma}{\varkappa} \eta_0 + O(\gamma^2) \tag{75}$$

Furthermore, it is assumed that the Reynolds shear-stress normalized with u_{τ}^2 is a function of η , *i.e.*

$$g(\eta) = -\frac{\overline{u_1' u_2'}}{u^2}. (76)$$

Using equation 70 to rewrite the right hand side of equation 57 gives, together with equations 59, 71, 72 and 76 a momentum equation of the following form

$$\frac{1}{H_{12}}g'(\eta) = \eta F'(\eta) +$$

$$+ \gamma \left\{ \frac{1}{\varkappa} \left(\eta F(\eta) \right)' - F'(\eta) \left(\int_{\eta_0}^{\eta} F(\xi) d\xi + \eta_0 F(\eta_0) + \frac{\eta_0}{\varkappa} \right) \right\} + O(\gamma^2)$$
(77)

This equation can be solved in the region where the exponential velocity defect law, (14), was found to agree well with experimental data.

We may express the normalized Reynolds shear-stress as a series expansion in γ ,

$$g(\eta) = g_0(\eta) + \gamma g_1(\eta) + O(\gamma^2) \tag{78}$$

To zeroth order accuracy in γ we get

$$g_0'(\eta) = H_{12}\eta F'(\eta).$$
 (79)

Integration with respect to η gives

$$g_0(\eta) - g_0(\eta_0) = H_{12} \frac{C_1}{C_2} \left\{ (C_2 \eta + 1) \exp(-C_2 \eta) - - (C_2 \eta_0 + 1) \exp(-C_2 \eta_0) \right\},$$
(80)

in the region where the velocity defect exhibits an exponential behaviour. For first order accuracy in γ we obtain, by combining equations 77 and 78, the following correction term to the Reynolds shear-stress,

$$g_{1}(\eta) - g_{1}(\eta_{0}) = H_{12} \frac{C_{1}}{2C_{2}\varkappa} \left\{ 2C_{2} (\eta - \eta_{0}) \exp(-C_{2}\eta) + \right. \\ + C_{1}\varkappa \exp(-2C_{2}\eta) - 2C_{1}\varkappa (C_{2}\eta_{0} + 1) \exp(-C_{2}(\eta - \eta_{0})) + \right. \\ \left. + C_{1}\varkappa (2C_{2}\eta_{0} + 1) \exp(-C_{2}\eta_{0}) \right\}$$

$$(81)$$

The complete expression for the normalized shear-stress, to first order accuracy in γ , is found by introducing 80 and 81 into equation 78.

Paper 6

Universality of probability density distributions in the overlap region in high Reynolds number turbulent boundary layers

By Björn Lindgren¹, Arne V. Johansson¹ and Yoshiyuki Tsuji²

¹Dept. of Mechanics, KTH, SE-100 44 Stockholm, Sweden ²Dept. of Energy Eng. & Science, Nagoya University, Nagoya 464-8603, Japan

Submitted for publication in Phys. of Fluids

The probability density functions, PDFs, in high Reynolds number turbulent boundary layers have been studied and the hypothesis of self-similar, normalized, PDFs has been tested using the KTH data-base of high Reynolds number zero pressure-gradient turbulent boundary layer flow. The self-similarity was tested using the Kullback-Leibler divergence measure and it was found that the region of self-similar PDFs starts at about 180 viscous wall units and ends at about 0.18 boundary layer thicknesses (δ_{95}). This region is slightly larger than the logarithmic overlap region. An outer limit for the logarithmic overlap region is defined using an assumed form of the streamwise rms velocity distribution in inner scaling allowing a logarithmic velocity law for the velocity to be derived from the PDF equation. This outer limit agrees well with previous outer limits for the log-layer. The PDFs in the log-layer are close to Gaussian allowing a Gram-Charlier expansion to be used for approximating the measured PDFs. Within the range studied the expansion shows no Reynolds number trend for its coefficients which are related to skewness, flatness, hyper skewness and hyper flatness.

1. Introduction

The scaling of the mean velocity profile and other flow quantities in the overlap region has recently attracted much interest. In the characterization of the flow features in this region and their degree of self-similarity we direct our attention, in this study, to the probability density distributions of the fluctuating streamwise velocity in zero pressure-gradient turbulent boundary layer flows. For this purpose we analyze data from the KTH data-base (Österlund (1999)) that covers a Reynolds number range of about $2700 < Re_{\theta} < 27000$.

The aim of the present study was to test the hypothesis of self-similar Probability Density Functions, PDFs, of the streamwise velocity in the log-layer of high Reynolds number turbulent boundary layers. Requiring self-similar PDFs in the log-layer is a very strict criteria for self-similarity in the region. The idea of self-similar PDFs in the overlap region was proposed by Tsuji & Nakamura (1999) who tested the idea in an experimental study of turbulent boundary layers at relatively low Reynolds numbers. They found no extended region of self-similar PDFs in their study because of the low Reynolds numbers, $Re_{\theta} < 4000$, that according to Österlund et al. (2000) are too small to contain a logarithmic region. However some positive indications were found since the region of self-similar PDFs appears to be larger than the logarithmic region and thus appears at lower Reynolds numbers.

In analogy with present tests Dinavahi et al. (1995) found from channel flow DNS data at low Reynolds number, $Re_{\tau} \leq 395$, that outside the buffer region the PDFs of the velocity fluctuations are independent of wall-normal distance and Reynolds number.

2. The KTH data-base of zero pressure-gradient turbulent boundary layer flow

The measurements used here to evaluate the hypothesis of self-similar probability density distributions in the logarithmic overlap region were taken in the low turbulence level MTL wind-tunnel at KTH. The excellent flow quality of that wind-tunnel is reported in Lindgren & Johansson (2002). For instance the streamwise turbulence intensity is less than 0.02% and the total pressure variation is less than 0.01% across the test section cross section. The measurements were performed on a flat plate mounted in the test section with single- and cross-wire hot-wire probes. The friction velocity was determined by various methods including oil-film interferometry, Preston tubes and velocity profile fitting using DNS data. The wall position was measured using a laser distance meter and microscope. All the measurements were originally reported in Österlund (1999).

3. Results

3.1. Kullback-Leibler divergence

The evaluation of the shape of the PDFs is made using the Kullback Leibler Divergence, KLD, extensively used in information theory, see Kullback (1959). It is a positive scalar measure of probability distribution differences which is sensitive to small variations and it is zero for equal distributions. Robert & Sommeria (1991) analyzed the potential for the use of KLD in fluid dynamics. With discrete probability density distributions the KLD is defined as follows,

$$D(P||Q) \equiv \sum_{\{s\}} P(s_i) \ln(P(s_i)/Q(s_i)),$$
 (1)

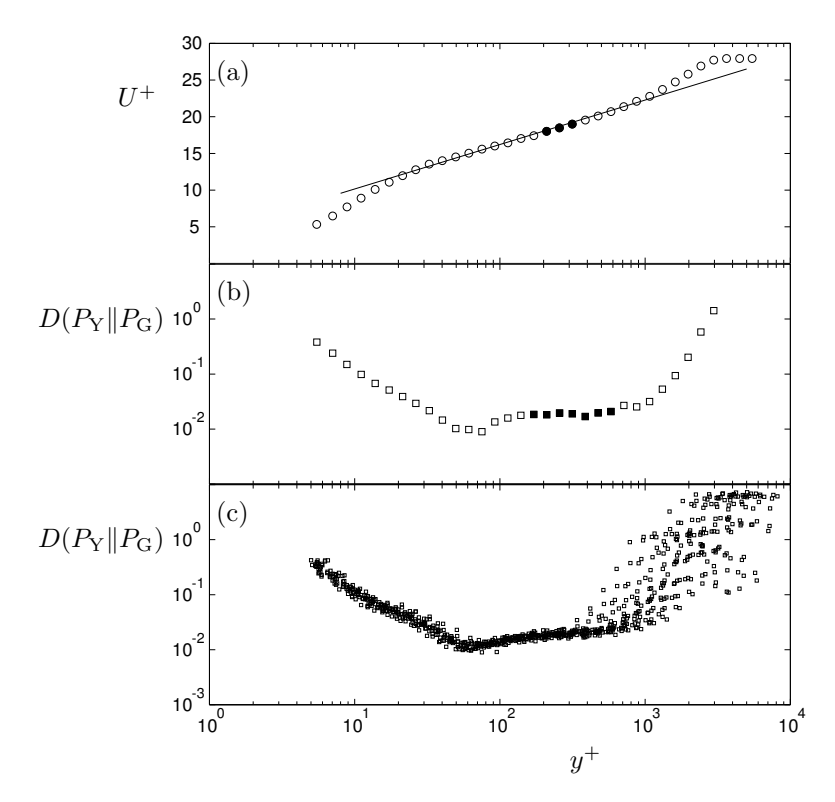


FIGURE 1. (Top) Mean velocity profile in inner scaling at $Re_{\theta} = 9707$. The filled markers correspond to the log-layer, $y^+ > 200 \& y/\delta_{95} < 0.15$. The solid line represents the log law with $\varkappa = 0.38$ and B = 4.1. (Middle) The KL-divergence of the streamwise velocity at $Re_{\theta} = 9707$. The filled markers correspond to the constant divergence region. (Bottom) The KL-divergence for 18 velocity profiles with wire length $l^+ < 15$ at $2532 < Re_{\theta} < 12633$.

where P(s) and Q(s) are two discrete probability distributions. Here P(s) was chosen to be the experimentally determined PDF, P_Y , and Q(s) was chosen as the Gaussian distribution, $P_{\rm G}$, see Tsuji & Nakamura (1999). In the log-layer of a turbulent boundary layer the PDFs are close to the Gaussian distribution which makes it a good choice for the comparisons. The entire tails of the PDFs are used in the evaluation so no truncation of the data have been done.

If the shape of the PDFs is self-similar in the log-layer the KLD measure will be constant in that region. In figure 1, (middle), the KLD measure is shown for the streamwise velocity in inner scaling at $Re_{\theta} = 9707$. The region with constant divergence starts at $y^{+} \approx 150 - 180$ and ends at $y/\delta_{95} \approx 0.3$ (filled markers). This region can be compared to the log region shown in figure 1 (top), defined by Österlund et al. (2000) to be between $y^{+} > 200$ and $y/\delta_{95} < 0.15$. The inner limit of the constant divergence region corresponds well to the inner limit of the log region. The outer limit of the constant divergence region is twice as large as the corresponding limit of the log region.

It is noteworthy that at a wall normal position of approximately 70 plus units, independent of the Reynolds number, there is a minimum in the KLD, see figure 1c, i.e. the PDFs are here close to Gaussian. This wall normal position corresponds to the maximum of the hump in the mean velocity profile as seen in figure 1a. This minimum in the KLD reinforces the indication that there is a physical explanation to the "hump" in the mean velocity profile although at this moment it is still unexplained. The "hump" has previously been explained by non accurate determination of the location of the solid wall and also by probe effects, see e.g. the corrections introduced by MacMillan (1956) when Pitot tubes are used. Here hot-wire anemometry is used and the experimental uncertainties are not large enough to completely explain the phenomenon of the "hump" in velocity profile. As will be seen later in this paper second order corrections to the log-law can at least partly explain the "hump", (see also Oberlack (2001) and Lindgren et al. (2002)).

3.2. Logarithmic mean velocity law

A partial differential equation coupling the mean streamwise velocity with the streamwise rms velocity and the Reynolds shear-stress can be derived assuming self-similar PDFs, zero wall-normal component and zero streamwise pressure gradient. In inner variables it reads

$$\frac{\partial^2 U^+}{\partial y^{+2}} - C u_{\text{rms}}^+ \frac{\partial u_{\text{rms}}^+}{\partial y^+} = 0, \tag{2}$$

$$C = \frac{-\langle u'v'\rangle}{u_{\rm rms}^2},\tag{3}$$

For a complete derivation of equations 2 and 3 see Tsuji & Nakamura (1999). See also Pope (1985). Now, assuming the following expression (see Tsuji & Nakamura (1999)) for the rms distribution,

$$u_{\rm rms}^{+} = \alpha + \beta (y^{+} - \gamma)^{-1} + h.o.t.$$
 (4)

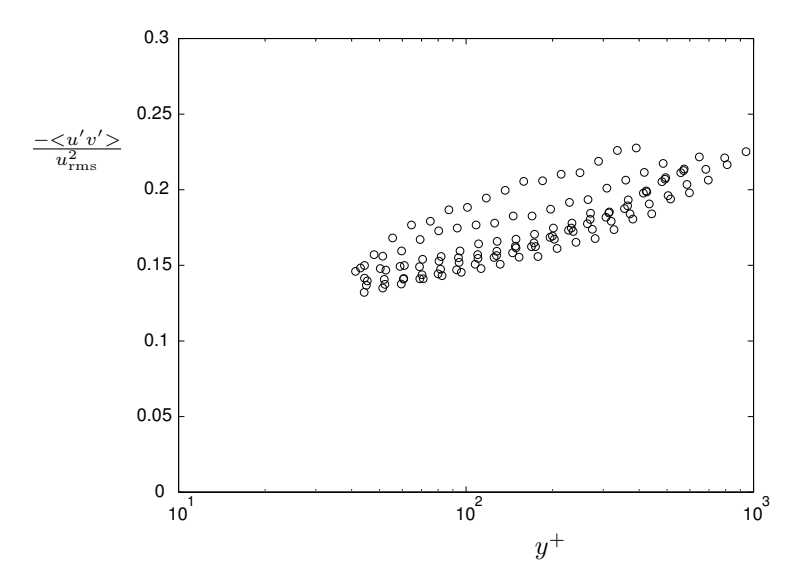


FIGURE 2. The Reynolds shear stress normalized $u_{\rm rms}^2$. Circles: experimental data at $6928 < Re_{\theta} < 17621$.

where α , β and γ are constants to be determined and the following expression for C,

$$C = C_1 + \epsilon \log_{10} \left(\frac{y^+}{10^{C_1/\epsilon}} \right), \tag{5}$$

with $C_1 = 0.2$ and a small value for $\epsilon \ (\approx 0.1)$ from experimental data, see figure 2, which means that $C \approx C_1$ in the log-layer. We can then derive an expression for the mean velocity profile from equations 2 and 3. The velocity profile in the log region then reads

$$U^{+} = \frac{1}{\varkappa} \ln(y^{+}) + B + \frac{C_1 \beta^2 \varkappa - \gamma}{\varkappa y^{+}} + h.o.t.$$
 (6)

where B is a constant. One can note that there is an interesting direct relationship between the Kármán constant, \varkappa , and the constants α , β , and C_1 , $\varkappa = \ln(10)/(C_1\alpha\beta)$. The constants α , β were determined from experimental data, with $\gamma = 5$, and found to be slightly dependent on Reynolds number with $\alpha = 0.33Re_{\theta}^{0.21}$ and $\beta = 91.8Re_{\theta}^{-0.21}$, see figure 3. Note that the product of α and β is constant and independent of Reynolds number which gives a Kármán constant, \varkappa , that is independent of Reynolds number.

Although the second order term in equation 6 is dependent on Reynolds number, it is always small, $< 6/(\varkappa y^+)$, and decreasing with Reynolds number. A similar type of log-law can be derived from Lie group symmetry methods, see Oberlack (2001), and it was evaluated using the KTH data-base by Lindgren

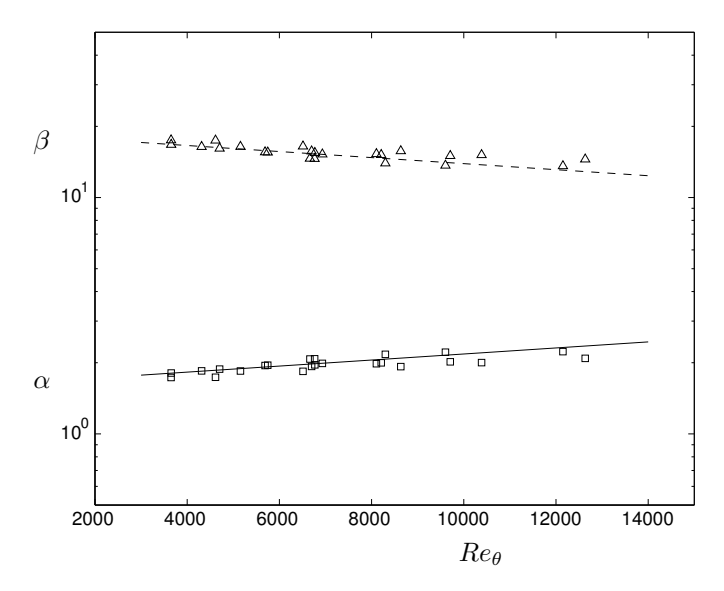


FIGURE 3. The coefficients α and β as function of Reynolds number; circles: α , triangles: β , solid and dashed lines: linear fit to experimental data.

et al. (2002) who found $C_1\beta^2\varkappa - \gamma \approx 5$. Which agrees well with the values found here, but since this value is small in the considered range compared to $\varkappa y^+$ its influence on the log-law velocity profile is also small and of negligible influence on high Reynolds number boundary layers.

In figure 4 the measured $u_{\rm rms}^+$ profile at Reynolds number at $Re_\theta=9707$, (circles) is plotted together with equation 4 (solid line). The filled markers correspond to a range from the start of the log-layer to the outer limit where equation 4 fits the measured data. This point is located, in outer scaling, around $y/\delta_{95}\approx 0.15-0.20$ independent of Reynolds number and is here considered as the outer limit of the log region. It corresponds well to the Österlund et al. (2000) results, who determined the outer limit to be around $y/\delta_{95}\approx 0.15$, although the log-layer is here extended slightly outwards.

When using the herein determined limits of the log-layer $(y^+ > 150 - 180$ and $y/\delta_{95} < 0.15 - 0.20)$, the constants \varkappa and B was found to agree well with the results of Österlund *et al.* (2000) who found \varkappa to be 0.38 and B to be 4.1.

3.3. Gram-Charlier expansion

The PDFs can be expanded in a Gram-Charlier series, a series expansion based on orthonormal Hermite polynomials proposed by Kampé de Fériet (1966), see also Lumley (1970). The Gram-Charlier expansion is well suited for expanding

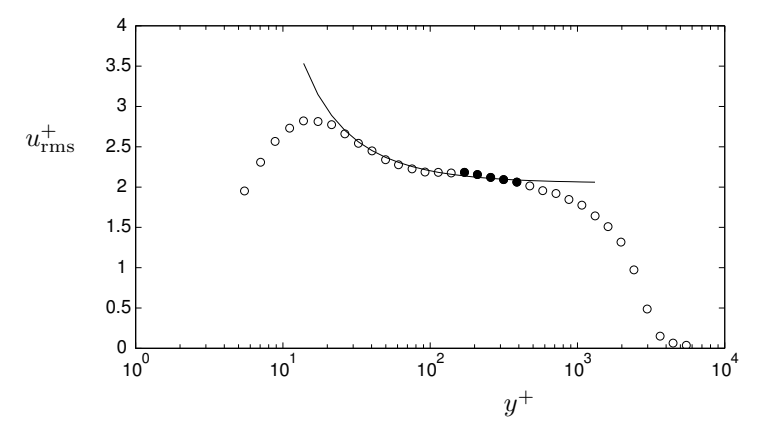


FIGURE 4. The $u_{\rm rms}$ profile at $Re_{\theta} = 9707$. solid line: equation 4; circles: measured data; filled circles: log region.

probability density distributions that are close to the Gaussian shape. Previously, Durst $et\ al.\ (1992)$ applied the Gram-Charlier expansion to wall bounded turbulent flows. They found that the Gram-Charlier expansion gives a good approximation to the measured PDF also for higher order moments. Since its coefficients are directly related to the moments, a study of the higher order coefficients related to hyper skewness and hyper flatness gives further information on Reynolds number dependence etc. The definition of a Gram-Charlier expansion reads

$$p(x) = c_0 + \phi(x) + \frac{c_1}{1}\phi'(x) + \dots + \frac{c_n}{n!}\phi^{(n)}(x)$$
 (7)

$$\phi^{(n)}(x) = (-1)^n H_n(x)\phi(x) \tag{8}$$

where $H_n(x)$ are Hermite functions and $\phi(x)$ is the Gaussian distribution. The coefficient $c_0 = 1$, $c_1 = c_2 = 0$, $c_3 = -S$ and $c_4 = F - 3$ where S and F are the skewness and flatness factors respectively. Higher order coefficients are related to hyper skewness and hyper flatness in the following way

$$c_5 = -H_S + 10S, (9)$$

$$c_6 = H_F - 15F + 30, (10)$$

where H_S is the hyper skewness and H_F hyper flatness defined as the fifth moment normalized by the standard deviation to the power of 5 and the sixth moment normalized by the standard deviation to the power of 6.

The expansion was truncated at $\phi^{(6)}(x)$ due to increasing measurement uncertainties for higher moments. In figure 5 the measured PDF at $Re_{\theta} = 9707$ and $y^{+} = 387$ is shown together with the Gram-Charlier expansion and the Gaussian PDF. The Gram-Charlier expansion follows the experimental data

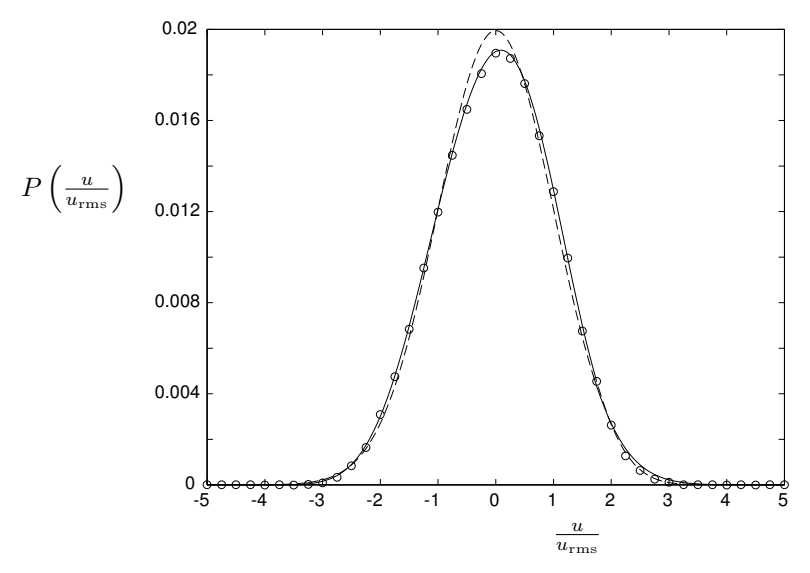


FIGURE 5. The probability density function in the log-layer at $Re_{\theta} = 9707$ and $y^{+} = 387$. solid line: Gram-Charlier expansion; dashed line: Gaussian distribution; circles: experimental data. $(c_{3} = 0.06, c_{4} = -0.32, c_{5} = -0.29, c_{6} = 0.68)$

well in the log region. The difference between the moments calculated directly from experimental data and from the Gram-Charlier expansion is very small in most parts of the boundary layer. Significant differences were found only very close to the wall and at the outer edge of the boundary layer. These regions of the boundary layer are of course not considered here.

Note that the measured PDFs in the log-layer are close to the Gaussian PDF which was already indicated in figure 1c where the Kullback-Leibler divergence was shown to be small in this region.

In figure 6 the Gram-Charlier expansions for all wall-normal positions in the log-layer at Reynolds numbers between $4312 < Re_{\theta} < 9707$ are shown. (In total 57 PDFs). The collapse is very good and further emphasizes the hypothesis of self-similar PDFs in the log-layer indicated by the constant divergence region in figure 1c.

To further investigate the variation in the PDFs with wall-normal distance and Reynolds number the individual coefficients, c_3 to c_6 in the Gram-Charlier expansion corresponding to the skewness, flatness, hyper skewness and hyper flatness as mentioned above, are plotted against Reynolds number in figure 7. It can be seen that the variation in Reynolds number is not larger than the variation with wall-normal position and that variation is very small also for the

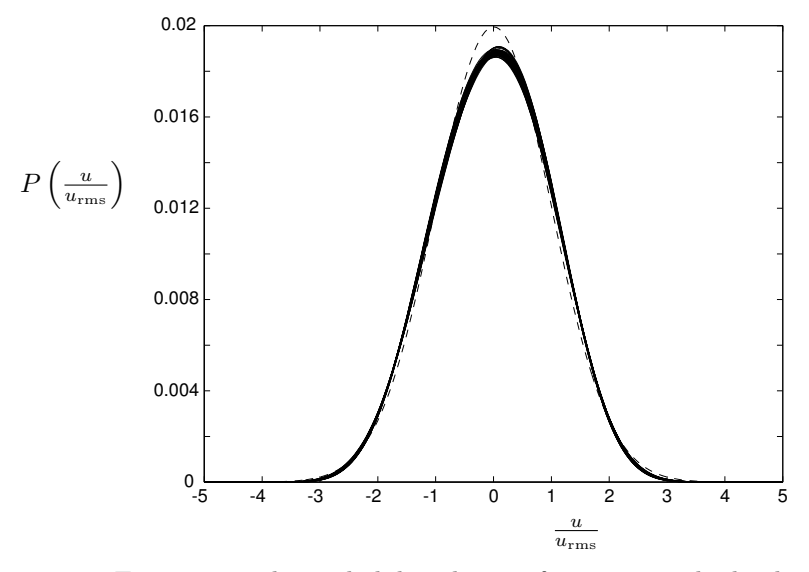


FIGURE 6. The probability density functions in the log-layer at $4312 < Re_{\theta} < 12633$ (57 density distributions). solid line: Gram-Charlier expansion; dashed line: Gaussian distribution.

higher order coefficients c_5 and c_6 . This strongly indicates the existence of a self-similar velocity region in the overlap of a turbulent zero pressure gradient boundary layer.

4. Concluding remarks

The hypothesis of self-similar probability density functions in the overlap region of a turbulent zero pressure gradient boundary layer at high Reynolds numbers have been tested and confirmed. The Kullback-Leibler divergence was used to quantify the degree of self-similarity. The region of self-similarity was found to be slightly larger than the logarithmic overlap region starting at approximately the same wall-normal position, $y^+ \approx 150 - 180$, but extending further out towards the wake region, $y/\delta_{95} \approx 0.3$.

A minimum in the Kullback-Leibler divergence was found at a wall-normal position of approximately 70 viscous length units independent of Reynolds number. This minimum corresponds to the maximum in the "hump" in the mean velocity profile towards the inner limit of the logarithmic region. A second order correction to the classic log-law can be derived from the PDF equation. This correction could partly explain the "hump" but the correction is very small compared to the leading order term and its relative influence decreases with Reynolds number.

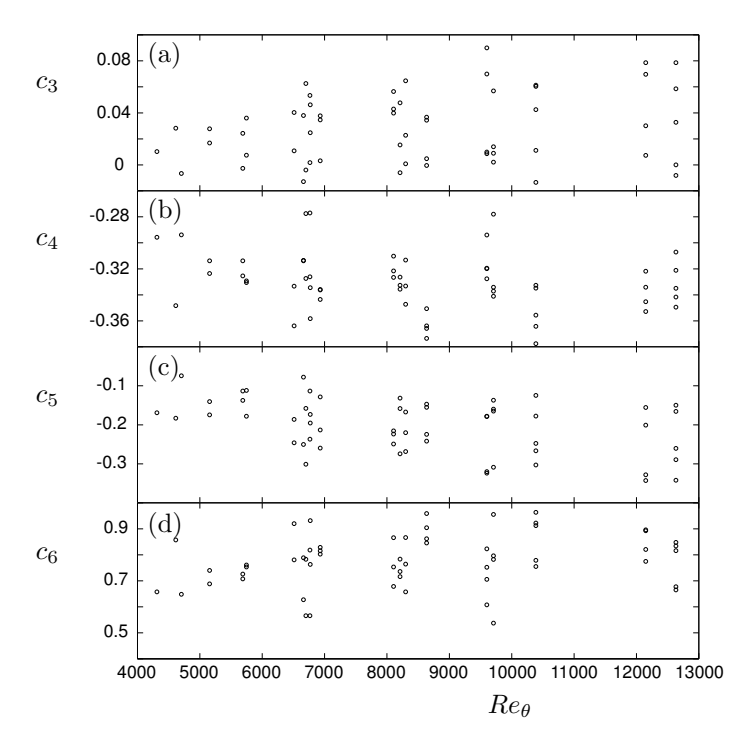


FIGURE 7. Gram-Charlier coefficients $c_3 - c_6$. (a) -S; (b) F-3; (c) $-H_s+10S$; (d) $H_F-15F+30$.

From the derivation of a logarithmic velocity law from the partial differential equation of the PDF an outer limit for the log-layer could be estimated and was found to be $y/\delta_{95}\approx 0.15-0.18$ which is close to the earlier estimation of $y/\delta_{95}\approx 0.15$ by Österlund et al. (2000). Estimating the Kármán constant, \varkappa , and the additive constant, B, using the new limits for the logarithmic region gives values that also agree well with the Österlund et al. (2000) results.

The measured PDFs were approximated by a Gram-Charlier expansion to the sixth order, and were found to be self-similar in the log-layer. All PDFs in the log-layer at different wall-normal positions and Reynolds numbers were found to collapse onto one distribution. The Gram-Charlier coefficients which are related to skewness, flatness, hyper skewness and hyper flatness were found to be constant with Reynolds number at sufficiently high Reynolds numbers (> 4000). This strongly indicates a self-similar behaviour of the PDFs in the logarithmic overlap region.

5. Acknowledgment

Dr. Jens Österlund is gratefully acknowledged for providing us the experimental data necessary for this study. Financial support from the Swedish Research Council is also gratefully acknowledged.

References

- DINAVAHI, S. P. G., BREUER, K. S. & SIROVICH, L. 1995 Universality of probability density functions in turbulent channel flow. *Phys. Fluids* 7 (5), 1122–1129.
- DURST, F., JOVANOVIC, J. & JOHANSSON, T. G. 1992 On the statistical properties of truncated Gram-Charlier series expansions in turbulent wall-bounded flows. *Phys. Fluids A* 4 (1), 118–126.
- Kampé de Fériet, J. 1966 David Taylor model basin report no. 2013. *Tech. Rep.*. Naval Ship Research and Development Center, Washington D.C.
- Kullback, S. 1959 Information theory and statistics. Wiley, London.
- LINDGREN, B. & JOHANSSON, A. V. 2002 Evaluation of the flow quality in the low-speed MTL wind-tunnel. Trita-Mek Report 2002-13. Department of Mechanics, KTH.
- LINDGREN, B., ÖSTERLUND, J. M. & JOHANSSON, A. V. 2002 Evaluation of scaling laws derived fron lie group symmetry methods in turbulent boundary layers. In *Proc. 40th Aerospace Sciences Meeting & Exhibit. AIAA 2002-1103*. Reno, Nevada, USA.
- Lumley, J. L. 1970 Stochastic tools in turbulence. Academic, New York.
- MACMILLAN, F. A. 1956 Experiments on Pitot-tubes in shear flow. $Tech.\ Rep.\ 3028.$ Aero. Res. Counc. R. & M.
- OBERLACK, M. 2001 A unified approach for symmetries in plane parallel shear flows. J. Fluid Mech. 427, 229–328.
- ÖSTERLUND, J. M. 1999 Experimental studies of zero pressure-gradient turbulent boundary-layer flow. PhD thesis, Department of Mechanics, Royal Institute of Technology, Stockholm.
- ÖSTERLUND, J. M., JOHANSSON, A. V., NAGIB, H. M. & HITES, M. H. 2000 A note on the overlap region in turbulent boundary layers. *Phys. Fluids* **12** (1), 1–4.
- POPE, S. B. 1985 PDF methods for turbulent reactive flows. *Prog. Energy Combust. Sci.* 11, 119.
- Robert, R. & Sommeria, J. 1991 Statistical equilibrium states for two-dimensional flows. J. Fluid Mech. 229, 291–310.
- TSUJI, Y. & NAKAMURA, I. 1999 Probability density function in the log-law region of low Reynolds number turbulent boundary layer. *Phys. Fluids* 11 (3), 647–658.

Paper 7

Measurements in a plane asymmetric diffuser with 8.5° opening Angle. Part I: General flow characteristics

By Björn Lindgren, Olle Törnblom and Arne V. Johansson

Dept. of Mechanics, KTH, SE-100 44 Stockholm, Sweden

To be submitted

The flow in an asymmetric plane diffuser with opening angle 8.5° has been studied in detail experimentally. The inlet condition was fully developed turbulent channel flow at a Reynolds number based on the inlet channel height and the friction velocity of $Re_{\tau} = 2000$. The mean and fluctuating velocities have been measured in all directions (streamwise, spanwise and wall-normal). A separated region is found on the inclined wall with a mean separation point at 9 and a mean reattachment point at 31 inlet channel heights downstream the diffuser inlet. Separation never occurs upstream of 5 inlet channel heights and reattachment never occurs downstream of 35 inlet channel heights. Two regions of special interest have been observed in the flow. A strong shear-layer between the separated region and the "outer" flow fluctuates substantially in wall-normal direction, interacting with the large scale vortices in the separated region. It is also influenced by the large adverse pressure-gradient and the rapid change in flow direction at the diffuser inlet corner on the inclined wall. The static wall pressure through the diffuser was measured and compared to a case where vortex generators are used to suppress the separation. The pressure coefficient was found to be almost 10% higher at the diffuser outlet for the case with vortex generators.

1. Introduction

Separation and the need for controlling the separation are essential in many applications of fluid flows. Particularly diffuser flows, *i.e.* duct flows subjected to a positive pressure gradient in the streamwise direction, are very common in many industrial applications. The aim of this study is to determine the characteristics of the separated plane asymmetric diffuser flow, to provide a reliable data-base for the turbulence modeling community and to identify flow mechanisms that can be used in future schemes for efficient separation control.

Many studies have been performed on geometry induced separated flow and adverse pressure gradient flows with separation. The backward facing step and the blunt plate have been investigated by e.g. Cherry et al. (1984), Eaton & Johnston (1981) and Kiya & Sasaki (1983). Ruderich & Fernholz (1975) performed an investigation on a normal bluff plate with a splitter plate using pulsed hot-wire anemometry. Some investigations closer to ours on turbulent boundary layer separated flow are reported by e.g. Perry & Fairlie (1975) Dianat & Castro (1991) and Angele (2002). There is also a review on the topic by Simpson (1989). Here, however we will concentrate on the plane asymmetric diffuser flow with fully developed turbulent channel flow as inlet condition.

The problem of computing the flow in this choice of geometry or to realize it experimentally are both very challenging tasks. The range of scales, the high turbulence intensities and the high strains encountered in this flow together with a large separated region makes it a demanding, and thereby well suited, problem for testing and developing turbulence models. The fairly simple geometry, for which a numerical conformal mapping for an orthogonal curvilinear grid can be derived, see e.g. Brüger (2002), simplifies the possibility to perform LES and DNS calculations in the future.

In the first part of our study, presented in this paper, we will concentrate on the mean flow characteristics of the flow in the diffuser and its nearby surroundings. The main reason is to provide good data of mean flow properties, such as mean and rms velocities, in the three spatial directions along the streamwise centerline of the diffuser where the flow is expected to be most two-dimensional. We will also investigate the extension of the separated region and look at measures such as the back-flow coefficient determining the features of the flow in the separated region.

In the second part of the study titled, Measurements in a plane asymmetric diffuser with 8.5° opening angle. Part II: Comparison with model predictions for turbulence characteristics, we present properties especially interesting for turbulence modeling comparisons. We will look at characteristics of existing models and compare them to the behaviour of the flow in the diffuser.

Flow in this geometry has previously been studied experimentally by e.g. Obi et~al.~(1993a), Obi et~al.~(1993b), Obi et~al.~(1997), Buice & Eaton (2000a) and Buice & Eaton (2000b). The opening angle of the diffuser was in all these studies slightly larger, 10° , than that (8.5°) used in the present work. The reason for choosing a smaller diffuser opening angle was here to reduce the size of the separated region, and thereby, in combination with a high aspect ratio of the diffuser, achieve a high degree of two-dimensionality of the flow and moderate unsteadiness of the separation and reattachment points. From a control study point of view a smaller separation bubble is desired to keep actuator amplitudes moderate. It is also more common to find flows at the verge of separation in practical applications, e.g. draft tubes, wind-tunnel diffusers, ventilation ducts etc.

Furthermore the intention of this study was to measure all necessary velocity components to be able to calculate the turbulent kinetic energy and to form the anisotropy tensor throughout the diffuser. These are very useful measures for the turbulence modeling community when new improved models are developed and evaluated. These data, mainly obtained from PIV images with a rather coarse grid, (each interrogation area is $4 \times 4 \text{ mm}^2$), are to be complemented with measurements of velocity profiles with more data points to resolve the flow near the boundaries.

Among the above mentioned studies, Obi et al. (1993a) studied the plane asymmetric diffuser flow using a single component LDV. The measurements were then compared to calculations with two different turbulence models, (standard $k-\varepsilon$ and a basic version of SMC (second moment closure)). The agreement between the experimental data and the calculations were not very good although the SMC was better than the $k-\varepsilon$ model. They concluded that it is essential to capture the redistribution of energy between the different components, in this highly anisotropic flow, in the turbulence models.

Later Obi et al. (1993b) continued to study the same flow experimentally by inserting a periodic perturbation to the flow. The perturbation was generated by periodic blowing and suction through a slit in the spanwise direction. They investigated the influence of the perturbation frequency on the size of the separation bubble and found an optimum non-dimensional frequency, based on the inlet channel height and the inlet channel centerline velocity, around St=0.03. They also concluded that at this perturbation frequency the enhancement of transport of momentum across the diffuser was maximized.

In Obi et al. (1997) they further investigated the effect of the perturbation on the production of the turbulent Reynolds shear stress separating the contributions from the perturbation and the mean flow. They found that at the optimum frequency the production of Reynolds shear stress and the interaction between the mean flow and the perturbation were both enhanced.

Buice & Eaton (2000a), Buice & Eaton (2000b) also made an experimental investigation in the same geometry (with 10°) increasing the diffuser aspect ratio and used primarily pulsed hot-wires to determine the flow in the separated region. Thermal tufts were used to find the separation and reattachment points. They also measured the wall shear-stress using pulsed wall-wire probes. Their results were used for comparison in a Large Eddy Simulation by Kaltenbach et al. (1999).

Brunet et al. (1997) made an experimental investigation on pressure effects on turbulent flow in a plane asymmetric diffuser with a smooth (10°) inclined wall. They compared their results to calculations using the $k-\varepsilon$ model and found that the model was particularly deficient in capturing the behaviour of the Reynolds shear-stress.

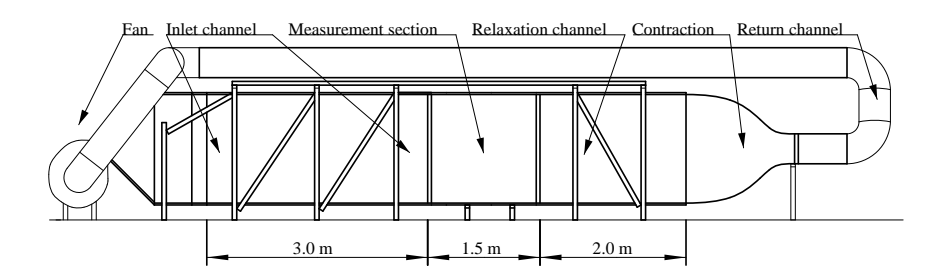


FIGURE 1. The wind-tunnel used in the experiments. The flow is circulating counter clockwise.

In the introduction to the second part of this paper there is a review of the numerous numerical and modeling efforts so far made using the plane asymmetric diffuser geometry. Some of these efforts have used the Obi $et\ al.\ (1993a)$ and foremost the Buice & Eaton (2000a) experimental data for comparison.

In future studies in the present set-up, control of the flow separation in the diffuser will also be investigated in co-operation with developers of control schemes. There have been a number of investigations involving control in various diffuser flow configurations, e.g. Coller et al. (2000); Obi et al. (1993b, 1997) but there is still much work to be done in this field.

2. Experimental setup

2.1. Description of the wind-tunnel

The experiments were performed in a closed loop wind-tunnel built specifically for this investigation. The wind-tunnel can be seen in figure 1. It consists of a blowing centrifugal fan delivering 11 kW of power followed by a section transforming the rectangular cross section shape of the blower outlet to another one with much higher aspect ratio. In this section splitter plates and screens ensure an even distribution of the fluid over the cross section area. The transformer is followed by a straight duct (settling chamber) which contains two screens at its upstream end to further even out mean flow variations. The settling chamber is followed by a two-dimensional contraction. The contraction further evens out mean flow variations and decreases the cross section height to 30 mm.

The contraction is followed by a turbulence generating grid and a 3.2 m long channel with a cross section area (width to height) of $1525 \times 30 \text{ mm}^2$. The length to height ratio of the channel is thus larger than 100 ensuring fully developed channel flow at the outlet (see Comte-Bellot (1965)). This is important in order to obtain a well defined inlet condition to the diffuser which can also be easily produced in numerical calculations. At the downstream end of the inlet channel, the end walls (limiting the spanwise width of the channel)

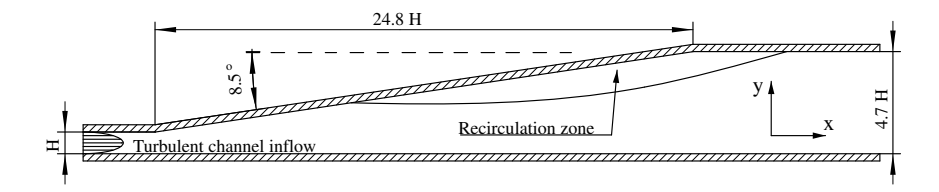


FIGURE 2. The measurement section of the wind-tunnel. A part of the inlet channel is seen to the left and part of the outlet channel is seen to the right. The view is from the top as referred to figure 1.

are perforated with 2 mm holes. This section is 100 mm long and the end wall boundary layers are removed through these holes by means of suction to prevent end wall boundary layer separation in the diffuser. Such a separation would destroy the two-dimensionality of the mean flow.

The inlet channel is followed by the diffuser. The diffuser has an inclined wall on one side and a straight wall on the other. The end walls are straight and equipped with three rows of vortex generators to further minimize the risk for boundary layer separation. The inclined wall has an angle of 8.5°, see figure 2. At the upstream corner of the inclined wall there is a radius of 100 mm to prevent separation at this corner. The inclined wall is made of an aluminum sandwich plate. Pressure taps are located along the centerline in the downstream direction at every 100 mm. These pressure taps were used to confirm that the pressure on both the straight and inclined walls were similar at all downstream measurement positions. The straight wall and the end walls are made of Plexiglas[®] to allow the use of optical measurement techniques such as LDV and PIV. The straight wall is also equipped with pressure taps along the centerline in the downstream direction at an interval of 25 mm. There are also pressure taps in the spanwise direction 100 mm upstream the diffuser inlet on each side at 100 mm interval. These pressure taps are used to check the two-dimensionality of the incoming flow. The high aspect ratio, 50 at the diffuser inlet, is crucial to achieve a high degree of spanwise uniformity.

The diffuser is followed by an outlet channel which is 141 mm high $(4.7 \, \text{m})$ inlet channel heights $(4.7 \, \text{H})$) and 2.5 m long. The purpose of this channel is to avoid upstream influence on the flow from devises located further downstream. This channel is partly made of Plexiglas[®] to facilitate measurements and partly of Plywood. Here, there are also two hatches giving access to the inside of the tunnel. Along the extent where it is made of Plexiglas[®] there are also pressure taps along the spanwise centerline with the same interval as in the diffuser.

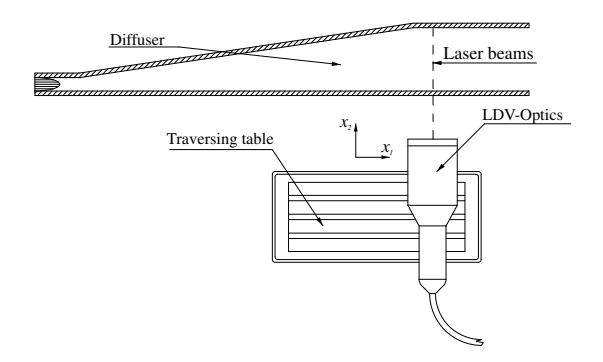


FIGURE 3. A sketch of the LDV measurement setup. The scattered light from the particles are received through the same optics as the emitted light.

The outlet channel is followed by a three-dimensional transformer changing the aspect ratio of the cross section area towards unity. The contraction is followed by a heat exchanger which is necessary in a closed return wind-tunnel to keep the temperature steady. A temperature sensor is located in the outlet channel and a computer logged the temperature which was found to be steady within $\pm 0.5^{\circ}$ C. This is sufficient since the experiments performed here are not very temperature sensitive due to the fact that optical measurement techniques (LDV and PIV) are used instead of hot-wire anemometry.

Following the heat exchanger the cross section is converted from a rectangular to a circular shape. A pipe with 400 mm diameter then leads the flow back to the fan. At the end of the pipe the seeding particles (in this case smoke, see section 2.2.3) are injected into the flow. Just in front of the fan there is a slit ensuring atmospheric pressure at the fan inlet. This is important since it provides a constant reference pressure.

2.2. Measurement techniques

The measurement techniques used in this investigation were primarily Particle Image Velocimetry, PIV and Laser Doppler Velocimetry, LDV. Pressures were measured using a Furness Control FCO 510 differential pressure transducer with an accuracy of 0.25% of full scale (2000 Pa).

2.2.1. LDV measurements

The LDV is a one component FlowLite $^{\circ}$ system from Dantec. It has a He-Ne Laser of 10 mW emitting light with a wave length of 632.8 nm. The light beams have a Gaussian intensity distribution and the beam diameter was 3.23 mm between the beam expander and the focusing lens. The measurement volume

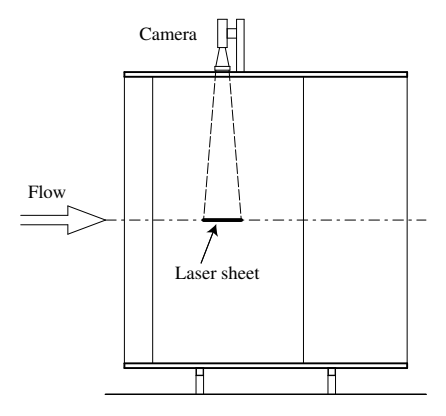


FIGURE 4. A sketch of the PIV measurement setup. The laser sheet is orientated horizontally, *i.e.* perpendicularly to the paper.

diameter using a lens with a focal length of 310 mm and a beam separation of 73 mm was 77 μ m. The measurement volume length was 0.66 mm. In figure 3 a sketch of the LDV setup is shown. Note that the scattered frequency shifted light from the particles are received through the same optics as the emitted light, *i.e.* backscatter receiver technique.

The LDV was calibrated against a rotating wheel and used to measure flow components in the spanwise direction, *i.e.* W and $w_{\rm rms}$. The measurements of the spanwise component were made along the spanwise centerline of the diffuser at intervals of 50 mm. A total of 29 profiles were measured. In the wall normal direction, the interval varied with proximity to a wall and the downstream position, from 0.1 mm to 5 mm. These data were later also interpolated to give values on a common measurement grid. This grid have a spacing between points of 10 mm in the downstream direction and 2 mm in the wall normal direction.

Between 25000 and 100000 samples were taken at each measurement point for the ensemble average with the sampling rate varying between 200 and 1000 Hz. The time for collecting data was set to a minimum of 120 s at each point.

2.2.2. PIV measurements

In the streamwise and wall normal directions the velocity components were measured using a PIV system from Dantec. In figure 4 a sketch of the PIV setup is shown. The laser sheet is orientated horizontally and perpendicular to the paper in the sketch, and the camera takes images from above.

The system consists of a Spectra Physics 400 mJ double-pulse Nd-Yag laser, a megaplus ES1.0 digital double frame camera from Kodak and hardware processing and software from Dantec.

The infrared light emitted by the laser is doubled in frequency to obtain a visible light of 532 nm. CCD chips are most sensitive to light around this wave length. The duration of the pulses emitted by the laser is on the order of a few nano seconds. The light beam is guided from the laser through a Dantec flexible arm allowing changes in the light sheet position and orientation. A cylindrical lens at the end of the flexible arm converts the circular Gaussian beam into a light sheet with a thickness on the order of 1 mm. The intensity distribution of the light in the sheet is approximately Gaussian.

The CCD camera has a light sensitive chip of 1018×1008 pixels and an integrated memory chip allowing two images to be taken within 1 μ s. The gray-scale resolution of the CCD chip is 256 levels. A f=60 mm lens was used together with a large aperture (f2.8) giving a very light sensitive image over an area of about the size of the outlet channel height in both directions.

The hardware, including all of the image processing, was supplied by Dantec. Through the hardware the camera and laser are synchronized. The image processing allowed for 32 double frame samples to be taken into each burst at a sampling rate of approximately 7.5 Hz depending on the maximum velocity in the image. Extra time for image processing was then needed to empty the memory containing the images before another burst could be recorded.

The software used to evaluate the images and calculate the velocity vectors was FlowManager 2.12 from Dantec. The software used sub-pixel interpolation to increase the velocity resolution assuming a Gaussian distribution. The datasets exported from the FlowManager software were, the velocity components, the streamwise and wall-normal position in the laser sheet plane, the peak ratio, *i.e.* the ratio between the two largest peaks in the cross correlation function between the two images, and an indicator, (0 or 1), indicating if the velocity vector was rejected according to the rejection criteria set in the software. A new evaluation with extended rejection criteria was later performed with Matlab based software.

The image size of the PIV was calibrated against a ruler that was inserted into the laser sheet before each measurement. Data was collected from 2048 images to form reliable mean and rms values. The size of the interrogation areas were 32×32 pixels. In physical space this is equivalent to approximately 4.5×4.5 mm². A 50% overlap between the interrogation areas were used throughout the measurements. In the inlet channel just upstream of the diffuser a more highly resolved image was used with another lens, (180 mm), to obtain more velocity vectors in this narrow channel. With the 1018×1008 pixel CCD chip, an interrogation area of 32×32 pixels and 50% overlap, the images contain 62×62 velocity vectors. Adding the fact that each interrogation area is 4.5×4.5

 $\rm mm^2$ the physical size of the images are $145\times145~\rm mm^2$ which just covers the outlet channel height of 141 mm.

The time between frames was optimized for each set of pictures and varied with the downstream position. In general each measurement of 2048 frames took about 30 min to collect. To cover the entire measurement section PIV images were obtained at 11 downstream positions. A GUI Matlab script was used to match the streamwise and wall normal positions from the 11 sets of data.

These data were then, together with the LDV wall normal profiles of the spanwise velocity component interpolated on a common grid with a mesh size of 10 mm by 2 mm in the streamwise and wall-normal directions respectively. This grid is used whenever contour plots of the flow in the entire measurement section are shown in the section 3 of this paper.

2.2.3. Seeding particles

In both the PIV and LDV measurements the air was seeded with smoke from a smoke-generator ZR12-AL from Jem using a mixture of glycerol and water. By varying the amount of water the density of the smoke can be optimized to give good results. The smoke was inserted through the reference pressure slit just upstream of the fan and was sufficiently spread out in the measurement section due to the mixing in the fan and in the inlet channel. No attempt to measure the physical size of the seeding particles has been made but from previous investigation using the same type of smoke we can conclude that they typically are a few μm in diameter.

2.2.4. Error sources in PIV and LDV measurements

It is very important to study the errors in the velocity measurements using the PIV and LDV techniques. Kristian Angele has investigated the error sources found in digital PIV (which is used here). His results will appear in a paper currently under preparation and the references here to his investigation is through private communication. Angele found that even carefully made measurements can have large errors but most of the errors can be eliminated by using appropriate validation criteria. PIV random error sources can e.g. be noise which can come from background disturbances, poor image contrast or resolution. Using a digital FFT to process the data will introduce small random uncertainties.

Another error source is the so called loss of pairs which means that a particle is only present in one of the images in an image pair. This is evidently more likely to happen for fast particles which gives a bias towards lower velocities. If the particle density is too low this problem will increase since the number of particles that form the correlation pair are fewer. This problem can be relieved by applying a weight function to the correlation plane, see *e.g.* Raffel *et al.* (1997).

A large velocity gradient over an interrogation area will not only cause the problem of integration but it will also decrease the signal to noise ratio. Following a criterion based on the velocity gradient, the time between images and interrogation area size in physical units and pixels introduced by Adrian & Keane (1992) makes sure this error source is kept small.

Finally peak-locking errors, *i.e.* the tendency of instantaneous particle displacements towards integer pixel values, is thoroughly investigated by Angele. An interrogation area is usually too small to give more than 8-16 possible discrete velocities. Therefore a curve-fit is applied in the correlation plane to get sub-pixel accuracy. This does not always eliminate the error which can be seen in the probability density distributions. Angele found that the limiting factor for peak-locking is that the ratio between the discretization velocity and the rms-velocity, *i.e.* the number of velocity peaks distributed over the probability density distribution. A symptom of peak-locking error is a shaky $u_{\rm rms}$ -profile in flows with strong wall-normal gradients. There are some symptoms of peak-locking problems in our measurements, see figure 7 as the mean velocity variation in our case is rather high.

LDV error sources may be reflections close to the wall decreasing the signal to noise ratio substantially and making it impossible to measure. Very close to a wall vibrations of the wall causes erroneous velocity peaks in the probability density distribution also largely affecting the measurements.

When measuring with an LDV system it is important to collect statistically independent samples i.e. a single burst shall only be sampled once. It is also important to correct errors from high velocity bias, i.e. high velocity particles are more often detected than low velocity particles. The correction can be made by weighting the sample with its residence time, i.e. the time the particle are within the measurement volume. Arrival time averaging can be used to correct for low velocity bias at low data rates, see e.q. Fischer et al. (2001).

Averaging effects over the measurement volume while measuring in velocity gradients is an error source that can be quite substantial but it can be corrected for. Durst *et al.* (1998) derived an equations for correcting the mean and fluctuating velocity assuming elliptical shape of the measurement volume and that the scattering particles are mono-disperse.

Measuring at high mean velocity with limited fluctuating velocity can be difficult if the mixing and filter frequencies are limited in the LDV system. This is a result of the low resolution of the velocity probability density distribution which causes large errors in the measured fluctuating velocity. Our LDV system have these limitations and therefore we only used the LDV for the spanwise velocity component which has zero mean velocity. Many of the difficulties described above such as velocity gradient effects are therefore avoided.

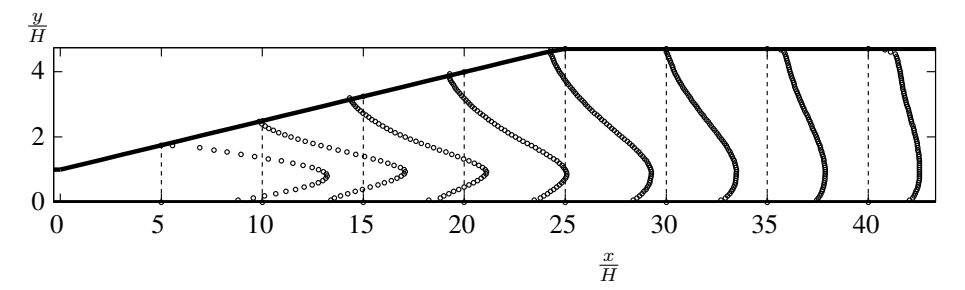


FIGURE 5. Streamwise mean velocity, $\left(U_{\rm fig}=10\frac{U}{U_{\rm b}}+\frac{x}{H}\right)$, at 8 streamwise positions (x/H=5,10,15,20,25,30,35~&~40). Dashed lines indicate zero level for each streamwise velocity profile.

3. Results

We here focus on the mean velocity components and fluctuation intensities. Results are also presented for the turbulence kinetic energy as well as for the stream function and back-flow coefficient, which both characterize the mean properties of the separated region at the inclined wall. Furthermore, the static wall-pressure along the spanwise centerline downstream through the diffuser is presented from which the pressure coefficient can be calculated.

3.1. Velocity components

In this study we measured all three velocity components and their fluctuations using PIV for the streamwise and wall-normal components and LDV for the spanwise component. Here, results for all these quantities are presented with the exception of the mean spanwise component which is zero within the measurement accuracy. The coordinate system is here defined as x in the "streamwise" direction, y in the "wall-normal" direction and z in the spanwise direction. The corresponding average velocities are denoted respectively by U, V and W. The y-component is of course only normal to the lower, straight wall but because of the relatively small opening angle, we prefer here to refer to the x and y velocity components as streamwise and wall-normal. In all figures the spatial coordinates are normalized with the inlet channel height, H=0.03 m, and the velocities are normalized with the inlet channel bulk velocity, $U_{\rm b}=20.0$ m/s, defined as

$$U_{\rm b} = \frac{1}{H} \int_0^H U \, \mathrm{d}y. \tag{1}$$

3.1.1. Streamwise mean and fluctuating velocities

The diffuser can be divided into a region below the maximum velocity peak, *i.e.* close to the straight wall, and a region, above the velocity peak, including

the separated flow region closer to the inclined wall, see figure 5. On the side close to the inclined wall an inflection point is created almost immediately downstream the inlet in the streamwise velocity profile. The inflectional profile is enhanced downstream in the diffuser until the inclined part of the wall ends. Thereafter it relaxes towards the same profile as on the straight wall although at the maximum downstream position in this study the complete streamwise velocity profile is far from symmetric. The peak in streamwise velocity diverges slightly towards the centerline of the diffuser as it decreases in strength, but this process is very slow and still at our most downstream measurement position the streamwise velocity maximum is much closer to the straight wall than the inclined wall.

The inflection streamwise velocity profile creates a strong shear-layer which is important as it distributes momentum from the outer flow towards the separated region. The non-zero components in the Reynolds stress tensor, $(-u_{\rm rms}^2, -v_{\rm rms}^2, -w_{\rm rms}^2$ and $-\overline{uv})$ all have their peaks within this shear-layer.

The very high fluctuation level of this flow with instantaneous velocity profiles very far from the mean value is illustrated in figure 6 through a sequence of instantaneous velocity fields in the streamwise, wall-normal plane. We can observe very large velocity variations which are of large scale in this region which includes the first (upstream) part of the separated region. High speed fluid (shown in white) emerging from the inlet channel is deflected towards the inclined wall directly downstream the inlet, but occasionally, an almost jet like character (figure 6q) can be observed with a resulting large separation region. This motion can, with a larger opening angle, lead to instantaneous separation along the straight wall. As will be shown later this is not the case here and we can conclude that the 8.5° opening angle is small enough to also avoid straight wall separation.

The motion of this high velocity region is of course intimately linked to the shedding process in the separated region. Unfortunately the sampling frequency of the measurement system is too low to be able to detect the shedding process. A sampling frequency 10 times higher than the 7.5 Hz available with our PIV system should be enough to resolve this process that is expected (loosely from Obi et al. (1993b) and Kaltenbach et al. (1999)) to have a mean frequency of about 20 Hz although a large variation in frequency is expected from these earlier studies and also judged from our instantaneous velocity images.

The fluctuating streamwise velocity is in general very large in this flow as was shown above in the instantaneous velocity fields. The fully developed turbulent inlet flow generates a $u_{\rm rms}$ distribution which is symmetric and with peaks close to each wall and a local minimum at the centerline where the streamwise velocity gradient is zero. The development of these two peaks are rather different as the flow propagates downstream through the diffuser. The

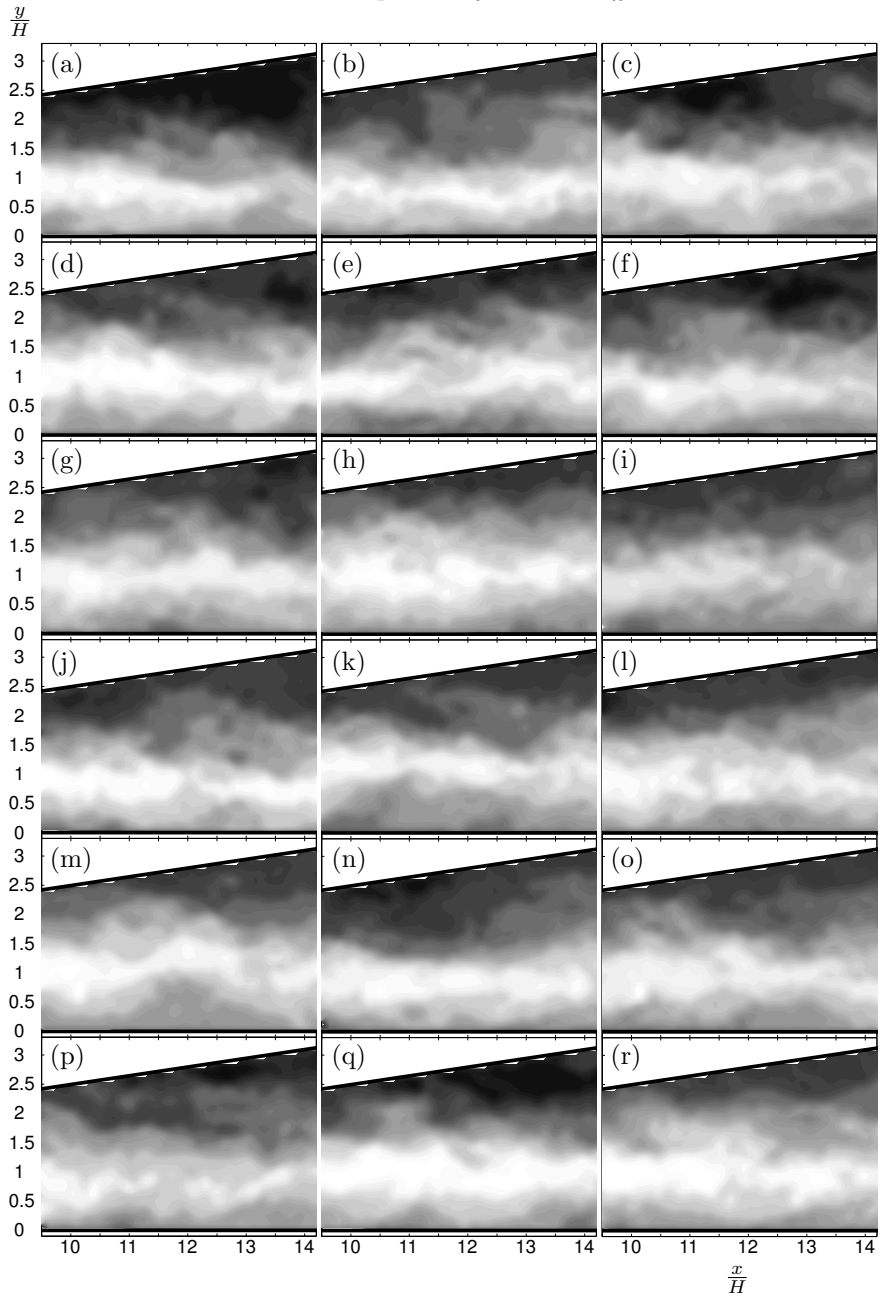


FIGURE 6. Time sequence of instantaneous velocity fields (U-V plane). $\Delta t = \frac{2}{15} \mathrm{s}$ between images. White: High positive velocity fluid (17 m/s). Black: Negative velocity fluid (-1 m/s).

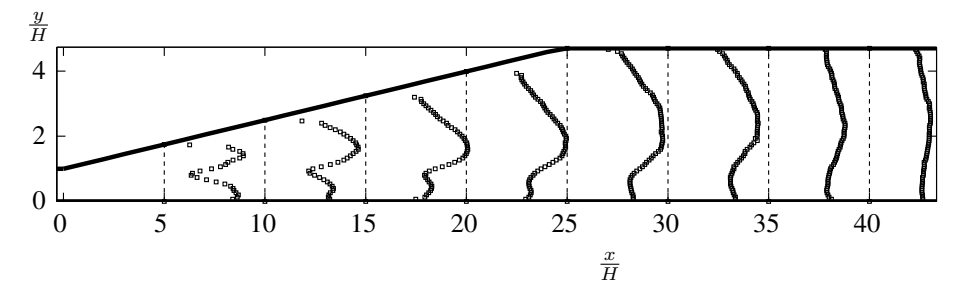


FIGURE 7. Root mean square of streamwise fluctuating velocity, $\left(u_{\rm rms,fig}=40\frac{u_{\rm rms}}{U_{\rm b}}+\frac{x}{H}\right)$, at 8 streamwise positions (x/H=5,10,15,20,25,30,35~&~40).

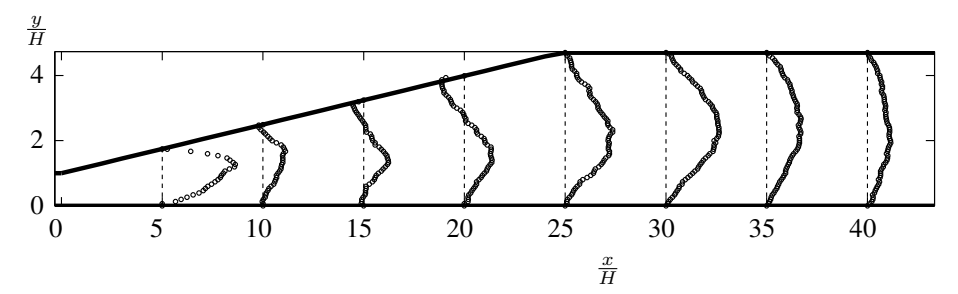


FIGURE 8. Wall-normal mean velocity, $\left(V_{\mathrm{fig}}=100\frac{V}{U_{\mathrm{b}}}+\frac{x}{H}\right)$, at 8 streamwise positions (x/H=5,10,15,20,25,30,35~&~40). Dashed lines indicate zero velocity for each streamwise velocity profile.

peak close to the straight wall is first slightly reduced downstream and eventually it is almost overtaken by the growing local maximum emerging from the upper part of the inlet channel. This peak grows and reaches its maximum at about x/H=20-25, see figure 7. The location of this peak detaches from the inclined wall and follows the strong shear-layer outside the separated region. Eventually the fluctuating streamwise velocity reaches a symmetric distribution across the outlet channel with small variations along the profile. Thereby a distribution with two peaks at the inlet develops towards a distribution with one peak at the centerline. As the flow in the outlet channel is developing, the turbulent channel flow distribution will eventually be recovered far downstream.

3.1.2. Wall-normal mean and fluctuating velocities

The wall-normal velocity, V (i.e. normal to the straight wall, and almost normal to the inclined wall) is very small in most parts of the diffuser. Close to

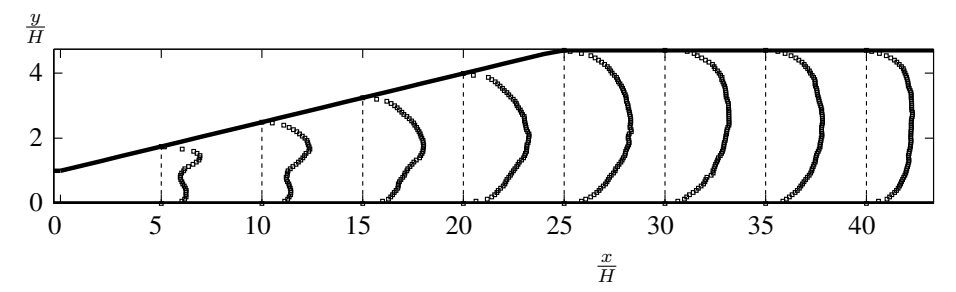


FIGURE 9. Root mean square of wall-normal fluctuating velocity, $\left(v_{\rm rms,fig} = 40 \frac{v_{\rm rms}}{U_{\rm b}} + \frac{x}{H}\right)$, at 8 streamwise positions (x/H = 5, 10, 15, 20, 25, 30, 35 & 40).

the corner at the diffuser inlet where there is a rather abrupt change in the direction of the wall causes the flow to turn leading to locally high values of the wall-normal velocity (Not shown in figure 8). Further studies of this region is required with a better spatial resolution.

The wall-normal velocity decreases downstream (until about x/H=15-20) where its peak slowly starts to grow again due to the decreasing height of the separation bubble. The location of this peak follows the strong shear-layer outside the separated region, see figure 8. The maximum value is found close to the centerline of the diffuser and the magnitude of the maximum increases up to approximately x/H=30. Further downstream the peak follows the centerline of the outflow channel while decreasing in magnitude. The presence of a vertical velocity in the core region of the outflow channel is of course due the asymmetry of the streamwise velocity component.

The fluctuating wall-normal, $v_{\rm rms}$, velocity behaves much like the streamwise fluctuating velocity with peaks on either side of the centerline in the inlet channel and with a growth of the peak closest to the inclined wall and a reduction of the other peak. The variation of the wall-normal fluctuating velocity is however substantially smaller than for its streamwise counterpart and it reaches a symmetric profile at quite an early stage with a maximum at the outlet channel centerline. The maximum is reached at a downstream position approximately equal to the point where the inclined part of the wall ends as is also the case for the wall-normal mean velocity.

3.1.3. Spanwise fluctuations, Reynolds stress and turbulence kinetic energy

The development of the fluctuating spanwise velocity, $w_{\rm rms}$, downstream through the diffuser resembles very much its streamwise counterpart. The main difference lies in the smaller magnitude of the spanwise component. The wall-normal location of the maximum is also slightly different, with the maximum for the spanwise fluctuating velocity closer to the inclined wall, but still within

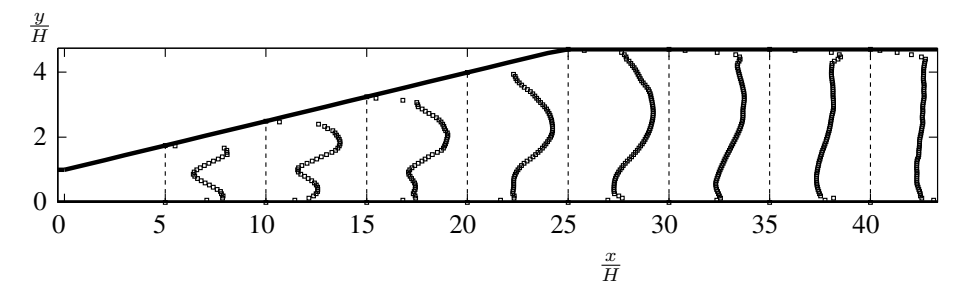


FIGURE 10. Root mean square of spanwise fluctuating velocity, $\left(w_{\rm rms,fig}=40\frac{w_{\rm rms}}{U_{\rm b}}+\frac{x}{H}\right)$, at 8 streamwise positions (x/H=5,10,15,20,25,30,35~&~40).

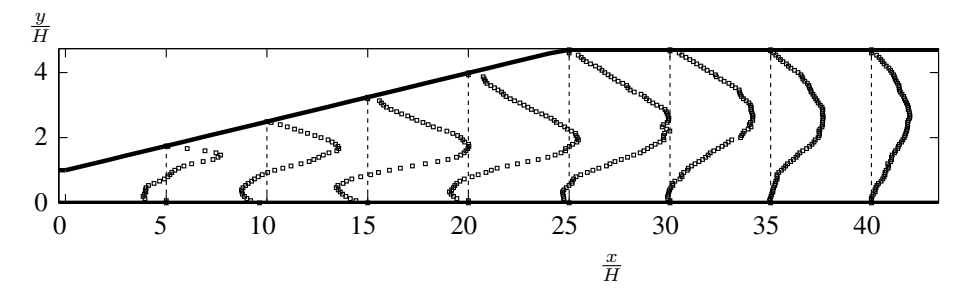


FIGURE 11. Reynolds stress in the streamwise wall-normal plane, $\left(\overline{uv}_{\text{fig}} = 1000 \frac{\overline{uv}}{U_{\text{b}}^2} + \frac{x}{H}\right)$, at 8 streamwise positions (x/H = 5, 10, 15, 20, 25, 30, 35 & 40).

the shear-layer outside the separated region. The maximum in streamwise direction is found at x/H = 20 - 25 which is similar to that for $u_{\rm rms}$.

If the spanwise component cannot be measured in an experiment, it seems possible to obtain a first order estimate by rescaling of the streamwise fluctuating velocity. The main reason for making such an estimate would be to be able to estimate the turbulence kinetic energy without having to measure all three velocity components. This has been done in other studies, however, it is of course more appropriate to directly measure all components to get a correct value for the turbulence kinetic energy that can be used in comparison with results from e.g. turbulence model predictions.

The Reynolds shear-stress is a very important quantity since it redistributes momentum from high velocity regions to low velocity regions. A high level of Reynolds shear-stress is thus instrumental in suppressing separation, see e.g. Obi $et\ al.\ (1993b)$. The amount of Reynolds shear-stress scales with turbulence kinetic energy which makes a flow like this, with fully developed turbulent

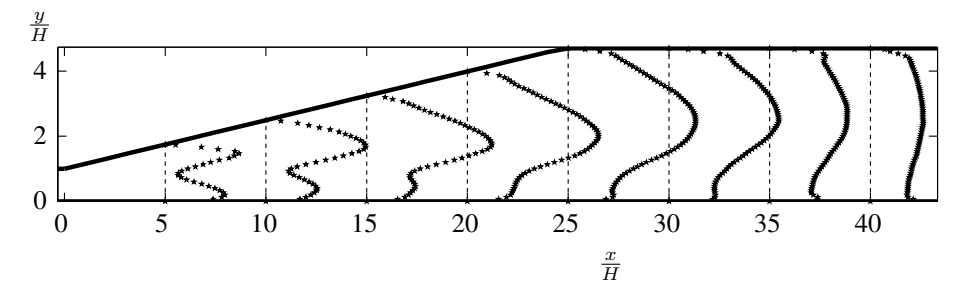


FIGURE 12. Turbulence kinetic energy, $\left(K_{\text{fig}} = 400 \frac{K}{U_b^2} + \frac{x}{H}\right)$, at 8 streamwise positions (x/H = 5, 10, 15, 20, 25, 30, 35 & 40).

channel flow as inlet condition, quite capable of handling a strong adverse pressure gradient and thereby reduce the size of the separated region.

The Reynolds shear-stress in the streamwise wall-normal plane, \overline{uv} , is antisymmetric in the inlet channel. With this coordinate system the negative peak is near the straight wall and the positive peak closer to the inclined wall. As the flow develops downstream in the diffuser the positive peak grows while the negative peak is suppressed, see figure 11. The maximum Reynolds shear-stress is found at x/H=20-25 and thereafter it decreases in magnitude. The location of the positive peak follows the location of maximum shear in the shear-layer outside the separated region. At the end of the measurement region the Reynolds shear-stress attains a symmetric profile with the maximum located near the outflow channel centerline.

The turbulence kinetic energy, K, is a primary quantity for comparisons with turbulence model predictions since most models rely on transport equations for this quantity where one or more terms have to be modeled. Comparisons with numerical results can be improved if direct and accurate measurements of the turbulence kinetic energy are made. New insights that can assist in the development of new turbulence models can thereby be obtained. The dissipation rate, ε , can here however not be measured directly although some attempts using the PIV technique have been made e.g. by Baldi et~al. (2002). The dissipation rate is needed for a complete comparison with turbulence models where it is included, directly or in some other form (ω, τ) , through a transport equation.

In figure 12 the turbulence kinetic energy at eight streamwise positions is plotted. It is for natural reasons, similar in character to the individual intensities shown in previous figures. It is defined as

$$K = \frac{1}{2} \left(u_{\rm rms}^2 + v_{\rm rms}^2 + w_{\rm rms}^2 \right). \tag{2}$$

The maximum value is located at about x/H = 20 - 25 in the shear-layer outside the separated region as for the individual fluctuating components. The kinetic energy profile does not quite reach a truly uniform shape at our most downstream position.

It should be noticed that our measurements are not resolving the very near wall regions. Therefore our conclusions are excluding phenomena occurring in the immediate vicinity of the walls. In the future these measurements will be complemented by new experiments covering the near wall regions as well as a more detailed investigation of the upstream corner on the inclined wall where the expanding part of the diffuser begins. There we expect to find locally high levels of turbulence intensity and anisotropy as well as a strong streamline curvature. Some clues to these statements can be seen if the whole velocity field is studied rather than the isolated velocity profiles presented here.

3.2. Characterization of the separated region

To further study the separated region, extending the information gained by looking at the velocity profiles the stream-function, generating streamlines and the back-flow coefficient are useful tools. The back-flow is also studied through a sequence of instantaneous images.

3.2.1. Stream-function

The stream-function is here defined as

$$\Psi(x,y) = 1 - \frac{1}{HU_b} \int_0^y U(x,y) dy.$$
 (3)

In figure 13, constant values of the stream function (streamlines) are plotted throughout the measurement region. This definition of the stream function gives a value of $\Psi=0$ at the dividing streamline. The dividing streamline separates the (averaged) recirculation zone from the outer flow. The two positions where the dividing streamline reaches the "upper" wall are the mean separation and reattachment points, respectively. From figure 13, the mean separation point is found to be located at 9 channel heights downstream the diffuser inlet $(x/H \approx 9)$ and the mean reattachment point is located at $x/H \approx 31$.

In figure 13 the gray-scale levels represent a measure of the speed in the diffuser, i.e. here $\sqrt{U^2+V^2}$, with an increment of 2 m/s. The figure shows how the flow with maximum velocity first is deflected at the inlet corner towards the inclined wall but when it approaches the separation point it is deflected back towards the straight wall. Thereafter, there is a very slow relocation of the maximum towards the center of the outlet channel. It can also be noted that the decrease in speed is slower through the diffuser compared to an attached flow case. This follows from the constriction caused by the separated region, which decreases the adverse pressure gradient and slows down the retardation of the flow speed and spreads it out over a larger downstream length.

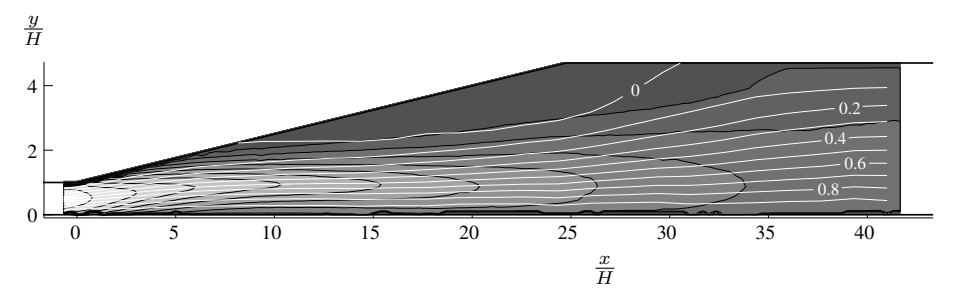


FIGURE 13. Streamlines shown as white curves. The stream function is integrated from the inclined wall. Gray-scale background with separating black curves shows the speed, with a contour increment of 2 m/s.

3.2.2. Back-flow coefficient

A very interesting quantity is the back-flow coefficient which relates the number of samples with negative velocity (along the inclined wall) to the samples with positive velocity. A back-flow coefficient of 1 means that all samples have negative velocity and a back-flow coefficient of zero thus means that all samples have positive velocity. The back-flow coefficient then reads

$$\chi(x,y) = \frac{1}{N} \sum_{k=1}^{N} \frac{1 - \text{sgn}(u_k(x,y)\cos(\alpha) + v_k(x,y)\sin(\alpha))}{2},$$
 (4)

where N is the total number of samples, sgn is the sign function, u_k the streamwise velocity in the k^{th} sample, v_k the wall-normal velocity in the k^{th} sample and $\alpha = 8.5^{\circ}$ the diffuser opening angle.

First, we notice in figure 14 that along the straight wall there seems to be no samples with back-flow although the rather poor resolution might allow for a very thin separation bubble very close to the wall. It is important that there is no separation on the straight wall since this may destroy the "stability" of the separation bubble on the inclined wall with a separation altering side from the inclined wall to the straight wall back and forth. Our choice of opening angle, 8.5° is thus small enough to avoid this kind of flow state.

Focusing our attention on the separation bubble on the inclined wall the back-flow coefficient gives us the streamwise locations on the inclined wall for the most upstream instantaneous separation point that in figure 14 is shown to be $x/H \approx 5$. The flow is separated 80% of the time downstream $x/H \approx 14$. In real time the separation point moves back and forth along the inclined wall and at some occasions the flow is completely attached. A back-flow coefficient of 0.5 gives the mean separation point, already shown to be $x/H \approx 9$ from the dividing streamline, and the mean reattachment point at $x/H \approx 31$. The

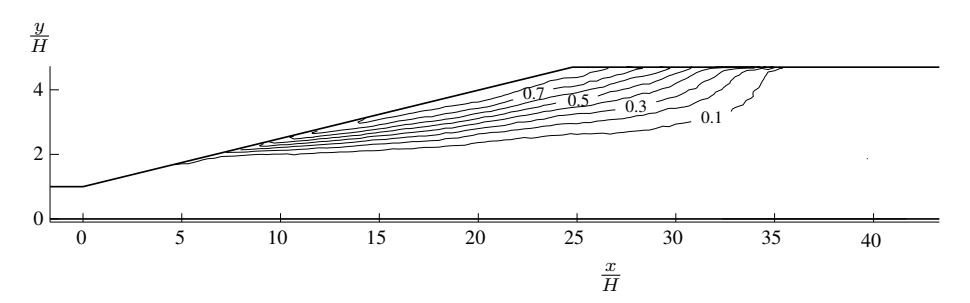


FIGURE 14. Back-flow coefficient, χ .

reattachment point never moves downstream of $x/H \approx 35$ where the flow thus always is attached.

To study the separation more in detail in time, figure 15 shows the instantaneous back-flow in a sequence of images. Black is large negative velocity along the inclined wall and white is positive velocity. It is clear from this sequence that sometimes the flow is almost fully attached (e.g. 15i and 15m) and sometimes there are large regions of flow with negative velocity. The formation of spanwise vortices can be seen in some of the frames in the time sequence of figure 15.

3.3. Static wall-pressure distribution

The static wall-pressure has been measured along the spanwise centerline in the downstream direction. Measurements on both the inclined and straight walls were performed but with a much better spatial resolution on the straight wall. The measurements on the inclined wall were made to confirm that the static pressure is constant in the wall-normal direction (within our measurement accuracy) through the diffuser. This is true for most of the downstream measurement positions except at the upstream corner where the rapid change in wall direction leads to large curvature of the streamlines and consequently pressure differences between the two sides.

Shown in figure 16 is the pressure coefficient, C_p , defined as

$$C_{\rm p}(x) = \frac{p_{\rm w}(x) - p_{\rm w}(x=0)}{\frac{1}{2}\rho U_{\rm b}^2},$$
 (5)

where $p_{\rm w}$ is the static wall-pressure and ρ the density of the air is shown. The diamonds in figure 16 represent the pressure coefficient with undisturbed flow. The start of the separation can be seen where the diamonds deviate from the circles. The following rather flat region is caused by the constriction to the outer flow produced by the separated region that decreases the pressure gradient.

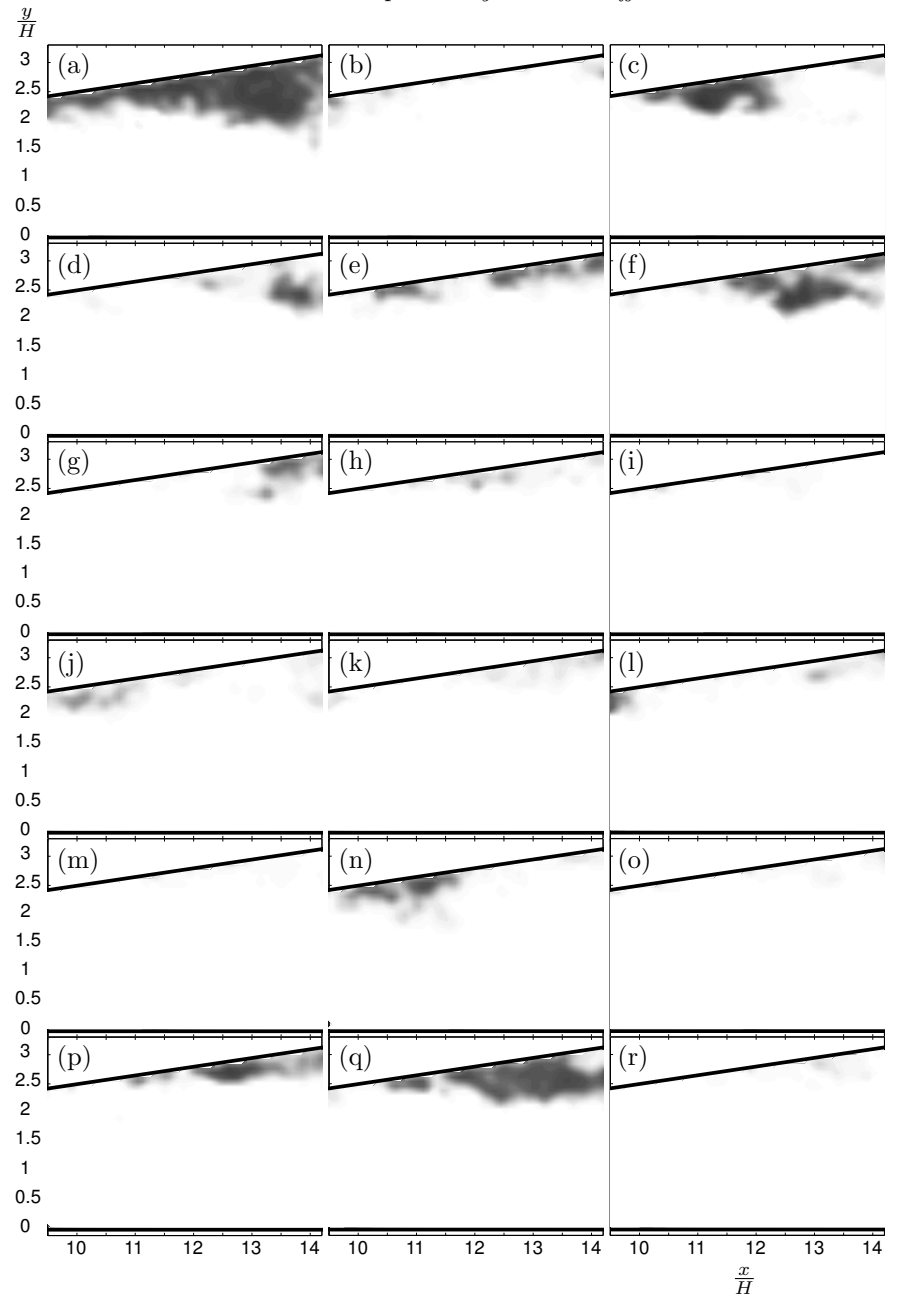


FIGURE 15. Time sequence of images of instantaneous negative streamwise velocity (x-y plane). $\Delta t = \frac{2}{15}$ s between images. White: Zero or positive streamwise velocity. Black: Strong streamwise negative velocity.

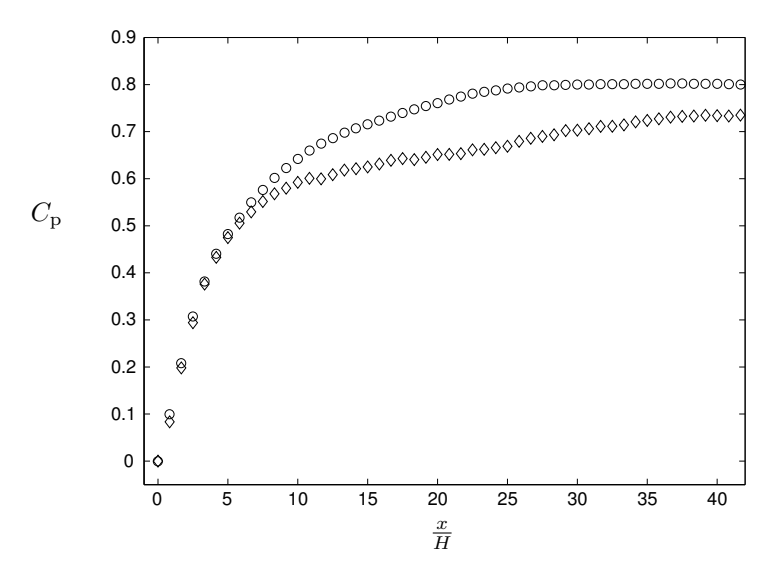


FIGURE 16. Static wall-pressure coefficient, $C_{\rm p}$. Diamonds represent flow without vortex generators. Circles represent flow with vortex generators.

The circles represent a reference case where vortex generators have been installed to suppress the separated region. These vortex generators are positioned in a spanwise row at a downstream location of about x/H=7. Their height is 20 mm and the angle of the vertical plates to the mean flow is 20° . The spanwise spacing between the vortex generators is 100 mm which gives a total of 15 generators covering the entire span of the diffuser. As can be seen in figure 16 the pressure coefficient continues to rise where the flat region, indicating separation in the uncontrolled case (diamonds), starts. The final pressure recovery increases with vortex generators from approximately 0.73 to 0.80 despite the extra pressure loss generated by the vortex generators themselves through the streamwise vortices they create.

4. Concluding remarks

The flow in an asymmetric plane diffuser has been studied with extra attention paid to ensuring good two-dimensionality of the mean flow. The focus in this paper is on the overall flow characteristics, *i.e.* mean velocities, turbulence intensities and Reynolds stresses, together with an investigation of the separated region using instantaneous velocity fields, streamlines and the back flow coefficient.

The streamwise mean velocity, U, gives us indications of where in the diffuser flow the most interesting flow features can be found. These are apart from

the separated region at the inclined wall the strong shear-layer outside the separated region and the region just downstream of the diffuser inlet. Studies of instantaneous velocity fields reveal that a region of high velocity fluid emerges from the inlet channel, that gives almost a "jet-like" structure to the flow with large amplitude and large scale coherence of the fluctuating field, interacting with the large scale structures in the separated region. There is a certain risk for a small separation on the straight wall when the flow is attached along the inclined ditto but the rather moderate opening angle used here (8.5°) does not produce large enough gradients for this to happen. The inflectional streamwise velocity profile found around the edge of the separated region creates a strong shear-layer that is important as it distributes energy from the outer flow towards the separated region. The non-zero components in the Reynolds stress tensor, $(-u_{\rm rms}^2, -v_{\rm rms}^2, -w_{\rm rms}^2$ and $-\overline{uv})$ all have their peaks in this shear-layer.

The wall-normal velocity, V, is very small in most parts of the diffuser, but close to the upstream corner at the diffuser inlet where the change in the direction of the wall is rather abrupt, locally high values of the wall-normal velocity and high streamline curvature are found. This region is not studied in detail in this paper since a better spatial resolution in the measurements is required.

The streamwise fluctuating velocity, $u_{\rm rms}$, increases in magnitude down-stream in the diffuser and peaks between x/H=20-25. The typical, $u_{\rm rms}$, two peak profile in the inlet channel flow is redistributed towards a one peak profile with the peak following the shear-layer outside the separated region and eventually its location in the outflow channel is close to the centerline. The other two components of the fluctuating velocity, $v_{\rm rms}$ and $w_{\rm rms}$, are subjected to the same transformation as the streamwise component, although the magnitude is smaller with $v_{\rm rms}$ (about half the size of $u_{\rm rms}$) and the magnitude of $w_{\rm rms}$ lies in between $v_{\rm rms}$ and $u_{\rm rms}$. The location of the peaks in wall-normal direction is also somewhat different from the streamwise case.

The Reynolds shear-stress, $-\overline{uv}$, in the streamwise wall-normal plane is large in the shear-layer outside the separated region. Since the Reynolds shear-stress contributes to a redistribution of momentum toward regions with lower mean velocity it helps to delay the separation in the diffuser. The turbulent inlet channel flow contains a fair amount of turbulent kinetic energy which makes this diffuser flow more resistant to separation than if a laminar flow would have been chosen as the inlet condition.

The flow detaches on the inclined wall at approximately 9 inlet channel heights downstream from the diffuser inlet. The separation point moves, in time, up and down along the inclined wall but never above x/H=5 as shown by the back flow coefficient figure. This movement is coupled to the shedding process in the separating region. The reattachment point is of course also moving in its location with the furthest downstream location of 35 inlet channel

heights. The mean reattachment point was found to be at x/H=31. By studying the instantaneous images of back flow in the separated region we get a fairly good view of the vortices created and swept downstream through the diffuser although the sampling rate of our PIV system is too low to be able to determine a mean "shedding" frequency. Using other measurement techniques or combining the PIV with a detection/trigging signal it may be possible to determine this frequency. One should of course keep in mind that one cannot expect a well-defined single frequency in a phenomenon like this, but rather a fairly broad-band peak.

The static wall pressure was measured at the spanwise centerline in the streamwise direction along the straight wall. An array of vortex generators was applied as a reference case of diffuser flow without separation. Comparing the two curves from flow with and without vortex generators clearly shows the separated region as a plateau present only in the case without vortex generators caused by the constriction of the outer flow by the separated region. The pressure coefficient at the measurement region outlet, achieved with vortex generators (0.80) is almost 10% higher than for the original case (0.72).

5. Acknowledgment

The authors would like to thank Ulf Landén for aiding in the manufacturing of the flow device and Kristian Angele for introducing us into the world of PIV. The Swedish Research Council and The Swedish Energy Agency are gratefully acknowledged for their financial support.

References

- Adrian, R. & Keane, R. 1992 Theory of cross-correlation in PIV. Applied scientific research 49, 191–215.
- Angele, K. P. 2002 Pressure-based scaling in a separating turbulent APG boundary layer. In *Advances in turbulence IX* (ed. I. Castro, P. E. Hancock & T. G. Thomas), pp. 639–642. CIMNE, Barcelona, Spain.
- Baldi, S., Hann, D. & Yanneskis, M. 2002 On the measurement of turbulence energy dissipation in stirred vessels with PIV techniques. In 11th Int. Symp. on Applications of Laser Techniques to Fluid Mech. Instituto superior técnico, Center for innovation, technology, and policy research, Lisbon, Portugal.
- Brüger, A. 2002 Higher order methods suitable for direct numerical simulation of flows in complex geometries. *Tech. Rep.* 2002:07. Lic. thesis, Dept. of Mechanics, KTH, TRITA-MEK.
- Brunet, L., Calzalbou, J. B., Chassaing, P. & Jervase, L. 1997 Experimental and computational study of pressure effects on turbulent flow in an asymmetric plane diffuser. In 11th Symp. on Turbulent Shear Flows, Grenoble, France, pp. 114–119.

- Buice, C. U. & Eaton, J. K. 2000a Experimental investigation of flow through an asymmetric plane diffuser. *Tech. Rep.* TSD-107. Thermo sciences Division, Dep. of Mechanical Eng. Stanford University, Stanford, Ca, USA, Report No.
- Buice, C. U. & Eaton, J. K. 2000b Experimental investigation of flow through an asymmetric plane diffuser. J. of Fluids Eng. 122, 433–435.
- Cherry, N. J., Hillier, R. & Latour, M. E. M. P. 1984 Unsteady measurements in a separated and reattaching flow. *J. Fluid Mech.* **144**, 13–46.
- COLLER, B. D., NOACK, B. R., NARAYANAN, S., BANASZUK, A. & KHIBNIK, A. I. 2000 Reduced-basis model for active separation control in a planar diffuser flow. In AIAA Fluids 2000, 19-22 June 2000, Denver, CO, USA, AIAA-2000-2562.
- COMTE-BELLOT, G. 1965 Écoulement turbulent entre deux paroix parallèles. Publications scientifiques et techniques 419. Ministère de l'air, 2, Avenue de la Porte-d'Issy, Paris.
- DIANAT, M. & CASTRO, I. P. 1991 Turbulence in a separated boundary layer. *J. Fluid Mech.* **226**, 91–123.
- DURST, F., FISCHER, M., JOVANOVIĆ, J. & KIKURA, H. 1998 Methods to set-up and investigate low Reynolds number, fully developed turbulent plane channel flows. ASME J. Fluids Eng. 120, 496.
- EATON, J. K. & JOHNSTON, J. P. 1981 A review of research on subsonic turbulent flow reattachment. AIAA J. 19, 1093–1100.
- FISCHER, M., JOVANOVIĆ, J. & DURST, F. 2001 Reynolds number effects in near-wall region of turbulent channel flows. *Phys. Fluids* **13** (6), 1755–1767.
- KALTENBACH, H. J., MITTAL, M., FATICA, R., LUND, T. S. & MOIN, P. 1999 Study of flow in a planar asymmetric diffuser using large-eddy simulation. J. Fluid Mech. 390, 151–185.
- KIYA, M. & SASAKI, K. 1983 Structure of a turbulent separation bubble. J. Fluid Mech. 137, 83–113.
- Obi, S., Aoki, K. & Masuda, S. 1993a Experimental and computational study of turbulent separating flow in an asymmetric plane diffuser. In 9th Symp. on Turbulent Shear Flows, Kyoto, Japan, August 16-18, p. 305.
- Obi, S., Ishibashi, N. & Masuda, S. 1997 The mechanism of momentum transfer enhancement in periodically perturbed turbulent separated flow. In 2nd Int. Symp. on Turbulence, Heat and Mass Transfer, Delft, The Netherlands, pp. 835–844.
- Obi, S., Ohizumi, K. & Masuda, S. 1993b Turbulent separation control in a plane asymmetric diffuser by periodic perturbation. In *Engineering Turbulence Modeling and Experiments* 2, pp. 3633–642.
- Perry, A. E. & Fairlie, B. D. 1975 A study of turbulent boundary-layer separation and reattachment. *J. Fluid Mech.* **69**, 657–672.
- RAFFEL, M., WILLERT, C. & KOMPENHANS, J. 1997 Particle Image Velocimetry, A practical guide. Springer Verlag.
- RUDERICH, R. & FERNHOLZ, H. H. 1975 An experimental investigation of a turbulent shear flow with separation, reverse flow, and reattachment. *J. Fluid Mech.* **163**, 283–322.

Simpson, R. L. 1989 Turbulent boundary-layer separation. Ann. Rev. Fluid Mech. 21, 205-234.

Paper 8

Measurements in a plane asymmetric diffuser with 8.5° opening angle. Part II: Comparison with model predictions for turbulence characteristics

By Olle Törnblom, Björn Lindgren, Johan Gullman-Strand and Arne V. Johansson

Dept. of Mechanics, KTH, SE-100 44 Stockholm, Sweden

To be submitted

The separating turbulent flow in a plane asymmetric diffuser is studied experimentally. Careful measurements of the velocities have been made in all three spatial directions. The Reynolds number based on the inlet channel height and friction velocity was Re_{τ} =2000. Emphasis is put on the study of the turbulence in the diffuser. The Reynolds-stress anisotropies and the corresponding anisotropy invariants are calculated and studied. The production terms in the transport equations for the Reynolds stresses are investigated. Comparisons with RANS-solutions using the Wallin & Johansson (2000) explicit algebraic Reynolds stress model (EARSM) are made. It is observed that the EARSM under-predicts the size of the separation bubble. The size of the predicted bubble is approximately 60% of the measured one and the main reason for this is the large level of wall-normal turbulence intensity predicted by the EARSM at the diffuser inlet.

1. Introduction

This is the second part of a study of the flow in an asymmetric plane diffuser with an opening angle of 8.5°. Here, we will concentrate our work on evaluating measurement data for quantities that are particularly interesting in turbulence modelling. The aim is to provide new insight into the dynamics that are essential in the modelling of this flow, and thereby help in testing existing models or in the development of new models. We will compare the measurement data with an Explicit algebraic Reynolds stress model (EARSM) calculation, based on the code presented in Gullman-Strand (2002).

The first part of this study entitled Measurements in a plane asymmetric diffuser with an 8.5° opening angle. Part I: General flow characteristics (Lindgren et al. (2002)) concentrated on the general flow characteristics of this

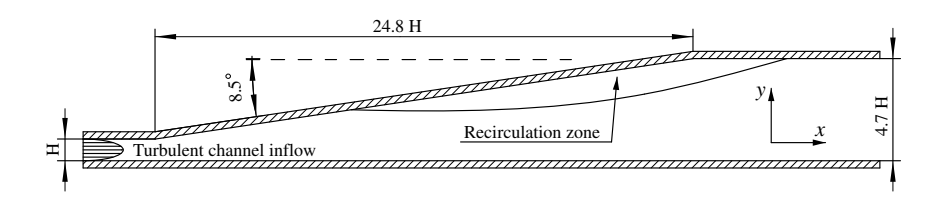


FIGURE 1. The measurement section of the wind-tunnel. A part of the inlet channel is seen to the left and part of the outlet channel is seen to the right.

diffuser flow such as mean velocity and turbulence intensity in the three spatial directions. It also includes measures of the extension of the separation bubble, its character and strength and the average pressure distribution. For information hereabout we refer to that paper. In this paper we focus on turbulence statistics which are compared with predictions based on RANS computations carried out by the third author.

The diffuser used in both these studies has one inclined wall with an opening angle of 8.5°. The opposite wall is straight, see figure 1. The diffuser is preceded by a 3.2 m channel with a height of 30 mm and a width of 1525 mm. This ensures fully developed turbulent channel flow as inlet condition into the diffuser (see e.g. Comte-Bellot (1965)). It is important when computations and experiments are compared, to have a well defined inlet condition. The diffuser is followed by a 2.5 m long outlet channel which is 141 mm high and 1525 mm wide. The purpose is here to minimize upstream influence from disturbances from other wind-tunnel parts located further downstream. The primary measurement techniques used are Particle Image Velocimetry in the streamwise wall-normal plane and Laser Doppler Velocimetry in the spanwise direction. An advantage of these measurement techniques is that they can measure both direction and absolute value of a fluid particle which is necessary when there is back-flow involved. The Reynolds number based on the inlet channel height and the friction velocity is 2000.

The flow in the diffuser is characterized by a long thin separation bubble located at the inclined wall. The separation point is located about 9 channel heights downstream the diffuser inlet and the reattachment point is located 31 inlet channel heights downstream the inlet channel (see Lindgren et al. (2002)). The maximum thickness of the separation bubble is approximately 1.6 inlet channel heights occurring at the end of the diffuser.

Some numerical studies on this geometry have been performed previously. However, all these studies used a geometry with a larger opening angle (10°) than that in the present study. An extensive numerical study of the plane asymmetric diffuser flow was made by Kaltenbach et al. (1999), who performed a large eddy simulation at a Reynolds number of 1000 based on the inlet channel height and the inlet friction velocity. Their data showed good agreement with the Buice & Eaton (1997) experimental data for velocity profiles. The point of separation also agreed well but some discrepancy was found in the location of the reattachment point. A possible reason for this can be the relatively small spanwise width of the computational domain which may tend to artificially enhance spanwise coherence of large scale structures. Kaltenbach et al. (1999) found that the sub-grid scale model plays an essential role to calculate the flow correctly, since sub-grid stresses are a major contribution to the wall-shear stress. The sub-grid scale model must also adapt to the increase in turbulence level in the downstream part of the diffuser.

Other numerical studies involving more or less advanced closures based on eddy-viscosity models, (differential) Reynolds stress models (RSM) and EARSM models have been performed by a number of research groups. For instance, Apsley & Leschziner (1999) tested a number of linear and non-linear eddy viscosity models as well as differential stress-transport models. They found that strain dependent coefficients and anisotropy resolving closures are needed. However no models tested were capable to resolve all flow features in the diffuser. Apsley & Leschziner (1999) also points out the possibility to encounter problems related to the "flapping" motion of the unsteady separation.

In an Ercoftac workshop (Hellsten & Rautaheimo (1999)), different numerical approaches with varying turbulence models were used and compared to the Buice & Eaton (1997) data-base. Models used comprised $k-\varepsilon$, $k-\omega$, RSM and LES. The agreement was, for the more simple models, in general fairly poor due to the complex flow in the diffuser.

The plane asymmetric diffuser has also been used as a test case for commercial codes. The investigation performed by Iaccarino (2000) aimed at finding the limits of the versatile commercial codes in this complex geometry. The codes tested were CFX, Fluent and Star-CD. Two turbulence models were tested, $(k-\varepsilon)$ and $\overline{v^2}-f$ for the three codes. The results were compared to the Obi et al. (1993) and Buice & Eaton (1997) data-bases. The $k-\varepsilon$ model was unable to capture the recirculation zone but the $\overline{v^2}-f$ model did so with an accuracy in separation length of 6%. The agreement for the friction coefficient was also fairly good.

As is seen above, an ample amount of numerical tests of closures in plane asymmetric diffusers exists already today. Some of the major challenges in turbulence modelling are related to near-wall turbulence and pressure-gradient induced separation, phenomena which are represented in an ideally generic manner in the plane asymmetric diffuser flow. The present choice of opening angle ensures a separation-free flow near the straight wall, and the aspect ratio

together with end-wall boundary layer control measures ensure a high degree of spanwise uniformity. This makes the present case ideal for detailed tests of turbulence modelling aspects that may require a high degree of accuracy in the turbulence statistics to evaluate differences in modelling approaches among high-level single-point closures, and sub-grid scale models in the LES-approach. The presently created data-base, containing information on all velocity components and related second order statistics, would, for instance, be well suited for tests of modern nonlinear RSM:s and newly developed approaches, including curvature corrections etc, within the concept of EARSM.

2. Turbulence models

2.1. The RANS equations

The by far most common approach to compute turbulent flows is to decompose the velocity and pressure field into a mean and a fluctuating part, and form equations for the mean velocity and single-point turbulence statistics. This approach is called the Reynolds decomposition and a detailed explanation of this standard technique can be found in *e.g.* Johansson & Burden (1999). The (incompressible) RANS equations,

$$\frac{\partial U_i}{\partial t} + U_j \frac{\partial U_i}{\partial x_i} = -\frac{1}{\rho} \frac{\partial P}{\partial x_i} + \frac{\partial}{\partial x_j} \left(2\nu S_{ij} - \overline{u_i' u_j'} \right) \tag{1}$$

$$\frac{\partial U_i}{\partial x_i} = 0,\tag{2}$$

which govern the ensemble averaged velocities (U_i) and the average pressure (P) are identical to the corresponding Navier-Stokes equations for the instantaneous velocities and pressure with one important exception, the Reynolds stress term. Since the flow considered is incompressible, we will consider the kinematic Reynolds stress tensor $-R_{ij} \equiv -\overline{u_i'u_j'}$, where u_i' are the velocity fluctuations. The aim of single point closures is to construct a closed set of equations for this quantity, to be inserted into equations 1. An ensemble average is herein denoted with a bar over the respective quantity.

2.2. Eddy-viscosity based two-equation models

In CFD for engineering applications, the by far most commonly used method of closing the RANS set of equations is the eddy-viscosity based two-equation model approach. The eddy-viscosity hypothesis, introduced by the French physicist and mathematician V.J. Boussinesq in 1877, approximates the increased diffusivity due to turbulence by using a turbulent viscosity (ν_T), analogous to the well known kinematic viscosity for a Newtonian fluid. Using the eddy-viscosity hypothesis the Reynolds stresses are approximated by

$$-\overline{u_i'u_j'} = 2\nu_T S_{ij} - \frac{2}{3}K\delta_{ij}.$$
 (3)

Where $K \equiv \overline{u_i'u_i'}/2$ is the turbulence kinetic energy and $S_{ij} \equiv (U_{i,j} + U_{j,i})/2$ is the mean rate of strain tensor. By simple dimensional analysis it is easy to see that in order to estimate the turbulent viscosity one needs to know at least one time (or velocity) scale and one length scale of the turbulence. In so called two-equation models these scales are determined by solving transport equations for two turbulence quantities. Usually one of these quantities is the turbulence kinetic energy K and the other can be e.g. the dissipation rate of turbulence kinetic energy ε , or the inverse timescale of the most energetic eddies ω .

Such standard two-equation models can be reasonably accurate for predicting attached flows without large influences from mean flow streamline curvature or system rotation and the inclusion of two transport equations for turbulence quantities means that some history effects of the turbulence can be captured. In the Boussinesq hypothesis there is no dependence of the stresses on the rotation rate tensor $(\Omega_{ij} \equiv (U_{i,j} - U_{j,i})/2)$, a deficiency which can influence the ability to predict e.g. separating flows. A more elaborate description of eddy-viscosity based two-equation models can be found in e.g. Wilcox (1993) and Johansson & Burden (1999).

2.3. Differential Reynolds stress models (DRSM)

A straightforward way to generalize the modelling approach as compared to the two-equation model approach, is to introduce the transport equations for the Reynolds stresses

$$\frac{DR_{ij}}{Dt} = \mathcal{P}_{ij} - \varepsilon_{ij} + \Pi_{ij} + \mathcal{D}_{ij}. \tag{4}$$

Such a model is referred to as a differential Reynolds stress model (DRSM) and pioneering work on this kind of model was done by Launder *et al.* (1975). Due to the symmetric nature of R_{ij} , six equations plus one for a turbulence 'length' scale, has to be solved in 3D flow problems. The production term \mathcal{P}_{ij} is explicit in the Reynolds stresses and the mean velocity gradient tensor and does not have to be modelled within this modelling context.

The trace of the dissipation rate tensor ε_{ij} is usually determined by an extra transport equation for ε which is also used to determine the turbulent 'length' scale, and the anisotropy of the dissipation rate is often assumed to be negligible or modelled through use of the Reynolds stress anisotropies.

The pressure strain rate tensor Π_{ij} is a correlation between the fluctuating pressure and the fluctuating strain rate. This term represents the intercomponent redistribution of the Reynolds stresses and its modelling is a key element in this type of closure. The models are based on solutions of the Poisson equation for the fluctuating pressure. The diffusion term \mathcal{D}_{ij} is normally modelled with a gradient diffusion formulation.

In a DRSM much more of the turbulence physics are of course captured as compared to a two-equation eddy-viscosity model, but at the prize of five more equations to solve. As an alternative, the performance of a two-equation model can be improved if the eddy-viscosity approach is abandoned and the transport equations for the Reynolds stresses are approximated with an algebraic equation for the Reynolds stress anisotropy tensor.

2.4. Explicit algebraic Reynolds stress models (EARSM)

From equation 4 an equation for the Reynolds stress anisotropy tensor can be derived. The Reynolds stress anisotropy tensor is defined as

$$a_{ij} \equiv \frac{\overline{u_i' u_j'}}{K} - \frac{2}{3} \delta_{ij}. \tag{5}$$

Assuming that the flow is in so called 'weak equilibrium' one can discard the advection and diffusion terms in the transport equation for the anisotropy tensor. Weak equilibrium means that the timescale on which the anisotropy relaxes to some quasi-equilibrium state prescribed by the mean flow and the turbulent scales, is small. If the pressure-strain rate and dissipation rate anisotropy are modelled in terms of S_{ij} , Ω_{ij} , a_{ij} and the turbulence velocity and length-scales (e.g. K and ε), the weak equilibrium assumption implies that the Reynolds stress anisotropy is completely determined by the local values of the mean strain and rotation rate tensors (normalized by the turbulence time scale), i.e.

$$f_{ij}(\mathbf{a}, \mathbf{S}^*, \mathbf{\Omega}^*) = 0. ag{6}$$

Equation 6 represents an implicit relation between the anisotropy tensor (a) and the normalized strain (\mathbf{S}^*) and rotation rate ($\mathbf{\Omega}^*$) tensors. The weak equilibrium assumption does not hold in slowly distorted turbulence where $\mathcal{P}/\varepsilon \ll 1$, e.g. in the outer part of a boundary layer or in the center of a jet or a channel-flow.

Using the weak equilibrium assumption together with isotropic assumption for the dissipation rate tensor and linear model for the pressure strain rate tensor one can derive an explicit algebraic equation for the anisotropy (see e.g. Gatski & Speziale (1993) and Wallin & Johansson (2000)), i.e.

$$a_{ij} = a_{ij}(\mathbf{S}^*, \mathbf{\Omega}^*). \tag{7}$$

This equation depends exclusively on the mean flow, or more precisely on the mean strain-rate and rotation-rate tensors. Such an expression requires very little effort to be evaluated, so the increase in computational effort for an EARSM compared to a standard two-equation model is almost negligible. The explicit expression is also a good way of ensuring robustness of the computational scheme.

The EARSM has several advantages over an ordinary eddy-viscosity based two-equation model, where

$$a_{ij} = 2C_{\mu}S_{ij}^{*}. (8)$$

The EARSM has been shown to improve near-wall behavior and thereby reduce the need for near-wall damping, as compared to eddy-viscosity models. Effects of system rotation and streamline curvature can also be captured in the EARSM:s through extensions analyzed by e.g. Girimaji (1997) and Wallin & Johansson (2002). Curvature corrections are not included in the model used for comparisons herein.

3. Results

In this section results from the analysis of the turbulence data are presented and comparisons with computations are made. For a detailed description of the experiment, the mean flow and the Reynolds stresses, consult Lindgren *et al.* (2002) and for details on the computational aspects, consult Gullman-Strand (2002).

The numerical results have been obtained using a finite element code solver created by an automated code generation procedure, first described by Amberg et al. (1999). The system of equations are the RANS equations with the Wallin & Johansson (2000) combined with the Wilcox low-Re $K-\omega$ formulation. The RANS equations were solved in a time-dependent fractional step scheme described by Guermond & Quartapelle (1997) and a decomposition of $\omega = \tilde{\omega} + \omega_w$ decreased the demand of grid resolution close to the walls. A more detailed description of the code generation procedure, formulation of the equations and solution strategy can be found in Gullman-Strand (2002).

The geometry used in the computations were identical to the experiments with respect to diffuser angle and height ratio but with inlet and outlet lengths of $10\ x/H$ and $60\ x/H$ respectively. The mesh was a structured triangular grid with 318 nodes in the streamwise direction, of which 100 were located in the diffuser and 75 nodes stretched in the wall-normal direction. The short inlet channel was possible since the turbulent channel inlet conditions were calculated by the same code but in a separate channel geometry, consistent with the guidelines of Hellsten & Rautaheimo (1999) for the 10° case.

To facilitate interpretation most of the data presented in this section have been plotted in the diffuser geometry, in all these plots the axis scales are x/H and y/H in the horizontal and vertical directions respectively, where H is the inlet channel height. Velocities are normalized with $U_{\rm b}$, being the inlet channel bulk velocity.

3.1. Mean velocities

A comparison of profiles of the streamwise average velocity can be seen in figure 2, the most noticeable difference between the computation and the measurements is that the separation bubble in the computation is much thinner. The maximum thickness of the recirculation zone is only 60% of that of the

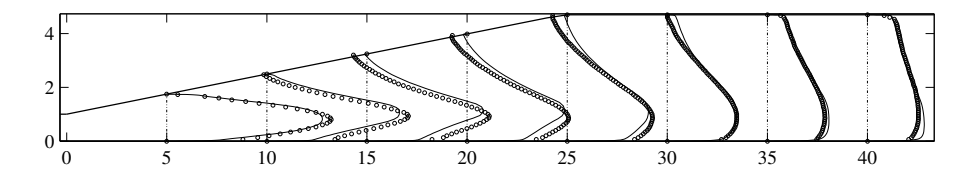


FIGURE 2. The mean velocity in the streamwise direction for experiment (\circ) and EARSM (—); $10\frac{U}{U_0} + \frac{x}{H}$.

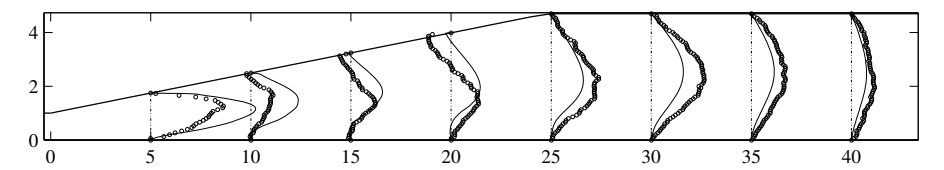


FIGURE 3. The mean velocity in the wall-normal direction for experiment (\circ) and EARSM (—); $100\frac{V}{U_{\rm h}} + \frac{x}{H}$.

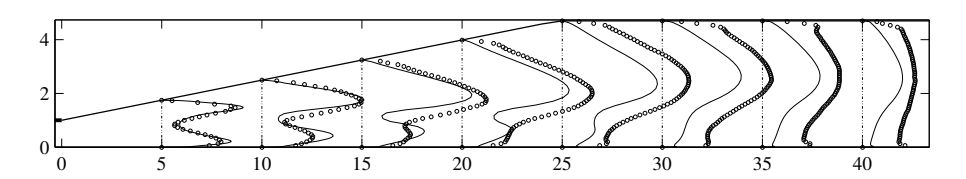


FIGURE 4. The turbulence kinetic energy for experiment (o) and EARSM (—); $400 \frac{K}{U_{\rm p}^2} + \frac{x}{H}$.

measured separation. This discrepancy has a large influence on the whole flow-field. Since the smaller separation bubble constitutes a smaller displacement the whole flow-field is shifted towards the inclined wall as compared to the measured field. The experimentally determined separation point is located at x/H=9 while in the computation it is at x/H=11. The height of the computed bubble also grows much slower in the downstream direction than the measured. The reattachment points are located at x/H=31 and x/H=27 for the experiment and the computation respectively.

The wall-normal mean velocity in figure 3 is highly affected by the smaller separation zone in the simulation since the flow follows the inclined wall more closely. Accordingly it is larger than in the experiments in the diverging part of the diffuser and smaller in the exit channel where the flow is attached.

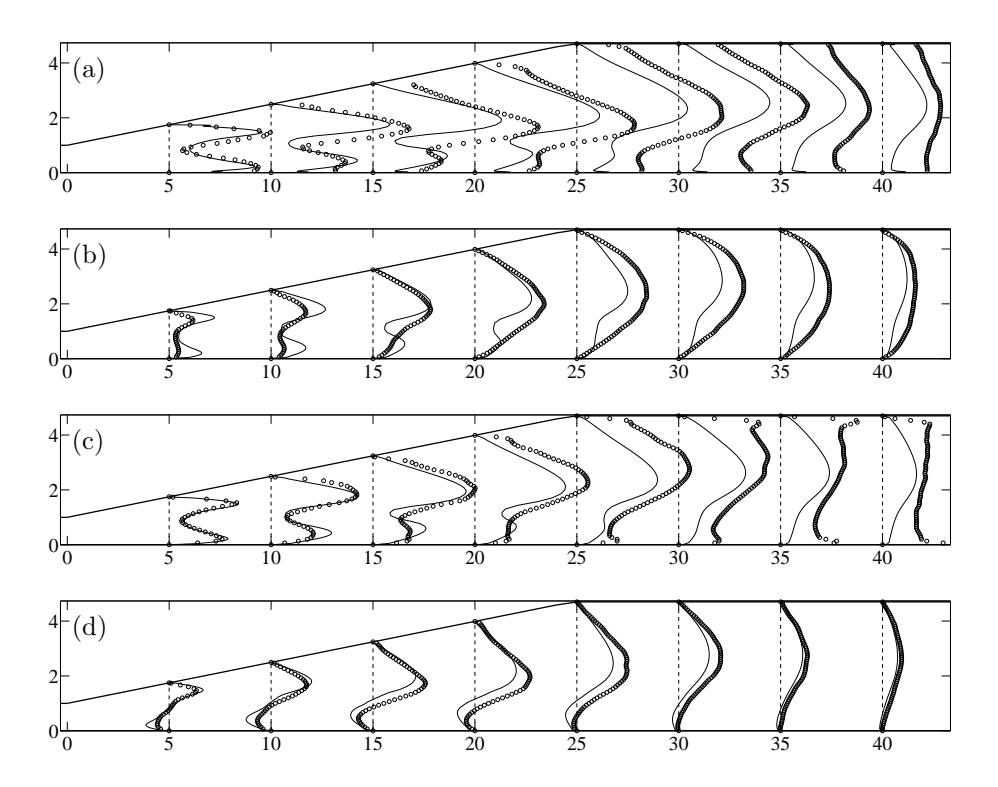


FIGURE 5. Measured (\circ) and computed (\longrightarrow) variance of turbulent fluctuations and Reynolds shear stress; (a) $\overline{u'^2}$, (b) $\overline{v'^2}$, (c) $\overline{w'^2}$ and (d) $\overline{u'v'}$, displayed as $500\frac{\overline{u'_iu'_j}}{U_b^2} + \frac{x}{H}$.

3.2. Turbulence intensities and Reynolds shear stress

There is good agreement for the turbulence kinetic energy K (see Figure 4) at the first station, at x/H=5, when neither the simulated nor the experimental flow has separated. The agreement then deteriorates further downstream. In general the turbulent kinetic energy is smaller in the simulation, something which might be attributed to the lower levels of shear in the region outside the separation bubble. The mean velocity profiles at x/H=35 in figure 2 are very similar but the simulated K-levels at the same position are much smaller than the measured. This indicates that the supply of turbulent kinetic energy to this position from upstream positions is underestimated.

Looking closer into the components of K, shown in figure 5a–d, one can see that the computed $\overline{v'^2}$ is larger than the measured at the beginning of the

FIGURE 6. Measured Reynolds stress production rates; \mathcal{P}_{11} (—), \mathcal{P}_{22} (- - -) and \mathcal{P}_{12} (· · ·), displayed as $1000\frac{\mathcal{P}_{ij}H}{U_s^2} + \frac{x}{H}$.

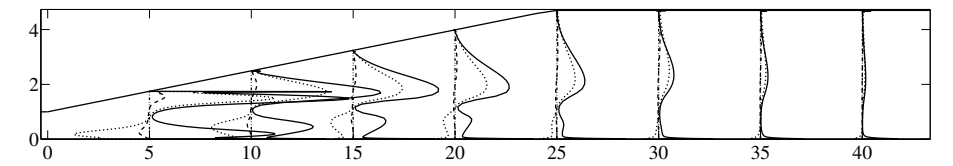


FIGURE 7. Calculated Reynolds stress production rates; \mathcal{P}_{11} (—), \mathcal{P}_{22} (- - -) and \mathcal{P}_{12} (· · ·), displayed as $1000\frac{\mathcal{P}_{ij}H}{U_{\rm b}^3} + \frac{x}{H}$.

diffuser, at the same location $\overline{u'}^2$ is slightly under-estimated in the computations while the peak heights of $\overline{w'}^2$ agree well. The experimental data show broader and higher variance peaks in the shear-layer over the separated region at the end of the diverging section than the computations, which is natural due to the larger separation bubble, while the peak near the plane wall is more accentuated in the computations. This is extra obvious in the profiles of $\overline{w'}^2$. The agreement of $\overline{u'v'}$ between the measurements and the computations is good except at the first two positions, where it is over-estimated in the computations near the inclined wall.

3.3. Reynolds stress production

The turbulent stresses in a flow produce new turbulence by interaction with the mean rates of strain and rotation

$$\mathcal{P}_{ij} = -\overline{u_i' u_k'} \frac{\partial U_j}{\partial x_k} - \overline{u_j' u_k'} \frac{\partial U_i}{\partial x_k}.$$
 (9)

In the plane asymmetric diffuser flow, there is homogeneity in the spanwise direction, so only \mathcal{P}_{11} , \mathcal{P}_{22} and $\mathcal{P}_{12} = \mathcal{P}_{21}$ are non-zero. Hence, all turbulent energy in the spanwise component $(\overline{w'w'})$, which is fairly high (see figure 5) has been redistributed from the two other components via the pressure strain rate term in equation 4, illustrating the importance of adequate modelling of Π_{ij} .

Figure 6 shows the three non-zero components of the production rate tensor. The highest production rates are found in the 11-component in the strong shear-layer above the separation bubble. This is due to the high level of mean

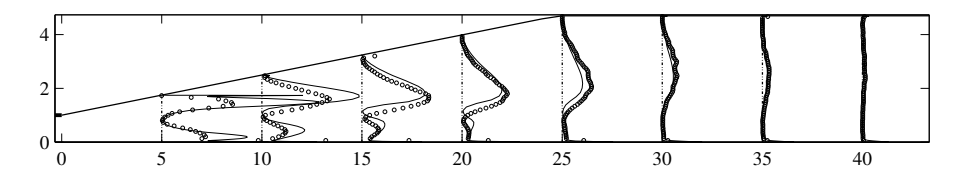


FIGURE 8. Turbulence kinetic energy production rate, \mathcal{P} ; experiment (o), EARSM (—), displayed as $1500\frac{\mathcal{P}H}{U_{\circ}^{2}} + \frac{x}{H}$.

shear $(\partial U/\partial y)$ in combination with the peak in $\overline{u'v'}$ at this location cf. figure 5. Almost no production of the 11-component takes place at the location of the maximum peak for the streamwise velocity, which is consistent with the small mean shear in that region. For the \mathcal{P}_{12} -component the maximum peak is located at the same position as for the \mathcal{P}_{11} -component, also due to the high mean shear, but its strength is only about 60% of the 11-peak. The \mathcal{P}_{12} -component cross the zero level at the y-position where the streamwise mean velocity peaks and has a minimum in the 'boundary layer' on the straight wall. Compared to the other two components the \mathcal{P}_{22} -component is very small. At some locations this component attains negative values due to the deceleration of the flow along the plane wall. At the most downstream profile all production components are very small due to the very flat mean velocity profile here.

Figure 7 shows the computed components of the production rate tensor. All three components are significantly overestimated at the two most upstream positions, while the agreement is better further downstream.

In figure 8, a comparison is made for the production rates of turbulence kinetic energy (\mathcal{P}) . In the first profiles at x/H=5 and 10 the EARSM substantially overestimates the production rate. The peak levels are almost twice those of the experiment at the most upstream position. However, since the K levels in this region agree well, the dissipation rate must also be overestimated. The shift of the EARSM profiles towards the inclined wall can, of course, be observed in \mathcal{P} too. Further downstream the predicted production rate decreases in amplitude faster than the measured and this can explain why the produced quantity, K, is underestimated in the downstream part of the diffuser and in the exit channel.

3.4. Reynolds stress anisotropy tensor

The a_{ij} -tensor has two independent scalar measures which are invariant to the choice of coordinate system. These are defined as

$$II_a \equiv a_{ij}a_{ji} \quad \text{and} \quad III_a \equiv a_{ij}a_{jk}a_{ki},$$
 (10)

and are referred to as the second and third anisotropy invariants respectively. The experimental determination of these scalar measures is quite sensitive since

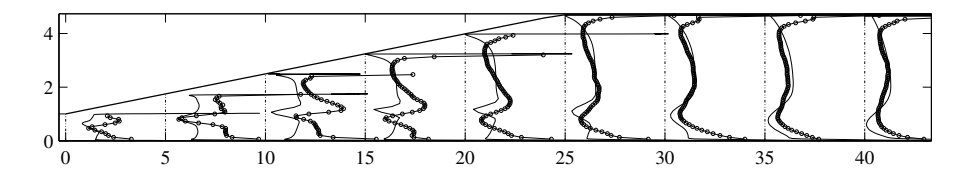


FIGURE 9. The second invariant of the turbulence anisotropy tensor for experiment (\circ) and EARSM (—); $5II_a + \frac{x}{H}$.

an error in the rms of the fluctuating velocity is taken to the fourth and sixth power in II_a and III_a , respectively.

Figure 9 shows the variation of II_a over the cross section at different streamwise positions in the diffuser. Throughout the whole diffuser II_a has maxima near the walls due to the damping of the wall-normal turbulence intensity. A minimum is also found in all II_a -profiles at the same y-position as the maximum U-velocity. The low levels of shear here allows the turbulence to relax and become more isotropic. The position of the maximum in II_a lies directly above the minimum in the positive y-direction. This is in between the locations of the maximum shear and the maximum velocity.

Figure 10 shows the four non-zero Reynolds stress anisotropy components. The streamwise component a_{11} is generally the largest, the only exception to this is found far downstream close to the wall were the spanwise component is larger. The wall-normal component a_{22} is negative at all positions, signifying a $\overline{v^2}$ content smaller than 2/3 of the kinetic energy. The perhaps most obvious discrepancy of the computed data in figure 11 as compared to the measurements is that the computed a_{33} is identically zero making a_{22} a mirror image of a_{11} , this approximation in the EARSM is not altogether valid for this flow according to the measurements.

The second invariant of the Reynolds stress anisotropy tensor II_a is compared in figure 9. At the first station, where the computed profile of the turbulence kinetic energy agrees well with the experimental values, the second invariant is severely underestimated. The large difference between the streamwise and the wall-normal turbulence components (c.f. figure 10) is not captured correctly. The position and value of the minimum near the center is well predicted but the high levels of anisotropy on either sides of the minimum are underestimated. This underestimation of the anisotropy comes from an overestimation of the wall-normal velocity fluctuations ($v_{\rm rms}$) by the EARSM in the region near the upstream corner of the inclined wall. The fact that the EARSM overestimates the $v_{\rm rms}$, and also $\overline{u'v'}$ slightly, in the beginning of the diffuser is probably the reason for the delayed separation. This overestimation can in turn be a consequence of the omission of streamline curvature effects in this particular model. An addition of a curvature correction would reduce

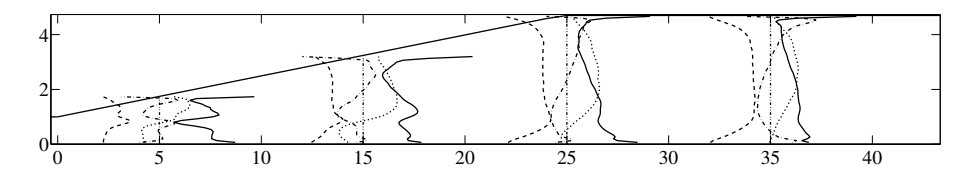


FIGURE 10. Measured Reynolds stress anisotropies; a_{11} (—), a_{22} (- - -), a_{33} (- · -) and a_{12} (· · ·), displayed as $5a_{ij} + \frac{x}{H}$.

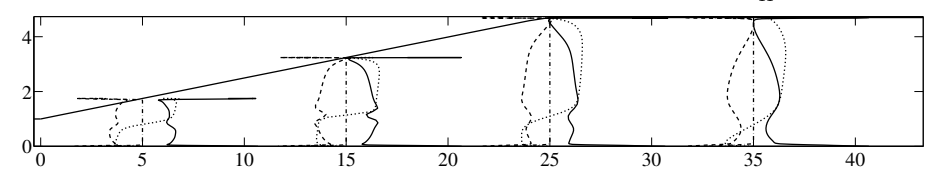


FIGURE 11. Computed Reynolds stress anisotropies; a_{11} (—), a_{22} (- - -), a_{33} (- · -) and a_{12} (· · ·), displayed as $5a_{ij} + \frac{x}{H}$.

the turbulence levels near the upstream corner of the inclined wall. Further downstream at the stations x/H=10–25 the maximum values of the experimental anisotropy is gradually decreased and the quantitative agreement with the computations is increased, but on the other hand the discrepancy in the location of the minimum peak increases due to the smaller separation bubble in the computation. The best agreement is found at the most downstream stations in the exit channel, but the behavior close to the walls is, as in all profiles, quite different. The measured second invariant increases more slowly with increasing distance from the walls as compared to the computed invariant.

The pressure distributions on the plane wall are plotted in 12, normalized with a dynamic pressure based on the inlet channel bulk velocity. They clearly reflect the difference in strength of the separation. The EARSM gives a slightly higher pressure recovery than the experiment and the effects of displacement by the separation bubble are much smaller.

4. Concluding remarks

The plane asymmetric diffuser with 8.5° opening angle has shown to be a challenging flow case for turbulence model testing with several important phenomena, e.g. flow separation and reattachment, highly anisotropic turbulence, high levels of turbulence and some streamline curvature effects. These complex flow phenomena all occur within a relatively simple two-dimensional geometry. The smaller angle of the diffuser compared to that (10°) in the earlier experiments by Obi et al. (1993) and Buice & Eaton (2000) seems to give a separation which is even more difficult to predict and hence constitutes a truly challenging test case for turbulence closures.

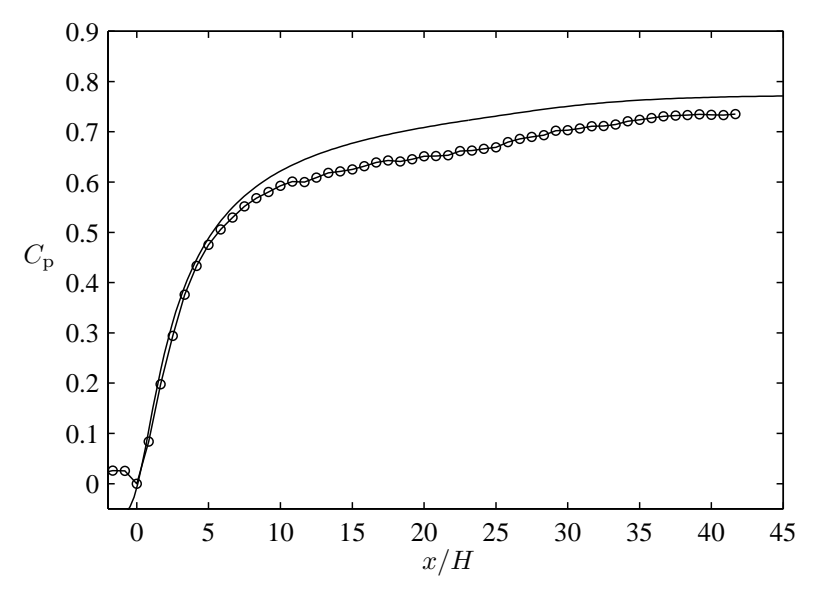


FIGURE 12. Comparison between the measured pressure distribution (\circ) and the EARSM (—).

The data-base of measurements has proven to be useful for comparison with computations, but more data from the near-wall regions are desirable. Especially in the region near the upstream corner of the inclined wall where streamline curvature is suspected to influence the turbulence. Furthermore, Kaltenbach et al. (1999) noted in an LES-calculation that a very small separated region formed in the viscous layer in this region. Accurate modelling and fine resolution of the flow in this region is crucial in order to obtain the correct behavior of the separating boundary layer on the inclined wall.

The EARSM manages to predict a separation bubble, but the size of it is not in close agreement with the measurements. The main reason for this is believed to be the overestimation of v_{rms} in the beginning of the diffuser. This can be related to the above-mentioned complicated flow in this region. The curvature correction described in Wallin & Johansson (2002) has not been implemented in the EARSM with which the comparisons are made. Adding curvature corrections would reduce the overestimated Reynolds-stress components at the inclined wall. History effects related to advection of the anisotropy along streamlines may also be of influence here. To account for these a DRSM modelling approach would be the normal choice.

However, Apsley & Leschziner (1999) tested four different DRSM:s on the 10° case, two of the models used wall functions and two were low Reynolds number models, without getting satisfying results. It was argued that the

difficulties related to the modelling of the wall-asymptotic behavior could be a reason. This would indicate that a DRSM with nonlinear models for Π_{ij} etc. would be interesting for this case. The DRSM of Sjögren & Johansson (2000) is such a model that has been proven to satisfy near-wall asymptotic behaviors through satisfaction of strong realizability. Apsley & Leschziner (1999) also mention the possible problem of periodic shear-layer instabilities provoked by the upstream corner of the diffuser as a reason for the general failure of all models to resolve the initial development of the boundary layer on the inclined wall.

5. Acknowledgement

The authors would like to thank Ulf Landén for aiding in the manufacturing of the wind-tunnel and measurement equipment. The Swedish Research Council, The Swedish Energy Agency and the Integral Vehicle Structures research school are gratefully acknowledged for their financial support.

References

- Amberg, G., Törnhardt, R. & Winkler, C. 1999 Finite elemet simulations using symbolic computing. *Mathematics and Computers in Simulation* 44, 275–274.
- Apsley, D. D. & Leschziner, M. A. 1999 Advanced turbulence modelling of separated flow in a diffuser. Flow, Turbulence and Combustion 63, 81—112.
- Buice, C. U. & Eaton, J. K. 1997 Experimental investigation of flow through an asymmetric plane diffuser. *Tech. Rep.*. Department of mechanical engineering, Stanford university.
- Buice, C. U. & Eaton, J. K. 2000 Experimental investigation of flow through an asymmetric plane diffuser. *J. of Fluids Eng.* **122**, 433–435.
- COMTE-BELLOT, G. 1965 Écoulement turbulent entre deux paroix parallèles. Publications scientifiques et techniques 419. Ministère de l'air, 2, Avenue de la Porte-d'Issy, Paris.
- GATSKI, T. B. & SPEZIALE, C. G. 1993 On explicit algebraic stress models for complex turbulent flows. J. Fluid Mech. 254, 59–78.
- GIRIMAJI, S. S. 1997 A Galilean invariant explicit algebraic Reynolds stress model for turbulent curved flows. Phys. Fluids 9, 1067–1077.
- Guermond, J. L. & Quartapelle, L. 1997 Calculation of incompressible vicous flow by an unconditionally stable projection FEM. *Journal of Computational Physics* **132** (CP965587), 12–33.
- Gullman-Strand, J. 2002 Turbulence modeling using automated code generation applied to asymmetric diffuser flow. Dept. of mechanics, KTH, Stockholm, Sweden, licentiate thesis.
- Hellsten, A. & Rautaheimo, P., ed. 1999 Workshop on refined turbulence modelling. ERCOFTAC/IAHR/COST.

- IACCARINO, G. 2000 Prediction of the turbulent flow in a diffuser with commercial CFD codes. *Tech. Rep.*. Center for Turbulence Research.
- JOHANSSON, A. V. & BURDEN, A. D. 1999 An introduction to turbulence modelling. In *Transition, Turbulence and modelling* (ed. A. Hanifi, P. Alfredsson, A. Johansson & D. Henningsson), chap. 4. Kluwer academic publishers.
- Kaltenbach, H.-J., Fatica, M., Mittal, R., Lund, T. S. & Moin, P. 1999 Study of flow in a planar asymmetric diffuser using large-eddy simulation. *J. Fluid Mech.* **390**, 151–185.
- Launder, B., Reece, G. & Rodi, W. 1975 Progress in the development of a Reynolds-stress turbulence closure. *J. Fluid Mech.* 41.
- LINDGREN, B., TRNBLOM, O. & JOHANSSON, A. V. 2002 Measurements in a plane asymmetric diffuser with 8.5° opening angle. part I: General flow characteristics. To be submitted .
- OBI, S., AOKI, K. & MASUDA, S. 1993 Experimental and computational study of turbulent separating flow in an asymmetric plane diffuser. In *Ninth Symp. on Turbulent Shear Flows*, p. 305. Kyoto, Japan.
- SJÖGREN, T. & JOHANSSON, A. V. 2000 Development and calibration of algebraic nonlinear models for terms in the Reynolds stress transport equations. *Phys. Fluids* 12 (6), 1554–1572.
- Wallin, S. & Johansson, A. V. 2000 An explicit algebraic Reynolds stress modell for incompressible and compressible turbulent flows. J. Fluid Mech. 403, 89–132.
- WALLIN, S. & JOHANSSON, A. V. 2002 Modeling streamline curvature effects in explicit algebraic Reynolds stress turbulence models. Int. J. of Heat and Fluid Flow. 23, 721–730.
- WILCOX, D. C. 1993 Turbulence modeling for CFD. DCW Industries Inc., USA.